UNIVERSITE ECOLOGIE BRETAGNE GEOSCIENCES LOIRE AGRONOMIE ALIMENTATION

UNIVERSITÉ DE NANTES

THÈSE DE DOCTORAT

UNIVERSITÉ DE NANTES
COMUE UNIVERSITÉ BRETAGNE LOIRE

École Doctorale N° 600
École doctorale Écologie, Géosciences, Agronomie et Alimentation
Spécialité : Planétologie

Par
Jonas L'HARIDON

Diagenetic processes on Mars: analysis by the ChemCam instrument on the Curiosity rover

Thèse présentée et soutenue à Nantes, le 29 novembre 2018
Unité de recherche : UMR CNRS 6112 LPG

Rapporteurs avant soutenance :

Bruno BOUSQUET	Professeur (HDR), Université de Bordeaux
Sylvain BOULEY	Maître de Conférences (HDR), Université Paris-Sud

Composition du Jury :

Président		
Examinateurs	Sylvestre MAURICE	Astronome 1ère classe, Observatoire Midi-Pyrénées
	Cathy QUANTIN-NATAF	Professeur (HDR), Université Claude Bernard Lyon 1
	Cécile FABRE	Maître de Conférences (HDR), Université de Lorraine
	Véronique CARRÈRE	Maître de Conférences (HDR), Université de Nantes
Dir. de thèse	Nicolas MANGOLD	Directeur de Recherches CNRS, LPG, Université de Nantes

This is Major Tom to Ground Control
I'm stepping through the door
And I'm floating in a most peculiar way
And the stars look very different today

For here
Am I sitting in a tin can
Far above the world
Planet Earth is blue
And there's nothing I can do

Though I'm past one hundred thousand miles
I'm feeling very still
And I think my spaceship knows which way to go

—David Bowie, “Space Oddity” (1969)

ACKNOWLEDGMENTS

At long last, the time comes for me to thank the long list of people that helped me get through with the Ph.D., one way or another.

I think the only way to start with is to thank the people without whom I would not even be writing these lines. First, I would like to thank my advisor, Nicolas Mangold, for giving me the opportunity to take part in such an incredible space adventure, only barely dreamed of as a kid. I can only hope that the bet you took in recruiting an earth-bound engineer to do a planetary researcher's work paid off in your mind. I would also like to thank Roger Wiens and Sylvestre Maurice, as ChemCam PI and Co-I, for putting such an impressive piece of technology in space and allowing me to explore some of the rocky mysteries of our red neighbor with it.

I would like to address special thanks to Sylvain Bouley and Bruno Bousquet for reviewing the manuscript. Thanks also to the other members of the jury, Cathy Quantin-Nataf, Cécile Fabre and Véronique Carrère, and again to Sylvestre Maurice for presiding over it.

I would then like to thank all the scientists and engineers on the MSL mission that work relentlessly to make sure that the rover stays in shape and always *curious* up there. Among them, I would also like to especially thank each of the ChemCam team members, on both sides of the Atlantic, for welcoming me in their midst. I have benefited greatly from the scientific interactions with my American colleagues Abigail Fraeman, Jeff Johnson, Frances Rivera-Hernandez, and Jens Frydenvang among others.

On the French side of the force, I am grateful to Olivier Gasnault for his constant support and kind words, and the tremendous amount of work he achieves daily for the ChemCam team. Olivier Forni and Jérémie Lasue for their insights on the inner workings of ChemCam. Agnes Cousin for her contagious optimism, wits, and spot-on remarks. Pierre-Yves for sharing his overextending passion for everything. Marion Nachon for paving the way as a fellow diagenetic enthusiast. Laetitia Le Deit for her patience and useful advices. Suzanne Schroeder for savvy discussions on the LIBS technique. William Rapin and Valérie Payré for setting the bar so high as fellow ChemCam students, as well as Gael David for his already impressive work on the team. And Erwin Dehouck for the fascinating discussions and for showing me the ropes in geochemistry.

In Nantes, I give my thanks to all members of the LPG laboratory. I notably thank Anne Gaudin and Jean-Pierre Lorand for bearing with the experimental setbacks at the start. Erwan Le Menn and Carole La for their help at that stage as well. Stéphane Le Mouélic for being such a passionate fellow LEGO enthusiast, and for introducing me with François Civet to the wonders of the virtual worlds. Thanks to my fellow Ph.D. students, postdocs and engineers for the support and the “good times” spent together. Fabien, Marion R., Dorine, Anais, Marion C., Filipe, Antoine T., Jasin, Antoine B., Camilo, Diego, Barbara, Gwénaël and many others!

Finally, I would thanks all my friends, for putting up with my expansive outer space rambling and legendary lack of tact. I daresay that I do not know half of you half as well as I should like, and I like less than half of you half as well as you deserve! I would also like to thank my family, brother, sister and parents for pretty much getting me to where I am today.

And thank you Sophie, big time.

RÉSUMÉ ÉTENDU

À travers l'observation du ciel nocturne et de la multitude d'étoiles qui le composent, l'humanité a vite pris la mesure des immensités qui s'étendent par-delà des frontières de notre planète. L'une des grandes questions qui ne cesse de hanter l'esprit des hommes sera par la suite de savoir si la Terre constitue le seul îlot de vie du cosmos, ou si d'autres formes de vie existent—ou ont pu exister—ailleurs. Depuis l'avènement de l'ère spatiale, nous nous sommes lancés dans l'exploration de ces espaces extra-terrestres, par le biais de sondes robotiques, afin d'apporter quelques éléments de réponse à cette question.

Dans le cadre de l'exploration du système solaire, l'une de nos voisines planétaires—Mars—fait l'objet d'une attention particulière. Cet intérêt est en partie dû à sa proximité avec la Terre et de la relative aisance avec laquelle les sondes spatiales peuvent en atteindre l'orbite ou la surface, par rapport aux autres corps du système solaire (excepté la Lune). Mais c'est surtout de par son histoire que Mars se distingue, probablement très similaire à celle de la Terre au cours du premier milliard d'années ayant suivi leur accrétion. En effet, il y a 3.7 milliards d'années, la vie est apparue à la surface de la Terre, même s'il n'en reste aujourd'hui que d'infimes traces dans ses archives géologiques. Sur Mars, les terrains anciens de son hémisphère sud, correspondant à cette époque, préservent quant à eux des indices morphologiques et minéralogiques d'une activité hydrologique importante en surface. L'étude géologique des roches sédimentaires formées dans ce contexte a notamment permis de reconstituer les conditions climatiques présentent lors de la sédimentation, et révèle ainsi que la surface de Mars a autrefois pu héberger des conditions potentiellement propices à l'apparition de la vie.

Pour autant, la formation de roches sédimentaires ne se limite pas au transport et au dépôt des sédiments, qui reflètent les conditions prévalant en surface, mais impliquent également les processus physico-chimiques par lesquels les sédiments sont transformés en roches après leur enfouissement—et qui constituent ensemble la diagénèse. Ces processus impliquent souvent des fluides circulant en profondeur, pouvant modifier la texture, la chimie et/ou la minéralogie des sédiments de manière significative bien après leur dépôt. Aussi, il apparaît nécessaire de prendre en compte le rôle de ces processus dans la formation des roches sédimentaires afin d'éviter des erreurs d'interprétations sur leurs environnements de dépôt et leur implications exo-biologiques.

Les travaux présentés dans ce mémoire de thèse s'intéressent précisément aux interactions fluides-roches lors de la diagénèse sur Mars, à travers l'étude des roches sédimentaires du site d'atterrissage de la dernière mission *in situ* en date, Mars Science Laboratory, et de son rover, *Curiosity*. En particulier, l'instrument ChemCam présent à son bord permet une mesure chimique à petite échelle, particulièrement adaptée à l'analyse d'éléments diagénétiques.

CHAPITRE 1 – LE CYCLE SÉDIMENTAIRE SUR MARS

Durant ces dernières décennies, les différentes missions orbitales et *in situ* ont catalogué les indices attestant d'une activité hydrologique sur Mars, et notamment en lien avec la formation de dépôts sédimentaires. Ces observations indiquent un changement climatique global sur Mars au cours de son histoire, marquant la transition d'une atmosphère primitive dense permettant la présence d'eau liquide en surface par le passé au climat aride et sec que l'on observe aujourd'hui.

En effet, les observations de réseaux de vallées dendritiques et de paléolacs dans les terrains du Noachien (> 3.7 milliards d'années) mais également dans certaines régions de l'Hespérien tardif (~3.1

milliards d'années) indiquent la présence d'anciens systèmes fluvio-lacustres. Par ailleurs, de nombreuses détections de minéraux hydratés (comme les argiles), datés du Noachien, impliquent une altération des minéraux primaires en présence d'eau liquide—liée à des processus supergènes (en surface), hydrothermaux (à température élevée) ou diagénétiques (en sub-surface). Enfin, les détections de sulfates à l'Hespérien (liés à des environnements de dépôts évaporitiques et/ou acides), et d'oxydes de fer anhydres dans les terrains plus récents de l'Amazonien (formés par l'altération lente en surface et en conditions arides) reflètent l'aridification progressive de la surface de la planète.

Par la suite, si les explorations *in situ* ont pu confirmer la présence de cette activité aqueuse en surface, elles ont également pu faire apparaître la complexité géologique des dépôts sédimentaires étudiés, invisible depuis l'orbite. Ainsi, les roches observées par les deux Mars Exploration Rovers (MER) ont subi des épisodes d'altérations successifs: liés à une activité hydrothermale dans le cas de *Spirit*, et à l'interaction avec des eaux souterraines lors de la diagénèse dans le cas d'*Opportunity*. Par ailleurs, sur le site de Meridiani Planum, *Opportunity* a démontré que les détections orbitales d'hématite ne sont pas liées à des conditions particulières lors de la sédimentation, mais sont associées à des concrétions diagénétiques d'hématite (communément nommées « blueberries ») qui, après exhumation, forment un dépôt résiduel par érosion différentielle de l'encaissant et recouvrent partiellement la surface.

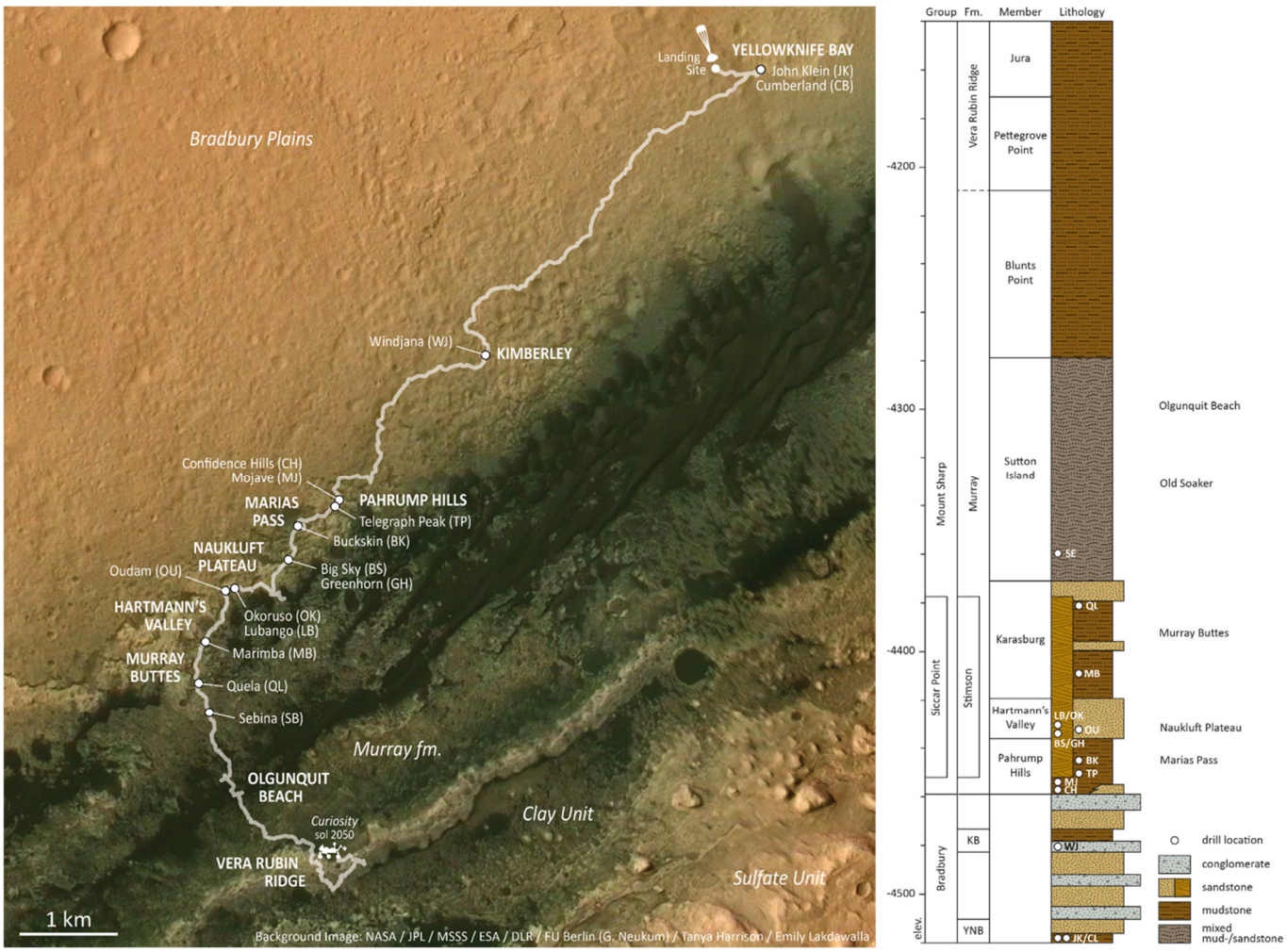

Figure A : Traverse du rover *Curiosity* (à gauche), depuis le site d'atterrissage nommé Bradbury jusqu'à sa position au sol 2050, au niveau de la terrasse topographique nommée Vera Rubin Ridge, après un parcours de près de 20 km de distance. Log stratigraphique (à droite) des faciès sédimentaires rencontrés par le rover. Le nom et l'acronyme des différents forages réalisés par le rover sont annotés.

Dans ce contexte, le rover *Curiosity* a atterri en 2012 au fond du cratère Gale, au nord-ouest des strates sédimentaires du mont Sharp qui en occupe le centre (Figure A). Ce site d'étude a été sélectionné en partie du fait de l'exposition d'une séquence stratigraphique de dépôts d'argiles et de sulfates, identifiée depuis l'orbite sur la base du mont Sharp. Ces détections, associées à la présence de nombreuses vallées fluviales incisant les remparts du cratère suggèrent que celui-ci abritait autrefois un paléolac. La datation de ces dépôts sédimentaires entre ~3.6 et 3.2 milliards d'années indique également que cette transition phyllosilicates – sulfates dans les roches sédimentaires retrace un changement climatique sur Mars lors de l'Hespérien [*Milliken et al.*, 2010].

Sur place, l'exploration des plaines du cratère (e.g. Yellowknife Bay) et des strates inférieures du mont Sharp (Murray formation) a permis d'attester d'une activité fluvio-lacustre prolongée par le passé, et de conditions potentiellement habitables, ayant perduré pendant plusieurs centaines de milliers d'années [*Grotzinger et al.*, 2015]. Cependant, les affleurements de Gale sont aussi imprégnés de figures diagénétiques (veines, nodules et concrétions) formées par la circulation de fluides en sub-surface et témoignant de l'évolution des sédiments après leur dépôt. En particulier, des veines claires de sulfate de calcium sont observées dans toutes les unités géologiques traversées par le rover.

En soi, la diversité et la complexité des figures diagénétiques observées dans les roches sédimentaires du cratère Gale constituent une opportunité unique d'étudier les processus diagénétiques à l'œuvre sur Mars et d'en déduire les conditions redox et pH des fluides associés ainsi que leur influence sur l'évolution des sédiments après enfouissement.

CHAPITRE 2 – L'INSTRUMENT CHEMCAM ET LE ROVER *CURIOSITY*

Afin d'explorer les dépôts sédimentaires du cratère Gale, le rover *Curiosity* apporte avec lui une suite de 10 instruments scientifiques, pour la plupart contribuant à la caractérisation géologique des roches. Même si les études présentées dans ce manuscrit portent principalement sur les données de l'instrument ChemCam, les autres instruments du rover sont aussi fréquemment utilisés afin de fournir du contexte à ses analyses, ainsi que des informations complémentaires.

Parmi ceux-ci, les deux caméras Mastcam fournissent des images couleurs à l'échelle de l'affleurement, permettant de contextualiser les observations ChemCam et d'extrapoler les observations chimiques et minéralogiques aux affleurements se trouvant hors de portée des instruments analytiques du rover. Ces caméras permettent également d'effectuer des observations multi-spectrales dans le domaine du visible – proche infrarouge (VNIR), complémentaires aux observations passives de ChemCam. La caméra MAHLI, montée sur le bras articulé du rover, permet quant à elle d'obtenir des images couleurs de très haute résolution, à la manière d'un microscope, fournissant des informations détaillées sur la texture et la structure des éléments géologiques étudiés. Leur composition minéralogique est quant à elle déterminée par l'instrument CheMin, mais seulement sur des prélèvements de sols et les quelques forages réalisés par le rover. Le dernier instrument mentionné dans cette étude, APXS, fournit des analyses chimiques « bulk » complémentaires aux analyses ponctuelles ChemCam, procurant une détection plus fine sur certains éléments chimiques (non-métaux et halogènes) mais particulièrement sensible à la poussière omniprésente à la surface de Mars.

L'instrument ChemCam (Figure B) embarque pour la première fois sur Mars (et dans l'espace) la spectroscopie sur plasma induit par laser (LIBS), qui permet d'obtenir des analyses chimiques qualitatives et quantitatives sur la composition élémentaire des roches, à distance (entre 1.5 et 7 m). Cette technique consiste à exciter un matériau en focalisant une impulsion laser à sa surface, ce qui entraîne la vaporisation de la matière et la formation d'un plasma. L'analyse spectrale des rayonnements émis par ce plasma permet ensuite d'en identifier les éléments constitutifs (ions et atomes, voire quelques molécules). En effet, les différentes espèces chimiques présentes sous un état excité dans le plasma émettent des photons à des longueurs d'ondes caractéristiques en retournant à leur état d'énergie initial, permettant de les identifier grâce à leurs pics d'émission respectifs. La LIBS de ChemCam est par ailleurs couplée à un micro-imageur RMI fournissant des images détaillées de la cible analysée.

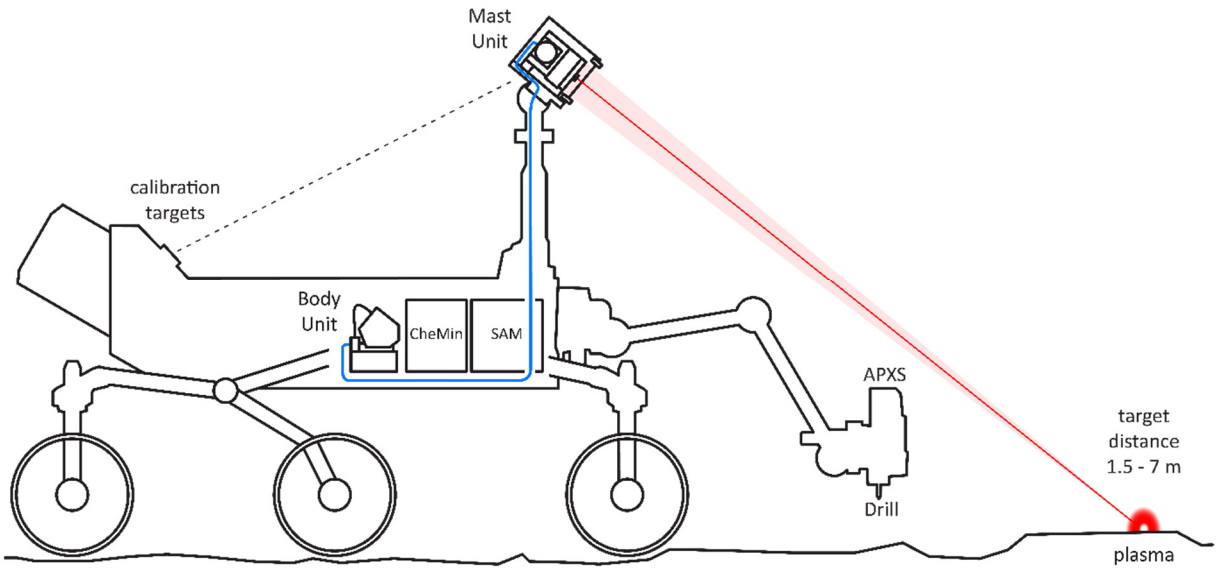

Figure B : Représentation schématique de l'instrument ChemCam embarqué sur le rover *Curiosity*

Une observation ChemCam consiste typiquement en une trame de plusieurs points d'analyse rapprochés, chaque point étant lui-même constitué de 30 tirs lasers sur une zone de ~300 à 600 µm de diamètre et quelques µm de profondeur. La poussière omniprésente à la surface Mars est « balayée » par les premiers tirs, permettant l'analyse de la roche sous-jacente. Par ailleurs, après chaque observation LIBS, ChemCam acquiert un spectre passif (sans utilisation du laser) enregistrant la réflectance de la cible étudiée dans le visible – proche infrarouge (400–840 nm). Ces observations passives permettent notamment d'obtenir des informations sur la présence de fer ferrique (Fe^{3+}) dans l'échantillon.

Enfin, ChemCam quantifie l'abondance des éléments majeurs et de certains éléments mineurs à partir d'analyses multivariées (majeurs) et univariées (mineurs), permettant de déduire la composition chimique de l'échantillon en fonction de l'intensité des pics d'émission dans les spectres LIBS. Ces méthodes de calibration reposent sur la comparaison des analyses ChemCam à une base de données de 408 standards synthétiques et naturels propre à l'instrument, et *a priori* représentative de la gamme de compositions chimiques rencontrée sur Mars.

CHAPITRE 3 – VARIABILITÉ CHIMIQUE DANS LES VEINES DE SULFATE DE CALCIUM

Des veines blanches sont observées dans le cratère Gale dès les premières observations du rover *Curiosity*, peu de temps après son atterrissage, et sont caractérisées par une composition quasi-pure de sulfate de calcium par ChemCam (bassanite ; $CaSO_4 \times 0.5H_2O$) [*Nachon et al.*, 2014; *Rapin et al.*, 2016]. Elles sont associées à des fractures linéaires présentant une distribution aléatoire d'orientations, suggérant une formation par fracturation hydraulique après lithification des sédiments, et donc lors des phases tardives de la diagénèse. Ces fractures recoupent par ailleurs toutes les autres figures diagénétiques observées, constituant vraisemblablement l'un des derniers épisodes diagénétiques associés à la formation des dépôts sédimentaires. Depuis ces premières observations, le rover n'a cessé de croiser ces veines, incisant toutes les lithologies explorées jusqu'à présent. Cependant, ces veines présentent des variations de textures notables et sont localement associées à la formation d'autres figures diagénétiques de compositions diverses. Les analyses réalisées par ChemCam de manière régulière sur ces veines montrent une composition facilement identifiable (i.e. distinguable des autres mesures de l'instrument) et relativement uniforme à travers les unités stratigraphiques observées par *Curiosity*. Ainsi, les variations chimiques associées à ces veines de sulfate de calcium, même relativement faibles, constituent un proxy pour retracer les conditions liées à leur emplacement lors de la diagénèse et les potentielles variations par rapport à la stratigraphie.

En comparant les intensités relatives de pics d'émission du Fe, du Mg, et de l'Al par rapport au Si, nous avons pu identifier des enrichissements en Fe, Mg et Al (en dessous des limites de quantification), associés à la formation des veines de sulfate de calcium au cours des 1700 premiers sols (jours martiens) de la mission [*L'Haridon et al.*, 2018b]. Par ailleurs, les phases détectées ne sont pas liées à une contribution de la roche encaissante car non corrélées à des enrichissements en Si, ou Ti (i.e. minéraux silicatés primaires ou secondaires) et suggèrent donc des conditions de formation particulières lors de l'emplacement de ces veines.

Des veines anastomosées présentant une faible résistance à l'érosion et une texture plus grossière, associées à des enrichissements en Fe, sont observées en dessous de la discordance entre les dépôts lacustres de la formation de Murray et les dépôts éoliens sus-jacents de la formation de Stimson. L'analyse des spectres en réflectance souligne la présence de fer ferrique (Fe^{3+}) dans ces veines, indiquant des conditions de formation oxydantes. Par ailleurs, des halos riches en Si sont également observés le long de larges fractures à proximité, recoupant les formations de Stimson et Murray, et suggèrent probablement l'altération de la roche encaissante par des fluides acides lors de la diagénèse. Cette proximité suggère la formation de veines de sulfate de calcium dans des conditions acides à cet endroit, potentiellement corroborée par les quelques détections d'Al dans ces veines. Ainsi, des fluides acides auraient mobilisé le Fe (et l'Al) après l'enfouissement des sédiments, formant par la suite des oxydes de Fe^{3+} lors de la formation des veines de sulfate de calcium.

Curiosity a observé des fentes de dessiccation dans les sédiments lacustres indiquant un dépôt dans des eaux peu profondes. À ce niveau, les veines de sulfate de calcium sont associées à la présence d'oxydes de Fe et de Mn, sur lesquels le P est probablement absorbé [*Gasda et al.*, 2018; *Meslin et al.*, 2018], ainsi que quelques enrichissements épars en Mg. L'observation de niveaux subparallèles à la stratification présentant des compositions similaires indique que ces oxydes se sont probablement formés lors de la sédimentation ou lors des phases précoces de la diagénèse dans un environnement oxydant. Par la suite, ces oxydes sont incorporés sous forme d'inclusions nodulaires dans les veines de sulfate de calcium et potentiellement réduits lors de ce processus. Ceci permettrait d'expliquer les

spectres passifs associés, suggérant l'absence de Fe^{3+} et la présence probable de Fe^{2+}. Les conditions réductrices (ou simplement anoxiques) suggérées par ces observations semblent par ailleurs concorder avec l'observation de zones d'altération de couleur grise le long de fractures de sulfate de calcium à proximité, au sein d'une roche encaissante de couleur rouge-orangée (réduction des oxydes de Fe^{3+}, rouges, en Fe^{2+} typiquement gris).

La variabilité géochimique observée dans ces veines de sulfate de calcium retrace donc des conditions de fluides distinctes lors de la diagénèse, acides et oxydantes à la base de la formation de Murray, et probablement plus réductrices au niveau de Old Soaker [*L'Haridon et al.*, 2018b] (c.f. Figure C).

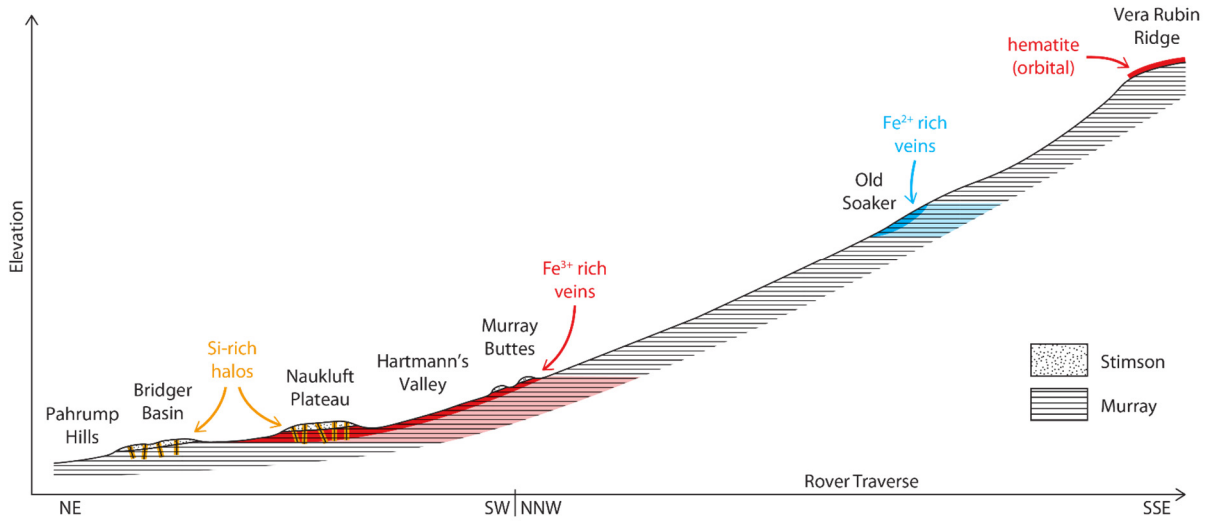

Figure C : Coupe schématique des dépôts sédimentaires le long de la traverse du rover *Curiosity* illustrant la distribution des veines de sulfate de calcium présentant des enrichissements en Fe^{3+} et Fe^{2+}. Les enrichissements en Fe^{3+} (en rouge) sont localisés en dessous de la discordance entre les dépôts lacustres de la formation de Murray et les dépôts éoliens de la formation de Stimson, à proximité d'halos riches en Si observés le long de larges fractures (en jaune). Les enrichissements en Fe^{2+} (en bleu) sont quant à eux limités au site de Old Soaker où l'observation de fentes de dessiccation suggère des conditions de dépôt dans un lac peu profond, mais dans un contexte géologique par ailleurs dominé par la présence d'hématite.

CHAPITRE 4 – MOBILITÉ DU FER LORS DE LA DIAGÉNÈSE

Après plus de 5 ans à la surface de Mars, et environ 18 km parcourus, le rover *Curiosity* a finalement atteint l'une des principales structures sédimentaires identifiées depuis l'orbite dans le cratère Gale, formant un relief topographique connu sous le nom de Vera Rubin Ridge (VRR) et constituant un des objectifs principaux de la mission. En effet, cette structure marque les contreforts de l'unité d'argiles en amont, et est caractérisée par une signature importante d'hématite depuis l'orbite, suggérant des conditions de formation oxydantes en présence d'eau liquide, liées à l'altération des sédiments en surface (lors du dépôt) et/ou à la circulation de fluides lors de la diagénèse [*Fraeman et al.*, 2013].

L'exploration *in situ* de ces escarpements n'a pour autant pas permis de mettre en évidence des variations nettes dans la composition chimique des roches sédimentaires (peu de variations dans les teneurs en Fe ni d'autres éléments), ni un changement de faciès marqué par rapport aux mudstones lacustres de la formation de Murray sous-jacente, indiquant donc une continuité dans les conditions de dépôt [*Edgar et al.*, 2018]. Par contre, des variations latérales de couleurs de patines sont observées dans les affleurements du membre supérieur de la formation de VRR—Jura—associées à des variations dans leur composante ferrique [*Fraeman et al.*, 2018]. En effet, les spectres en réflectance (ChemCam,

Mastcam) des roches sédimentaires à patine grise (dites « grises ») sont caractérisés par l'absence de bandes d'absorption ferriques, contrastant avec les signatures d'hématite caractéristiques des affleurements de VRR et particulièrement présentes sur les roches à patine rouge (dites « rouges ») qui leur sont adjacentes.

ChemCam observe par ailleurs de nombreuses phases minérales sombres diagénétiques au niveau de ces affleurements « gris », présentant une composition chimique quasi-pure d'oxyde de fer. Ces phases sont observées en association avec des veines de sulfate de calcium, formées lors de la diagénèse tardive, sous forme d'inclusions et de remplissage partiel dans ces mêmes fractures. Les veines de sulfate de calcium sont également observées dans les affleurements « rouges », mais ne présentent pas cette association avec ces figures diagénétiques sombres d'oxyde de fer. D'autre part, l'encaissant autour de ces phases minérales sombres présente un aspect blanchi, comme lessivé, ainsi qu'une composition appauvrie en fer, suggérant ainsi que le fer a été mobilisé de la roche encaissante pour former ces figures diagénétiques d'oxyde de fer.

Le rover observe également des formes cristallines automorphes, composant des agrégats cristallins rappelant l'habitus du gypse (clivage en fer de lance ou pied d'alouette, agrégats étoilés). Elles présentent une couleur blanche et une texture proche des veines de sulfate de calcium dans les roches « rouges », concordant avec leur interprétation en tant que cristaux de gypse. Ces formes cristallines sont également observées dans les affleurements « gris », où le matériel clair les composant est partiellement (voire complètement) remplacé par un matériel sombre enrichi en Fe (probablement oxyde de fer), indiquant une pseudomorphose. Enfin, l'absence de déformation dans les laminations sédimentaires autour de ces cristaux et leur forme automorphe suggèrent leur formation avant induration (automorphe) et compaction (absence de déformation) des sédiments. Ainsi ces cristaux se sont probablement mis en place lors du dépôt des sédiments, ou très tôt dans la diagénèse.

Ces observations suggèrent donc que la formation authigenétique d'oxyde de fer dans les zones « grises » des affleurements de Jura implique : (1) la mobilité du fer dans la roche encaissante lors de la diagénèse probablement liée à la circulation de fluides après enfouissement formant ces zones d'altération « grises », par réduction isochimique des phases ferriques (hématite) observées dans les roches de VRR ; (2) la formation d'oxydes de fer lors de l'interaction avec des fluides riches en sulfates. Cette interaction résulte soit de la dissolution des cristaux automorphes de gypse (formés lors de la sédimentation, ou peu après) soit de la mise en place des veines de sulfate de calcium lors de la diagénèse tardive.

Enfin, la chronologie relative des évènements permettant de reconstituer la séquence paragénétique lors de la diagénèse est complexe (Figure D). L'hypothèse la plus probable se base sur le fait que la circulation de fluides réducteurs requiert une porosité relativement connectée pour former ces zones d'altération diffuses, et interviendrait donc avant l'induration des sédiments. Par la suite, la formation des oxydes de fer en association avec les veines, seulement observée au sein des zones « grises » de l'encaissant, implique la remobilisation du fer lors de leur mise en place par fracturation hydraulique (après induration). Cette remobilisation est probablement facilitée par la présence de phases minérales réduites dans ces zones d'altération, plus solubles que les phases minérales ferriques observées dans les autres affleurements de VRR. Par ailleurs, l'observation de pseudomorphose par dissolution/recristallisation sur les cristaux automorphes *a priori* déconnectés du réseau de fractures suggère que celle-ci est liée à la circulation de fluides provenant de zones d'altération dans un sédiment partiellement cimenté, et non à la fracturation hydraulique postérieure à la cimentation.

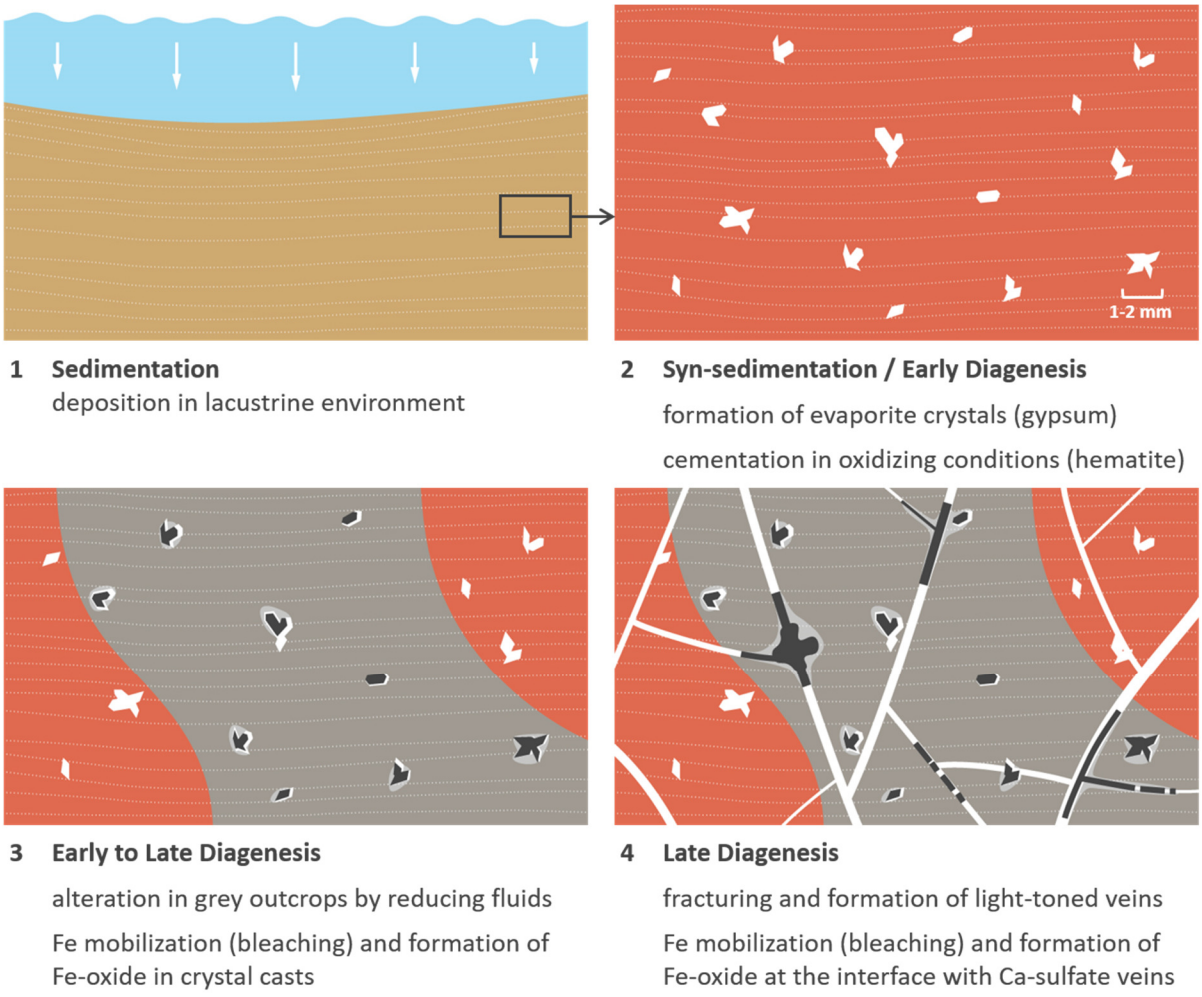

Figure D : Schéma de la séquence d'évènements impliqués dans la formation des roches sédimentaires de la formation de Jura, sur Vera Rubin Ridge, rendant compte de la formation des zones d'altérations « grises » et de la formation d'oxydes de fer (phases minérales sombres) en association avec les figures de sulfate de calcium (cristaux automorphes et fractures).

Ainsi, sur VRR, les observations de ChemCam rendent compte de processus diagénétiques complexes, impliquant notamment la mobilité locale du fer, et soulignent le rôle non-négligeable de la diagénèse et de la circulation de fluides en sub-surface dans la formation de structures sédimentaires visibles depuis l'orbite sur Mars [*L'Haridon et al.*, 2018c].

CHAPITRE 5 – DIAGÉNÈSE ET PROCESSUS REDOX DANS LE CRATÈRE GALE : IMPLICATIONS

L'exploration des roches sédimentaires à Gale a par ailleurs révélé l'importance des processus d'oxydoréduction (ou redox) dans leur formation, exprimés par des tendances minéralogiques et géochimiques dans l'encaissant ainsi que par la mise en place de figures diagénétiques. En effet, la composition minéralogique des roches sédimentaires montre des variations en fonction de la stratigraphie, notamment marquées par l'abondance relative entre magnétite (oxyde de Fe^{2+} et Fe^{3+}) et hématite (oxyde de Fe^{3+}) indiquant des conditions redox distinctes au cours de l'évolution des sédiments (Figure E).

La formation de ces faciès minéralogiques est interprétée par une stratification redox dans les eaux du paléolac [*Hurowitz et al.*, 2017], présentant des conditions en surface oxydantes du fait de l'interaction avec l'atmosphère (UV et O_2) sous lesquelles se forment les oxydes de Fe^{3+} (hématite), tandis qu'en

profondeur les conditions demeurent anoxiques et favorisent la formation de phase plus réduite (magnétite). Cependant, plusieurs observations en lien avec l'évolution de ces sédiments au cours de la diagénèse mettent en doute la pertinence de ce modèle.

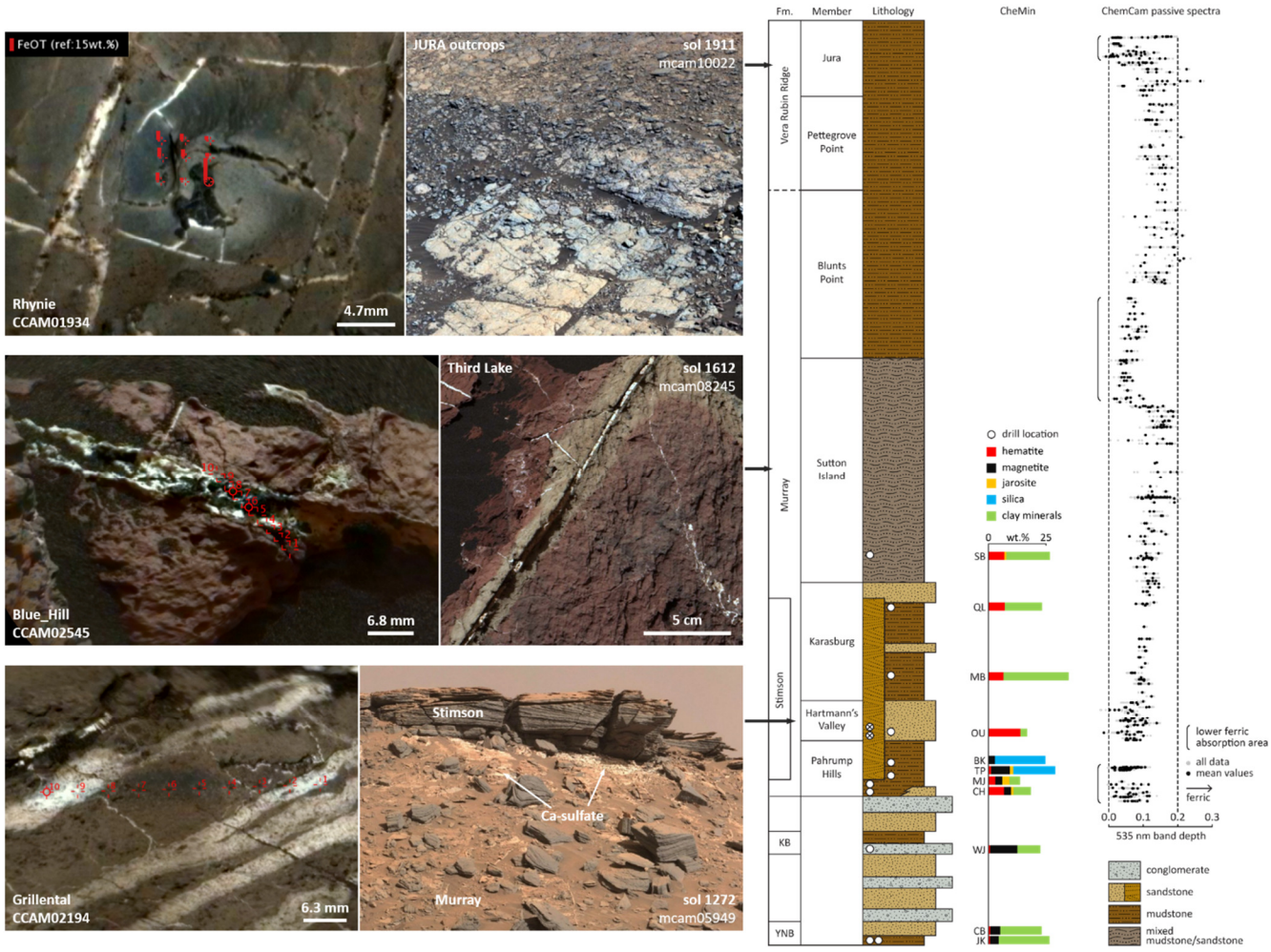

Figure E : Localisation des principales observations de ChemCam impliquant la mobilisation du Fe associée à la formation de veines de sulfate de calcium lors de la diagénèse tardive (à gauche), par rapport à la stratigraphie et aux observations de minéralogie dans l'encaissant (à droite ; données CheMin et spectres passifs ChemCam).

Tout d'abord, la formation de magnétite et d'argile dans les roches de Yellowknife Bay résulte probablement de l'altération isochimique de minéraux primaires (olivine) lors de la diagénèse [*Vaniman et al.*, 2014; *Tosca et al.*, 2018]. En effet, la présence d'abondantes cavités circulaires dans ces affleurements s'explique par la production de bulles de gaz (H_2) associées à ces réactions d'altération, après l'enfouissement des sédiments [*McLennan et al.*, 2014; *Stack et al.*, 2014], et sans lien apparent avec les conditions en surface lors de la sédimentation. D'autre part, la présence de magnétite en association avec des phases minérales siliceuses à la base de la formation de Murray (Pahrump Hills) survient dans un contexte géochimique spécifique marqué par le lessivage en conditions acides de certains éléments chimiques (e.g. Fe, Mg, Mn, Zn et Ni), et ce après l'enfouissement des sédiments [*Rampe et al.*, 2017]. L'implication de fluides acides lors de la diagénèse est par ailleurs corroborée par (i) des détections de jarosite (sulfate de fer formé à pH < 2) dans l'encaissant associées à certaines figures diagénétiques [*Nachon et al.*, 2016], (ii) la formation localisée de veines riches en F et Ge (éléments mobiles en conditions acides) en association avec les veines de

sulfate de calcium [*Nachon et al.*, 2016; *Berger et al.*, 2017] et (iii) l'observation de halos d'altération riches en Si (résultant en partie du lessivage en conditions acides des autres éléments) le long de fractures traversant le contact stratigraphique avec la formation de Stimson sus-jacente [*Frydenvang et al.*, 2017; *Yen et al.*, 2017].

De ce fait, si la présence d'hématite est globalement interprétée comme reflétant des conditions oxydantes en surface lors de la sédimentation, les variations minéralogiques observées en fonction de la stratigraphie semblent impliquer des processus diagénétiques plutôt que des conditions distinctes lors de la sédimentation. Les études présentées dans ce manuscrit indiquent en particulier que la mise en place des veines de sulfate de calcium est associée localement à la mobilisation du fer dans l'encaissant et à la formation d'oxydes de fer lors de la diagénèse (Figure E). Par ailleurs, notre travail a démontré, par une analyse thermodynamique du système Fe-S, que la formation d'hématite est plus probable que celle de la magnétite lors de l'interaction avec des fluides riches en ion sulfate (SO_4^{2-}), survenant par oxydation et/ou neutralisation du pH. Ainsi, les détections par ChemCam de la formation d'oxyde de fer en association avec les veines de sulfates de calcium ont permis d'identifier localement l'implication de conditions acides (Hartmann's Valley) [*L'Haridon et al.*, 2018b] et/ou réductrices (Vera Rubin Ridge) [*L'Haridon et al.*, 2018c] lors de la diagénèse des dépôts sédimentaires du cratère Gale.

CONCLUSION

Les travaux réalisés au cours de cette thèse ont permis de mettre en évidence l'implication de processus d'oxydo-réduction lors de la diagénèse des dépôts sédimentaires du cratère Gale, à partir de l'analyse géochimique de veines de sulfate de calcium et des figures diagénétiques associées, par l'instrument ChemCam à bord du rover *Curiosity*. Ces résultats démontrent notamment l'importance des interactions fluides-roches en sub-surface dans l'évolution des sédiments sur ce site d'étude, probablement représentatif des terrains sédimentaires formés au cours de l'Hespérien—époque charnière dans l'évolution climatique de Mars. Par ailleurs, la formation de ces sédiments dans un contexte fluvio-lacustre représente des conditions potentiellement habitables par le passé. Afin d'éviter toute erreur d'interprétation sur les conditions en surface par le passé et l'intérêt exo-biologique des sites étudiés, il est essentiel de bien contraindre les processus affectant l'évolution des sédiments après leur dépôt.

Enfin, les circulations d'eaux souterraines sur Mars, potentiellement toujours actives aujourd'hui, constituent des environnements encore peu explorés qui présentent un fort potentiel pour la préservation de matière organique, et éventuellement habitables par des micro-organismes. Aussi, de tels environnements représentent un fort intérêt pour les futures missions de retour d'échantillons.

TABLE OF CONTENTS

ACKNOWLEDGMENTS 5

RÉSUMÉ ÉTENDU 7

TABLE OF CONTENTS 18

LIST OF ACRONYMS 21

INTRODUCTION 23

CHAPTER 1 THE SEDIMENTARY CYCLE ON MARS 29

1.1 Sedimentary processes on Mars 29

1.1.1 Orbital observations 29

1.1.2 Mars aqueous history 32

1.1.3 *In situ* observations 36

1.2 Gale Crater and diagenesis 38

1.2.1 Gale Crater geological context 38

1.2.2 *Curiosity* rover traverse and Gale sedimentary stratigraphy 40

1.2.3 Diagenesis 42

1.3 Problem statement and research objectives 43

CHAPTER 2 THE CHEMCAM INSTRUMENT AND THE *CURIOSITY* ROVER 49

2.1 *Curiosity*, Chemistry, and Camera 49

2.1.1 The *Curiosity* rover scientific payload 49

2.1.2 ChemCam 51

2.2 LIBS technique and ChemCam data processing 54

2.2.1 Laser-Induced Breakdown Spectroscopy (LIBS) 54

2.2.2 ChemCam LIBS data processing 57

2.2.3 Elemental quantifications 57

2.2.4 Low abundance variations in major elements 59

CHAPTER 3 CHEMICAL VARIABILITY IN CALCIUM SULFATE VEINS IN GALE CRATER 63

3.1 Introduction 69

3.2 Material and methods 70

3.2.1 ChemCam instrument 70

3.2.2 Elemental composition and quantification 71

3.2.3 Identification of enrichments in specific elements 72
3.3 Results 74
3.3.1 Chemical variability observed in light-toned veins 74
3.3.1.1 Major element enrichments in light-toned veins 74
3.3.1.2 Minor, trace and volatile elements 79
3.3.1.3 Passive spectra 81
3.3.2 Texture and orientation of the veins in relation to chemical variability 83
3.3.3 Localization within the Gale stratigraphy and relationship with adjacent diagenetic features 84
3.4 Discussion 88
3.4.1 Mineralogical interpretations 88
3.4.2 Implications for fluid chemistry 89
3.4.3 Potential sources of chemical variability in light-toned veins 90
3.5 Conclusion 91
CHAPTER 4 IRON MOBILITY DURING DIAGENESIS ON VERA RUBIN RIDGE 97
4.1 Introduction 102
4.2 Methods 102
4.2.1 ChemCam instrument 102
4.2.2 Elemental composition and quantification 103
4.2.3 Mastcam and MAHLI cameras 104
4.3 Geological setting 104
4.3.1 Stratigraphy 104
4.3.2 Composition 106
4.4 Results 106
4.4.1 Description of diagenetic features 106
4.4.1.1 Light-toned veins 106
1.1.1.1 Crystal pseudomorphs 108
4.4.1.2 Dark-toned nodules and fracture fills 110
4.4.2 ChemCam compositional observations 111
4.4.2.1 Chemistry (major and minor elements) 111
4.4.2.2 Passive spectra observations 113
4.5 Discussion 115
4.5.1 Diagenetic history of Vera Rubin Ridge 115

4.5.2 Potential chemical processes involved during diagenesis 117
4.6 Conclusion 119
CHAPTER 5 DIAGENESIS AND REDOX PROCESSES AT GALE CRATER: IMPLICATIONS 123
5.1 Redox and pH conditions inferred from *Curiosity*'s observations 123
5.1.1 Varying redox conditions 125
5.1.2 Varying pH conditions 127
5.1.3 Increasing variability in the upper Murray formation 128
5.2 Variability associated with the Ca-sulfate light-toned veins 129
5.3 Implications for fluid conditions 131
5.4 Evolving redox and pH conditions at Gale Crater and broader implications 135
CONCLUSION 139
ANNEX A CONTRIBUTION TO CHEMCAM OPERATIONS 145
ANNEX B RECONSTRUCTION OF DIGITAL OUTCROP MODELS FROM THE *CURIOSITY* ROVER IMAGES 157
ANNEX C OTHER RESOURCES 165
REFERENCES 167

LIST OF ACRONYMS

APXS	Alpha Particle X-Ray Spectrometer
ChemCam	Chemistry and Camera
CheMin	Chemistry and Mineralogy
CIA	Chemical Index of Alteration
CRISM	Compact Reconnaissance Imaging Spectrometer for Mars
DOM	Digital Outcrop Model
ESA	European Space Agency
HiRISE	High Resolution Imaging Science Experiment
LIBS	Laser-Induced Breakdown Spectroscopy
MAHLI	MArs Hand Lens Imager
MARDI	MARs Descent Imager
Mastcam	Mast Camera
MSL	Mars Science Laboratory
MER	Mars Exploration Rovers
MRO	Mars Reconnaissance Orbiter
NASA	National Aeronautics and Space Administration
Navcam	Navigation Camera
OMEGA	Observatoire pour la Minéralogie, l'Eau, les Glaces et l'Activité
PIXE	Particle-Induced X-ray Emission
USGS	United States Geological Survey
RMI	Remote Micro-Imager
SPDL	Science Payload Downlink Lead
SPUL	Science Payload Uplink Lead
STG	Science Theme Group
TES	Thermal Emission Spectrometer
VRR	Vera Rubin Ridge
XRD	X-Ray Diffraction
XRF	X-Ray Fluorescence

INTRODUCTION

Starring at the night sky and the stars it holds, humanity soon began to catch on just how vast the expanse of space that lies beyond the borders of our planet is. Since then, the minds of men have been left wondering about their place in the Universe: Are we alone? Earth may seem like a lonely island of life lost in the cosmos, but life could potentially exist—or have existed—elsewhere. Since the dawn of the space age, we have begun to explore the suburbs of this immensity using robotic probes, to look for the beginning of an answer.

In the space exploration programs, our planetary neighbor—Mars—draws a lot of attention to itself. Part of this interest may be explained by its close proximity to our planet and the relative ease with which we manage to reach its orbit and surface, in comparison with the other objects of the solar system (except for the Moon). More relevant is the fact that Mars and Earth likely shared a similar history during the first billion years following their accretion. Around that time, as early as 3.8 to 4.4 billion years ago [Mojzsis et al., 1996; Dodd et al., 2017], life arose on the surface of our planet. Unfortunately, little evidence of its origin was retained in its geological records, as the earth's crust was extensively recycled throughout its history by erosion, alteration, and tectonic activity. On Mars, however, the ancient terrains of its southern hemisphere, of similar age, still preserve morphological and mineralogical evidence that water once flowed on its surface. The study of the sedimentary rocks associated with this aqueous activity revealed that the red planet experienced a dramatic shift in climatic conditions over the course of its history [Bibring et al., 2006] and that potentially habitable environments may have prevailed in the past [Grotzinger et al., 2014]. As such, by analogy, Mars could hold precious information on the evolution of our planet in its infancy and its study may shed some light on the processes by which life appeared on Earth.

Nevertheless, the formation of sedimentary rocks is not restricted to the transport and deposition of sediments, which only reflect the conditions on the surface at the time of deposition. It also involves the physical and chemical processes through which sediments are transformed into rocks after burial—collectively referred to as diagenesis. These processes are often associated with groundwater systems and can significantly alter the texture, chemistry, and/or mineralogy of the sediments after deposition. As such, interpretations on depositional environments and paleoclimates may be misleading if the influence of the diagenesis over the formation of sedimentary deposits on Mars is not thoroughly understood and taken into account. It also has direct implications on the exobiological potential of such deposits.

The recent *in situ* exploration of the Martian surface by landers and rovers has unveiled the geological complexity of the sedimentary deposits on the ground, with variations in texture, chemistry, and mineralogy at the outcrop scale that could not be perceived from orbit. Notably, the geological terrains surveyed by the rover *Opportunity*, at Meridiani Planum, showed extensive evidence of groundwater interactions after the burial of the sediments [McLennan et al., 2005]. The diagenetic Fe-oxide concretions formed by such interactions later constituted lag-deposits mantling the surface through differential erosion, and likely contributed to the orbital detections of hematite at that location—initially interpreted to reflect surface water activity [Christensen et al., 2000]. This example illustrates the importance of *in situ* investigations to test working hypotheses and models derived from orbital observations against the "ground-truth", before jumping to conclusions on past environmental conditions.

In this context, the Mars Science Laboratory mission constitutes a major milestone in the exploration of Mars, bringing in an advanced geological laboratory on its surface with the rover *Curiosity*. It landed in 2012 within the Gale impact crater to investigate the layered sedimentary deposits of its central mound, which likely record the shift in climatic conditions on Mars. As such, it will be able to confront orbital observations and climate evolution models with *in situ* observations. At the time of writing, the rover has traveled more than 20 km across mostly fluvio-lacustrine deposits that attest of significant surface water activity in the past, which potentially persisted for hundreds of thousands of years [Grotzinger et al., 2015]. Nevertheless, the rover also observed widespread evidence for post-depositional fluid circulations in the same outcrops, indicating that sub-surface aqueous alteration processes were involved in the formation of Gale Crater sedimentary rocks.

The work presented in this manuscript will thus focus on the study of these diagenetic water-rock interactions at Gale Crater. In order do so, the *Curiosity* rover carries onboard the ChemCam instrument, which provides remote fine-scale chemical analysis, especially suited to investigate the various geological features that formed during diagenesis.

First, **Chapter 1** will review the current state of knowledge on the sedimentary rock record on Mars, and the contributions from both orbital and *in situ* observations. From there, the Gale Crater geological context and its importance in the study of diagenetic processes on Mars will be discussed.

Afterward, **Chapter 2** will introduce the *Curiosity* rover scientific payload with an emphasis on the ChemCam instrument. We will then define the LIBS analytical technique, on which ChemCam relies, and outline its data processing and the analytical methods used to provide chemical quantifications.

The first case study of diagenetic features on Mars will be covered in **Chapter 3**, describing the chemical variability associated with the formation of the widespread late-diagenesis Ca-sulfate veins. ChemCam tracked the composition of the features along the rover traverse, and highlight specific locations where their emplacement is notably associated with the authigenic formation of Fe-phases, providing insights into the fluids compositions.

A second case study will be covered in **Chapter 4**, relating to the formation of a prominent topographic structure, Vera Rubin Ridge, characterized by strong hematite signatures from orbit. *In situ* observations, in particular from ChemCam, indicate that sediments on the ridge have experienced multiple fluid events during diagenesis, involving the mobility of Fe, and highlight the significant role such fluids played in its formation.

Finally, **Chapter 5** will review the distinct chemical and mineralogical observations from the rover exploration of Gale Crater sedimentary deposits, comparing bulk host rock trends with diagenetic observations, and discuss the various hypothesis proposed to account for the observed trends. Then, geochemical models will provide some insights into the diagenetic fluid conditions at Gale, and potential reaction paths proposed to lead to the formation of the observed diagenetic assemblages.

The manuscript will conclude on the insights provided by these studies on the evolution of the Gale sedimentary deposits after burial. In the end, we will discuss the broader implications of *ChemCam* discoveries regarding diagenesis in the context of the planet, and the related outstanding questions to be addressed by future *in situ* missions.

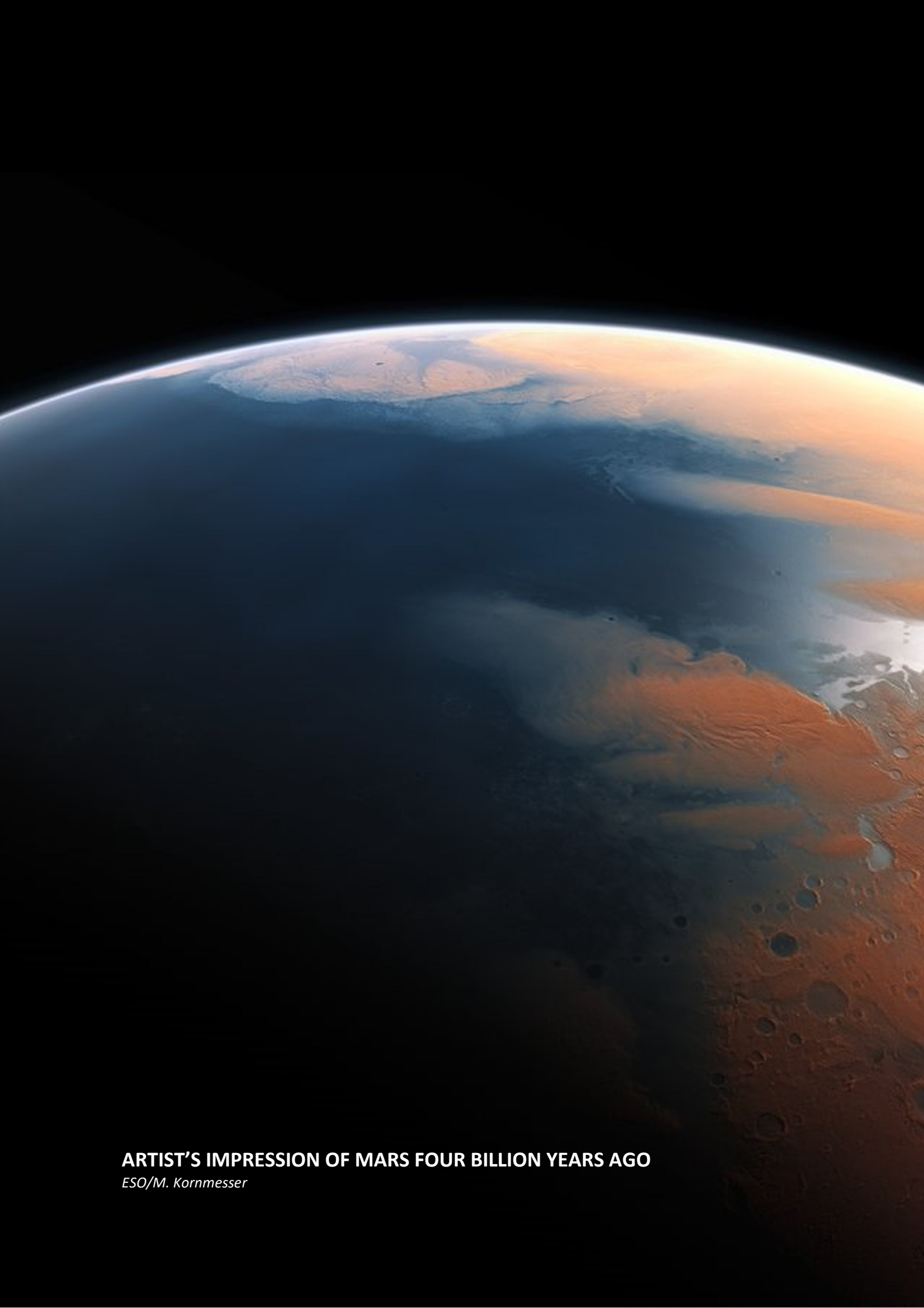

ARTIST'S IMPRESSION OF MARS FOUR BILLION YEARS AGO
ESO/M. Kornmesser

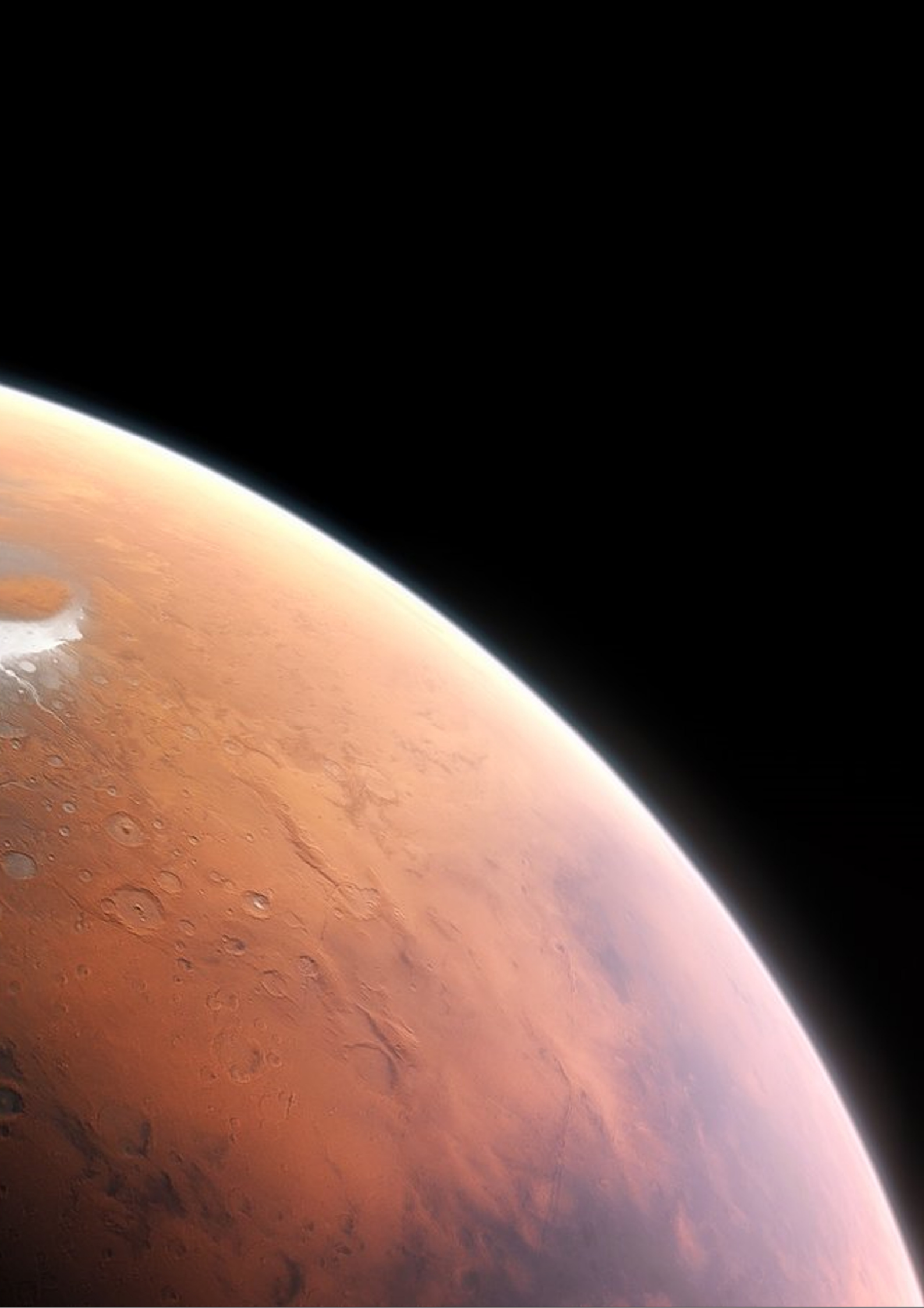

CHAPTER 1

THE SEDIMENTARY CYCLE ON MARS

Mars has long been viewed as the cold and dry basaltic world it appears to be today. The geological exploration of the planet over the past ~40 years, however, provided evidence—first geomorphic and later mineralogical—that sedimentation processes were heavily involved in shaping the Martian landscapes. The presence of sedimentary rocks on Mars has opened up a wide array of investigations into the past of the planet, as they record the story of their formation. Indeed, the grains that accumulated in the sediments are insights into the source rock composition while their sizes, shapes, and distribution indicate the way they were transported (either wind-blown or waterborne). Chemical and mineralogical weathering trends also provide information on climatic conditions at the time of deposition. Afterward, diagenesis records the physical and chemical processes involved in the transformation of sediments into indurated rocks after burial. Notably, cementation and alteration processes trace groundwater chemistry while fractures and cracks formation relate to the physical stresses subjected to the rocks.

In this chapter, we will review the present state of knowledge on the Martian sedimentary records, from both orbital and *in situ* observations, and interpretation on processes involved in the formation of sedimentary deposits. Lastly, we will introduce the Gale Crater geological context and its importance in the study of diagenetic processes on Mars.

1.1 Sedimentary processes on Mars

1.1.1 Orbital observations

The first evidence for sedimentary processes on Mars came from orbital probes and the fly-bys of the planet by the *Mariner* missions. The first successful fly-by mission—*Mariner* 4 in 1964—depicted a Moon-like planet with limited surface activity, interpreted as a desert and (mostly) inert world since the formation of its ancient cratered surface [*Leighton et al.*, 1965]. Incidentally, it also dispelled the more exotic theories of an inhabited world that were popularized in the past century. This picture was however soon challenged by *Mariner* 9—the first spacecraft to enter into orbit around another planet in 1971—which arrived in the midst of a global dust storm showing that important eolian activity on Mars persists to this day. The mission highlighted major structures on the surface of the planet [*Masursky*, 1973]: the Tharsis volcanic plateau and its massive shield volcanoes (Olympus Mons, Ascraeus Mons, Pavonis Mons et Asia Mons), the ice-covered polar caps, the vast canyons of Valles *Marineris* and the crustal dichotomy separating the younger lowlands of the Northern hemisphere from the older cratered highlands of the Southern hemisphere. In addition, the mission allowed for the first identification of sedimentary deposits on Mars with the observations of layered deposits near the poles [*Cutts and Smith*, 1973; *Sharp*, 1973], as well as fluvial landforms hinting at widespread aqueous activity [*Masursky*, 1973; *Milton*, 1973].

Shortly after, the two *Viking* orbiters (launched in 1976) provided an extensive coverage of the Martian surface (50,000 images from 30 to 200 m/pixel), including the most stunning global view of the planet to this day (Figure 1.1). The data acquired was instrumental in deciphering the geological history of the planet [*Tanaka*, 1986], and in building its first detailed geological maps [*Scott et al.*, 1986; *Greeley and Guest*, 1987; *Tanaka and Scott*, 1987]. The orbiters notably observed extensive layered deposits in

Valles *Mariner*is and in the ancient southern highlands [*Lucchitta et al.*, 1994] as well as high albedo features eroded in yardangs, which could be consistent with eolian erosion of fine-grained deposits [*Ward*, 1979]. However, the resolutions of the *Mariner* and *Viking* cameras still proved insufficient in order to provide definitive interpretations as to the origin of the sedimentary deposits, whether eolian, aqueous or volcanoclastic [*Ward*, 1979; *Nedell et al.*, 1987; *Williams and Zimbelman*, 1994].

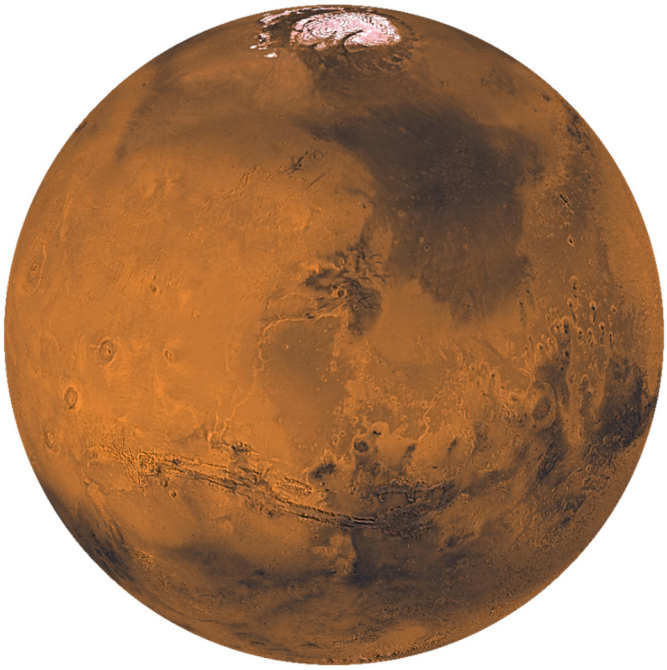

Figure 1.1: Global color coverage of Mars at 1km/pixel resolution by the *Viking* orbiters [image credit: NASA/JPL-Caltech/USGS]

Afterward, the Martian exploration experienced a quiet period with few missions launched, notably the Russian Phobos 2 mission that, although focused on the largest Martian moon, provided the first hyperspectral images of the planet. The 1990s then saw several attempts to reach the red planet fail, including the ambitious Russian Mars 96 mission lost at launch.

Mars Global Surveyor (MGS), launched in 1996, would spur the Martian exploration forward again. The Mars Orbiter Camera (MOC) was a leap forward in image spatial resolution (1.5 m/pixel) compared to previous missions, allowing the study of small-scale morphological structures and geological outcrops [*Malin*, 1998]. It notably enabled the observations of gullies on crater walls and on the sides of depressions or valleys that are not superimposed by landforms or cross-cutting features such as impact craters or eolian deposits, thus indicating a relatively young age of formation [*Malin and Edgett*, 2000]—and even still occurring nowadays [*Malin et al.*, 2006; *McEwen et al.*, 2007]. The formation of these gullies is thought to involve aqueous activity [*Costard et al.*, 2002; *Mangold*, 2003; *de Haas et al.*, 2015], though alternative formation processes have also been recently suggested such as the destabilization of the regolith from carbon dioxide sublimation [*Dundas*, 2016; *Pilorget and Forget*, 2016]. Another important result of the mission was the detection by the TES instrument (Thermal Emission Spectrometer) of localized crystalline hematite deposits in Aram Chaos (Sinus Meridiani) and Valles *Mariner*is [*Christensen et al.*, 2000], which not only suggest involvement of liquid water in its formation but also redox-driven chemical reactions that are especially interesting when considering past habitable conditions.

The mission also unveiled remanent magnetic anomalies in the oldest crustal rocks of the southern highlands [*Connerney*, 1999] which are reminiscent of the Earth oceanic crust magnetic structures. The absence of such anomalies within major impact basins and volcanic structures put constraints on the time of the internal dynamo shutdown, and subsequent loss of its magnetic field, estimated between -4.1 and -3.6 billion years ago [*Lillis et al.*, 2009; *Milbury et al.*, 2012]. Without a magnetic field to protect it, the primitive Martian atmosphere was gradually stripped away by the solar wind and lost to space. Thus, the evolution of the Martian atmosphere is in part tied to the evolution of its magnetosphere—the former being currently under study by Maven and TGO (Trace Gas Orbiter; part of the larger ExoMars mission), in orbit since 2014 and 2018 respectively.

In 2001, the Mars Odyssey orbiter reached the Martian orbit with only three instruments onboard, including GRS (Gamma-Ray Spectrometer) to determine the near-surface elemental composition. GRS notably reported elevated hydrogen abundances in the first meter beneath the surface near the pole (up to ±45° latitudes), which suggests the presence of water a few centimeters below ground [*Boynton et al.*, 2002]. The *Phoenix* lander will later confirm it (in 2008), with the *in situ* detection of a shallow ice table beneath the surface at latitude 68°N [*Smith et al.*, 2009].

Mars Express, the first European probe to reach Mars (in 2003), carries on board several instruments initially designed for Mars 96 including the hyperspectral camera OMEGA. This instrument allowed for the first detections of hydrated minerals in the form of clays (phyllosilicates) and sulfates at several locations on the surface of the planet, interpreted as clear evidences of flowing liquid water during prolonged period of time in the past [*Bibring*, 2005; *Gendrin*, 2005; *Bibring et al.*, 2006]. Carbonates were however not observed on the surface of Mars by OMEGA [*Bibring*, 2005] as expected alteration products of basaltic rocks under CO_2-rich and "wet" atmospheric conditions—the presence of which could in part help explain the present-day low atmospheric pressure (as CO_2 sink) [*Booth and Kieffer*, 1978; *Morse and Marion*, 1999].

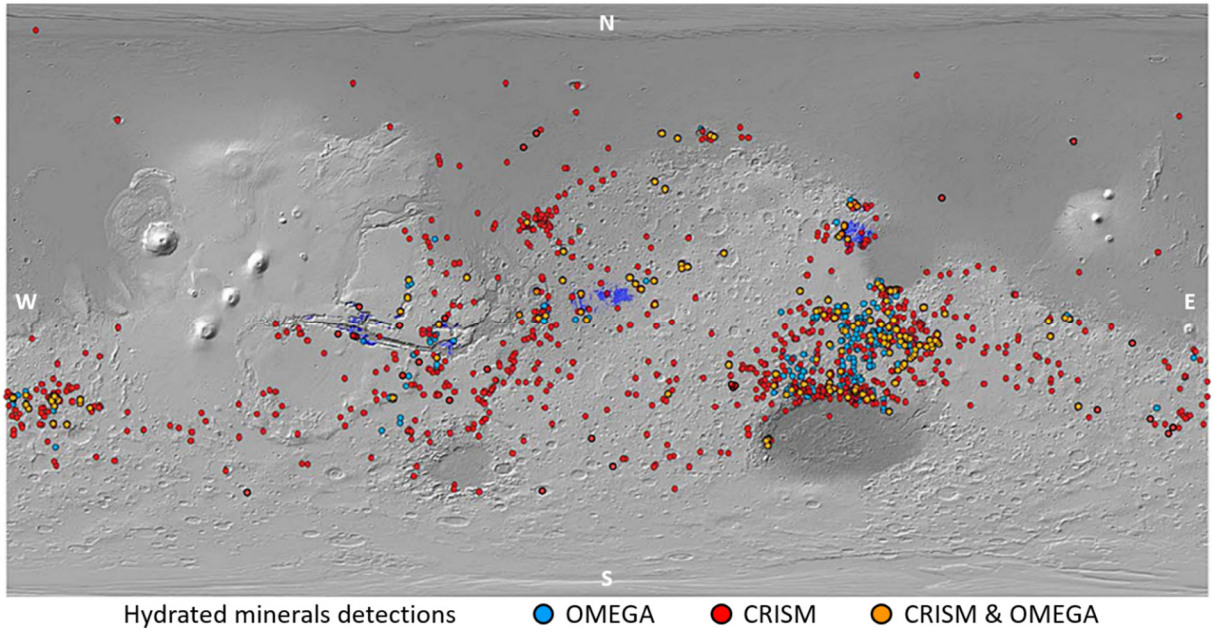

Figure 1.2: Global map of hydrated minerals detection (phyllosilicates) on Mars from OMEGA and CRISM [modified from *Carter et al.*, 2013]

The last orbiter devoted to the exploration of the Martian surface, Mars Reconnaissance Orbiter (MRO; arrived in 2006), includes a hyperspectral camera—CRISM—to cover smaller areas with an increased spatial resolution compared to OMEGA. Associated with the high-resolution HiRISE camera (up to 25 cm/px), it allows for the detailed study of specific sites of interests. An increasing diversity of minerals produced by aqueous alteration are identified on the surface of Mars with detections of kaolinite, serpentine, chlorites, micas, prehnite, zeolites and opal silica [*Milliken et al.*, 2008; *Mustard et al.*, 2008; *Ehlmann et al.*, 2009]. Jarosite, a Fe-sulfate associated with acidic environments on Earth, is also detected by CRISM [*Milliken et al.*, 2008; *Farrand et al.*, 2009]. Finally, CRISM would detect the carbonates that evaded OMEGA, albeit locally, within Nili Fossae [*Ehlmann et al.*, 2008] and in the central peak of several impact craters [*Michalski and Niles*, 2010]. The widespread distribution of hydrous clays detections from CRISM and OMEGA (Figure 1.2) [*Carter et al.*, 2013, 2015; *Ehlmann et al.*, 2013] show that aqueous alteration occurred on a global scale, in the form of hydrothermal, diagenetic and/or supergene (weathering) processes [*Ehlmann et al.*, 2013].

The HiRISE camera also allowed for the detailed monitoring of recent sedimentary landforms, including the aforementioned gullies [*Dundas et al.*, 2015], as well as the discovery of modern-day seasonal flows—or Recurrent Slope Lineae (RSL)—that occurs during the warmest months on steep Sun-facing inclines [*McEwen et al.*, 2011] (Figure 1.3). The processes behind the formation of RSL is currently debated, attributed to either briny discharges [*Ojha et al.*, 2015; *Stillman et al.*, 2017] or dry granular avalanches triggered by gas flow [*Dundas et al.*, 2017; *Schmidt et al.*, 2017].

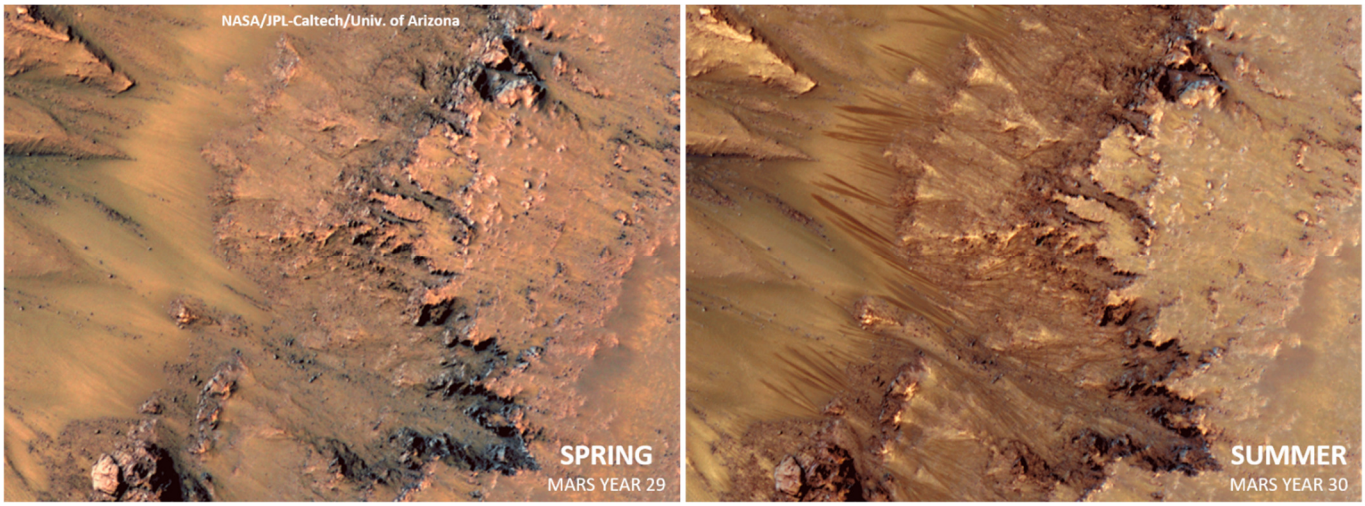

Figure 1.3: Recurring Slope Lineae observed during summer on the steep north-to-west–facing rim of a crater in Newton Basin [*McEwen et al.*, 2011]

1.1.2 Mars aqueous history

The successive orbital missions have thus uncovered significant geomorphic and mineralogical evidence for past, and possibly present, aqueous activity on the surface of Mars. The distribution of such observations across the planet, and the associated timing relative to its history provides insights into the evolution of its climate and atmospheric conditions.

The major geomorphic evidence for surface water activity, which comprises outflow channels, fluvial valley networks, deltas, and paleolakes appear to be limited to the Noachian and Hesperian highlands (Figure 1.2, 1.4 and 1.5).

- Fluvial activity is inferred from observations of dendritic valley networks that mainly incise the ancient cratered terrains of the Noachian, but also extend to some late-Hesperian locations (Figure 1.5). The morphologies associated with such landforms are consistent with surface rainwater runoffs over spatially limited drainage basins—similar to terrestrial river systems. However, the exact nature of the process behind their formation is still debated, as well as whether such systems could be sustained over geologically significant periods of time [*Carr*, 1995; *Mangold et al.*, 2004; *Irwin et al.*, 2005; *Hynek et al.*, 2010].

- Also reflecting surface water activity, the outflow channels are however quite distinct from fluvial valley landforms. These wide and extremely long channels with low sinuosity were most likely carved by flash floods that involved the discharge of huge volumes of water over very short period of times (days), exceeding the present-day discharge of the largest terrestrial rivers by several orders of magnitude [*Burr et al.*, 2002; *Manga*, 2004; *Williams and Malin*, 2004]. The catastrophic flow rates and water volumes involved could not be sourced by rainwater and would rather require the rapid release of massive long-term water storages, such as sub-surface aquifers or glaciers, following meteor impacts or volcanic activity [*Carr*, 1979].

- Lastly, paleolakes are located in a number of impact craters or other topographic depressions [*De Hon*, 1992; *Cabrol and Grin*, 2001], identified through the presence of alluvial fans, delta deposits, stratified terraces, and ancient shorelines and often associated with fluvial landforms upslope. The majority of the observed lacustrine systems are located within Noachian terrains (Figure 1.5), but some studies have shown that paleolakes could have persisted until the late-Hesperian [*Mangold et al.*, 2012].

While both paleolakes and outflow channels could also occur in cold and arid paleoclimates, i.e. as ice-covered lakes and from the rapid meltdown of the permafrost or an ice-caped aquifer, the occurrence of fluvial valley networks put tighter constraints on atmospheric conditions. Indeed, sufficient temperature and pressure are required for liquid water to be thermodynamically stable on the surface of the planet for prolonged periods of time. Fluvial activity appears nevertheless to have persisted until the end of the Hesperian [*Bouley and Craddock*, 2014], at a time in the planet's history for which climate models struggle to sustain an atmosphere dense enough to support liquid water [*Chassefière et al.*, 2007; *Lammer et al.*, 2013]. Additionally, the distribution of fluvial valley networks appear to be consistent with preferential ice—or water—accumulation along a tropical band south of the equator, predicted by climate models to have occurred during the Noachian and Hesperian [*Wordsworth et al.*, 2015]. Afterward, the emplacement of the Tharsis volcanism province would tilt the planet with respect to its spin axis to match its present-day orientation [*Bouley et al.*, 2016].

As such, the distinct geomorphic orbital observations suggest that a global climatic change occurred on Mars near the end of the Hesperian, transitioning from paleoclimates supporting fluvial and lacustrine activity on its surface—at least episodically—to the dry and cold conditions observed today.

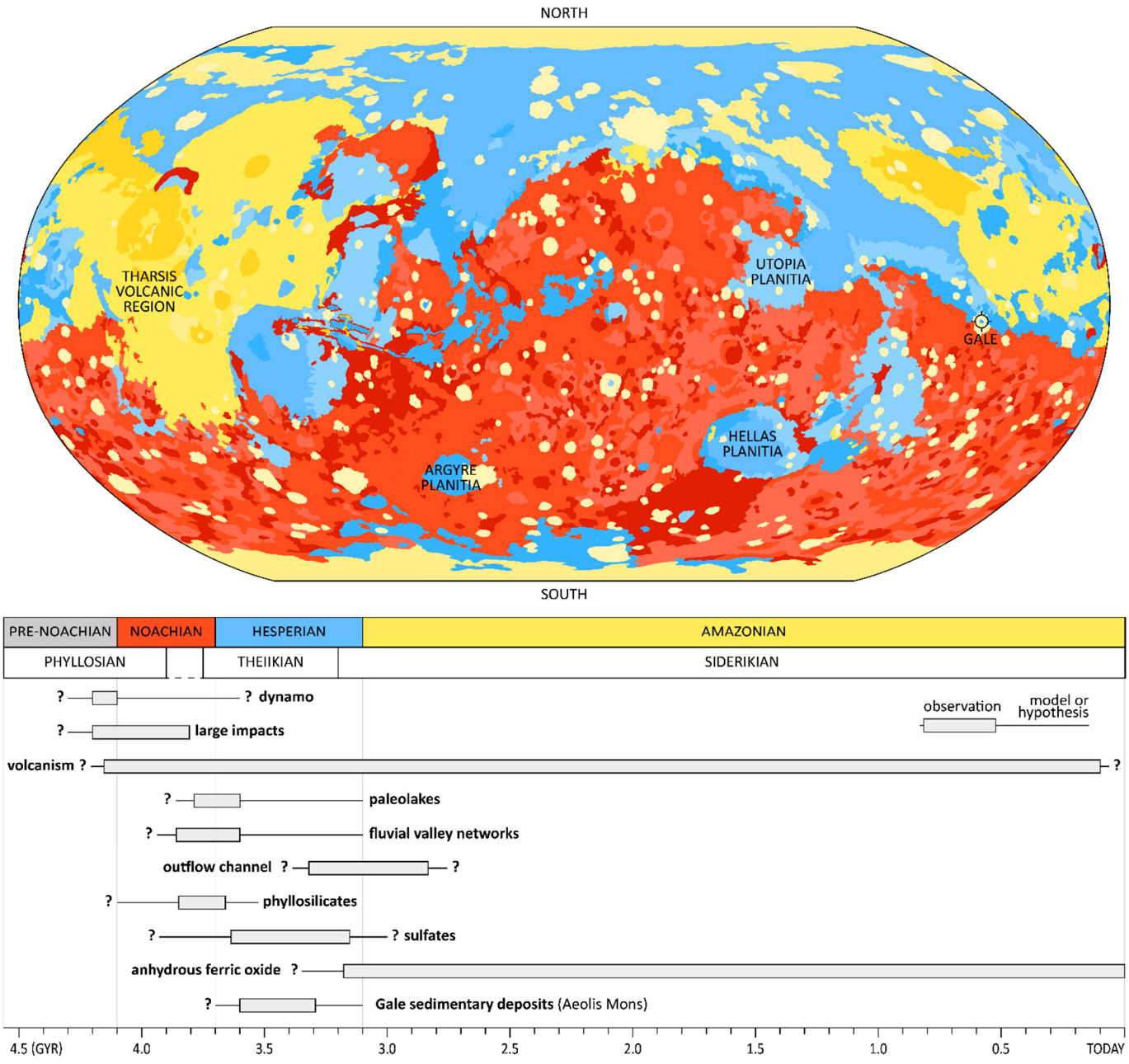

Figure 1.4: (Top) Schematic geologic map of Mars illustrating the crustal dichotomy that separates the ancient cratered highlands to the south (Noachian) from the more recent lowlands to the north (Hesperian-Amazonian) [modified from *Tanaka et al.*, 2014]. (Bottom) Timeline of the major geological processes in Mars history that notably depicts the timing of surface liquid water activity and occurrences of key mineral products associated with aqueous alteration [modified from *Ehlmann et al.*, 2011; *Rapin*, 2016]. The position of Gale Crater and the timing of formation of its sedimentary deposits are also indicated.

The mineralogical observations from OMEGA and CRISM are also consistent with this interpretation. Indeed, phyllosilicates are preferentially observed in the Noachian terrains [*Carter et al.*, 2013] (Figure 1.2) while sulfate and anhydrous ferric oxide are encountered in younger terrains (Hesperian and Amazonian), providing a mineralogy-based timeline (Phyllocian, Ttheiikian and Siderikian periods; Figure 1.4) that reflects the progressive desiccation of the planet [*Bibring et al.*, 2006].

- Phyllosilicate (clays) are produced from the alteration of primary minerals by the leaching mobile elements in presence of liquid water. Moreover, the formation of clays may reflect various alteration aqueous processes, including (1) hydrothermal activity following impact, volcanism or geothermal heating, (2) surface weathering (forming stratified alteration profiles, with Al-clays overlying Fe-Mg clays), and (3) diagenesis in relation with groundwater circulation after burial of the sediments—all of which are interpreted to have occurred on Mars [*Wray et al.*, 2009; *Milliken et al.*, 2010; *Carter et al.*, 2013; *Ehlmann et al.*, 2013]. The apparent lack of correlation between the distribution of phyllosilicates with geomorphic evidences for water activity on the surface (fluvial valleys and paleolakes; Figure 1.5) is consistent with their preferential association with impact craters [*Carter et al.*, 2013]—which exposed the older terrains below—and suggests that phyllosilicates formed mainly during the Noachian, early in the Martian history.

- Contrary to clay minerals observed in various geological contexts, sulfates are almost exclusively associated with layered sedimentary deposits distributed in an equatorial band from Valles *Marineris* and Meridiani Planum [*Gendrin*, 2005; *Chojnacki and Hynek*, 2008; *Mangold et al.*, 2008; *Massé et al.*, 2008; *Flahaut et al.*, 2010; *Sefton-Nash et al.*, 2012], some crater fills—including Gale Crater [*Milliken et al.*, 2010]— and eolian deposits along the northern polar cap [*Langevin et al.*, 2005; *Massé et al.*, 2010]. The formation of sulfates is interpreted to reflect evaporatively (desiccation) and acidic conditions (from volcanic outgassing and/or sulfide alteration) [*King and McLennan*, 2010; *Dehouck et al.*, 2012], consistent with the transition to progressively dryer and colder environments.

- Finally, the slow superficial weathering associated with limited water-rock interactions, consistent with the dry and cold atmospheric conditions of the Amazonian, produced widespread anhydrous ferric oxides [*Bibring et al.*, 2006], notably concentrated in the dust that covers the Martian surface and responsible for the red color that characterize the planet today (Figure 1.1).

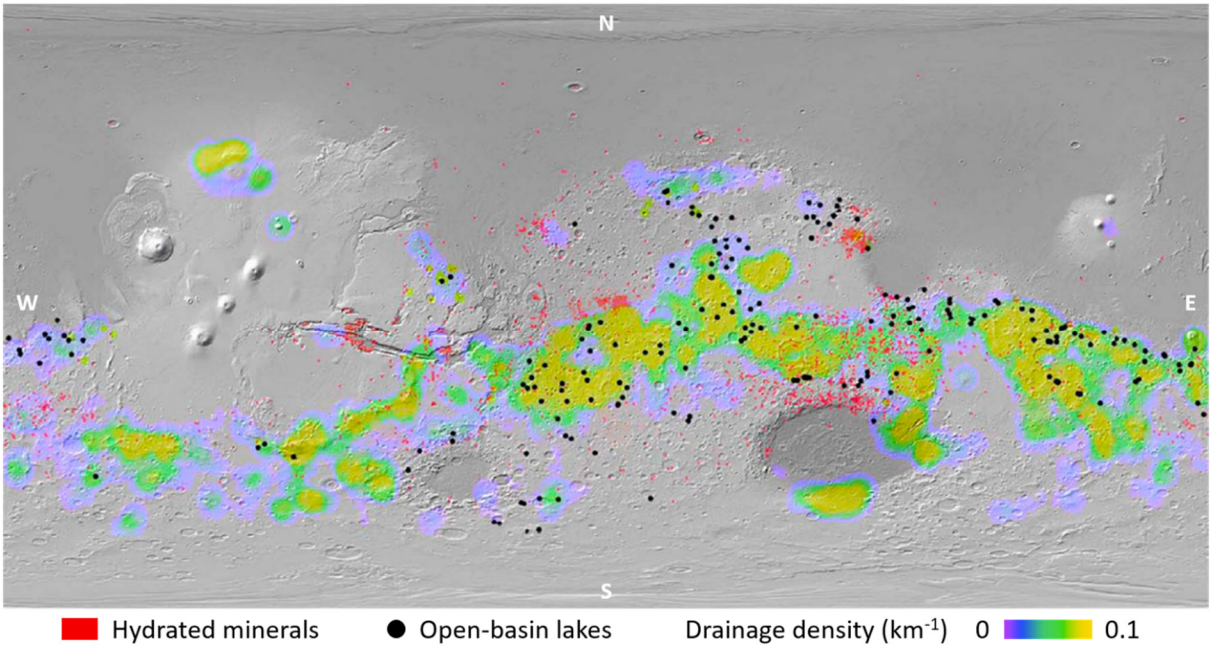

Figure 1.5: Location of fluvial landforms expressed as drainage density [*Hynek et al.*, 2010], open basin paleolakes (black dots) [*Fassett and Head*, 2008] and detections of hydrous minerals by CRISM and OMEGA (red) [modified from *Carter et al.*, 2013]

1.1.3 *In situ* observations

In order to build on orbital observations and test the derived geological interpretations against the ground truth, the Martian exploration programs gradually incorporated landers and rovers to reach the surface of the planet and provide *in situ* data.

The first ground-based analyses come from the two landers associated with both *Viking* missions, which provided measurements of the chemical composition of the atmosphere as well as the regolith surrounding both spacecraft. The composition of the Martian soil was similar at both landing sites (*Viking* 1 landed at Chryse Planitia while *Viking* 2 landed in Utopia Planitia) but does not correspond to an oxidized basaltic material as previously expected, with higher iron, chlorine and sulfur and insufficient aluminum compared to terrestrial or lunar compositions [*Clark et al.*, 1982]. Incidentally, *in situ* organic molecules were not detected by the landers [*Biemann et al.*, 1977], and the results from the three biology experiments remained inconclusive [*Klein*, 1978].

Afterward, instead of searching for signs of life on Mars, the subsequent robotic mission sent to the planet would rather look for water-rock interactions, under the "follow the water" mantra. In this context, the twin Mars Exploration Rovers (MER), *Spirit* and *Opportunity*, were sent to roam the Martian surface in 2003. *Spirit* landed in the Gusev Crater, initially thought to have harbored an ancient lac in the past. *Opportunity* landed shortly after at Meridiani Planum, in the midst of hematite-rich deposits identified from orbit by TES on MGS.

In Gusev, the plains of the crater turned out to be olivine-bearing basaltic flows, mainly reworked through meteor impact and eolian erosion, but with very limited signs of aqueous alteration [*Squyres et al.*, 2004; *Haskin et al.*, 2005]. The *Spirit* rover thus changed course and headed toward the elevated and older terrains of the Columbia Hills that would present petrological, chemical and mineralogical evidence for liquid water interactions. The West Spur outcrop of the Columbia Hills display layered granular deposits enriched in goethite and hematite [*Arvidson et al.*, 2006; *Morris et al.*, 2006a], and possible detection of phyllosilicates [*Wang et al.*, 2006]. The Husband Hills outcrop later revealed the presence of Fe^{2+} carbonates, possibly siderite [*Morris et al.*, 2010], and the investigation of the Home Plate stratified volcanoclastic plateau led to the discovery of sulfate minerals and opal deposits produced in hydrothermal environments [*Squyres et al.*, 2008; *Yen et al.*, 2008; *Arvidson et al.*, 2010; *Ruff et al.*, 2011]. The rover was lost in 2010, embedded in the sulfate-rich sands deposited next to Home Plate.

The *Opportunity* rover landed by chance in one of the few craters of the Meridiani plains, in front of a stratified outcrop constituted of sulfate-rich sandstones, with ripple patterns suggesting transport in a fluvial environment [*Squyres*, 2004]. Hematite spherical concretions were also observed in the outcrop and were interpreted as an expression of diagenetic alteration from a rising ground-water table, after deposition of the sandstones (Figure 1.6) [*Chan et al.*, 2004; *McLennan et al.*, 2005]. Then, exhumation and surface erosion weathered out the diagenetic concretions to form a lag deposit of abundant hematite spherules covering the surface (Figure 1.6), which likely contributed heavily in the orbital detections of hematite by TES at that location.

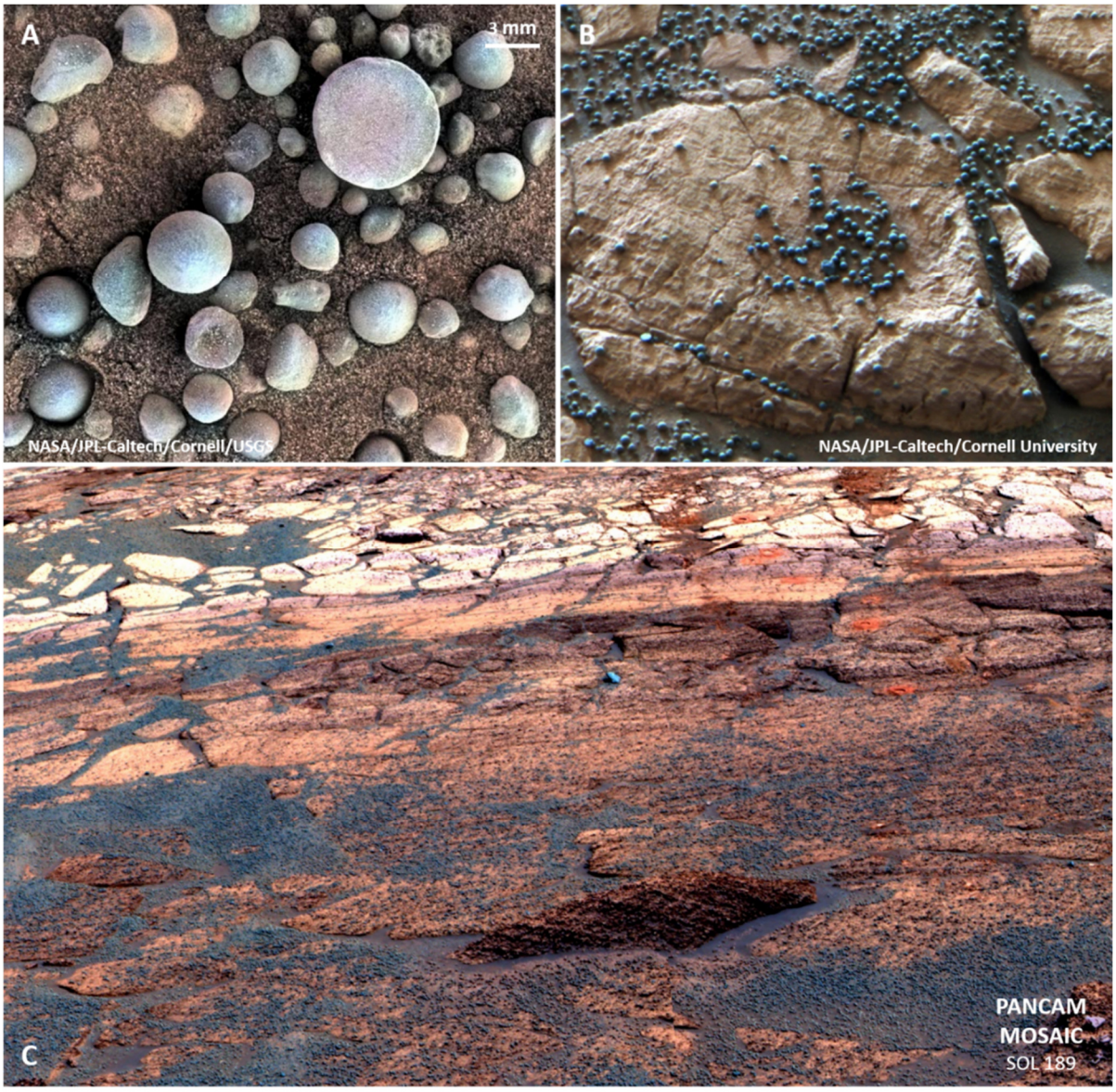

Figure 1.6: Micro-Imager (A) and Pancam (B, C) false color images of hematite spherules—"blueberries"—observed shortly after landing by the *Opportunity* rover at Meridiani Planum [*McLennan et al.*, 2005]. The hematite spherules initially formed as concretion in outcrops during diagenesis following groundwater recharge(s), which also produced the diagenetic cementation/recrystallization patterns visible as color gradients on the outcrops (C). The concretions then weathered out after exhumation to form a lag deposit of abundant hematite spherules covering the plains surface (C).

Afterward, the mission investigated the lateral continuity of sedimentary layers on exposed crater walls, notably in the larger Endurance Crater. The stratigraphic section explored by *Opportunity* in these craters form a set of genetically related strata known as the Burns geological formation [*Grotzinger et al.*, 2005], which can be subdivided into lower (eolian dune), middle (eolian sand sheet) and upper (mixed eolian sand sheet and interdune facies) units. Sedimentation appears to have been dominated by eolian processes, with the exception of the interdune facies, which is thought to have been deposited in a shallow subaqueous environment. Additionally, the sulfate-rich (up to 30 wt. %) nature of the eolian sandstones suggests that they constitute the reworked detrital products of sulfate-rich muds, which originally formed in evaporitic environments such as shallow playas [*Grotzinger et al.*, 2005; *McLennan et al.*, 2005].

Opportunity then moved on toward Endeavour Crater, searching for evidence of the aqueous alteration processes associated with the source rocks. The crater rim outcrops are dominated by the impact breccias of the Shoemaker formation, associated with the Endeavour impact, where localized Zn enrichments suggests subsequent hydrothermal alteration [*Squyres et al.*, 2012]. Finely laminated outcrops on the eastern side of the Cape York segment are attributed to the Matijevic formation, which unconformably underlies the Shoemaker formation breccias [*Arvidson et al.*, 2014]. Fe^{3+} smectite (clays) detected by CRISM in these deposits are interpreted to result from isochemical aqueous alteration, while more extensive leaching toward Al-smectite composition is observed in fracture zones, thus recording earlier episodes of aqueous activity [*Arvidson et al.*, 2014]. The rocks also exhibit coatings highly enriched in sulfate minerals and manganese oxide, inferred to have formed in the subsurface evaporative, and in the later-stage oxidizing, environment [*Arvidson et al.*, 2016]. Lastly, the gypsum-rich ($CaSO_4$ x 2 H_2O) veins that cut through the sedimentary rocks of the Burns and Majikevic formation are indicative of low-temperature aqueous fluid circulation during diagenesis, perhaps supporting local and transient habitable environments after the Endeavour impact [*Squyres et al.*, 2012; *Arvidson et al.*, 2014]. At the time of writing, *Opportunity* is still active and has traveled more than 45 km during its exploration of Meridiani Planum and Endeavour Crater.

In summary, the *in situ* exploration from the MER rovers have thus confirmed the presence of transient aqueous environments on the surface in the past, but also highlighted the complexity of the sedimentary deposits investigated, which often evades orbital detections and in some cases led to skewed geological interpretations. Indeed, at both MER sites, post-depositional processes heavily influenced the geological evolution of the sediments either through post-impact hydrothermal activity (*Spirit*) or diagenetic fluid circulations (*Opportunity*).

1.2 Gale Crater and diagenesis

1.2.1 Gale Crater geological context

The Mars Science Laboratory (MSL) rover, *Curiosity*, is currently the last mission to have successfully landed on the Martian surface (in 2012), within the basal plains of a ~155-km wide impact crater, Gale, located on fluvially dissected highlands along the dichotomy boundary (Figure 1.7A).

The crater was selected as the MSL landing largely due to the presence of the 5-km high Aeolis Mound (also referred to as Mount Sharp) at its center [*Grotzinger et al.*, 2012], constituted of layered sedimentary deposits. CRISM hyperspectral observations revealed stratigraphic trends in mineralogy in the lower part of the mound, with phyllosilicate bearing deposits (Clay Unit) in the lowermost layers giving way to hydrated sulfates and iron oxide up section (Sulfate Unit) [*Anderson*, 2010; *Milliken et al.*, 2010], suggesting that the Mount Sharp strata record global-scale environmental changes [*Thomson et al.*, 2011]. CRISM also identified significant crystalline hematite signatures on the upper-most part a ~6.5 km-long and 200-m wide erosion resistant ridge, known as Vera Rubin Ridge (formerly hematite ridge), that fringes the clay-bearing deposits [*Fraeman et al.*, 2013] (Figure 1.8).

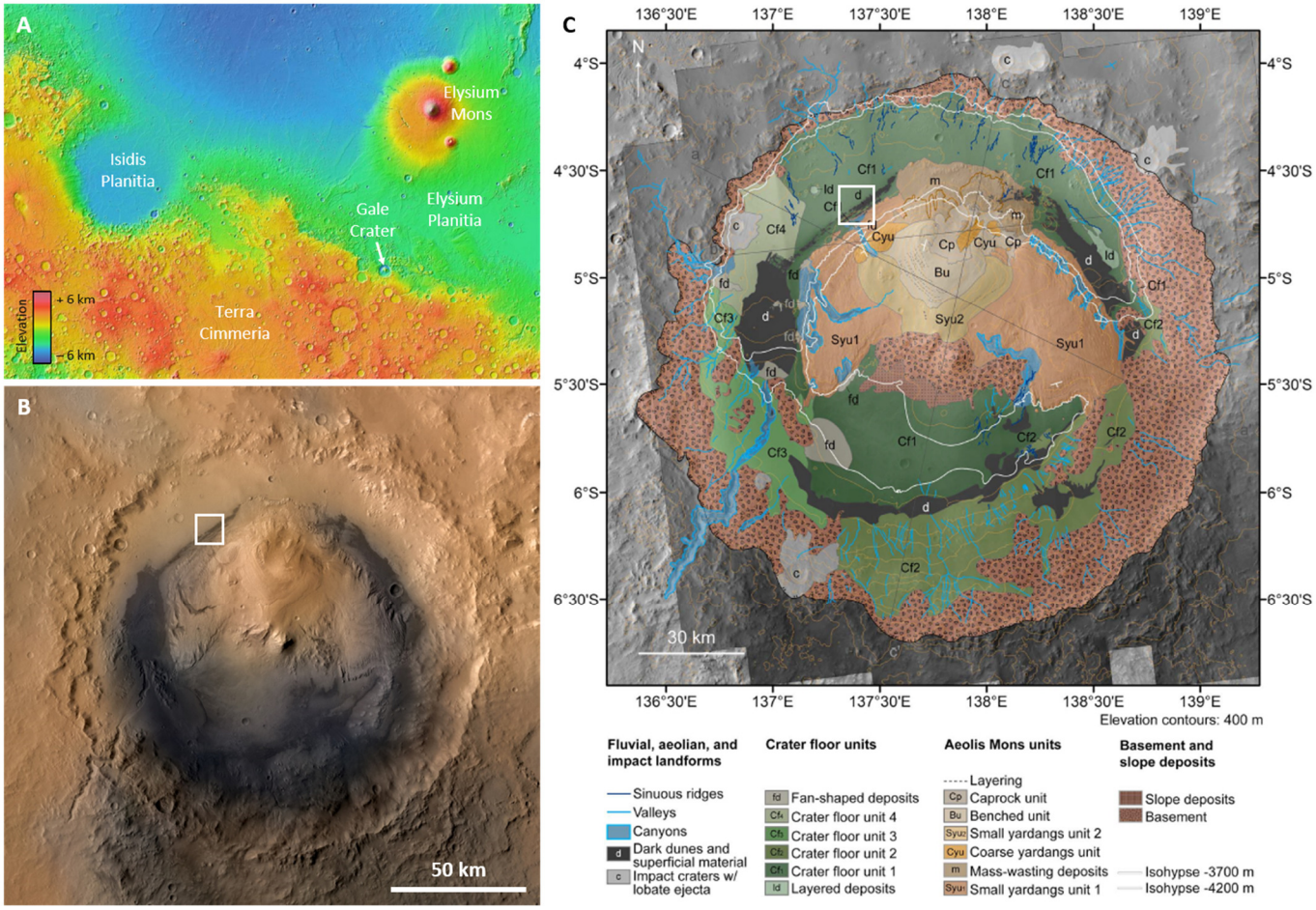

Figure 1.7: Gale Crater regional and geological context. (A) Topographic map (MOLA) showing the localization of the Gale Crater at the crustal dichotomy between the Elysium Planitia to the north and the ancient highlands of the Noachian to the south. (B) Orbital view of the crater from the HRSC camera (Mars Express). (C) Detailed geological map of the crater deposits [*Le Deit et al.*, 2013] highlighting canyons, valleys, and fan-shaped deposits interpreted to reflect past fluvial activity. The white box indicates the location of Figure 1.8.

In association with mineralogical evidence for past aqueous activity in the crater, the observations of fluvial channels that truncate crater rims and alluvial fan deposits [*Anderson*, 2010; *Le Deit et al.*, 2013] indicate that a shallow lake once occupied the crater floor (Figure 1.7C). However, geomorphic features suggestive of periglacial processes are also observed in Gale and may limit the extent of lacustrine activity to transient and local occurrences, only spawning the first thousands of years following its formation [*Le Deit et al.*, 2013]. Lastly, the impact-induced hydrothermal activity may also have contributed to the formation of sediments in the crater, potentially lasting for a few hundreds of thousands of years [*Schwenzer et al.*, 2012].

Crater counts place the Gale impact and associated crater formation between ~3.8 to 3.6 billion years ago [*Thomson et al.*, 2011; *Le Deit et al.*, 2013] and the deposition of sedimentary materials before 3.3 to 3.1 billion years ago (Figure 1.4) [*Grotzinger et al.*, 2015]. As such, the crater provides the opportunity to investigate the evolution of Mars ancient environments and paleoclimates, and notably whether conditions capable of sustaining liquid water on its surface persisted throughout the Hesperian.

1.2.2 *Curiosity* rover traverse and Gale sedimentary stratigraphy

At the time of writing, the *Curiosity* rover reached Vera Rubin Ridge, just short of the clay-rich deposits that were identified as the main objective of the mission before launch [*Grotzinger et al.*, 2012], after a cruise of ~20 km across sedimentary deposits from its landing site south of the "Peace Vallis" alluvial fans (Figure 1.8). During that time, it explored two stratigraphic groups of sedimentary rocks exposed in the Bradbury Plains (also known as Aeolis Palus) and the basal strata of Mount Sharp (Figure 1.9).

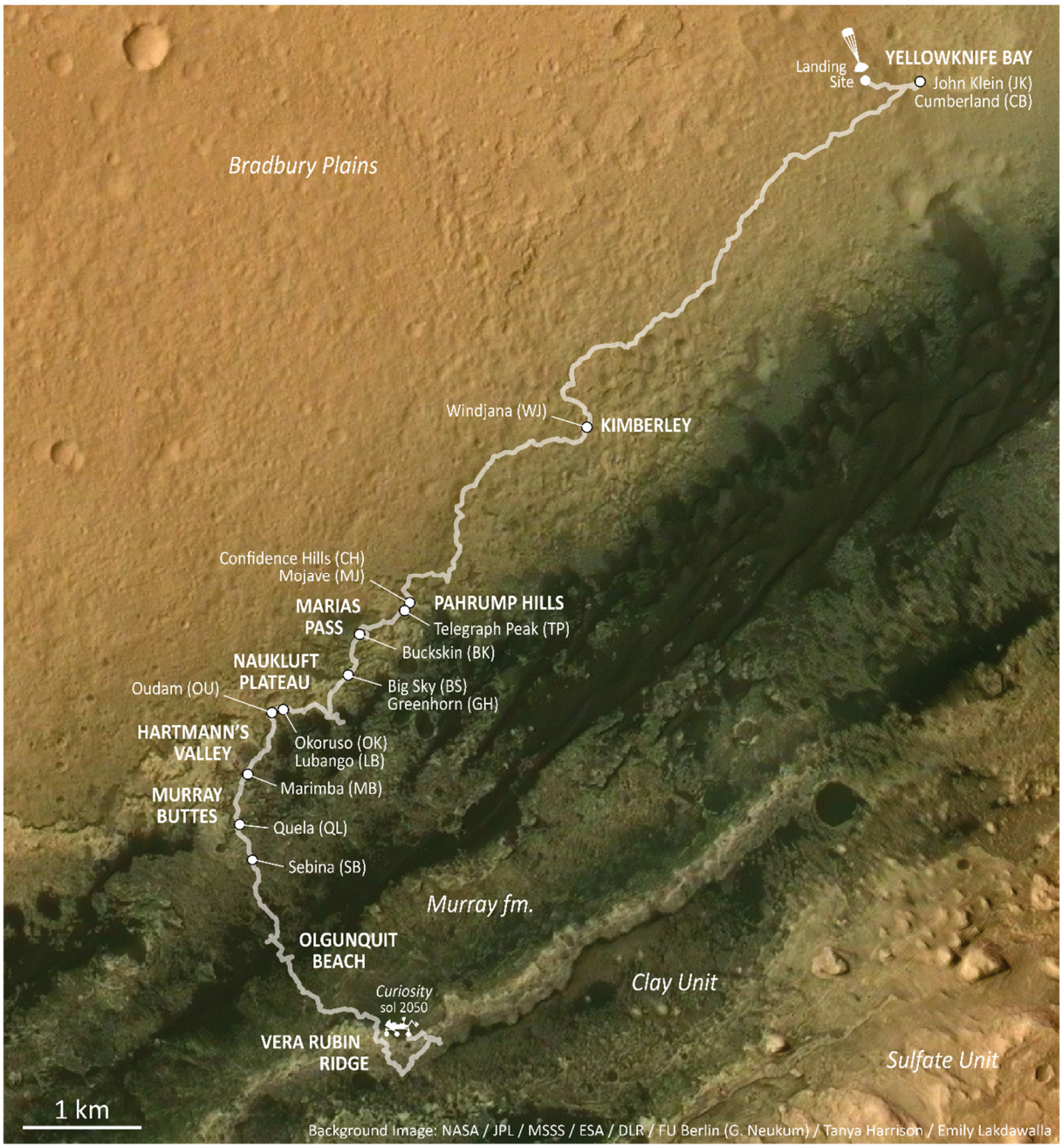

Figure 1.8: Traverse of the *Curiosity* rover (HiRISE images, colors from HRSC), from its landing at Bradbury to its location on sol 2050 at Vera Rubin Ridge. The localities of interest discussed in this manuscript are indicated along the traverse, as well as drill locations (white circles; acronyms are indicated in parentheses). The main geological units encountered *in situ* are also annotated (Bradbury Plains and Murray formation), as are the Clay and Sulfate Units identified from orbit and located upslope toward the Mount Sharp.

The Bradbury group designates the rocks observed at *Curiosity* landing site and continuously thereafter, up to the contact with the Mount Sharp strata, at Pahrump Hills (Figure 1.9). The Mount Sharp group consists of the sedimentary strata of Mount Sharp, including the basal Murray formation and the overlying hematite (Vera Rubin Ridge), clay, and sulfate units identified from orbit [*Milliken et al.*, 2010]. It is unconformably overlain by the eolian deposits of the upper parts of Mount Sharp (Siccar Point group), marking a sharp transition from rocks bearing hydrated minerals below the contact to rocks without obvious hydrated minerals above (Figure 1.9).

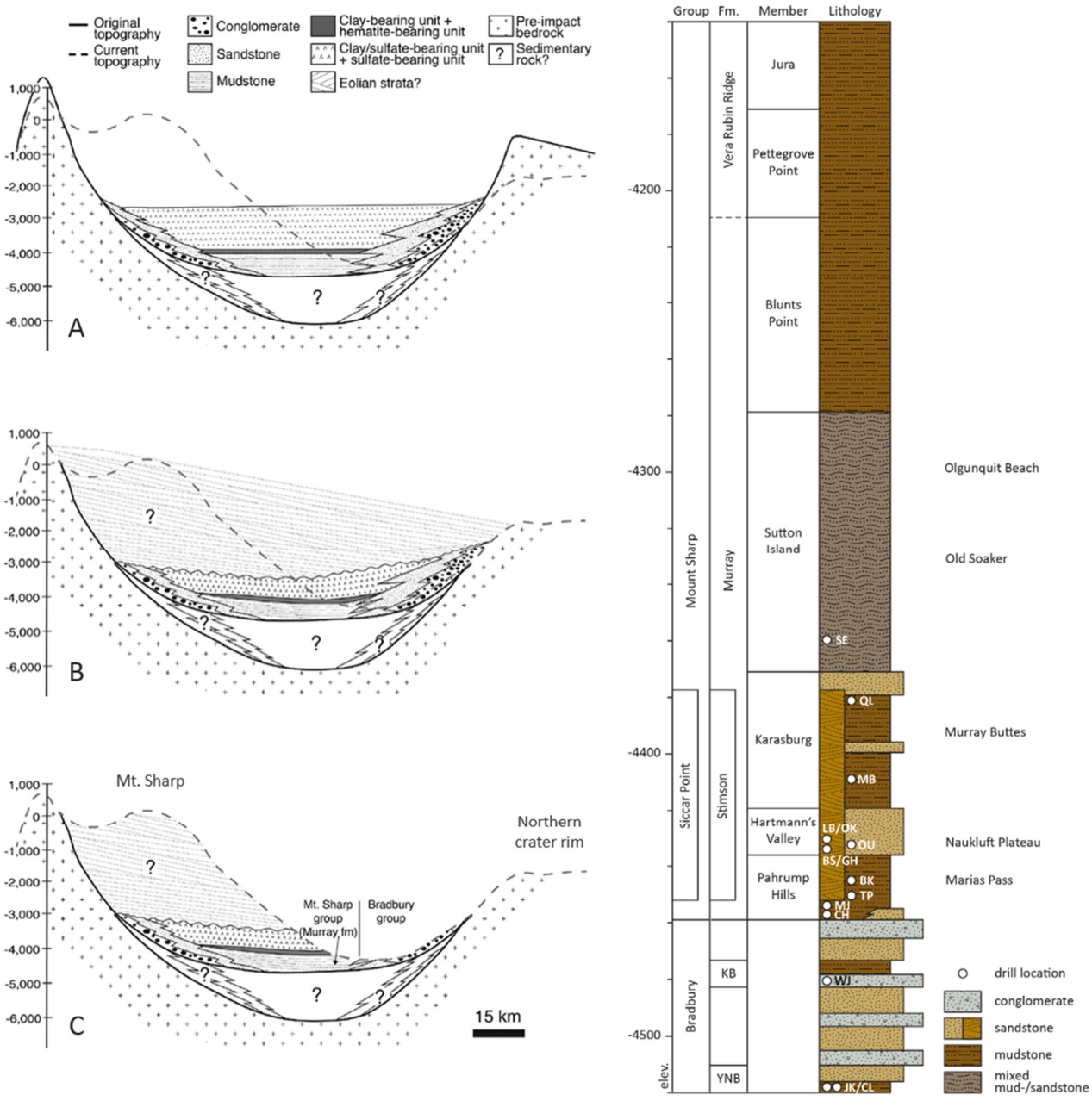

Figure 1.9: Modeled history of the infilling of Gale Crater and formation of Mount Sharp [modified from *Grotzinger et al.*, 2015] (left) and stratigraphic column reflecting the sedimentary rocks encountered so far by the rover (right; credit to the MSL Sed. Strat. Working Group). (A) Early sedimentation in fluvio-lacustrine environments filling the base of the crater. (B) Eolian deposition during the subsequent dry period, forming the bulk of Mount Sharp and compacting the underlying strata. (C) Exhumation of the crater-filling strata by wind-driven erosion. *Curiosity* landed amidst the sedimentary rocks of the Bradbury group (mainly fluvial and delta deposits), at the lowest point of the exhumed surface, then drove uphill to the south across a facies transition into the lacustrine sediments of the Murray formation, constituting the basal strata of the Mount Sharp group.

In the Bradbury group, *Curiosity* mainly observed sandstones (finely stratified, cross-stratified and clinoform) and conglomerates consistent with fluvio-deltaic deposits [*Williams et al.*, 2013; *Grotzinger et al.*, 2015; *Mangold et al.*, 2016] as well as locally finely laminated mudstones at the Yellowknife Bay and Kimberley study sites tracing transient lacustrine depositional environments over thousands to hundred thousands of years [*Grotzinger et al.*, 2014, 2015]. Phyllosilicates are detected in drill samples (CheMin) at Yellowknife Bay indicating neutral pH and low salinity lacustrine conditions [*Grotzinger et al.*, 2014; *McLennan et al.*, 2014; *Bristow et al.*, 2015]. The lack of evidence for chemical weathering further indicates that deposition/erosion occurred rapidly under arid and possibly cold paleoclimates [*McLennan et al.*, 2014]. Finally, the anomalously high potassium (sanidine) enrichments observed at Kimberley [*Le Deit et al.*, 2016; *Treiman et al.*, 2016] indicates variability in source rock composition, and together with chemical analysis on detrital igneous textures encountered along the traverse, revealed more evolved magmatic compositions (felsic) than previously thought on the planet [*Sautter et al.*, 2014, 2016; *Cousin et al.*, 2017; *Payré et al.*, 2017a].

Upon reaching the Pahrump Hills, the *Curiosity* rover crossed over to the lacustrine finely laminated mudstones of the Murray formation that constitutes the basal layers of Mount Sharp [*Grotzinger et al.*, 2015] (Figure 1.8 and 1.9). The transition from the Bradbury group to the Murray formation is progressive, interpreted to reflect north-to-south interfingering of coarser fluvio-deltaic facies of the Bradbury group with the fine-grained facies of the Murray formation consistent with alluvial fans prograding southwards from the northern crater [*Grotzinger et al.*, 2015]. However, this interpretation is still debated and the emplacement of the Bradbury group sedimentary rocks may be posterior to the lacustrine deposits of the Murray formation [*Stack and Grotzinger*, 2015], consistent with the inferred arid and cold climatic conditions [*McLennan et al.*, 2014].

The finely laminated mudstones of the Murray formation have been consistently observed from the Pahrump Hills onward, up to Vera Rubin Ridge, without significant change in facies suggesting that perennial lacustrine activity occurred over prolonged period of time (> 300 m in thickness; ~10^5–10^7 years) [*Grotzinger et al.*, 2015; *Hurowitz et al.*, 2017; *Fedo et al.*, 2018]. The erosional remnant of eolian deposits associated with the Stimson formation (Siccar Point group) are also encountered along the rover traverse, at the Naukluft Plateau and Marias Pass localities (Figure 1.8), overlying unconformably the Murray formation [*Banham et al.*, 2018]. Mineralogical observations from the numerous drill samples collected in the Murray formation [*Bristow et al.*, 2018] (Figure 1.9) and geochemical observations along the rover traverse [*Mangold et al.*, 2018b] show increased evidence for open-system chemical weathering up-section (formation of dioctahedral smectite and hematite), consistent with the shallowing and episodic lake desiccation (e.g. desiccation cracks) observed near the Ogunquit Beach locality [*Stein et al.*, 2018] (Figure 1.8). In essence, the Murray lacustrine mudstones record oxidizing [*Hurowitz et al.*, 2017] and fluctuating lake-level depositional environments, consistent with relatively warm and dense paleoclimates near the Noachian / Hesperian transition (Figure 1.4).

1.2.3 Diagenesis

The Gale Crater sedimentary deposits are also heavily influenced by post-depositional aqueous alteration processes, occurring after the burial of the sediments during diagenesis. Notably, widespread occurrences of Ca-sulfate bearing light-toned veins associated with hydro-fracturing are encountered in all geological terrains crossed by the rover [*Nachon et al.*, 2014, 2016; *Rapin et al.*, 2016] indicating that regional late-diagenesis S-rich fluid(s) circulation affected all sedimentary deposits observed so far at Gale Crater.

The Yellowknife Bay sedimentary rocks feature abundant hollow nodules, concretions and fracture-fills [*Léveillé et al.*, 2014; *Siebach et al.*, 2014; *Stack et al.*, 2014] indicating that groundwater interactions induced chemical and mineralogical changes in the sediments after deposition, possibly including clay and magnetite formation [*McLennan et al.*, 2014; *Tosca et al.*, 2018].

The Murray formation sedimentary rocks also display various evidences for groundwater interactions, including acidic leaching processes at Pahrump Hills [*Nachon et al.*, 2016; *Berger et al.*, 2017; *Rampe et al.*, 2017], thought to have significantly altered the chemistry and mineralogy of the lacustrine sediments during diagenesis, as well as the overlying eolian deposits of the Stimson formation [*Frydenvang et al.*, 2017; *Yen et al.*, 2017].

1.3 Problem statement and research objectives

As depicted in this section, the Martian sedimentary deposits record the environmental conditions at the time of deposition, and as such hold the key to solve the conundrum of the climatic evolution of the planet, and whether conditions compatible with the presence of liquid water on its surface could be sustained for geologically significant periods of time. The answer to this question also has significant importance on whether one of Earth planetary neighbors ever harbored habitable environments, potentially suitable to the emergence of life.

Orbital morphological and mineralogical observations in the past two decades have highlighted a shift in surface conditions on Mars over the course of the Hesperian, progressively transitioning from paleoclimate consistent with liquid water activity on its surface to the dry and cold planet, almost devoid of any atmosphere, it is today. *In situ* observations have in part confirmed that aqueous activity occurred on its surface, and even provided evidence for potentially habitable environments in the past, but also highlighted the complexity of the sedimentary deposits that cannot be resolved from the orbital scale. Amidst this complexity, the diagenetic evolution of the sediments after deposition and burial, notably involving groundwater systems, can modify significantly the original sediment chemistry and/or mineralogy—which was indeed observed by the three major *in situ* missions send to Mars over the last decade (*Spirit*, *Opportunity* and *Curiosity*). As such, interpretations on the depositional environment and derived climatic conditions may be misleading if the influence of diagenetic processes on the formation of sedimentary deposits is not thoroughly understood and taken into account.

Diagenetic processes are still poorly understood on Mars, notably because the few *in situ* missions capable of observing them only landed recently on its surface. Fortunately, the Gale Crater sedimentary deposits are teeming with opportunities to study the changes they were subjected to after burial. In addition, the *Curiosity* rover carries onboard the ChemCam instrument especially suited to the geochemical study of small-scales diagenetic features.

The MSL mission is thus able to tackle some of the outstanding questions on the evolution of sediments after deposition at Gale Crater, and by extension, on Mars. What are the characteristics of the diagenetic processes identified at Gale Crater? How and in what manner did such processes influence the formation of its sedimentary deposits? And more precisely, how and to what extent did such processes affect the texture, chemistry, and mineralogy of the sediments and sedimentary rocks after deposition and burial? Finally, what can be inferred from these observations on the evolution of sedimentary rocks after burial in the broader context of the planet?

In addition, the diagenesis of the sediments at Gale also involved the circulation of fluids in the sub-surface, such as groundwater flows and hydrofracturing, as evidenced by the presence of concretions and vein-fills in outcrops. What can be inferred on the chemical and thermodynamical properties of such fluids? And in what measure were post-depositional water-rock interactions (such as mineral alteration, leaching, and redox-driven reactions) involved in the formation of Gale sedimentary deposits?

In order to provide the beginning of an answer to some of these questions, this study will focus on the characterization of the geochemical variability in Ca-sulfate light-toned veins and on how they affect the surrounding host rock compositions. Indeed, these diagenetic features are observed consistently across all geological terrains observed so far by the rover, emplaced during the later-stages of diagenesis. As such, they can be used as a proxy for the study of the various diagenetic environments in Gale Crater. Notably, the mobility in specific elements, such as Fe, observed in association with the formation of Ca-sulfate veins at specific locations along the rover traverse provides information on the groundwaters redox and pH conditions. Consequently, the diagenetic processes inferred from these observations may provide alternative hypotheses in order to explain the chemical and mineralogical trends observed in the Gale sedimentary deposits, often inferred to reflect almost exclusively the conditions during deposition.



[Sol **1943**]
SELF-PORTRAIT OF THE CURIOSITY ROVER ON VERA RUBIN RIDGE
NASA/JPL-Caltech/MSSS



CHAPTER 2

THE CHEMCAM INSTRUMENT AND THE *CURIOSITY* ROVER

The Mars Science Laboratory (MSL) mission aims to explore the past and present habitability of Mars through the geological study of the Gale Crater sedimentary deposits. In order to do so, the *Curiosity* rover, a scaled-up version (900 kg, 3 x 2.8 x 2.2 min dimension) of the previous Mars Exploration Rovers (MER) *Opportunity* and *Spirit*, carries on-board an unprecedented suite of 10 scientific instruments. Among those, greyscale and color imagers will provide context and textural information, while chemistry and mineralogy will be derived from spectroscopic measurements and analyses of drilled rock samples. In addition, *Curiosity* brings for the first time on Mars, and more broadly speaking in space, the Laser-Induced Breakdown Spectroscopy (LIBS) analytical technique with the ChemCam instrument, which allows for remote fine-scale chemical analyses with limited contribution from the dust cover.

In this chapter, we will introduce the *Curiosity* rover scientific instruments used in our studies of Gale Crater geological features, with an emphasis on the ChemCam instrument. Afterward, we will define the LIBS analytical technique, and outline ChemCam data processing and analytical methods used to provide chemical quantifications for major and minor elements.

2.1 *Curiosity*, Chemistry, and Camera

2.1.1 The *Curiosity* rover scientific payload

The Mars Science Laboratory (MSL) mission embodies a paradigm shift in the NASA Mars exploration program, transitioning from the "follow the water" strategy, which yielded extensive evidences for aqueous activity throughout its history (c.f. Chapter 1), to a search for past and present habitable environments, or "habitability". Albeit loosely defined, the habitability of a planetary body (i.e. planets or natural satellites) indicates its potential to harbor environmental conditions under which life may have developed, and/or can be sustained. Based on the only form of life we know, our own, habitable conditions would require at least liquid water, a source of carbon (to enable organism metabolism) and a source of energy (to fuel organism metabolism) [*Grotzinger et al.*, 2012]. In essence, the search for habitable conditions in our nearest neighbor planet constitutes a major step forward in the search for life elsewhere in our solar system, and beyond.

To assess the past and present habitability of Mars, the MSL mission identified four scientific goals[1], including the geological characterization of the landing region (i.e. Gale Crater) through the investigation of the chemical, isotopic, and mineralogical composition of surface and near-surface materials, to which this study contributes. In order to do so, the *Curiosity* rover includes a range of scientific instruments and supporting engineering tools (Figure 2.1), in large majority participating in the characterization of geological features. The rover is designed to first identify geological items remotely, with instruments located on the Remote Sensing Mast (Navcam, Mastcam, and ChemCam), before proceeding to contact science observations (MAHLI and APXS) using its robotic arm, and finally, sample acquisition (scoop or drill, processed by CHIMRA) and analysis by the internal analytical laboratory instruments (SAM and CheMin).

[1] for more information on MSL science objectives, visit https://msl-scicorner.jpl.nasa.gov/ScienceGoals/

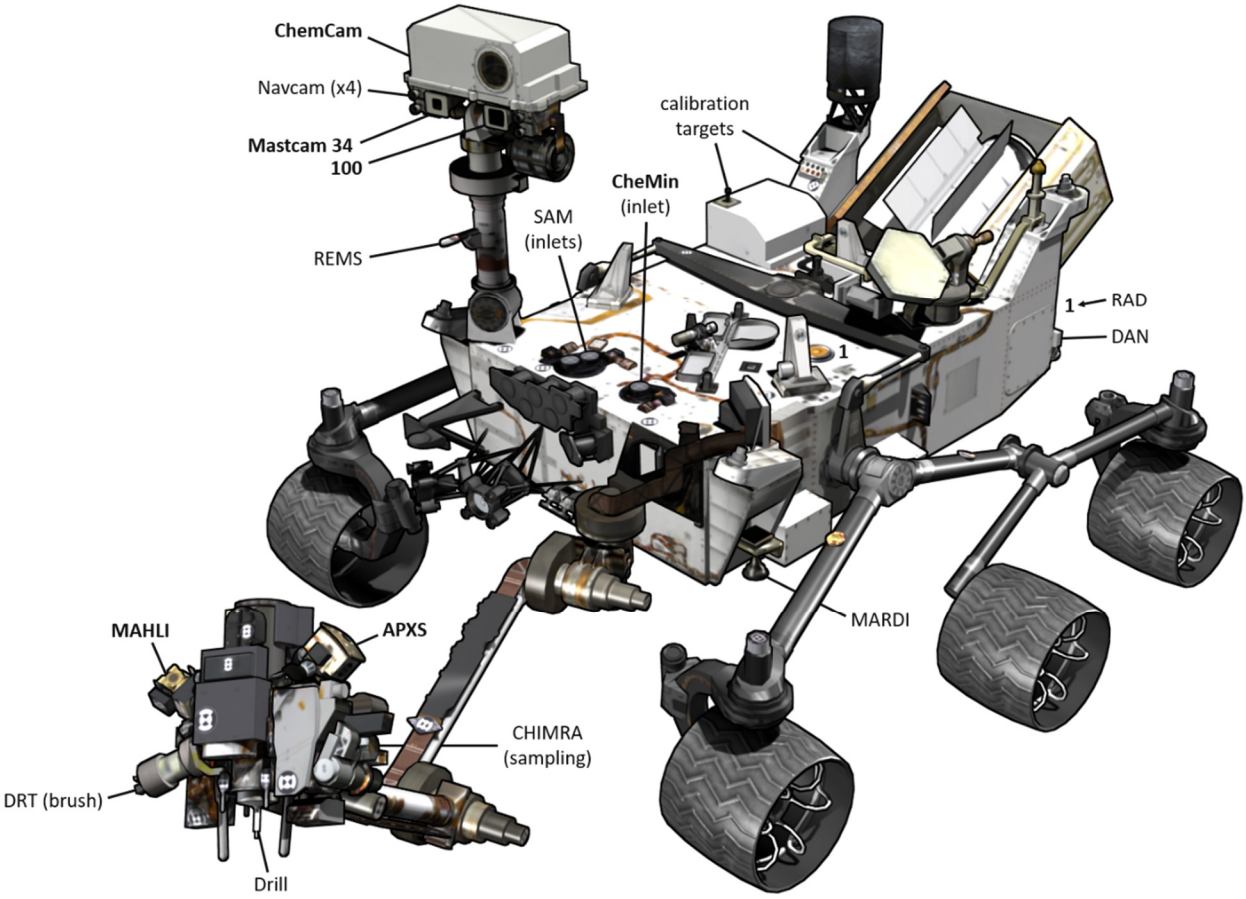

Figure 2.1: The *Curiosity* rover scientific payload and supporting engineering tools [modified from the NASA 3D model of the *Curiosity* rover]. Instruments discussed in this chapter are highlighted (**bold**).

Although the studies presented in this manuscript are heavily ChemCam-centric, they also refer to chemical and mineralogical observations from other instruments (notably APXS and CheMin) and make use of the contextual images and inherent textural information from other cameras (MAHLI and Mastcam).

The two Mastcam (Mast Camera) cameras (34 mm and 100 mm focal lengths) located on the rover mast (Figure 2.1), provide contextual "true color" (i.e. as seen by the typical human eye) images for ChemCam observations at the outcrop scale, with a 150 µm/pixel resolution at 2 m [*Malin et al.*, 2017], and are used to colorize greyscale ChemCam images. Mastcam also documents stratigraphic relationships and outcrops variability outside of the rover path, with a ≤10 cm resolution per pixel at 1 km, which can be used to extrapolate chemical and mineralogical observations. Mastcam can perform 12 narrowband filtering for visible and near-infrared spectroscopy (445–1013 nm), similar to the capabilities of the MER Pancam instrument [*Bell et al.*, 2003], to provide multispectral images used to map the variability in reflectance spectral properties, and as such surface mineralogical variations (notably for Fe-bearing minerals) [*Wellington et al.*, 2017]. Finally, the acquisition of stereo images can be used to compute photogrammetric quantitative 3-dimension (3D) models, useful for interpreting spatial relationships between strata and geomorphic features (c.f. Annex B). In parallel, the two Navcam stereo pairs (left and right) of engineering greyscale cameras provide extensive spatial coverage with significant overlap (360° panorama at each rover locations), well suited to photogrammetry [*Maki et al.*, 2012].

MAHLI (Mars Hand Lens Imager), mounted on the robotic arm of the rover (Figure 2.1), produces high-resolution (up to 14 µm/pixel at the minimum distance of 2.1 cm) close-up "true color" images of outcrops that provide fine-scale textural and structural information on geological features. MAHLI is able to resolve grain size down to coarse silt [*Edgett et al.*, 2012]. It also imparts valuable mineralogical information regarding the shape, cleavage, color, fluorescence, and luster of individual mineral grains. As such, MAHLI is instrumental for petrographic and mineralogical interpretation on rocks and regolith fines, especially when used in conjunction with other instruments providing information on chemistry (SAM, ChemCam, and APXS) and mineralogy (CheMin).

CheMin (Chemistry and Mineralogy) is a powder X-ray diffraction (XRD) instrument with additional X-ray fluorescence (XRF) capabilities, located inside the main body of the *Curiosity* rover (Figure 2.1), as part of the MSL analytical laboratory [*Blake et al.*, 2012]. The instrument returns accurate mineralogical identifications and quantitative phase abundances of powdered rock samples and/or soil (< 150 µm size fraction), with a minimum detection limit of 3 wt. %. CheMin also quantifies the X-ray amorphous component and its estimated chemical composition, which typically includes truly amorphous phases (e.g. volcanic glass) but also poorly crystalline phases such as opal-A, opal-CT and ferrihydrite [*Rampe et al.*, 2017]. CheMin observations are also fundamental in constraining mineral interpretations associated with chemistry-only observations from the ChemCam and APXS instruments.

Finally, the APXS (Alpha-Particle X-ray Spectrometer) instrument, located on the robotic arm of the rover (Figure 2.1), combines Particle-Induced X-ray Emission (PIXE) and X-ray fluorescence (XRF) analytical methods to provide bulk elemental chemistry, covering a sample area of about ~1.7 cm in diameter [*Campbell et al.*, 2012]. It reports abundances for major and trace elements (Z ≥ Z(Na), including Ni, Zn, and Ge), with high precision and low detection limits (notably for S, Cl, and Br), improving on the previous versions already present on Pathfinder and the twin MER rovers. The X-ray penetration depth varies as a function of the atomic mass of the elements, from a few micrometers for lighter elements (Na to Si) up to ~80 µm for heavier elements (e.g. Fe and Mn) [*Schmidt et al.*, 2014; *Gellert and Clark*, 2015]. As such APXS analyses are especially sensitive to the dust cover (notably for lighter elements), omnipresent on Mars, and often require dust removal (using the DRT brush) to limit its contribution and better reflect the chemistry of rock surfaces. Therefore, APXS procures complementary chemical information compared to the ChemCam instrument, with an increased accuracy and lower detection limits for some non-metal and halogen elements (S, P, Cl, and Br), as well as representative bulk rock chemistry.

2.1.2 ChemCam

The ChemCam (Chemistry and Camera) instrument consists of a Laser-Induced Breakdown Spectrometer (LIBS) coupled with a high-resolution camera, the Remote Micro-Imager (RMI) [*Maurice et al.*, 2012; *Wiens et al.*, 2012]. LIBS provides remote elemental composition on rocks and soils with limited contribution from the dust cover, while the RMI camera provides greyscale textural and morphological information.

The RMI covers a 20-mrad field of view at sub-millimeter resolution (~90 µrad). It is thus able to resolve 1 mm objects at 10 m of distance, which allows for the identification of LIBS laser impact points and reveals finer details on outcrops compared to Mastcam images [*Le Mouélic et al.*, 2015].

The LIBS system uses a temperature-controlled Nd:KGW laser that produces 5 ns pulses of 1067 nm photons with energies up to 35 mJ, focused by the telescope over a ~350 to ~550 µm sample area at 1.5 to 7 m distance [*Maurice et al.*, 2012]. The light collected by the telescope is allocated to three spectrometers by an optical demultiplexer, covering the 240-342 nm, 382-469 nm and 474-906 nm spectral domains (e.g. Figure 2.4) with respective spectral resolutions of 0.15 nm, 0.20 nm and 0.61 nm [*Wiens et al.*, 2012]. The onboard electronics do not have time-gating capability, i.e. the ability to synchronize the laser pulse with spectrometer acquisition (to the ns) in order to collect only the part of the plasma emission associated with elemental lines, and as such avoid the spectral noise from the continuum (c.f. section 0).

The ChemCam instrument is divided into two sub-sections (Figure 2.2): the Mast Unit, mounted on top the rover mast (Figure 2.1), consisting of the laser, telescope and RMI components [*Maurice et al.*, 2012]; and the Body Unit, inside the rover, comprising the optical demultiplexer and the three spectrometers [*Wiens et al.*, 2012]. ChemCam capabilities are articulated around the telescope (Schmidt-Cassegrain) that focuses the laser pulses on target but also convey light back to the spectrometers and the RMI camera via an optical fiber.

ChemCam also includes a set of 10 calibration targets on the rover deck [*Fabre et al.*, 2011; *Vaniman et al.*, 2012; *Wiens et al.*, 2012], to monitor the LIBS performance, correct instrument bias and assist calibration efforts on Mars. Ti metal, graphite and 4 glasses of igneous composition provide primary, homogeneous calibration targets while 4 granular ceramic targets provide compositions closer to soils and sedimentary materials expected to be encountered at Gale Crater (basalts, evaporites, and phyllosilicates).

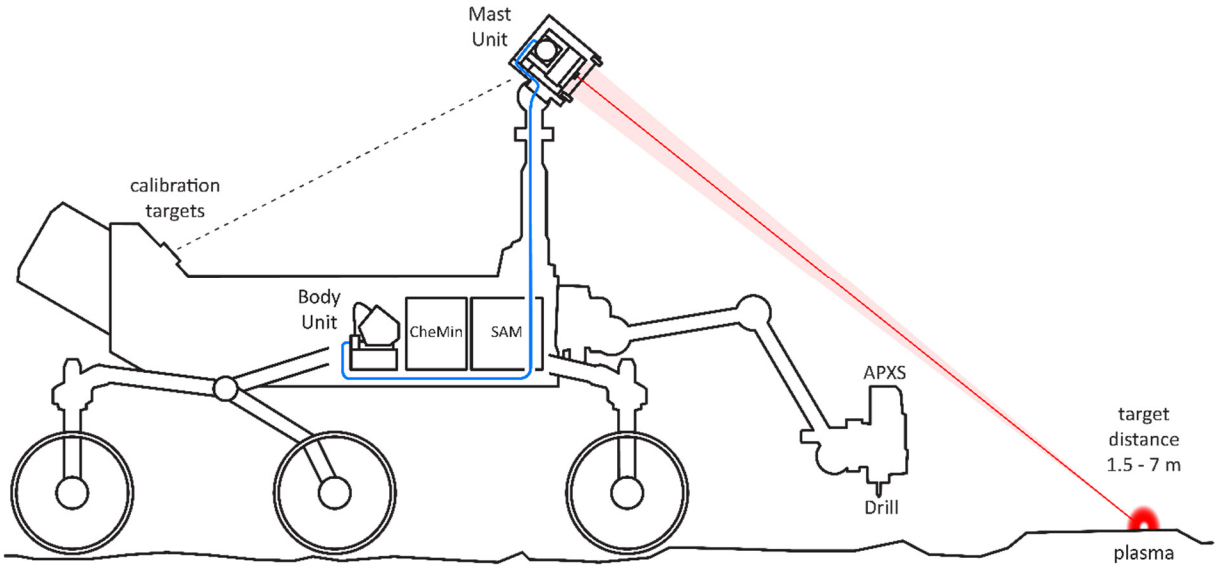

Figure 2.2: Schematic representation of the ChemCam instrument, composed of the Mast and Body Units as well as calibration targets on the rover deck [modified from *Rapin*, 2016]

Additionally, two replicas of the ChemCam Mast and Body Units (engineer models and flight spares) exist on Earth (one at LANL, in Los Alamos, United States; the other at IRAP, in Toulouse, France). They are routinely used for laboratory analyses and experiments with a setup almost identical to the ChemCam instrument on the *Curiosity* rover, in analog Martian atmospheric conditions. Duplicates of the calibration targets also exist, allowing comparison between Earth and Mars LIBS analyses.

ChemCam LIBS observations typically consist of 30 laser shots on a given point, and each ChemCam analysis usually comprises a "raster" of several closely spaced observation points. In this process, dust is removed from the surface of the target by the first few laser shots, thus enabling the analysis of the dust-free surface target material (Figure 2.3). The ablated area covers ~300 to 600 µm in diameter (i.e. roughly equal to the laser spot size), and up to a few micrometers in depth depending on the targeted material [*Maurice et al.*, 2012]. Additionally, repeated laser shots (up to ~1,500 shots) provide chemical depth-profiling capability to study weathering coatings (Figure 2.3) and probe the underlying rock chemistry if the coating is thinner than ~0.5 mm [*Wiens et al.*, 2012].

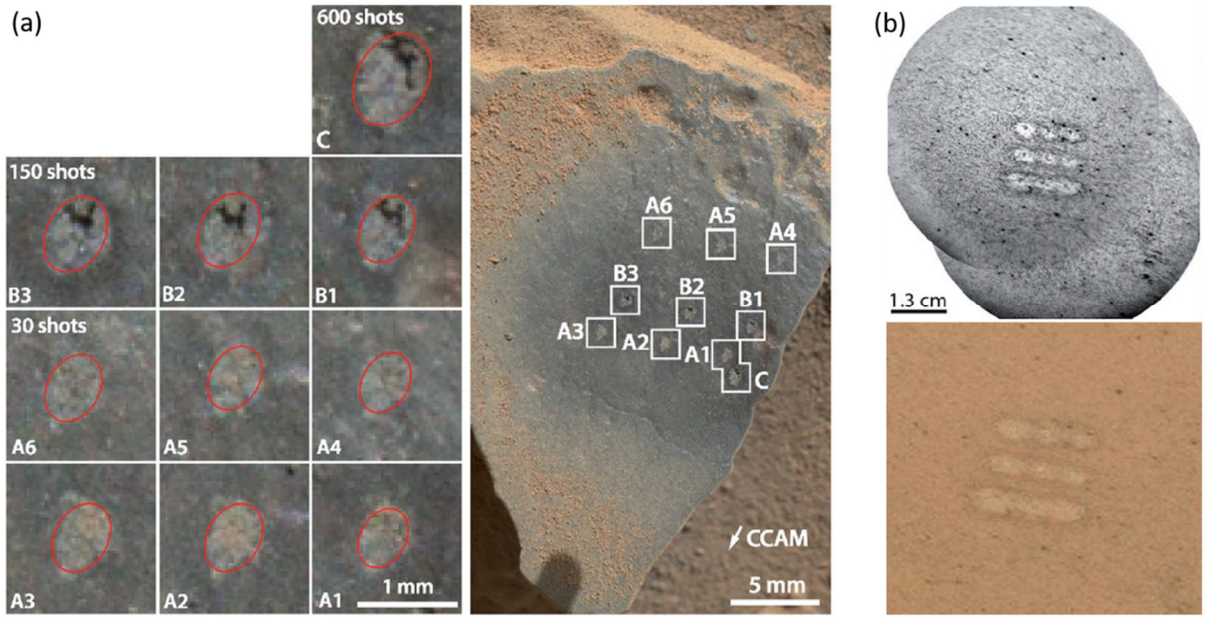

Figure 2.3: (a) MAHLI image (Sol 672) displaying various series of laser shots on "Stephen" (Sol 611-620-630) that illustrates the increasing area (red ellipses) and depth of laser impact pits with repeated laser shots. (b) Dust is effectively blown away by the LIBS laser impact shock wave, as illustrated on "Hanaupah" (3 x 3 raster, 30 laser shots, Sol 779) with RMI (top) and Mastcam (bottom) context images [from *Maurice et al.*, 2016]

In addition, after each LIBS observation, passive reflectance spectra (without active laser use) are also acquired using the ChemCam spectrometers, recording the Martian surface radiance in the visible/near-infrared (400-840 nm; Figure 2.4). The angular field of view of 0.65 mrad of the spectrometer corresponds to a 2 mm diameter area on the surface at 3 m distance from the rover (50% of ChemCam targets are within 2 to 3 m from the rover and 45% within 3-5 m [*Maurice et al.*, 2016]); it is thus wider than the LIBS ablation area.

Upon interaction with the targeted material, part of the incident light is absorbed at specific wavelengths from electronic and vibrational processes that are characteristic of the composition and crystalline structure of its constituting mineral species [*Burns*, 1993]. The ChemCam spectrometer covers part of the electronic processes that have absorptions in the VNIR (visible and near infrared; 400 - 1300 nm), but not the vibrational processes produced by the excitation of molecular or crystal lattice bonds that are observed in the SWIR (shortwave infrared; 1300 - 2500 nm) [*Hunt and Salisbury*, 1970].

The most common electronic processes observed in the spectra of minerals are due to electronic transitions (to higher energy states), especially within transition metals (e.g. Fe, Ni, Cu, and Mn), and charge transfer between the different valence states of the same metal [*Hunt*, 1977]. In this regard,

the main absorption features resolved by the ChemCam spectrometers corresponds to electronic transitions and charge transfers associated with iron, and in particular of the ferric ion (Fe^{3+}) [*Johnson et al.*, 2015]. The crystal structure also influences the position of the absorption bands, e.g. goethite and hematite have distinct positions for the Fe^{3+} adsorption bands.

As a result, the ChemCam passive spectra can provide information on the presence of Fe^{3+}-bearing mineral phases and their crystallinity, most notably hematite [*Johnson et al.*, 2015, 2016] – information otherwise inaccessible from LIBS analyses, which do not distinguish between the redox states of Fe.

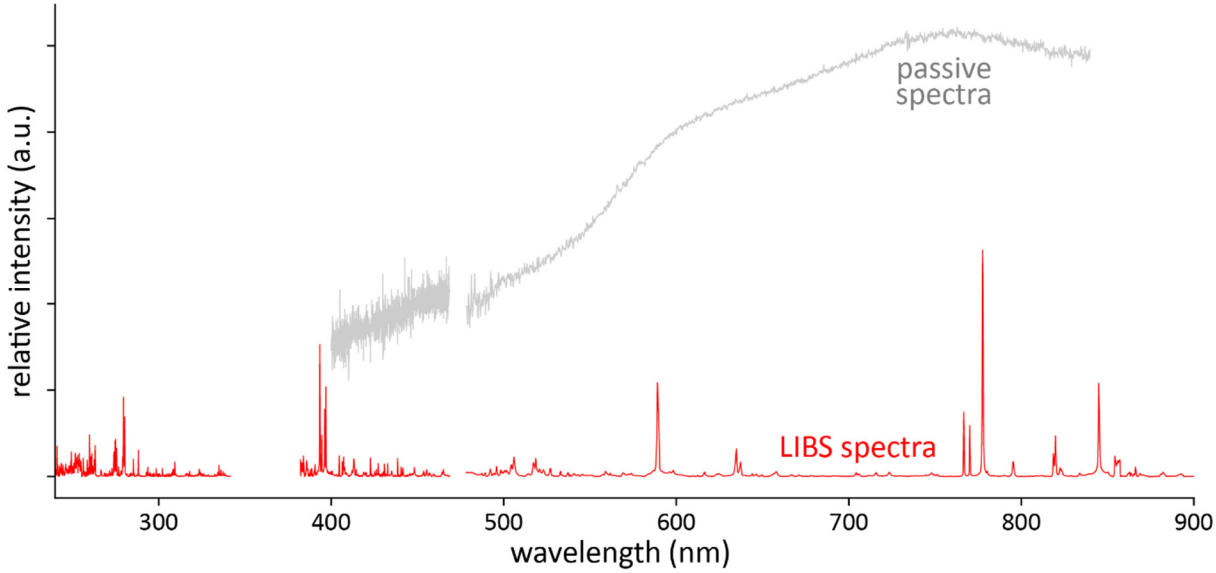

Figure 2.4: ChemCam LIBS spectra (in red) and passive reflectance (in grey; half intensity for clarity) for the point #1 of the Holyrood target.

2.2 LIBS technique and ChemCam data processing

2.2.1 Laser-Induced Breakdown Spectroscopy (LIBS)

The ChemCam instrument relies on the Laser-Induced Breakdown Spectroscopy (LIBS) technique in order to provide elemental chemistry. The LIBS involves focusing a pulsed laser beam on a given material with an irradiance of at least 1 GW/cm^2. The high photon flux beaks down the target material, ablating the atoms and atomic clusters in electronically excited states that form a rapidly expanding plasma. As the excited atoms, ions and molecules contained in the plasma decay to lower electronic states, they emit radiations at characteristic wavelengths resulting in a strong glow that lasts several µs (e.g. Figure 2.5). Thus, the spectral analysis of the light emitted by the plasma allows for the identification of its constituting elements (ions, atoms and even some molecules) by their specific spectral signatures (i.e. emission peaks at characteristic wavelengths) [*Miziolek et al.*, 2006].

The light produced by the plasma, however, does not solely reflect the spontaneous emissions from its ionic and atomic particles but is rather constituted of distinct components that evolve rapidly with time (Figure 2.6a).

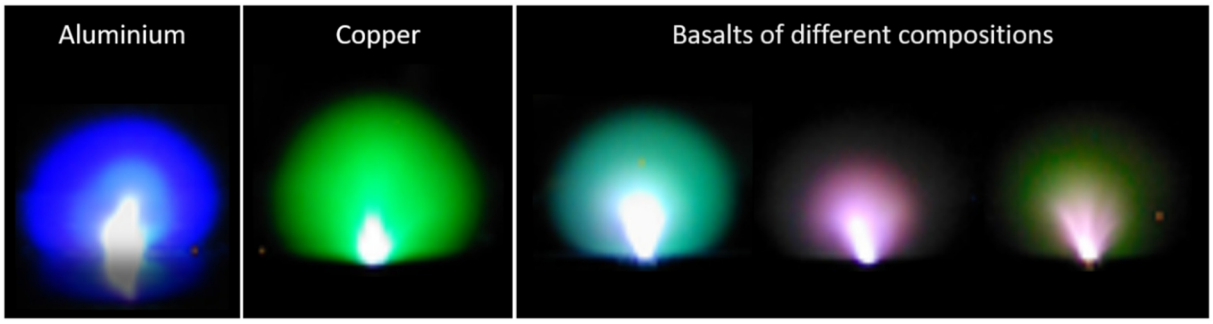

Figure 2.5: Image of LIBS generated plasma on different materials [modified from *Sirven et al.*, 2007]

The early light following plasma formation (first few ns) is dominated by a "white light" continuum, with little variation as a function of wavelength. The high plasma density at this stage favors complex collisions and interactions between particles that produce electromagnetic braking radiations (bremsstrahlung) from the deviation of free electrons, as well as ion-electron recombination radiations, resulting in this continuous "white light".

Afterward, the rapid expansion of the plasma (~10^6 m/s) [*Hahn and Omenetto*, 2010] leads to a drastic decrease in plasma density, diminishing the contribution from the continuum radiations. The specific emissions associated with the decay of particles to lower electronic states then dominate the spectra (during a few µs). Finally, as the plasma cools down, the relatively lower temperatures allow molecular combinations to occur from free atoms and ions, with the associated radiations contributing to the later stages of plasma light emissions (until its dissipation after ~10 µs).

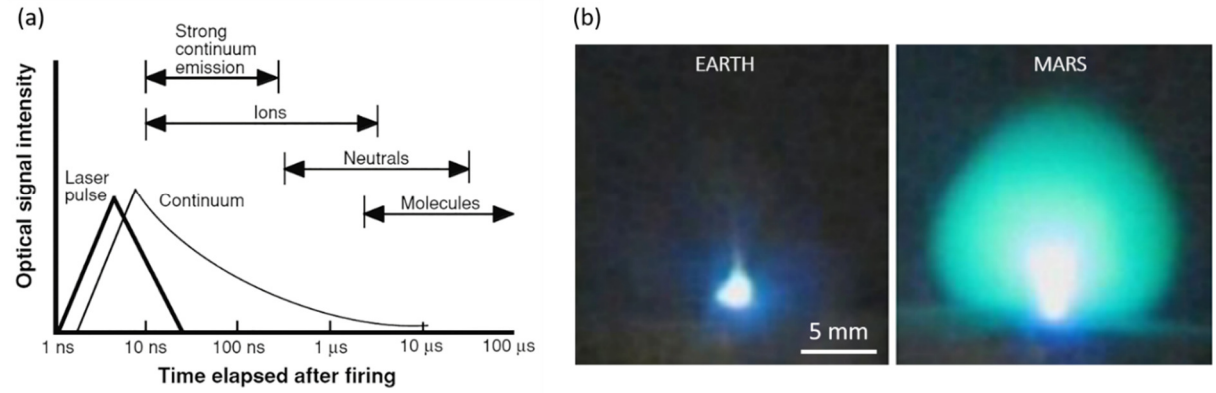

Figure 2.6: (a) Time periods after plasma formation during which emissions from different species predominate [modified from *Miziolek et al.*, 2006]. (b) Image of plasma generated by a LIBS laser on the same material, under Earth (1 bar) and Mars (~6 mbar) atmospheric pressure conditions [modified from *Lasue et al.*, 2012].

The quality of the signal also depends on environmental conditions, as plasma expansion is notably impacted by atmospheric pressure conditions (Figure 2.6b). Lower pressures improve the resolution of LIBS spectra with increased intensity and narrower width on emission peaks. Indeed, the associated lower plasma density leads to an increase in the ablated material [*Knight et al.*, 2000], due to lower plasma shielding effects (laser absorption by inverse bremsstrahlung), and also limit the Stark effect responsible for emission lines broadening (from perturbations by electron-generated electric fields in the plasma). Very low pressures (< 5 mbar), however, lead to a lack of confinement in the plasma and a degradation of the signal, due to a decrease in the frequency of particle collisions [*Knight et al.*, 2000] and expansion of the radiations outside of the spectral domains covered by the spectrometers.

With respect to Mars, atmospheric conditions (~6 mbar) are close to optimal for LIBS analyses [*Knight et al.*, 2000; *Brennetot et al.*, 2003; *Sallé et al.*, 2005], sufficiently low to favor plasma expansion but not too low as to degrade the signal, alleviating the need to time-gate the signal. Incidentally, LIBS applications in the exploration of other planetary bodies such as the Moon (P = ~3 x 10^{-15} bar) or Venus (P = ~93 bar) appear however to be more limited.

The nature of atmospheric gases can also influence the LIBS signal. Indeed, considering various gases such as He, Ar, CO_2 or air can alter the signal intensity by a factor of 10, mainly due to plasma shielding effects that depend heavily on the gas ionization potential and thermal conductivity (at fixed pressure) [*Iida*, 1990; *Lee et al.*, 1997; *Effenberger and Scott*, 2010]. Additionally, the dissociation of atmospheric CO_2 in the plasma limits the identification of carbonate species in LIBS emission spectra from intense C emission lines [*Ollila et al.*, 2011; *Beck et al.*, 2017]. Nevertheless, laboratory studies by [*Sallé et al.*, 2005] have shown that Mars atmospheric conditions (~7 mbar of CO_2) yielded more accurate calibrations for major elements, and reduced matrix effects, compared to lunar and terrestrial settings.

Finally, in LIBS spectroscopy, as in other plasma-related analytical spectroscopy techniques, elemental analyses typically rely on the verification of a few fundamental assumptions. Unfortunately, the ChemCam LIBS is unable to verify all of them and thus requires specific calibrations to derive elemental compositions (as discussed below). These fundamental assumptions are:

(1) Laser ablation is stoichiometric, i.e. the plasma composition truly reflects the sampled material composition. For most LIBS applications, ablation is inferred to be stoichiometric if the laser irradiance exceeds the 1 GW/cm^2 threshold [*Chan and Russo*, 1991; *Miziolek et al.*, 2006], which is the case for ChemCam over the entire range of stand-off distances covered (1.5 to 7 m) [*Maurice et al.*, 2012].

(2) In order to model the parameters of the laser-induced inhomogeneous and transient plasma, the plasma must be in Local Thermodynamic Equilibrium (LTE), i.e. in a state where all chemical species and radiations (or the distribution of particle velocities) are at the same temperature [*van der Mullen*, 1989]. If so, the plasma characteristics may be described by its excitation temperature and electronic density using the Saha–Eggert relation and Boltzmann-Maxwell distributions [*Cristoforetti et al.*, 2010; *Cremers and Radziemski*, 2013], including the distribution of chemical species in the plasma (e.g. calibration-free LIBS). ChemCam is, however, unable to characterize plasma parameters with sufficient accuracy, and instead relies on calibration standards of known composition to quantify major and minor elements (c.f. section 2.2.3), and as such does not require the verification of the LTE in order to provide information on chemistry [*Wiens et al.*, 2013].

(3) The plasma must be optically thin, i.e. not suffering from self-absorption [*Tognoni et al.*, 2002]. Atoms in the lower energy levels can easily reabsorb the radiation emitted by other atoms of the same element in the plasma, so it is less troublesome for elements present in low concentration in the plasma (e.g. trace elements). In order to mitigate the impact of self-absorption on the quantification of major elements, which are typically present in high concentrations, ChemCam relies on multivariate analysis which takes into account all resolved elemental lines of the considered elements over the entirety of the spectra [*Anderson et al.*, 2017; *Clegg et al.*, 2017]. In contrast, the univariate method that considers only a few emission lines per element (not self-absorbed) is favored for quantifying trace elements as it better maps low-intensity signal variations [*Payré et al.*, 2017a].

2.2.2 ChemCam LIBS data processing

In order to extract the information of interest from the LIBS data, the raw LIBS spectra acquired by ChemCam are all processed in the same way: removal of the non-laser-induced background (dark subtraction), de-noising, removal of the electron continuum, wavelength calibration and instrument optical response corrections [*Wiens et al.*, 2013].

Dark-subtraction consists in subtracting the non-laser data (passive spectra) from the associated LIBS spectra, thus reducing drastically the signal from the ambient light. Afterward, the spectral noise (white noise) is removed using a wavelet transform: at each wavelet scale, only the signal above 3-sigma of the noise standard deviation is preserved. The de-noised spectrum is then reconstituted by summing all modified wavelet scales. Similarly, the continuum background (due to bremsstrahlung and ion-electron recombination processes) is removed using a wavelet transform at low frequency, which provides a spline function interpolated between local minima [*Wiens et al.*, 2013].

In order to account for shifts in wavelengths attributed to thermal variations on the Martian surface, the spectrometers are frequently calibrated using the Ti plate on the rover. Indeed, Ti provides multiple emission peaks in all three of the spectral ranges covered by ChemCam, and allow for channel-to-wavelength adjustments on the spectrometers in order to align the Ti lines in the acquired spectra with the baseline [*Wiens et al.*, 2013].

The instrument optical response was also calculated in order to allow for comparison between instruments (i.e. between ChemCam and its replica) and to correct changes in optical response with time [*Wiens et al.*, 2012]. In association with the continuum removal, the instrument response corrections also reduce the effects of the target distance on the spectra [*Wiens et al.*, 2013].

Lastly, the processed LIBS spectra are typically normalized in order to minimize changes in ablated volume (i.e. line intensity) for elemental quantification. Depending on the element(s) considered, the intensity at each wavelength is either divided by the total emission intensity over all three spectrometers, or by the total emission intensity of its respective spectrometer [*Clegg et al.*, 2017].

2.2.3 Elemental quantifications

ChemCam is able to detect all major elements; their abundances are quantified in weight percent of oxides (SiO_2, TiO_2, Al_2O_3, FeO, MgO, CaO, Na_2O, and K_2O) using a combination of two multivariate analytical methods – namely the "Partial Least Squares" (PLS) and "Independent Component Analysis" (ICA) methods. The PLS method compares multiple emission lines for a given element to known standards composition from testbed samples on Earth [*Clegg et al.*, 2009; *Wiens et al.*, 2013]. This technique has been updated over the course of the mission using a number of sub-models covering compositional ranges observed for each element on Mars for more accurate predictions [*Anderson et al.*, 2017]. The ICA method stems from blind source separation research [*Hyvarinen*, 2001] and identifies a set of statistically independent components used to characterize the spectra, from which elemental abundances are derived using regression laws between ICA scores and reference spectra of known composition [*Forni et al.*, 2013]. The combination of PLS and ICA results in the multivariate oxide composition (MOC) dataset [*Clegg et al.*, 2017].

Expansion of the ChemCam calibration database to 408 standards (from the original set of 66) and associated recalibration was completed in 2015 [*Wiens and Maurice*, 2015; *Clegg et al.*, 2017]. The increased geochemical diversity covered by the revised database better reflect the rock compositions

observed at Gale Crater, and thus refines the quantification of major elements with the ChemCam instrument (notably for Ca-sulfates) [*Clegg et al.*, 2017, supplementary materials]. Nevertheless, the current calibration can still be improved, as some specific compositional configurations remain poorly quantified (e.g. high Fe composition, such as pure Fe-oxide or Fe-Ni meteorite, c.f. Chapter 4).

A number of minor and trace elements detected by ChemCam are also quantified using a univariate method, in which a single emission peak is calibrated for the abundance of that element. These include Mn [*Lanza et al.*, 2014], Sr, Li, Ba, Rb [*Payré et al.*, 2017a], Cu [*Payré et al.*, 2017b], Zn [*Lasue et al.*, 2016], B [*Gasda et al.*, 2017], and F [*Forni et al.*, 2015]. In addition, the hydration state for specific compositions can be derived from the H signal using recent calibration efforts [*Rapin et al.*, 2016]. Other volatile elements such as S, P, and Cl are so far only observed qualitatively, but are often used for chemical and mineralogical diagnostic studies [*Nachon et al.*, 2016; *Meslin et al.*, 2018], although some works are currently in progress to quantify them systematically [*Meslin et al.*, 2016; *Anderson et al.*, 2017; *Clegg et al.*, 2018; *Rapin et al.*, 2018; *Thomas et al.*, 2018].

The analytical limits of detection (LOD) for the major and minor elements observed by ChemCam are summarized in Figure 2.7.

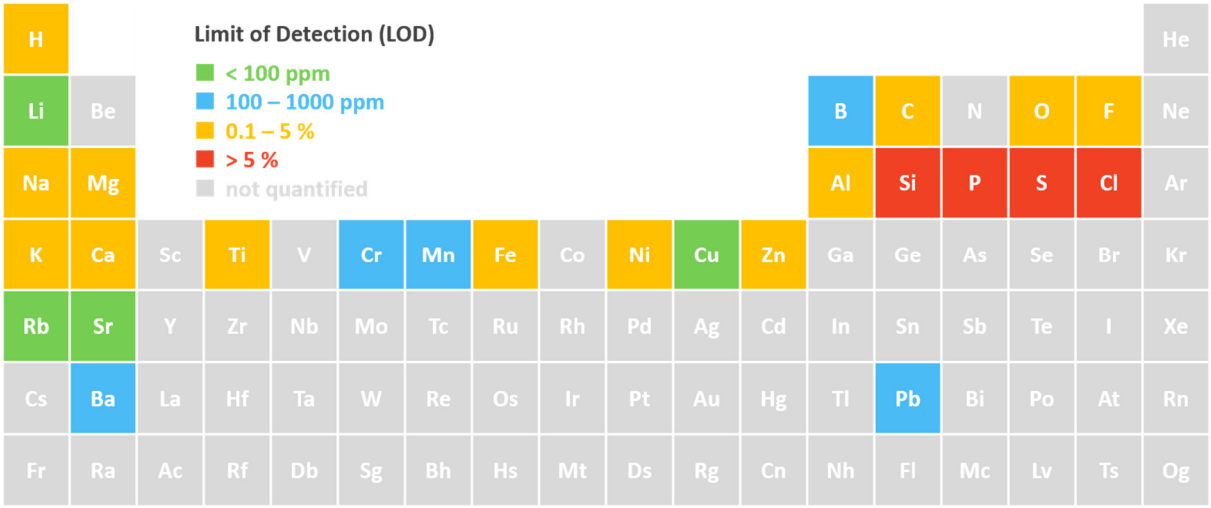

Figure 2.7: Simplified periodic table illustrating ChemCam LIBS detection limits [*Wiens et al.*, 2013; *Clegg et al.*, 2017; *Payré et al.*, 2017a]

The accuracy of ChemCam measurements is estimated by the root mean squared error of prediction (RMSEP) from a test set of standards of known composition. The test set for each major element was selected to have a distribution as similar as possible to the full training set used to generate the regression models [c.f., *Clegg et al.*, 2017]. The RMSEP is reported based on a leave-one-out cross-validation, using the difference between the predicted (p_i) and reference (r_i) values for each (sample i) of the n samples:

$$\mathrm{RMSEP} = \sqrt{\frac{1}{n}\sum_{i=1}^{n}(p_i - r_i)^2}$$

Furthermore, since the accuracy of ChemCam predictions varies with the sample composition, the RMSEP is reported as a function of the composition [*Anderson et al.*, 2017; *Clegg et al.*, 2017].

Finally, the measurement precision is defined as the reproducibility of the ChemCam predictions and can be estimated by the standard deviation of calibration target observations [*Wiens et al.*, 2013; *Clegg et al.*, 2017, and references therein]. On targets of unknown composition, the precision is reported as the standard deviation of the abundances derived from a shot-to-shot analysis [*Maurice et al.*, 2016].

As previously discussed, the ChemCam LIBS observations remove the dust that covers the targeted material with the first few laser shots. The first five spectra, however, typically retain some degree of contamination from the dust, and thus not considered for elemental quantifications. The subsequent spectra (usually 25) acquired are averaged, and this average spectrum is used to determine the elemental composition for each LIBS observation point [*Lasue et al.*, 2014].

Nevertheless, the quantified elemental abundances for each individual spectra at a given location are also considered to investigate compositional variations with depth (i.e. shot-to-shot profiles), which may provide information on the distinct mineral grains probed (through correlations between elements) or highlights the presence of weathering coatings.

2.2.4 Low abundance variations in major elements

Finally, in order to highlight low abundance variations in major elements (below the quantification accuracy), we use a similar approach to the univariate method [*Fabre et al.*, 2014]. However, instead of relying on a set of calibration standards to provide quantified abundances, we look for variations in the relative signal intensity on selected emission line(s) for the elements considered. These methods allow for the identification of small-scale enrichments in some elements over others (e.g. Fe over Si), which is notably useful in order to trace minor chemical variations in an otherwise similar composition such as Ca-sulfate bearing diagenetic features (c.f. Chapter 3).

The selection of the most relevant emission line(s) for each element consists in a trade-off between signal intensity, self-absorption (notably for neutral lines), relative standard deviation, and overlap with other elemental lines. In the context of low abundance variations, self-absorption (overall low under Martian conditions [*Sallé et al.*, 2005]) is minimized whereas overlap with other elemental lines, notably between the elements considered for relative comparison, and signal intensity (sufficient to detect low concentrations) are more determinant. In order to limit the interference of overlapping emission lines, the part of the spectra neighboring the considered line is fitted using a series of Voigt functions with a linear baseline. The Voigt profile matches the shape of LIBS emission lines under Martian pressure conditions, resulting from the convolution of Gaussian profiles produced by pressure broadening and Lorentzian profiles produced by natural broadening (uncertainty in energy related to the lifetime of an excited state). The line intensity area for the considered element is then derived from the area of the associated Voigt profile(s).



[sol **944**]
MINERALIZED CA-SULFATE VEINS AT ARTIST DRIVE
NASA/JPL-Caltech/MSSS



CHAPTER 3

CHEMICAL VARIABILITY IN CALCIUM SULFATE VEINS IN GALE CRATER

The Gale Crater sedimentary rocks host a wide variety of geological features that formed during the diagenesis of the sediments. Among them, light-toned veins are observed across all geological terrains crossed by the *Curiosity* rover during its exploration of the crater basal plains and the lower layers of the Mount Sharp.

First observed shortly after landing in the fluvio-lacustrine sedimentary deposits of the Yellowknife Bay formation [*Grotzinger et al.*, 2014], in the Bradbury group, the light-toned filled-fractures crosscut sedimentary structures (e.g. laminations, bedding planes and cross-stratification) as well as concretions and nodules of diagenetic origins [*Léveillé et al.*, 2014; *Nachon et al.*, 2014; *Siebach et al.*, 2014; *Stack et al.*, 2014]. As such, these veins constitute the latest diagenetic episode(s) observed so far in Gale Crater [*Kronyak et al.*, 2015]. Structural analyses on fracture network patterns show a lack of preferred orientation in fracture intersection angles, "wandering" morphologies and encapsulated host rock fragments (Figure 3.1), which argue for a hydraulic fracturing mode of formation, due to pore-fluid pressure build-up following burial and compaction [*Caswell and Milliken*, 2017].



Figure 3.1: Ca-sulfate veins observed in the Yellowknife Bay (YKB) formation and in the Murray formation exhibit a wide array of fracture orientations (vertical to sub-horizontal) and intersection angles, “wandering” morphologies (black arrow) and encapsulate host rock fragments (white arrow), which indicates hydraulic fracturing [from *Caswell and Milliken*, 2017]

ChemCam chemical analyses on the veins identified hydrated Ca-sulfate, based on high CaO abundances in association with S and H emission lines in the LIBS spectra (Figure 3.2) [*Nachon et al.*, 2014]. Sr enrichments are also observed consistently in the veins and reflect the substitution of Ca by Sr in the Ca-sulfate lattices [*Nachon et al.*, 2014]. Recent developments on H calibration for ChemCam data allowed for the quantification of water content [*Rapin et al.*, 2017] and reported H_2O levels consistent with the presence of bassanite ($CaSO_4$ x 0.5 H_2O), the semi-hydrated form of Ca-sulfate (Figure 3.3) [*Rapin et al.*, 2016]. Bassanite is interpreted to result from the dehydration of gypsum ($CaSO_4$ x 2 H_2O) upon exposure to the hyper-arid Martian surface conditions (near-surface desiccation) or from increase in temperature through burial and/or impacts, as anhydrite ($CaSO_4$) hydration and direct precipitation of bassanite are both unlikely from a thermodynamical perspective [*Robertson and Bish*, 2013; *Rapin et al.*, 2016]. Consequently, gypsum formation as a precursor to bassanite put some thermal constraints for the emplacement of these diagenetic veins as gypsum only precipitates below 60°C [*Warren*, 2016]. This implies maximum burial depths of 1.5 to 3 km at the time of formation based

on geothermal gradients hypotheses [*Borlina et al.*, 2015], which is also consistent with burial depth estimates derived from fracture morphologies [*Caswell and Milliken*, 2017]. Geochemical modelling of fluids involved in the diagenetic processes observed at Yellowknife Bay [*Schwenzer et al.*, 2016] surmise that light-toned vein formation results from the partial-dissolution of hypothetical pre-existing impure sulfate layer(s) at depth, in order to account for the pure nature of the observed Ca-sulfate composition (no Ba, Rb or Zn observed, typically associated with Ca-sulfate).

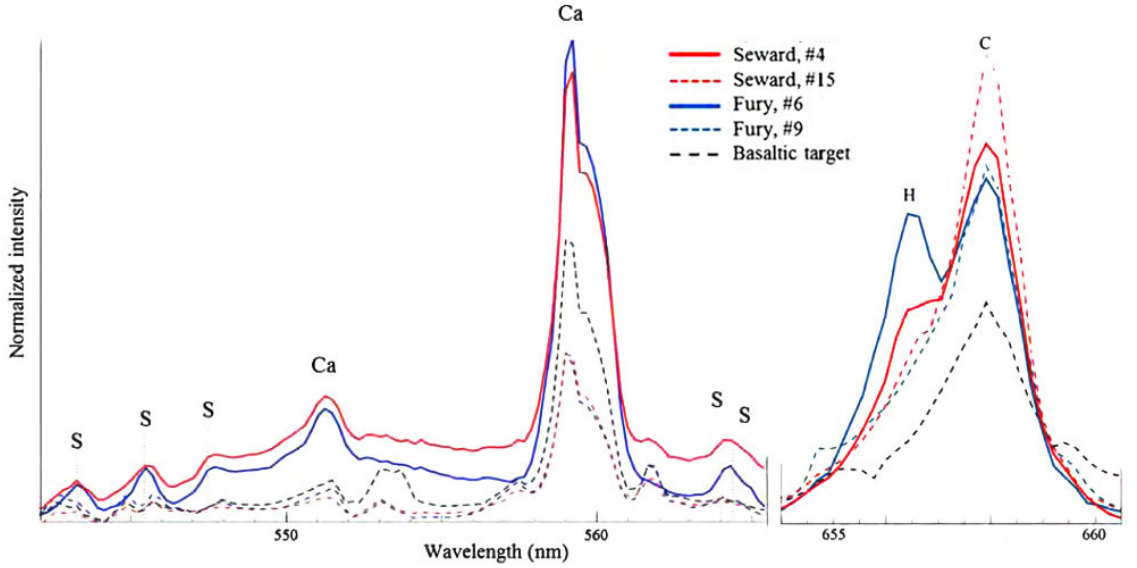

Figure 3.2: Detection S and H peaks on ChemCam LIBS spectra of light-toned veins (Seward #4, and Fury #6) associated with high Ca content, interpreted as Ca-sulfate [modified from *Nachon et al.*, 2014]

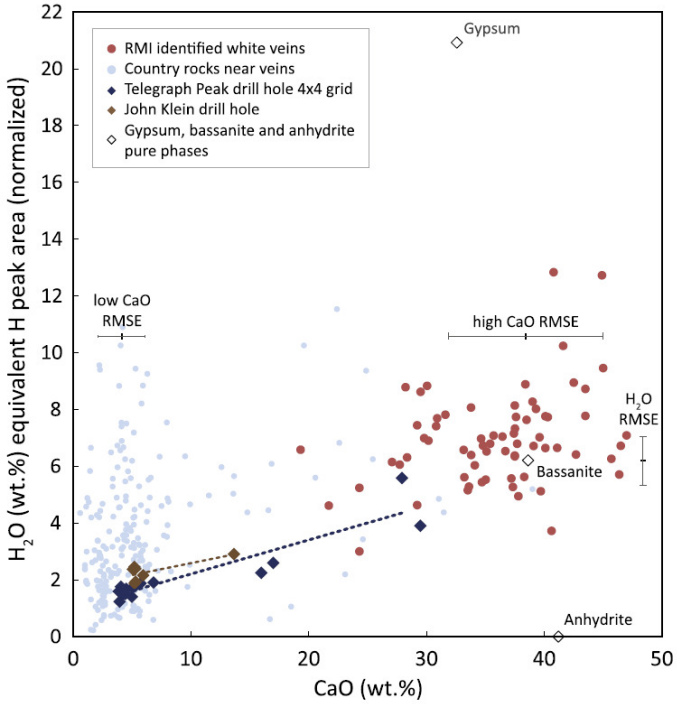

Figure 3.3: H_2O content observed in Ca-sulfate light-toned veins, consistent with the presence of bassanite [from *Rapin et al.*, 2016]

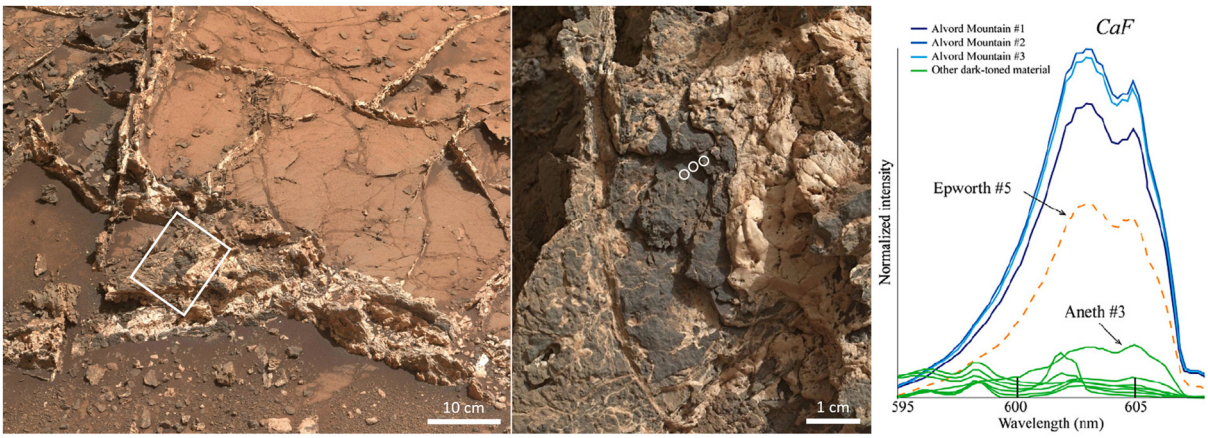

Figure 3.4: Garden City vein cluster (left) at Pahrump Hills featuring Ca-sulfate light-toned veins intertwined with a dark-toned material. ChemCam observations on the dark-toned material at Alvord Mountain (middle) show high F content associated with high Ca abundances that indicates the presence of fluorite (right; F content is derived from the CaF molecular band) [*Nachon et al.*, 2016].

At Pahrump Hills, the rover reached the lacustrine mudstones of the Murray formation, which constitutes the lowest strata of Mount Sharp, and observed a wide array of diagenetic features in complex association with pervasive Ca-sulfate light-toned veins. Notably, the Garden City outcrop at Pahrump Hills displays complex diagenetic vein clusters constituted of Ca-sulfate bearing light-toned veins intertwined with dark-toned fracture-fills (Figure 3.4). The dark-toned fills present enrichments in Mn, Ca and F (interpreted as fluorite, CaF_2), Mg and Li [*Nachon et al.*, 2016], as well as ~7 fold enrichments in Ge compared to adjacent host rock chemistry [APXS; *Berger et al.*, 2017]. The mobility of F associated with Ge, in particular, indicates acidic fluid conditions during diagenesis [*Nachon et al.*, 2016; *Berger et al.*, 2017], with F and Ge, probably leached from the phosphate (i.e. F-apatite) and silicate (for Ge) mineral phases identified in the adjacent host rock [*Rampe et al.*, 2017]. Detection of Fe-sulfate and Ni-rich Mg-sulfates in concretionary diagenetic features [*Nachon et al.*, 2016; *VanBommel et al.*, 2016] as well as increases in Zn, Mn and Ni content down-section in the host rocks [*Rampe et al.*, 2017] constitutes further evidences for acidic fluid conditions prevailing throughout the diagenetic history of the Pahrump Hills sedimentary rocks.

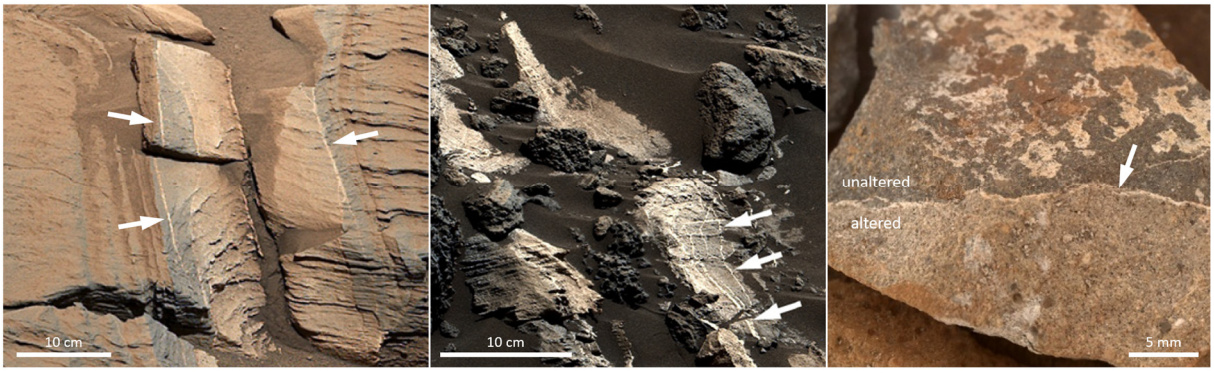

Figure 3.5: Si-rich alteration fracture-halos, associated with Ca-sulfate light-toned veins (white arrows) that form sharp boundaries between altered and unaltered bedrock (right) [modified from *Yen et al.*, 2017]

Additionally, light-toned alteration halos along fractures observed in both Stimson eolian sandstones and Murray lacustrine mudstones, stratigraphically above the Pahrump Hills outcrops, exhibit Si enrichments paired with depletion in other cations (including Fe, Mn, and Al). This silica enrichment has been interpreted as a remobilization of silica from Si-rich layers and acidic fluid circulation during

diagenesis [*Berger et al.*, 2017; *Frydenvang et al.*, 2017; *Yen et al.*, 2017]. Interestingly, Ca-sulfate veins are uniquely associated with fracture-associated halos (Figure 3.5), forming sharp boundaries between altered and unaltered sandstone [*Yen et al.*, 2017], but otherwise scarcely observed in the Stimson formation.

Aside from the Pahrump Hills peculiar geological context, Ca-sulfate-bearing light-toned veins are also observed ubiquitously across the Murray formation but exhibit a large diversity in textures and morphologies (Figure 3.6), including millimeter-wide hairline fractures, centimeter-scale single straight massive and clear-white veins that are resistant to mechanical erosion, as well as irregular anastomosing vein networks that exhibit uneven "pitted" textures. Light-toned veins are also locally associated with a range of diagenetic features, including dark-toned raised ridges located at the vein walls [*Forni et al.*, 2017] or dark-toned concretions, laminas and vein inclusions featuring enrichments in P and Mg associated with Fe and Mn hydroxides [*Meslin et al.*, 2018]. Other evaporite minerals are also observed in the Murray formation in association with Ca-sulfate, including halite (NaCl) near the veins walls [*Thomas et al.*, 2018] and borate within light-toned veins [*Gasda et al.*, 2017].

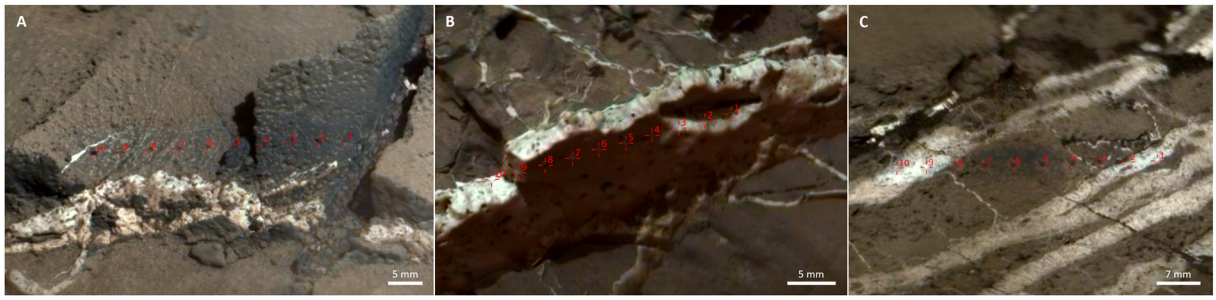

Figure 3.6: RMI examples of textural and morphological variability observed associated with Ca-sulfate light-toned veins in the Murray formation: (A) light-toned veins associated with dark-toned raised ridge that feature halite and F-apatite detections [*Forni et al.*, 2017]; (B) massive clear-white and straight veins on which boron was detected [*Gasda et al.*, 2017]; (C) recessive anastomosing light-toned veins with uneven "pitted" texture.

In the upper part of the Murray formation (Sutton Island and Blunts Point members), Ca-sulfate light-toned veins display different morphologies. In addition to sub-vertical fracture-fills associated with hydro-fracturing, light-toned fills are also observed as sub-horizontal layers that appear to follow planes of structural weakness in the sedimentary rocks (Figure 3.7), such as cross-bedding or laminations, and occur as cement in interbedded sandstones lenses [*Newsom et al.*, 2017]. In the Sutton Island member, the Old Soaker outcrop is marked by polygonal ridge networks (Figure 3.7) interpreted as desiccation cracks based on the predominance of T-junctions, suggesting periodic recession of the lake level and low-stand deposition environments [*Stein et al.*, 2018]. While Ca-sulfate light-toned sub-vertical veins attributed to late-diagenesis hydrofracturing are also observed in the Old Soaker outcrop – propagating along pathways of least resistance in the form of desiccation cracks but also crosscutting them [*Stein et al.*, 2018] – the observations of Ca-sulfate sub-horizontal layers and cements in association with a shallower lake environment could indicate a distinct episode of Ca-sulfate formation, during or shortly after sedimentation. In addition, the observation of Mg-sulfate [*Rapin et al.*, 2018] in the vicinity would support this near-surface evaporite formation hypothesis.

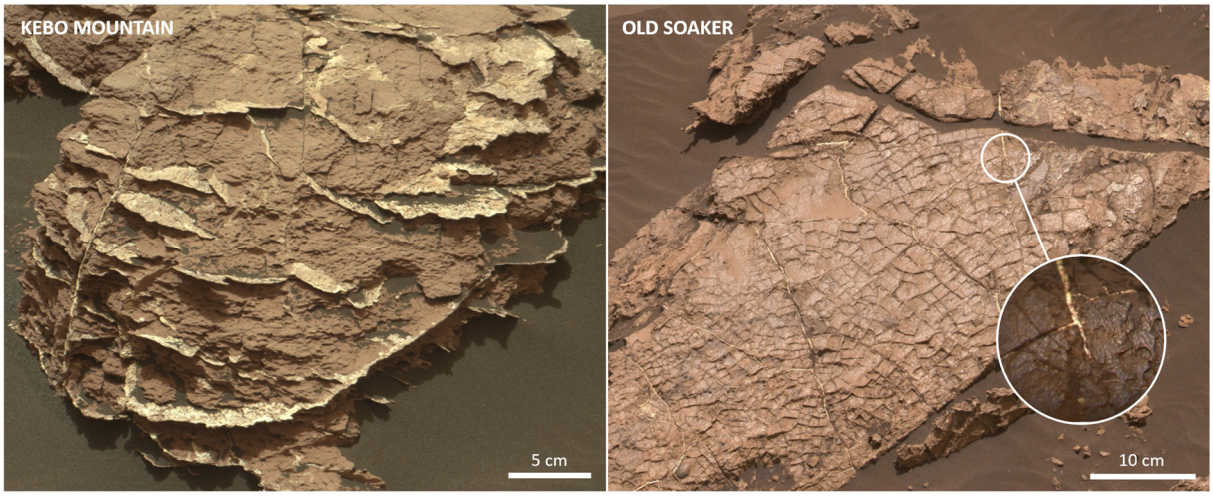

Figure 3.7: Sutton Island member Ca-sulfate light-toned material observations include sub-horizontal impure Ca-sulfate layers that follow planes of structural weakness (e.g. Kebo Mountain outcrop) and sub-vertical late-diagenetic veins that propagate along but also crosscut desiccation cracks observed on the Old Soaker outcrop.

In essence, the *Curiosity* rover observed Ca-sulfate consistently along its path in the form of diagenetic light-toned fracture-fills that exhibit textural and morphological variability and are associated locally with diverse diagenetic features, notably in the Murray formation. In this study, we look into the numerous ChemCam analyses on Ca-sulfate bearing light-toned veins to characterize chemical variability, in order to provide insights into the diagenetic fluid(s) conditions at the time of formation.

ChemCam chemical quantification has improved over the course of the mission thanks to re-calibration efforts and expansion of the calibration standard database to better represents specific compositional configuration, including Ca-sulfate rich compositions [*Clegg et al.*, 2017]. However, the accuracy (RMSEP) associated with quantification remains relatively high for several major elements, notably Si, Fe and Al that feature numerous emission lines in the spectral domains covered by the ChemCam spectrometers, and are thus particularly subject to matrix effects [*Anderson et al.*, 2017]. As such, enrichments in major elements in Ca-sulfate veins are easily missed or discarded when observed in low abundances, typically below 10 oxide wt.%, as quantified abundances fall within the range of the accuracy of the measure (i.e. prediction error, RMSEP). In order to identify compositional variability associated with authigenic enrichments in Ca-sulfate dominated compositions, as opposed to the mixed sampling of host rock silicate phases, we look for enrichments in Fe, Mg, and Al over Si on selected emission lines showing no significant convolution with other chemical elements.

Chemical variability in mineralized veins observed by ChemCam on the lower slopes of Mount Sharp in Gale Crater, Mars

L'Haridon J., Mangold N., Meslin P.-Y., Johnson J.R., Rapin W., Forni O., Cousin A., Payré V., Dehouck E., Nachon M., Le Deit L., Gasnault O., Maurice S. and Wiens R.C. (2018)
Icarus 311, 69–86. doi: 10.1016/j.icarus.2018.01.028

HIGHLIGHTS

- → Diagenetic Ca-sulfate veins are pervasive along *Curiosity* traverse in Gale Crater
- → ChemCam highlights local enrichments in Fe and Mg in these features
- → Passive reflectance shows that both ferric and ferrous phases are identified
- → Groundwater redox and pH conditions appear variable along the stratigraphy

ABSTRACT

ChemCam has observed a wide range of diagenetic features along the *Curiosity* rover traverse including pervasive Ca-sulfate veins. Observations by multiple instruments on *Curiosity* indicate that these veins are hydrated, formed during diagenetic fluid event(s). In this study, we delve into the chemical variability in these Ca-sulfate bearing veins and have identified two subsets in the Murray formation with enrichments in Fe and Fe + Mg. These chemical trends do not reflect a sampling mixture with the surrounding host rock but likely indicates the presence of authigenic phases formed during the emplacement of these veins. Based on passive reflectance spectral analysis and correlation with other elements, Fe^{3+} oxides and/or sulfates are proposed to account for the Fe-rich observations near the Naukluft Plateau whereas the Fe + Mg trend is also observed in adjacent dark-toned features with elevated Mn and P near the Old Soaker outcrop. The specific localization of these observations in the Gale stratigraphy implies changing pH and redox conditions in the groundwater at the time of formation of these veins, from oxidizing and likely more acidic near the Naukluft Plateau to more reducing conditions in the upper part of the Murray formation.

3.1 Introduction

The Mars Science Laboratory (MSL) mission has been exploring Gale Crater on Mars since the landing of the *Curiosity* rover on August 6, 2012. *Curiosity* has characterized the geology of the layered sedimentary rocks that compose the lower slopes of the 5-km high central mound – Aeolis Mons – informally known as Mount Sharp. During its first Martian year, the rover encountered fine-grained sandstones and mudstones at the Yellowknife Bay and Kimberley localities, both interpreted as fluvial and lacustrine deposits [*Grotzinger et al.*, 2014, 2015; *Vasavada et al.*, 2014]. Soon after, the rover reached the Pahrump Hills and the basal layers of Mount Sharp where it observed the fluvial and lacustrine fine-grained sandstones and mudstones of the Murray formation [*Grotzinger et al.*, 2015]. Eolian sandstones of the Stimson formation were then observed by the rover at Marias Pass, Bridger Basin and Naukluft Plateau, where they unconformably overlie the Murray formation [*Banham et al.*, 2016; *Watkins et al.*, 2016].

These formations have all shown to some extent geological features that attest to the circulation of fluids during diagenesis, after burial and induration of the sediments at a time when liquid water was probably no longer present locally at the surface of Mars, i.e. after deposition and burial of eolian sediments in a dryer environment. At Yellowknife Bay, the rover investigated raised ridges along fractures [*Léveillé et al.*, 2014; *McLennan et al.*, 2014; *Siebach et al.*, 2014], nodules [*Stack et al.*, 2014] and light-toned veins [*Nachon et al.*, 2014]. The light-toned veins appear to be pervasive to all geological units observed along the rover traverse and were later found in complex association with other diagenetic features, such as dark-toned veins and erosion-resistant features in the Murray mudstones of Pahrump Hills [*Blaney et al.*, 2015; *Nachon et al.*, 2016], where cross-cutting relationships indicate that they were formed after other diagenetic features in these sedimentary rocks [*Kronyak et al.*, 2015]. Similar veins were, however, scarcely observed in the overlying Stimson formation, and in many places were observed in association with silica-rich, fracture-associated halos [*Frydenvang et al.*, 2017; *Yen et al.*, 2017].

The light-toned veins show an almost pure Ca-sulfate chemistry [*Nachon et al.*, 2014], interpreted predominantly as bassanite ($CaSO_4 x\ 0.5\ H_2O$) at the surface [*Rapin et al.*, 2016]. A mixture of Ca-sulfate hydration states was found (gypsum, bassanite, and anhydrite) a few cms below the surface in the bedrock where no vein could be observed, but it suggests gypsum could also be found in the veins underneath [*Vaniman et al.*, 2017]. The formation of these veins has been proposed to occur through a regional fluid circulation event during the latest stages of diagenesis: the partial dissolution of a hypothetical deeper, impure sulfate-rich layer would have led to precipitation of gypsum in the fractures, some of which would have dehydrated to bassanite during burial and/or by near-surface desiccation [*Rapin et al.*, 2016; *Schwenzer et al.*, 2016; *Vaniman et al.*, 2017]. However, the proposed hypothesis for a unique late-diagenesis fluid circulation episode that led to the formation of Ca-sulfate veins observed along the *Curiosity* rover traverse needs to account for recent observations of similar features showing greater textural and chemical variability, as well as more complex and diverse interactions with the surrounding host rock and other diagenetic features.

Ca-sulfate bearing veins were also observed by the *Opportunity* rover in Endeavour crater (Squyres 2012). However, the geological setting is different there, consisting of impact breccia unconformably overlain by the sulfate-rich sandstones of the Burns formation [*Squyres*, 2004; *Grotzinger et al.*, 2005; *McLennan et al.*, 2005] and probably imprinted by hydrothermal fluid circulation. In addition, sulfate deposits were identified from orbit in several other sites on Mars [*Gendrin*, 2005; *Bibring et al.*, 2006],

including in the upper part of the Mount Sharp Group at Gale Crater [*Milliken et al.*, 2010; *Thomson et al.*, 2011; *Grotzinger et al.*, 2015]. The presence of sulfate deposits has been interpreted as evidence for past aqueous acidic environments at Meridiani Planum [*Tosca et al.*, 2005]. In addition, their local association with Fe-oxide in some places also suggests the involvement of diagenetic processes and post-depositional fluid circulation [*Bibring et al.*, 2007]. Hence, the study of Ca-sulfate bearing veins and other diagenetic features at Gale Crater may provide valuable insights into the processes involved in the formation of sulfates on Mars.

Here, we present new results with respect to the chemical variability observed by the ChemCam instrument in association with these light-toned veins, covering newly acquired data and previously published results [*Nachon et al.*, 2014, 2016; *Rapin et al.*, 2016] and using a new approach to identify elemental enrichments in these features. Furthermore, we discuss their implications for thermodynamical conditions in the parent fluid as well as their relationship with adjacent diagenetic features and their localization in the regional stratigraphy to propose an emplacement scenario for these veins that accounts for the observed chemical trends.

3.2 Material and methods

3.2.1 ChemCam instrument

The ChemCam instrument [*Maurice et al.*, 2012; *Wiens et al.*, 2012] on board the *Curiosity* rover is composed of a Laser-Induced Breakdown Spectroscopy (LIBS) system coupled with a Remote Micro-Imager (RMI) [*Le Mouélic et al.*, 2015]. A pulsed laser is focused on the target material (located up to 7 m from the mast of the rover), leading to the formation of a plasma. Light is emitted as the excited atoms, ions, and molecules contained in the plasma and decay to lower electronic states. The spectrum is analyzed by three spectrometers (covering the spectral domains of 240-342 nm, 382-469 nm, and 474-906 nm) that resolve emission peaks used for chemical analysis. ChemCam observations typically consist of 30 laser shots on a given point, and each ChemCam analysis usually comprises a “raster” of several closely spaced observation points. In this process, dust is removed from the surface of the target by the first few laser shots, thus enabling the analysis of the dust-free surface target material.

The ablated area covers about 300 to 600 µm in diameter, and up to a few micrometers in depth depending on the targeted material [*Maurice et al.*, 2012]. ChemCam thus provides fine-scale chemical analyses that are ideal for characterizing diagenetic features such as concretions and veins, on which direct chemical measurement is impossible with the other instruments on the rover. However, even at that scale, ChemCam observes a mixture of compositions if the LIBS point is located at the interface between distinct geological features, lithologies or individual mineral grains. Thus, mixed chemical composition such as between Ca-sulfate from light-toned veins and the surrounding hock rock silicate minerals are sometimes observed [*Nachon et al.*, 2014; *Rapin et al.*, 2016].

ChemCam is not designed to characterize the mineralogy of the rocks directly, and interpretation of mineralogy is usually obtained from cross-observations with other instruments (e.g., the CheMin X-ray diffractometer) onboard the *Curiosity* rover. However, the diagenetic features presented in this paper were only analyzed by ChemCam, as these features are too small for other instruments to analyze without significant contributions from the surrounding material. So far, diagenetic features have not been intentionally targeted by the drill and CheMin with the exception of two large alteration halos within the Stimson formation [*Yen et al.*, 2017]. Nevertheless, mineral phases can still be inferred from

ChemCam chemical compositions for diagenetic features when their size is comparable or larger than the laser spot size.

In addition, after each LIBS observation, passive reflectance spectra (without active laser use) are also acquired using ChemCam spectrometers that record the Martian surface radiance in the visible/near-infrared (400-840 nm). Passive spectra can provide information on the presence of Fe^{3+}-bearing mineral phases and crystallinity, most notably hematite [*Johnson et al.*, 2015, 2016] – information otherwise inaccessible from LIBS analyses, which do not distinguish between the redox states of Fe. The angular field of view of 0.65 mrad of the spectrometer corresponds to a 2 mm diameter area on the surface at 3 m distance from the rover (50% of ChemCam targets are within 2 to 3 m from the rover and 45% within 3-5 m [*Maurice et al.*, 2016]); it is thus wider than the LIBS ablation area but usually smaller than the probed diagenetic features.

3.2.2 Elemental composition and quantification

ChemCam is able to detect all major elements; their abundances are quantified in weight percent of oxides (SiO_2, TiO_2, Al_2O_3, FeO_T, MgO, CaO, Na_2O, and K_2O) using a combination of two multivariate analytical methods – namely the "Partial Least Squares" (PLS) and "Independent Component Analysis" (ICA) methods. The PLS method compares multiple emission lines for a given element to known standards composition from testbed samples on Earth [*Clegg et al.*, 2009; *Wiens et al.*, 2013]. This technique has been recently updated using a number of sub-models covering compositional ranges observed for each element on Mars for more accurate predictions [*Anderson et al.*, 2017]. The ICA method stems from blind source separation research [*Hyvarinen*, 2001] and identifies a set of statistically independent components used to characterize the spectra, from which elemental abundances are derived using regression laws between ICA scores and reference spectra of known composition [*Forni et al.*, 2013]. Expansion of the ChemCam calibration database from 66 to 408 standards, and associated recalibration, was completed in 2015 [*Wiens and Maurice*, 2015; *Clegg et al.*, 2017] thus refining the quantification of major elements with the ChemCam instrument, especially for compositional extremes (including Ca-sulfate) [*Clegg et al.*, 2017, supplementary materials]. The combination of PLS and ICA results in the multivariate oxide composition (MOC) dataset [*Clegg et al.*, 2017].

Accuracy for ChemCam quantifications is estimated through calculation of the root mean squared error of prediction (RMSEP) for a representative test set of standards for each major element. Since the accuracy varies with elemental abundance, a specific RMSEP value is calculated for each composition [*Clegg et al.*, 2017]. The measurement precision is mainly defined by ChemCam repeatability using the shot-to-shot prediction variations either on the target itself, selected homogeneous targets or the calibration targets [*Clegg et al.*, 2017, and references therein].

A number of minor and trace elements detected by ChemCam are also quantified using a univariate method, in which a single emission peak is calibrated for the abundance of that element. These include Mn [*Lanza et al.*, 2014], Sr, Li, Ba, Rb [*Payré et al.*, 2017a], Cu [*Payré et al.*, 2017b], Zn [*Lasue et al.*, 2016], B [*Gasda et al.*, 2017], and F [*Forni et al.*, 2015]. In addition, the hydration state for specific compositions can be derived from the H signal using recent calibration efforts [*Rapin et al.*, 2016]. Other volatile elements such as S, P, and Cl are so far only observed qualitatively, but are often used for chemical and mineralogical diagnostic studies [*Nachon et al.*, 2016], although some works are

currently in progress to quantify them systematically [*Meslin et al.*, 2016; *Anderson et al.*, 2017; *Clegg et al.*, 2017; *Thomas et al.*, 2017].

3.2.3 Identification of enrichments in specific elements

Light-toned veins have been characterized across the traverse by a Ca-sulfate dominated chemistry with apparent varying contribution from the host rock, mostly due to sampling of a mixture of vein and host rock where the ChemCam observation point is located at the interface. Even though recent improvements to the ChemCam standard database and quantification methods have refined the accuracy for major element quantifications in chemically "exotic" geological items such as diagenetic features, the RMSEPs for some major elements such as SiO_2, FeO_T and MgO are still within range of the observed low abundances in these features. Elemental quantification using the standard procedure is then insufficient to effectively sort out potential elemental enrichments of a few wt.% above zero (e.g., for relatively low abundances of SiO_2, Al_2O_3, FeO_T, MgO) in these features.

Thus, in addition to the MOC data that benefit from the multivariate approach (see section 2.2), we introduce a criterion based on the peak area ratio between a given major element (E) and silica (Si) as the simplest processing independent of the database of standards. This criterion allows us to identify enrichment in this particular element as opposed to host rock contribution, which would tend to reflect the chemistry of its constituent silicate minerals. ChemCam target points with E/Si ratios more than 3-σ above the local host rock mean ratio will, therefore, be considered enriched in a given element E compared to Si, effectively excluding enrichments linked to silicate mineral phases. This criterion can work if the lines are carefully chosen from the same ionization level and do not appear to be significantly affected by plasma temperature variations.

In order to do so, we have selected representative spectral peaks for selected major elements, preferably in the spectral region covered by the same ChemCam spectrometer and with as little overlap with neighboring peaks as possible. In this study, we primarily focus on Fe and Mg enrichments, as these elements are often found to some extent in the veins and in neighboring diagenetic features and for their importance in tracing redox conditions (Fe) and salinity (dissolved cations including Mg) in the parent fluid. The selected emission peaks for Fe (260.04 nm), Mg (285.25 nm) and for Si (288.24 nm), all from the neutral atom state, are presented for a vein target showing contributions from these elements in Figure 3.8. Only Si shows partial overlap with another element, namely Ti with an emission peak at 288.5 nm. In addition, the emission peak for Al at 308.31 nm has also been considered for enrichment in Al over Si as a potential indicator of an acidic environment [*Oelkers et al.*, 1994]. Peak area intensity for each emission peak has been derived from a peak-fitting routine using Voigt profiles (Figure 3.9).

This method has been used to analyze 462 individual ChemCam points over the entire rover traverse up to sol 1700, on light-toned vein material showing high calcium content (above 20 wt.%) associated with sulfur detection, and light-toned material on the RMI images (similar to Nachon et al. 2014, 2016 and Rapin et al. 2016). Points displaying Ca-sulfate chemistry without clear identification of light-toned material (even diffuse) were excluded.

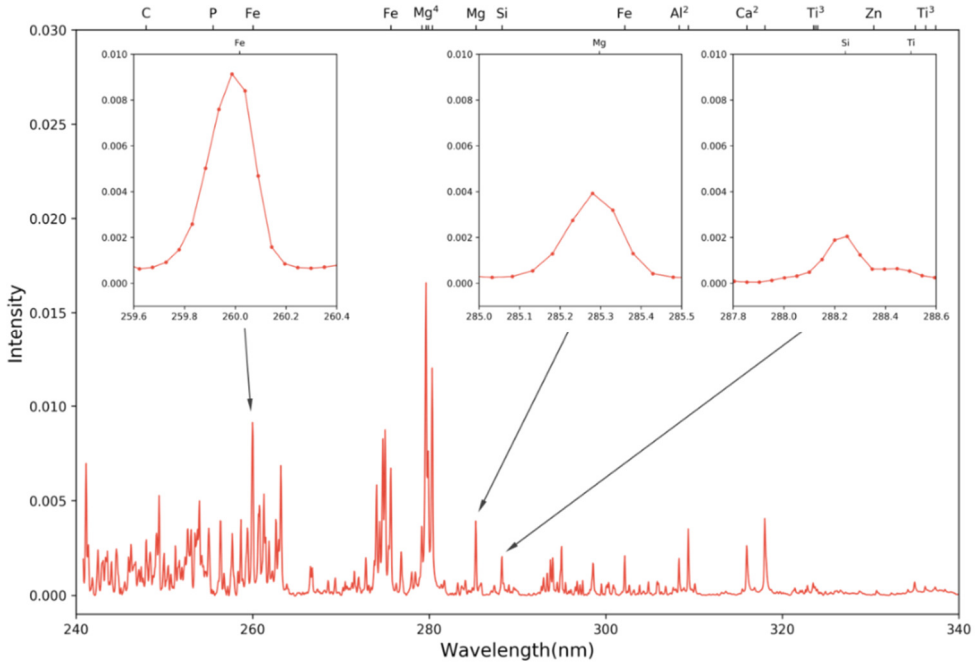

Figure 3.8: Normalized total spectrum of the point 14 on the Khoabendus target zoomed in on the UV and part of the visible spectral domain (background). The Fe (260.02 nm), Mg (285.3 nm) and Si (288.24 nm) peaks highlighted in the insets (dots represent the ChemCam LIBS data points) were selected for our study because of the minimum convolution and high intensity of these peaks. Peak areas for these peaks were calculated from Voigt fits in order to derive the intensity ratios Fe/Si and Mg/Si.

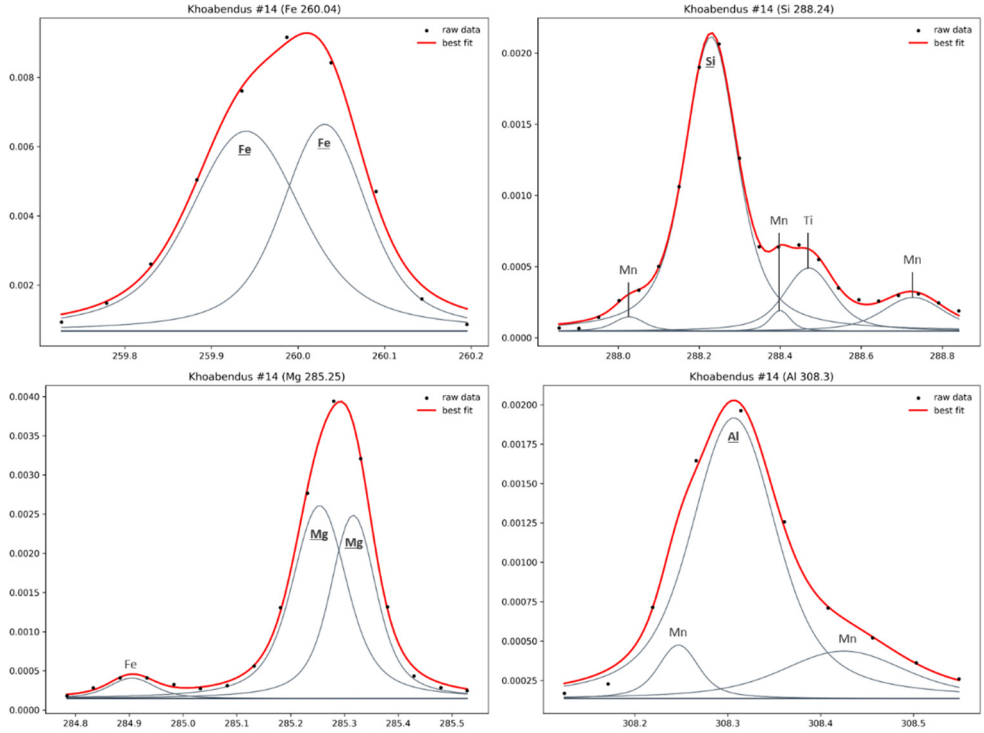

Figure 3.9: Fitted profiles for Fe, Si, Mg and Al emission lines on the "Khoabendus" ChemCam LIBS target (point 14). Black dots represent ChemCam LIBS data points. Individual elemental peaks (in grey) that compose the fit are each identified by the corresponding element name; peaks underlined are taken into account for the calculation of the intensity area. Each peak is fitted using Voigt profiles, with some degree of liberty given to the position of the peak (0.25 nm) and to the full width at half maximum (FWHM; 0.1 - 0.5 nm) based on the resolution of the ChemCam instrument in the UV (0.2 nm FWHM).

In order to assess the composition of the host rock along the rover traverse, we selected reference targets among the ChemCam observations within the drill holes in the Yellowknife Bay (Cumberland), Kimberley (Windjana), Murray (Telegraph_Peak, Oudam, Marimba, Quela and Sebina) and Stimson (Big_Sky and Okoruso) formations, as they correspond to freshly exposed host rock material representative of the full spectrum of "in-place" sedimentary rocks observed so far along the *Curiosity* traverse [*Treiman et al.*, 2016; *Yen et al.*, 2017]. The drill holes within Si-rich halos within the Stimson formation (i.e. Lubango and Greenhorn) and Si-rich bedrock within the Murray formation (Buckskin) were excluded because they are not representative of the unaltered host rock composition [*Morris et al.*, 2016; *Frydenvang et al.*, 2017; *Rampe et al.*, 2017; *Yen et al.*, 2017]. In addition, any ChemCam observation points showing clear contributions from diagenetic facies such as Ca-sulfate veins, either on RMI images or in the quantified chemistry were removed.

3.3 Results

3.3.1 Chemical variability observed in light-toned veins

3.3.1.1 Major element enrichments in light-toned veins

Several observations on light-toned veins, especially after reaching the Murray formation at Pahrump Hills, show local detections of FeO_T (~5-10 wt.%) associated with low to no SiO_2 abundance, alongside the expected high CaO abundance and S emission peaks characteristic of the presence of Ca-sulfate. Shot-to-shot analysis of the LIBS data obtained at each point shows that FeO_T and MgO are relatively constant and well above zero throughout the short depth profile after removal of the dust cover (first 5 laser shots), unlike SiO_2 that decreases in abundance to essentially zero after the first shots (Figure 3.10). Without a corresponding Si signal, Fe and Mg do not appear to be associated with the silicate minerals of the host rock and thus points toward a distinct chemical composition from the 'Host rock + Ca-sulfate' mixed observation that is often obtained on the edge of veins.

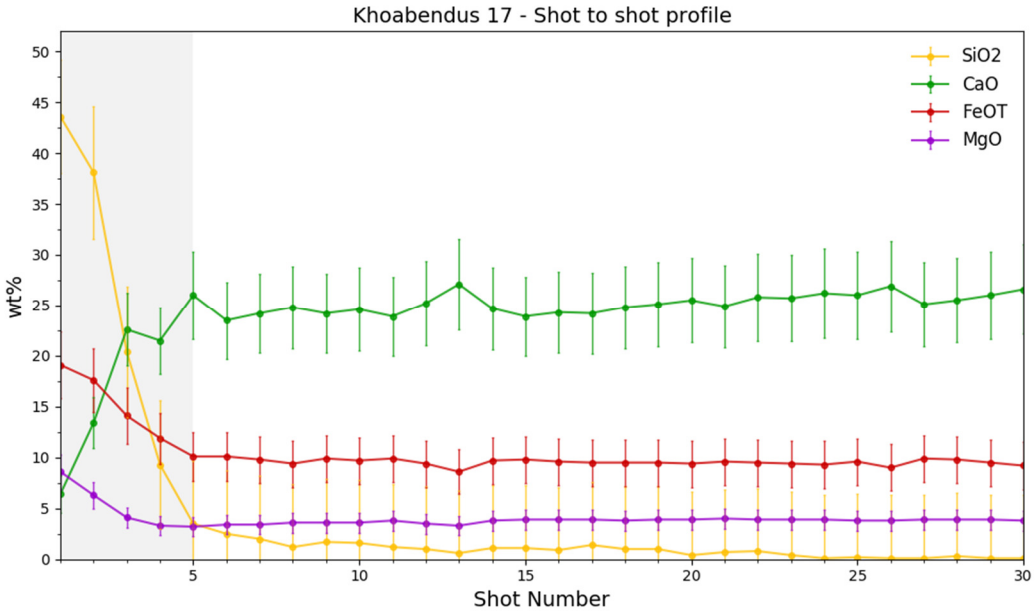

Figure 3.10: Shot-to-shot depth profile of ChemCam LIBS point #17 on target Khoabendus. The first five shots correspond to the dust cover and are typically not considered to calculate elemental abundances for each ChemCam point. CaO increases in the first shots to stabilize around ~25 wt.%, while FeO_T and MgO decrease to ca. 10 wt.% and 4 wt.% respectively, and SiO_2 almost completely disappears (< 1 wt.%).

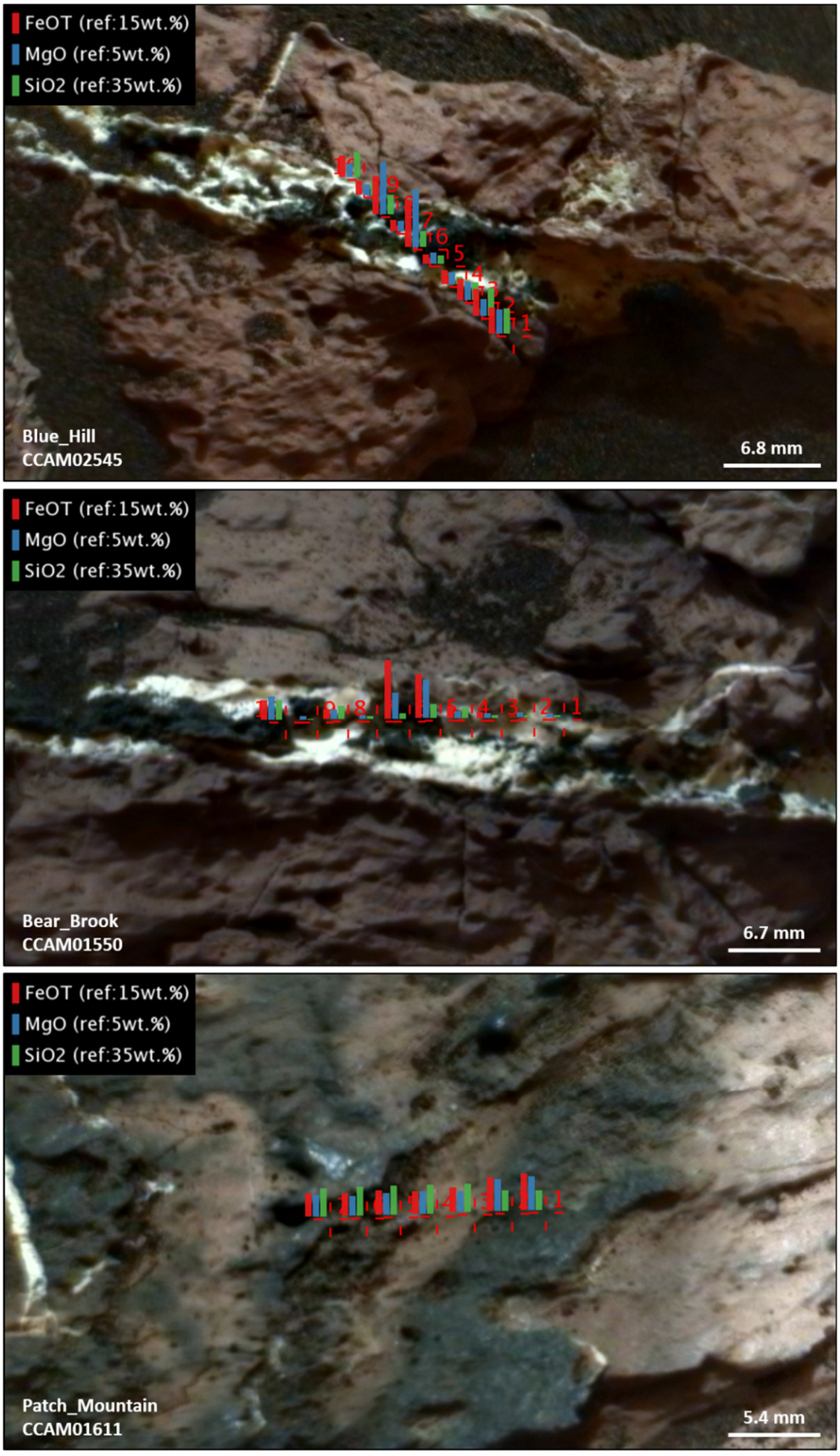

Figure 3.11: RMI images, colorized with Mastcam, of dark-toned inclusions (Blue_Hill, sol 1545 and Bear_Brook on sol 1550) within light-toned veins and dark-toned layers (Patch_Mountain on sol 1611), with quantified abundances of FeO_T, MgO and SiO_2 indicated by bar plots for each ChemCam point. These dark-toned features all present elevated FeO_T and MgO but depleted SiO_2 compared to the surrounding host rock.

Elevated Fe abundances were also observed on dark-toned features (inclusions in light-toned veins and resistant layers associated with light-toned veins; Figure 3.11), sampled by 16 ChemCam points between sols 1380 and 1611 [*Forni et al.*, 2017]. These enrichments are not associated with a Ca-sulfate component and still present significant amounts of SiO_2 and Al_2O_3 (although lower than in the surrounding host rock). Mg is also elevated in recent observations (sols 1545 to 1611) of dark-toned inclusions within light-toned veins (Figure 3.11). These features were thus included in this study, as a potential end member for Fe- and Mg- enrichments in light-toned veins.

Fe/Si and Mg/Si peak area ratios for the selected Ca-sulfate bearing vein targets are reported in Figure 3.12. Fe shows a clear trend toward higher Fe/Si ratios allowing for the identification of a subset of 34 points on light-toned veins with ratios 3-σ standard deviations above the host rock mean ratio. There are three overall trends seen in this figure. Mg displays variable Mg/Si ratios with low Fe/Si (along the y-axis), which we will show below likely reflects the observed variability of Mg in the host rock chemistry across the traverse. However, two other distinct chemical trends can be observed: (1) the first shows a correlation between Mg/Si and Fe/Si, indicating an enrichment in both Fe and Mg in these targets with ratios similar to observations on dark-toned features; (2) the second displays elevated Fe/Si ratios with relatively low Mg/Si ratios (near the x-axis), seen in light-toned veins.

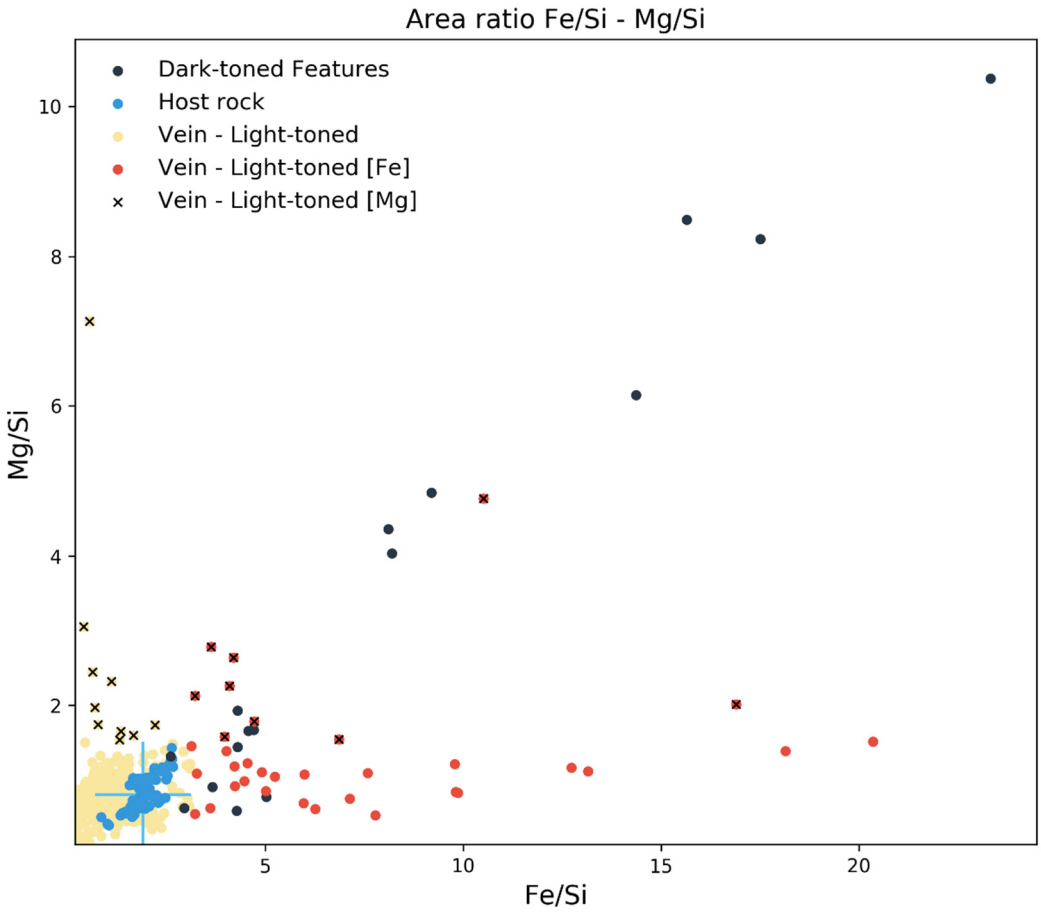

Figure 3.12: Bivariate plot of Fe/Si against Mg/Si ratios in peak area intensity illustrating the enrichment in Fe (red dots) and Mg (black x marks) in light-toned veins i.e. with ratios 3-σ above typical host rock ratios (the blue cross represents host rock mean and 3-σ standard deviations). Dark-toned features are also indicated for comparison.

The three chemical trends can also be observed on a SiO_2 – FeO_T + MgO – CaO ternary diagram (Figure 3.13). We highlight potential mixing lines: (1) between Ca-sulfate and Fe- / Mg-rich mineral phases (e.g., non-silicate phase such as oxide, sulfate or phosphate), along which plots most of the Fe-rich light-toned veins, and (2) between Ca-sulfate and dark-toned features, along which some Fe (+Mg) enrichments in light-toned veins are found. The light-toned veins that were seen in Figure 3.12 to be enriched in Mg but not in Fe appear to mostly lie along a mixing trend between the host rocks and pure Ca sulfates (Figure 3.13) although there is also some scatter in the direction of the other two trends.

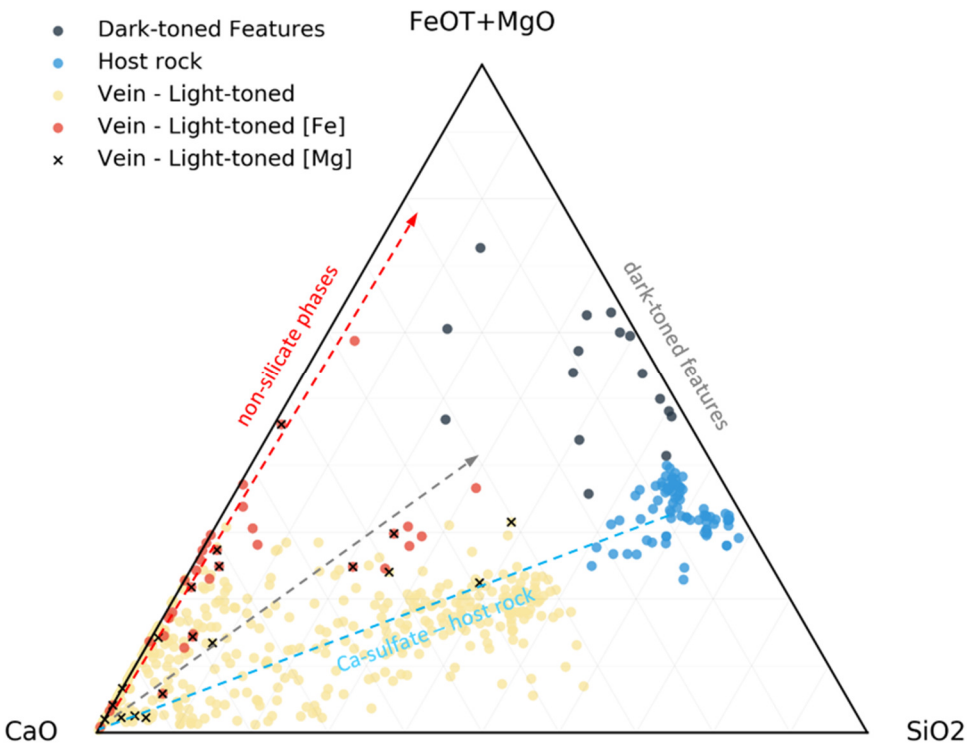

Figure 3.13: CaO – FeO_T + MgO – SiO_2 ternary diagram (normalized wt.%), illustrating the mixing line between Ca-sulfate and host rock (blue), dark-toned features (black) and oxide/sulfate (red), using the same symbols as in Fig. 4. Most of the Fe-rich light-toned veins points plot along the Ca-sulfate – Fe-oxide/sulfate mixing line indicating a Fe-rich non-silicate phase (no SiO_2), with some points displaying a Mg enrichment as well. A second trend can also be observed with several Fe-rich points, including Fe+Mg-rich points, plotting along the Ca-sulfate – dark-toned features mixing line; potentially reflecting a similar composition. Lastly, light-toned veins points showing enrichment in Mg only tend to plot close to the Ca-sulfate – host rock mixing line.

High Al/Si ratios were also detected on a few light-toned veins (Figure 3.14), including two targets that present elevated Fe/Si (Khoabendus #18 on sol 1380 and Malembo #1 & #3 on sol 1469). The highest Al_2O_3 content (18.8 wt.%) observed so far by ChemCam in the targets is located on a dark-toned inclusion within a light-toned vein (Khoabendus #14). High Al_2O_3 is also associated with high FeO_T (32.2 wt.%) and elevated Fe/Si and Al/Si ratios. On that point, Al_2O_3 appears to be correlated with FeO_T in the shot-to-shot analysis (Figure 3.14). SiO_2 is still present in a significant amount (23.3 wt.%), although in lower abundance than in the host rock (ca. 50 wt.%), and appears to be correlated with MgO but anti-correlated with FeO_T and Al_2O_3. Similar elevated Al contents were also reported in erosion-resistant features near the Naukluft Plateau, in association with light-toned veins, although not with Fe enrichment.

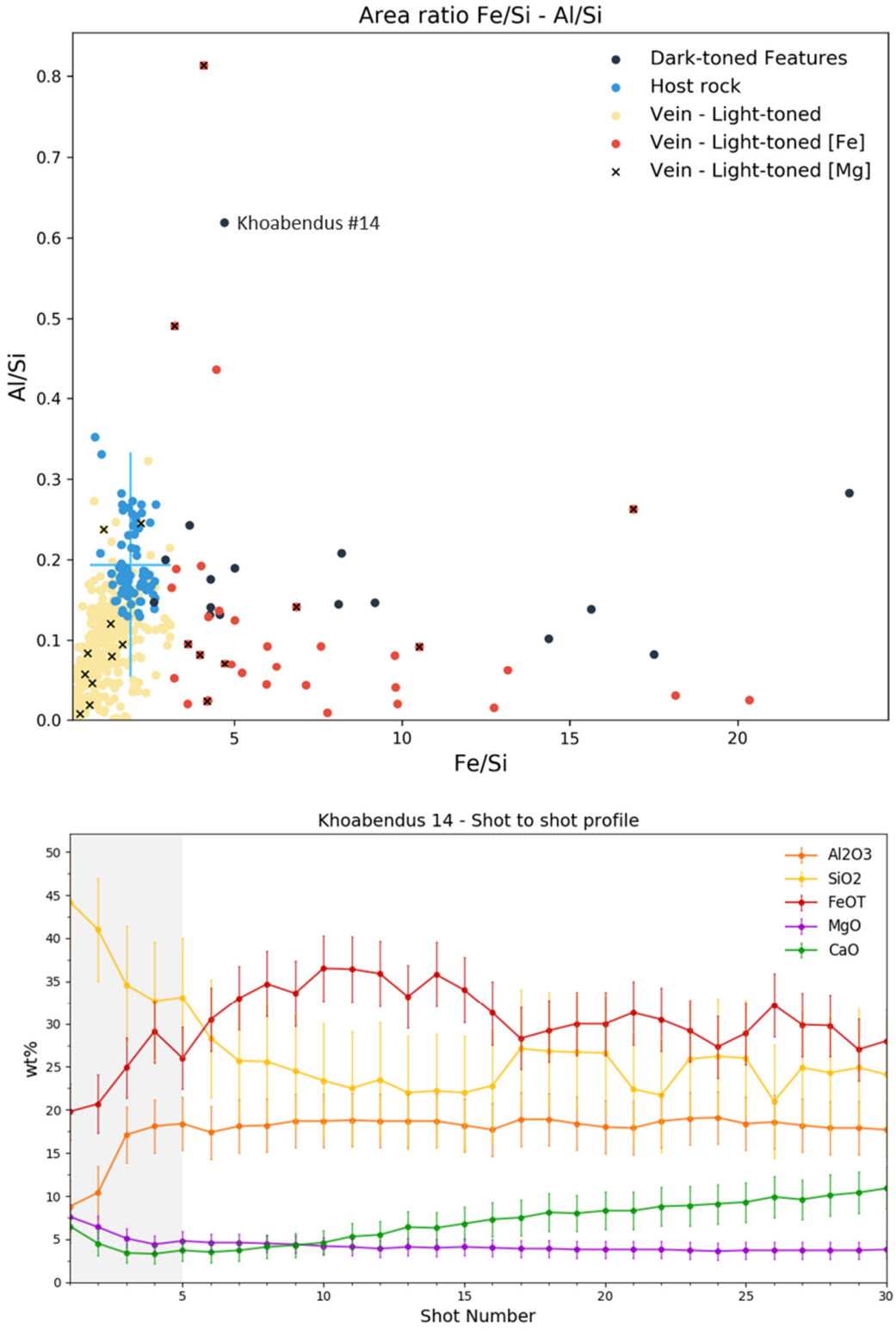

Figure 3.14: Bivariate plot (top) of host rock and diagenetic features (including veins) Fe/Si against Al/Si ratios in peak area intensity (blue cross represents host rock mean values and 3-σ standard deviations). Shot-to-shot profile (bottom) of the Khoabendus #14 ChemCam LIBS point. The first five shots correspond to the dust cover and are typically not considered to calculate elemental abundances for each ChemCam point. Al_2O_3 and FeO_T abundances increase after the first shots and appear correlated whereas SiO_2 and MgO decrease. CaO steadily increases with depth suggesting that the Ca-sulfate vein is present underneath.

Enrichments in alkali elements are observed on several vein targets (Figure 3.15). Indeed, 3 targets on light-toned veins, including Mg-rich Rooibank_60A #2, and 4 on dark-toned features show an enrichment in Na_2O (> 3.5 wt.%), associated in most cases with a chlorine detection. In addition, 8 vein targets show an enrichment in K_2O (> 0.5 wt.%), including 2 targets where it is associated with an enrichment in Fe (Manly #2 on sol 719 and Deep_Spring #9 on sol 728). This may reflect localized host rock enrichments in K such as seen in Kimberley [*Le Deit et al.*, 2016] or it could indicate minor abundances of jarosite, as observed by the CheMin instrument at the Mojave drill site on Sol 882 (Rampe et al. 2017).

TiO_2 does not appear to be correlated with either FeO_T or MgO in light-toned veins (Figure 3.15). The absence of a clear correlation between TiO_2 and FeO_T suggests that the Fe-rich phases are probably not of detrital origin, and thus favors an authigenic formation in the veins. However, TiO_2 abundances in these diagenetic features are typically below 0.5 weight percent, a chemical configuration in which errors on TiO_2 predictions are exacerbated [*Wiens et al.*, 2013; *Clegg et al.*, 2017].

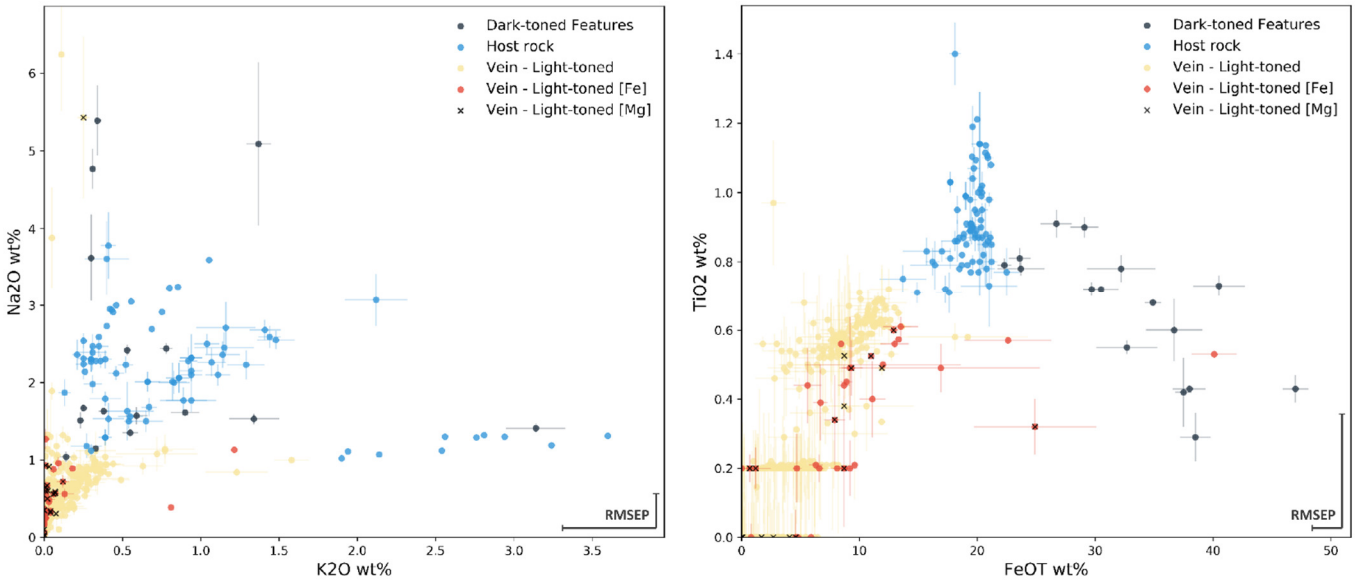

Figure 3.15: Bivariate plots of K_2O vs. Na_2O (left) and FeO_T vs. TiO_2 (right). The alkali plot illustrates Na_2O enrichment associated with Cl detection in a few light-toned veins (including 1 Mg-rich target) and dark-toned features as well as in K_2O in a few light-toned veins, including two Fe-rich targets. In addition, host-rock observations at the Kimberley have also shown elevated K_2O contents attributed to a more differentiated igneous source for the sediments.

3.3.1.2 Minor, trace and volatile elements

Minor element abundances for Ba, Li, Rb and Sr in light-toned veins are mostly depleted compared to host rock values (Figure 3.16) and do not show strong variability across the rover traverse (Figure S2). Higher abundances of Sr are, however, frequent in light-toned veins and are interpreted as due to its substitution for Ca [*Nachon et al.*, 2014]. Abundances of these elements in the Fe-rich and Mg-rich veins are overall on the lower end of detections within light-toned veins (Figure 3.16), except for Fe-rich Deep_Spring #9 which shows both elevated Ba and Sr.

Manganese content in light-toned veins is below the detection limit (ca. 0.06 wt.%; Lanza et al. 2014), lower than host rock values (Figure 3.16). Several Fe-rich and Mg-rich light-toned vein targets show slightly enriched Mn compared to other light-toned veins (Figure 3.16). In addition, Mn is quantified at 1-5 wt.% MnO in the dark-toned features, in association with elevated Fe and Mg except for Khoabendus #14 where it is associated with elevated Fe and Al.

Zinc and nickel are also detected qualitatively in a few spectra on light-toned veins, but not in association with enrichments in Fe or Mg. Zn is detected in 8 light-toned veins and in 2 points on dark-toned material, while Ni is detected in 4 light-toned veins (including 1 with Zn detection) and in 1 dark-toned point in association with Zn. All these targets were sampled from sol 1266 to 1550 in the Murray formation, where similar enrichments were observed in the host rock by the APXS instrument [*Rampe et al.*, 2017], except for one on sol 165 in the Yellowknife Bay formation.

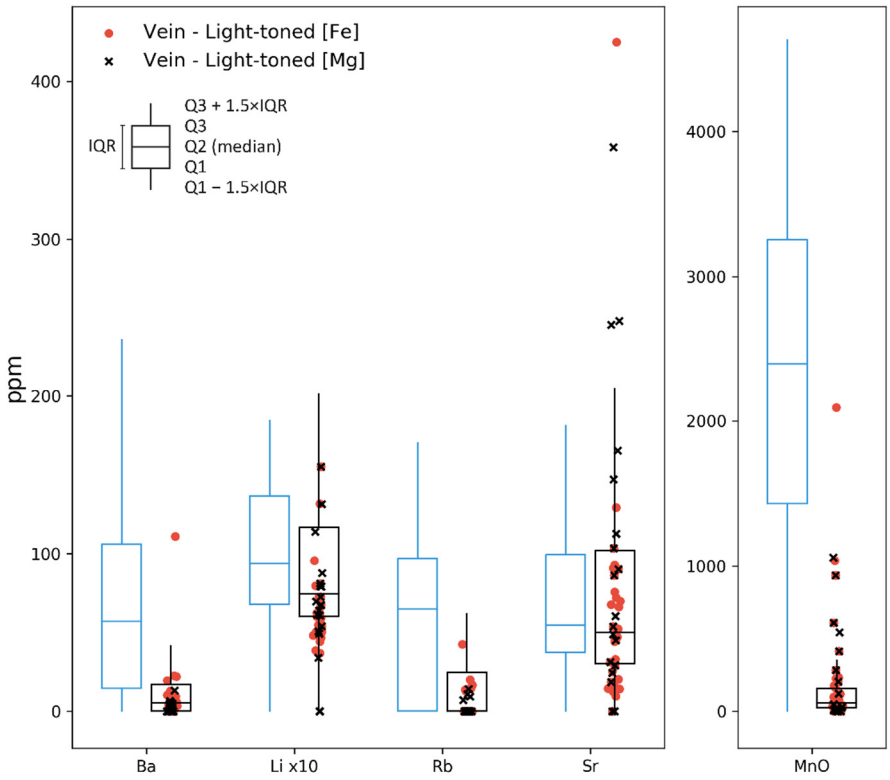

Figure 3.16: Box plots representing quantified abundances for Ba, Li, Rb, Sr and MnO in light-toned veins (black) and in host rock targets (blue). Abundances for Fe-rich (red dot) and Mg-rich (black cross) light-toned veins are also indicated and illustrate a slight enrichment in MnO in a number of these features, as well as 1 point (Deep_Spring #9) showing high Ba and Sr. The spread observed for Sr is expected within Ca-sulfate veins as it substitutes for Ca.

Phosphorus was detected in distinct diagenetic features in the Murray formation, including erosion-resistant ridges [*Meslin et al.*, 2016] and dark-toned features [*Forni et al.*, 2017]. P was also observed on 3 light-toned veins in association with Fe and Mg enrichments (Soyo #3, Blue_Hill #4 and #7). The presence of minor amounts of P, which may be expected within the light-toned veins where dark-toned inclusions are also observed, cannot be entirely ruled out at this point since the limit of detection of phosphorus is relatively high with ChemCam. P was also detected in association with Fe, Al, and Mn (Khoabendus #14). Fluorine was not detected in light-toned veins in association with Fe or Mg enrichments.

Chlorine observations on light-toned veins are associated with enrichment in Na and are localized on the edges of the veins. This result is consistent with previous observations at the host rock – vein interface and on erosion-resistant ridges present on the edge of light-toned veins [*Forni et al.*, 2017]. However, Cl was not detected conclusively in association with elevated Fe within light-toned veins.

Boron detections reported by ChemCam [*Gasda et al.*, 2017] in light-toned veins are associated in a few light-toned veins with elevated Fe. However, B emission peaks overlap a Fe emission peak at 250 nm, which may affect B detections and may thus reflect an artificial correlation between the two elements in these targets.

Sulfur is observed in all light-toned veins in association with elevated Ca, interpreted to be present as Ca-sulfate [*Nachon et al.*, 2014, 2016]. The limit of detection and precision of S measurements are not sufficiently constrained to allow for the study of variations in S abundances. Indeed, S is only detected for high SO_3 abundances (LOD ~10 wt.% SO_3), even though quantification efforts are on-going in order to improve ChemCam sensitivity to S [*Clegg et al.*, 2017]. Hydrogen content in these features is elevated and consistent with the hydration level of bassanite (see discussion above; [*Rapin et al.*, 2016]). No significant change in hydration level is observed in correlation with Fe content in the light-toned veins.

No carbon enrichment was observed in association with Fe or Mg in light-toned veins. However, detection of C in rocks is hindered by the presence of CO_2 in the Martian atmosphere, resulting in detection limits of 5 and 13 wt.% for both reduced and oxidized C [*Ollila et al.*, 2011; *Beck et al.*, 2017].

3.3.1.3 Passive spectra

Passive reflectance spectral analysis was conducted on the points showing a Fe-rich signature (representative spectra are shown in Figure 3.17). The spectra of 15 vein targets on sols 1162-1169, 1381-1445 and 1666 (e.g. Khoabendus #16, Luanda #3 and Tsumeb #9) are characterized by absorptions near 535 and 670 nm and a downturn after ~750 nm consistent with the presence of a Fe^{3+} phase such as hematite. Other Fe^{3+} bearing species cannot be excluded from these passive observations alone, such as ferric hydroxide (goethite) or ferric sulfate. Indeed, grain size, contaminants, and crystallinity can also impact these spectral features [*Johnson et al.*, 2015]. Similar spectral features are also observed on a dark-toned spot within a light-toned vein (Khoabendus #14). However, not all targets exhibiting a Fe-rich LIBS signature show spectral features consistent with the presence of a Fe^{3+} phase (for example, Rooibank #4 does not).

A possible falloff beginning near 600 nm is potentially associated with the presence of Fe^{2+}. This was observed on 4 vein targets: 1194 (Grillental #10), 1545 (Blue_Hill #4 & 7), 1548 (Blue_Hill_2 #3) and 1550 (Canon_Brook #2). Most of these observations occur on light-toned veins associated with dark-toned inclusions that also show a similar passive spectral signature (e.g. Patch_Mountain #1, Figure 3.17). These observations point toward a reduced Fe-rich phase such as ferrous sulfate (rozenite/melanterite). Alternatives such as ferrous phosphate (vivianite) exhibit peak reflectances at shorter wavelengths and are likely not significant components, and spectrally neutral ferrous oxide (magnetite) could contribute to the overall low reflectance of the dark-toned materials.

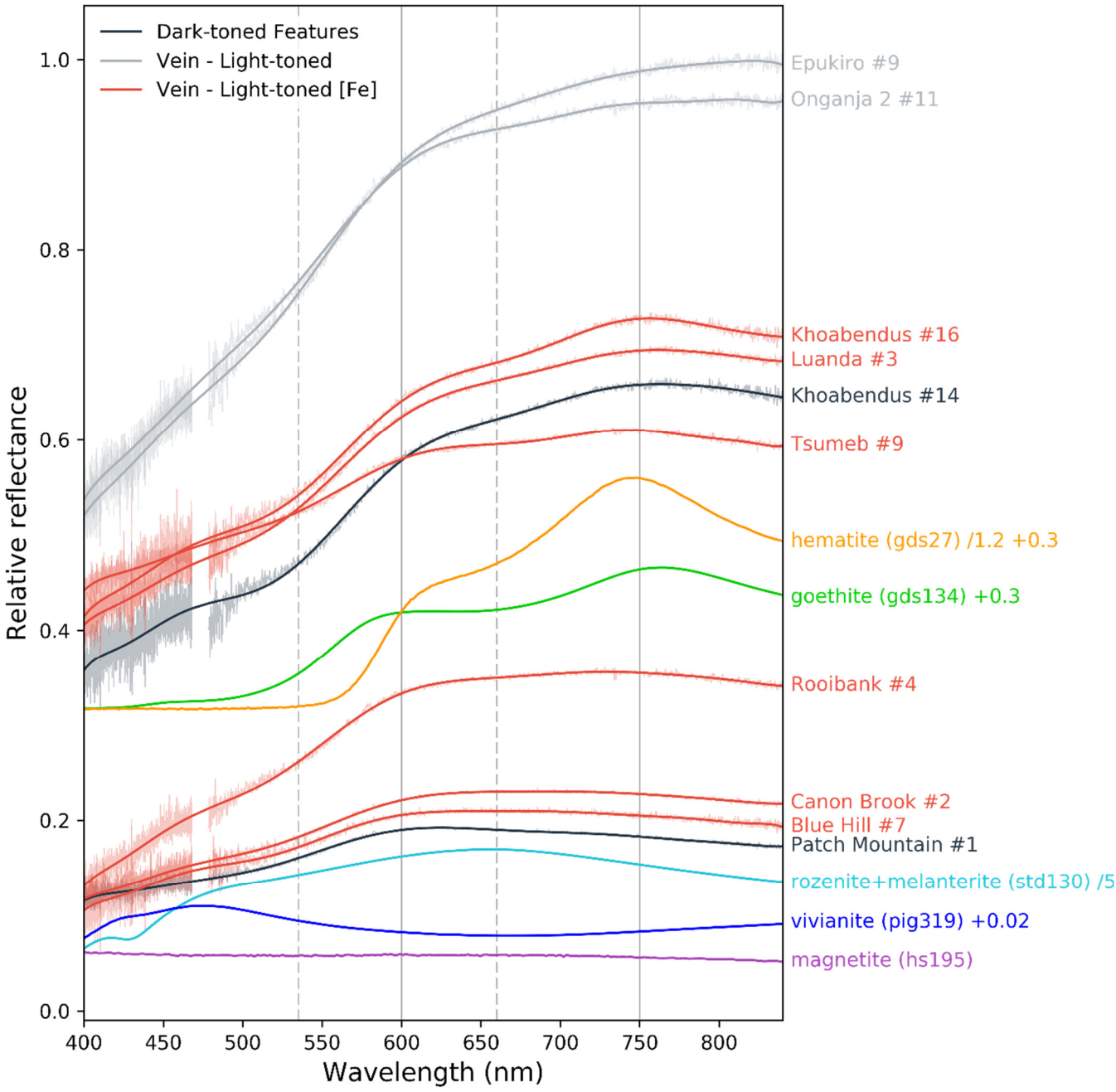

Figure 3.17: Passive reflectance spectra for Fe-rich light-toned vein targets (in red) and a dark-toned target (in black), the solid line overprinted on spectral data corresponds to the 15th order polynomial fit shown for clarity. Light-toned veins observed between sol 1150 and 1445 (Khoabendus #16, Luanda #3 and Tsumeb #9, +0.3 offset) present adsorption bands near 535 nm and 670 nm (dashed grey lines) and a downturn after 750 nm (solid grey line) consistent with Fe^{3+} phases, similar to Khoabendus #14 passive spectra (dark-toned material within vein, +0.3 offset). More recent observations on light-toned veins (in grey) from sol 1545 to 1611 (Canon Brook #2 and Blue Hill #7, +0.05 offset) often show a downward trend after 600 nm (solid grey line) which would, however, indicate the presence of Fe^{2+} bearing phases, also observed on dark-toned inclusions and layers (Patch Mountain #1, +0.05 offset). Passive reflectance spectra for light-toned vein targets with pure Ca-sulfate chemistry (Epukiro #9, Onganja 2 #11, +0.25 offset) are indicated for comparison (in grey). Library spectra from the USGS and Planetary Spectrophotometer Facility [*Cloutis et al.*, 2006] databases for hematite [Fe_2O_3], goethite [FeO(OH)], magnetite [$Fe^{2+}Fe^{3+}2O_4$] and ferrous sulfate (rozenite [$FeSO_4{\cdot}7H_2O$] + melanterite [$FeSO_4{\cdot}7H_2O$]) as well as ferrous phosphate (vivianite [$Fe_3(PO_4)_2 \cdot 8(H_2O)$]) are provided for comparison (scaling and offsets are indicated in the legend).

3.3.2 Texture and orientation of the veins in relation to chemical variability

Light-toned veins have shown a diversity of forms along the path of the rover including both straight and irregular morphology, emplaced as single veins or as part of a network of veins and with varying resistance to erosion.

The veins showing an enrichment in Fe present an irregular morphology with uneven vein walls and are often interconnected with similar veins forming a branched network of anastomosing veins (Figure 3.18). They have been eroded with the host rock, indicating a resistance to mechanical erosion equal to or lesser than the surrounding rocks. These particular veins also present an uneven and "pitted" texture with grey-toned spots and possible clasts observed within the bulk of the vein, contrasting with the clear white hue and massive texture of the pure Ca-sulfate veins. On the other hand, the veins that encompass dark-toned inclusions enriched in both Fe and Mg are single straight veins with a vuggy texture (Figure 3.11).

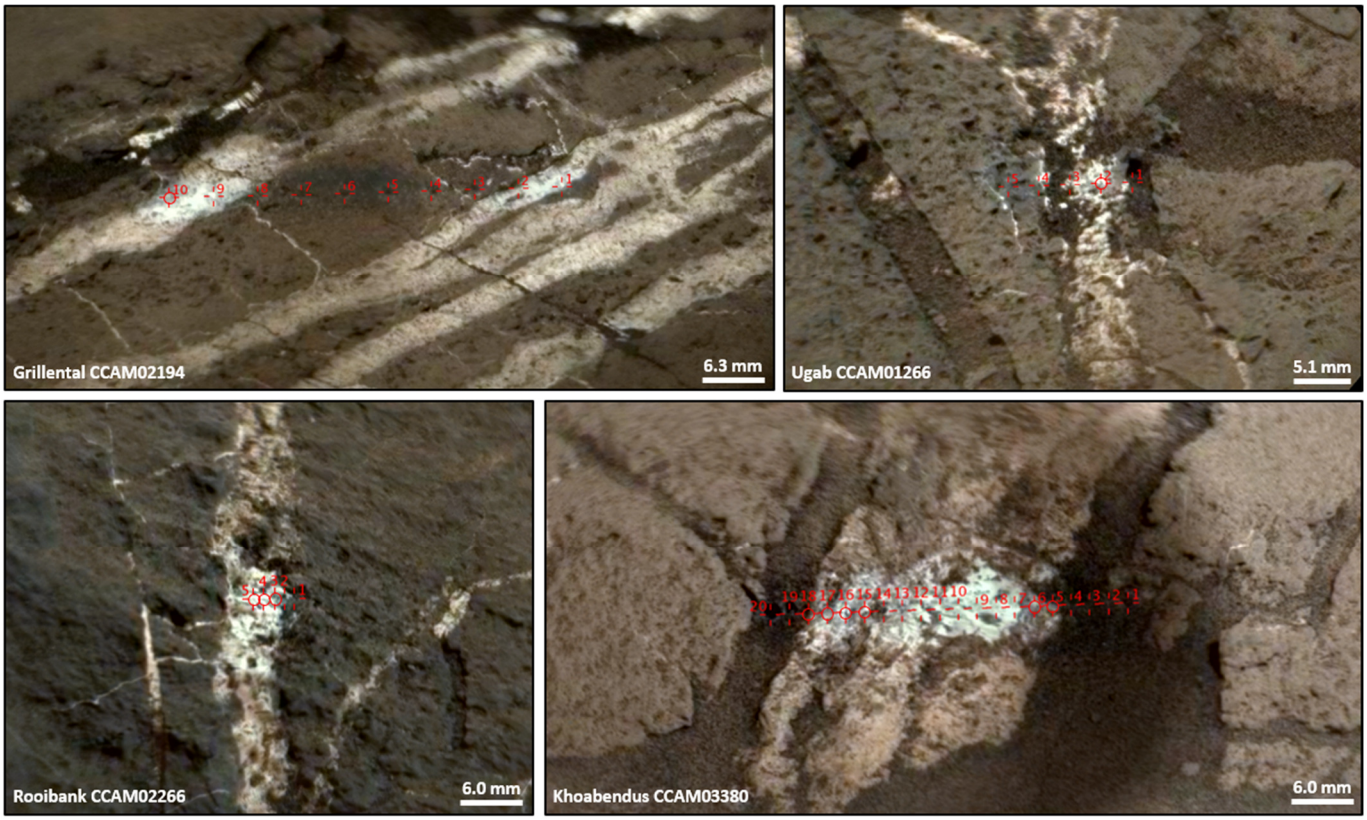

Figure 3.18: RMI images colorized with Mastcam of a selected subset of targets showing Fe-rich and Si-poor signatures within light-toned veins; the actual LIBS points of the subset are circled in red. These veins display a branched morphology for the most part and present a grey "pitted" aspect especially on the locations with elevated Fe/Si ratio. These detections in some cases appear only on part of the veins (e.g. Khoabendus target, with a clear white area showing a pure Ca-sulfate signature).

No particular growth morphology can be inferred from the RMI images, as crystal shape and arrangement within the veins cannot be resolved in these targets [*Le Mouélic et al.*, 2015]. The pitted aspect of these veins, however, suggests that a fibrous texture is unlikely. In that regard, they contrast with massive light-toned veins in the Murray formation at Pahrump Hills [*Kronyak et al.*, 2015] and Hartmann's Valley that occasionally display a suture line near the center of the vein and hints at a fibrous texture.

The light-toned veins are encountered preferentially along vertical fractures in the host rock and were probably emplaced by hydraulic fracturing during in the later phase of the diagenesis, as proposed for the formation of light-toned veins at Yellowknife Bay and Pahrump Hills [*Nachon et al.*, 2014, 2016; *Kronyak et al.*, 2015; *Caswell and Milliken*, 2017]. The branched and irregular morphology likely indicates a lower competence of the host rock and a higher porosity.

Recent observations on sub-horizontal light-toned veins or layers encountered in zones of structural weakness (e.g. between mudstone laminae or as cement in sandstone layers) in the upper part of the Murray formation do not show any indication of enrichment in Fe or Mg, nor are associated with any significant enrichment in minor elements as observed by ChemCam (Figure S2).

3.3.3 Localization within the Gale stratigraphy and relationship with adjacent diagenetic features

In order to place the light-toned Fe- and Mg-enriched veins within their geological context, these diagenetic features are plotted on the stratigraphic column of Gale Crater (Figure 3.19), reconstructed by the MSL Sedimentology Stratigraphy Working Group based on *Curiosity* observations along its traverse [*Grotzinger et al.*, 2014, 2015]. The light-toned veins showing an enrichment in Fe are mostly located at elevations corresponding to the localities of Bridger Basin – Naukluft Plateau (near -4430m) and Old Soaker (near -4335m) [*Stein et al.*, 2018], within the Murray formation. The transition from Fe^{3+} bearing phases toward Fe^{2+} is also indicated by the shift in the passive reflectance spectra peak positions from 750 nm toward ca. 600 nm [*Johnson et al.*, 2017b].

The sampled Naukluft Plateau and Bridger Basin localities correspond to areas where the *Curiosity* rover crossed over the Murray – Stimson unconformity and observed the Stimson eolian sandstones [*Banham et al.*, 2016]. Light-toned veins and other diagenetic features were observed in the Murray formation below the unconformity, on both sides of the Naukluft Plateau, in the Hartmann's Valley (Figure 3.20). A few occurrences of light-toned veins were observed within the Stimson formation and they are mostly encountered at the boundary between host rock and Si-rich alteration halos surrounding fractures, which extend to the Murray formation below [*Frydenvang et al.*, 2017; *Yen et al.*, 2017]. In addition, erosion-resistant ridges showing enrichment in FeO_T, Al_2O_3, K_2O and volatiles (P, Cl, F) were also observed at these locations [*Meslin et al.*, 2016] and are often found on the edges of Ca-sulfate veins, but were not directly observed in association with Fe-rich light-toned veins.

Old Soaker is located in the upper part of the Murray formation where an outcrop featuring desiccation cracks was encountered [*Stein et al.*, 2018] and just north of the Ireson Hill landmark (sol 1600, Figure 3.20). Dark-toned inclusions within light-toned veins were observed at this location (Figure 3.11). These features may be related to recent observations on dark-toned, erosion-resistant layers of similar composition (Fe+Mg rich associated with elevated Mn & P) alongside Ca-sulfate, present as cement in the host rock [*Newsom et al.*, 2017] and within light-toned horizontal layers or veins.

These observations are summarized in Table 3.1 and in Figure 3.21 with a sketch of the transect of Gale Crater along the rover traverse, illustrating the distribution of Fe^{2+} and Fe^{3+}-rich light-toned veins within the Murray formation.

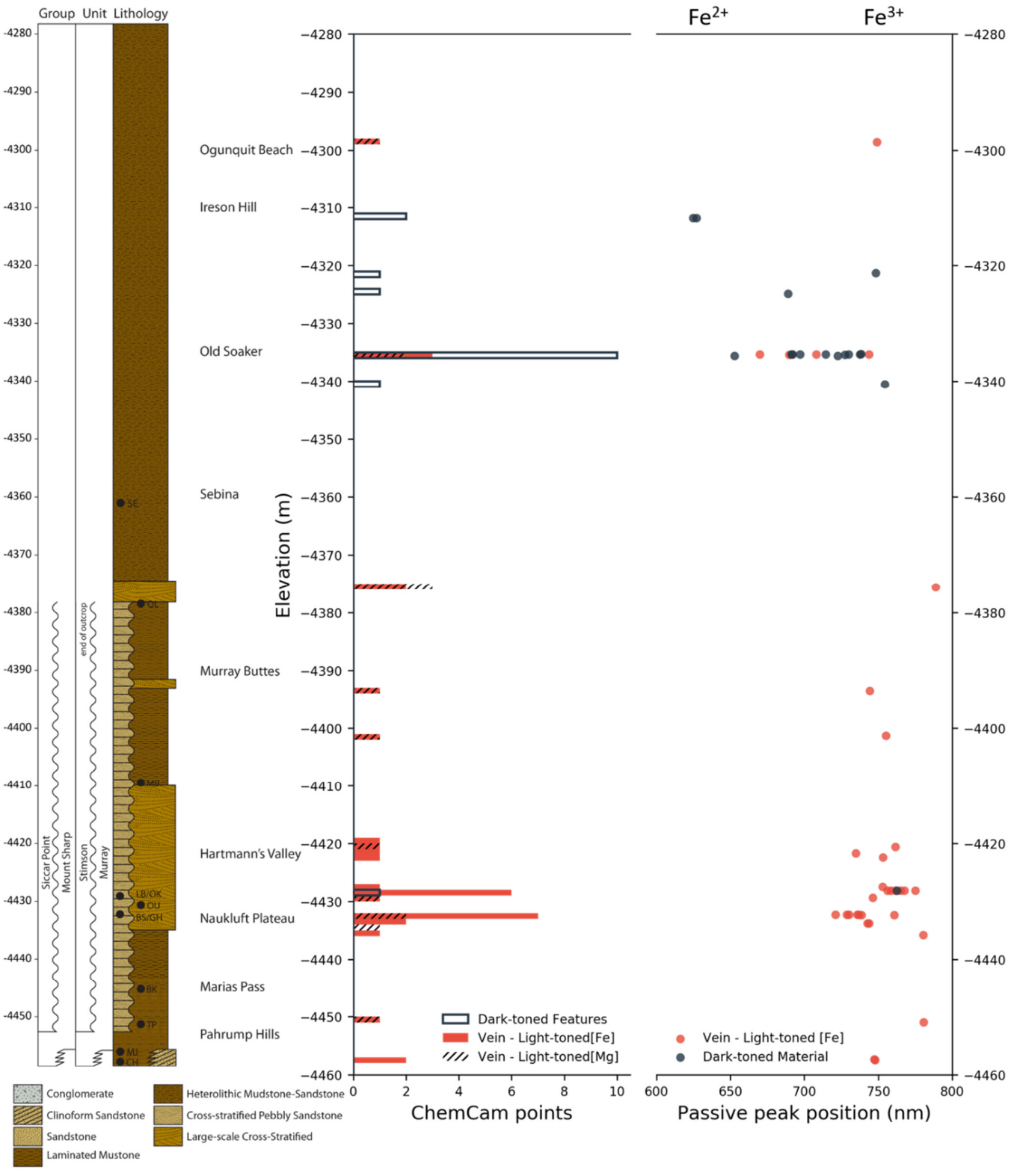

Figure 3.19: Distribution of Fe-rich and Mg-rich light-toned veins in the stratigraphy, highlighting the concentration of these targets in the Murray formation, especially in the Hartmann's Valley and near Old Soaker. The distribution of the dark-toned Fe ± Mg-rich material is also indicated. In addition, peak positions for passive reflectance spectra are reported as an indicator of the oxidation state of Fe, with peak position near 750 nm indicating a Fe^{3+} phase while a shift toward 600 nm suggests influence from Fe^{2+}.



Figure 3.20: Distribution of Fe-rich light-toned veins along the rover traverse. The unconformable contact between the Murray and Stimson formations are highlighted along the traverse by yellow markers. The Fe-rich light-toned veins are located in the Murray formation, especially below the Murray / Stimson unconformity observed at Bridger Basin and Naukluft Plateau, in the Hartmann's Valley. Topography along the rover traverse is shown schematically in Figure 3.21.

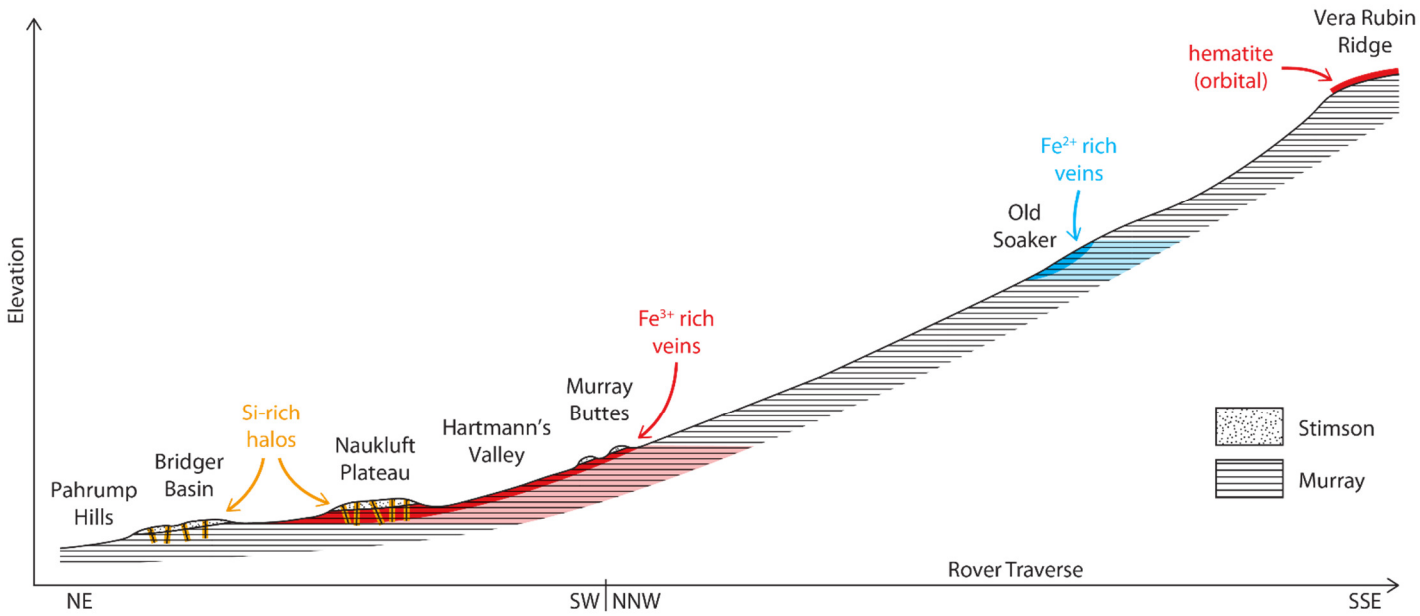

Figure 3.21: Sketch of the transect of Gale Crater along the *Curiosity* rover traverse illustrating the distribution of Fe^{2+} and Fe^{3+}-rich light-toned veins and relationship with elevation and geological landmarks. Fe^{3+}-rich light-toned veins (red patch) are mostly encountered below the unconformable contact between the Murray and Stimson formations, where Si-rich fractured halos were encountered (yellow contours). Fe^{2+} light-toned veins (blue patch) are mostly encountered near the Old Soaker outcrop, in a geological setting otherwise dominated by hematite and in close proximity with Vera Rubin Ridge.

	Feature	Major elements (Figure 3.12 to 3.15)	Minor elements (Figure 3.16)	Redox state (Figure 3.17, 3.19)	Description
Murray (≠ HV / OS)	Light-toned veins	high Ca, S other major oxides depleted	H, Sr (variable) occasional Cl (+ Na) near vein walls	none	Ranging from single straight vertical veins, locally more erosion resistant than host rock, to sub-horizontal irregular layers
Hartmann Valley (HV)	Light-toned veins (HV subset)	high Ca, S + high Fe/Si ± Mg/Si (Ti not correlated) + high Al/Si + high K	H, Sr (variable)	Fe^{3+} (not all)	Vertical veins with irregular morphology, uneven vein wall and pitted texture (grey-toned spots), forming branched networks (Figure 3.18)
	Dark-toned spot (Khoabendus #14)	high Fe/Si and Al/Si	Mn, P, Sr	Fe^{3+}	Dark-toned spot within light-toned vein (Figure 3.18)
	Raised ridges	high Al, Na & K	P, F, Ba, Cr, Li, Mn, Sr (variable)	none	Erosion resistant ridges associated with light-toned veins
Old Soaker (OS)	Light-toned veins (OS subset)	high Ca, S + high Fe/Si ± Mg/Si	H, variable Sr + Li, P detections	Fe^{2+} Fe^{3+}	Straight vertical veins with vuggy texture (Figure 3.11) that present dark-toned inclusions
	Dark-toned features	high Fe/Si + Mg/Si	Mn, P	Fe^{2+} Fe^{3+}	Nodular inclusions in light-toned veins and erosion resistant sub-horizontal layers (Figure 3.11)

Table 3.1: Summary of ChemCam observations on light-toned veins and related diagenetic features in the Murray formation

3.4 Discussion

3.4.1 Mineralogical interpretations

Even though ChemCam is not designed to characterize the mineralogy of the rocks directly, the observations presented in this study are localized on relatively large diagenetic features with limited host rock contribution. In this context, we can infer possible mineral phases to account for the observed chemistry, in association with passive spectral observations and the geological context.

Fe enrichment in Ca-sulfate-bearing light-toned veins is not associated with any particular chemical elements detectable by ChemCam other than Mg (although not consistently) in the most recent observations. This implies that the mineral phase(s) analyzed likely contain(s) little to no other major and minor elements aside from the Ca-sulfate phase observed in these light-toned veins.

For light-toned veins observed in the Hartmann's Valley (HV subset), we infer that the Fe is either present as oxides (or hydroxides) or in association with elements that are rather difficult to observe with ChemCam such as C, S, and P. Sulfide minerals such as pyrite are not considered here as they are unlikely to precipitate within diagenetic fluid circulation events [*Berner*, 1984] nor to co-exist with sulfates. Fe-carbonates are also unlikely, as no enrichment of C was detected in association with Fe, not even in the observations showing more than 8-10 wt.% FeO_T where C should be above detection limit [*Beck et al.*, 2017]. Thus, we will consider oxides, sulfates, and phosphates as reasonable mineral hypotheses.

P is observed in association with elevated Fe only in point #14 of the ChemCam Khoabendus target. However, this point also shows significant enrichment in Al and Mn and both elements were not observed in association with Fe in the majority of light-toned veins, including points within the same vein. It is thus unclear if P is found in association with Fe or a distinct, Al-bearing and/or Mn-bearing phase. Three observations on light-toned veins also showed an enrichment in Al associated with Fe (+Mg) and may reflect a similar mineral assemblage, though without detection of P. Thus, phosphate minerals are unlikely to account for the Fe enrichment in light-toned veins overall.

The distinction between Fe-oxides and Fe-sulfates is challenging in this geological context because S is observed within all light-toned veins due to the presence of Ca-sulfate. The precision on S abundances does not allow for the distinction between associations of Ca-sulfate with Fe-sulfates or Fe-oxides. Passive reflectance observations indicate that iron is probably present as ferric iron (Fe^{3+}) in most observations near the Naukluft Plateau, thus indicating the presence of ferric oxide (such as hematite). No evidence of ~430 nm absorptions associated with some ferric sulfates is observed (cf. [*Johnson et al.*, 2016]). No particular trend was observed in the hydrogen content within these veins, preventing interpretations on the hydration state of the Fe-bearing phase.

Old Soaker light-toned veins (OS subset) enriched in Fe and Mg do not present the elevated P or Mn contents observed in the associated dark-toned inclusions and layers. P detection in dark-toned inclusions associated with elevated Fe ± Mn could be explained by Fe-phosphate formation [*Egger et al.*, 2015] or adsorption of P onto oxides [*Berner*, 1973; *Geoffrey Wheat et al.*, 1996]. Later dissolution of P by diagenetic fluid(s) at the time of formation of Ca-sulfate may explain its absence within the veins. As for mineral phases, the observed compositions suggest the presence of a mineral assemblage, with Fe and Mg likely encountered as oxides and/or sulfates in these features. In addition, passive spectra indicate the presence of reduced Fe^{2+} in some of the light-toned veins and the dark-toned

inclusions, near Old Soaker, potentially in the form of ferrous sulfate or ferrous oxides, contrasting with generally Fe^{3+}-rich observations near the Naukluft Plateau (Figure 3.19 - 3.21).

3.4.2 Implications for fluid chemistry

Given the lack of correlation with the poorly soluble Ti and the absence of textural evidence for host rock fragments incorporated within the veins, we interpret the variability in chemistry observed in the light-toned veins as authigenic rather than detrital in origin. Thus, the enrichments reported here likely reflect different pH and redox conditions at the time of emplacement compared to previous light-toned vein observations at Yellowknife Bay and Pahrump Hills [*Nachon et al.*, 2014, 2016]. Indeed, Fe- and Mg-bearing phases such as oxides and sulfates in association with Ca-sulfate can form in a variety of environments including more acidic and/or oxidizing conditions.

Associations of Fe-sulfate with Ca-sulfate are reportedly encountered in highly acidic and oxidizing environments on Earth, such as acid mine drainage [*Valente and Leal Gomes*, 2009] or hydrothermal ponds [*Izawa et al.*, 2011]. Such assemblages were also reported at Meridiani Planum on Mars by the rover *Opportunity* with detection of jarosite in association with Ca-sulfate [*Squyres*, 2004], which were interpreted as alteration by acidic fluids [*Fernández-Remolar et al.*, 2005; *Tosca et al.*, 2005; *Morris et al.*, 2006]. Moreover, recent observations by the *Curiosity* rover CheMin and APXS instruments on Murray host rock with enrichments in metal ions such as Fe, Mg, Mn, Zn, Ni [*Rampe et al.*, 2017] and on Si-rich alteration halos [*Yen et al.*, 2017] near the Murray – Stimson boundary suggested that they formed to some extent in acidic conditions. Enrichment in Al in association with Fe as reported in a few ChemCam observations would also support this hypothesis, as Al is insoluble except at very low pH.

In this context however, detections of phosphates (fluorapatite) in the lower part of the Murray formation [*Rampe et al.*, 2017] are not easily explained, as phosphates tend to dissolve readily under acidic conditions [*Chaïrat et al.*, 2007] and suggest rather short-lived acidic diagenetic events [*Rampe et al.*, 2017]. On the other hand, P adsorption onto Fe-oxides increases with decreasing pH [*Gomez et al.*, 1999; *Antelo et al.*, 2005; *Zhou et al.*, 2005] and increasing Eh [*Patrick and Khalid*, 1974], which could be consistent with observations of P in association with Fe-oxide in dark-toned inclusions and layers [*Forni et al.*, 2017].

Fe-oxide formation in association with Ca-sulfate does not necessarily require low pH to form but rather attests to the redox conditions at the time of emplacement [*Beverskog and Puigdomenech*, 1996]. Indeed, the oxidation states of iron in solution and in the mineral phase are tied to the redox potential prevailing in the fluids at the time of formation. Fe^{2+} is soluble and can be found in solution in a wide range of pH under reducing conditions, while Fe^{3+} is insoluble and forms in an oxidizing environment. The observation of both Fe^{3+} and Fe^{2+} spectral features in passive reflectance spectra would thus indicate a drastic change of the redox conditions in the fluids leading to the formation of ferric species near Naukluft Plateau and ferrous species up section near Old Soaker.

Orbital and *in situ* mineralogy observations also point toward a change in redox conditions in the Murray formation, with magnetite giving way to hematite within the Murray formation at Pahrump Hills and after Bridger Basin [*Fraeman et al.*, 2013; *Rampe et al.*, 2017], as well as on the Vera Rubin Ridge (also known as the hematite ridge) toward which the *Curiosity* rover is heading [*Fraeman et al.*, 2013]. These observations suggest the presence of a redox boundary in the sediments [*Hurowitz et al.*, 2017] or subsequent oxidation during diagenesis [*Fraeman et al.*, 2018]. Fe^{3+} enrichments in light-

toned veins located just below the Stimson – Murray boundary were not observed consistently within the Murray formation and thus challenge a diagenetic origin, at least related to the emplacement of these veins. Furthermore, the localization of these Fe-rich light-toned veins at a specific level in the stratigraphy would support the hypothesis of a redox boundary in the host rock, upon which Fe^{2+} present in diagenetic fluids would oxidize to Fe^{3+} and precipitate alongside Ca-sulfate. However, the lack of Fe^{3+} and possible Fe^{2+} detections in the diagenetic features near Old Soaker are in apparent contradiction with observations in the surrounding host rocks and may indicate the reduction of the Fe^{3+} phases during diagenesis. In addition, recent observations of evaporation driven sedimentary structures such as desiccation cracks [*Stein et al.*, 2018] associated with minor levels of evaporites [*Newsom et al.*, 2017] may challenge a redox stratified lake model [*Hurowitz et al.*, 2017] and would favor periodic recession of the lake level and low-stand deposition environments.

3.4.3 Potential sources of chemical variability in light-toned veins

No clear evidence supports multiple fluid episodes to account for the diversity of light-toned vein occurrences observed over the course of the mission, although the diverse vein chemistry at Garden City near Pahrump Hills has been interpreted as due to an earlier stage of fluid deposition [e.g. *Nachon et al.*, 2016]. The light-toned veins are consistently observed as a late episode of fluid circulation in all geological units observed so far, including the Yellowknife Bay and Murray lacustrine mudstones as well as the overlying Stimson eolian sandstones. This seems to hold true for observations in the upper part of the Murray formation, where vertical light-toned veins give way to sub-horizontal layers along planes of structural weaknesses and higher porosity in the lacustrine mudstones. We thus suggest the possibility of a widespread late-stage diagenetic fluid event that emplaced light-toned veins by hydraulic fracturing and occurred after burial and lithification of the sedimentary rocks of the Murray and Stimson formations. In this setting, chemical observations of light-toned veins would thus result from the interaction of the light-toned veins' parent fluid with distinct local environments, such as pore-fluids, other diagenetic features or geochemical and redox boundaries.

The HV subset veins are preferentially localized below the stratigraphic unconformity with the Stimson formation (Figure 3.19 and 3.21). Previous studies have advanced either acid leaching [*Yen et al.*, 2017] or an active enrichment by Si-rich fluids [*Frydenvang et al.*, 2017], or both, for the formation of Si-rich, fracture-associated halos cross-cutting both Murray and Stimson formations. The close proximity of these features associated with Fe^{3+} oxide/sulfate observations (Figure 3.21) and local enrichments in Al would support an acidic scenario in which diagenetic fluids were enriched notably in Fe^{2+} and Al^{3+}, which would have been leached from the surrounding host rock. Precipitation would lead to the formation of Fe-oxides and/or Fe-sulfates alongside Ca-sulfate in the light-toned veins following changes in conditions in the fluid, i.e. more oxidizing conditions upon crossing a redox boundary (precipitation of Fe^{3+} from Fe^{2+} in fluids) and increase in pH (precipitation of Al-rich phases). In addition, the Stimson – Murray unconformable contact could act as a physical boundary or pressure seal for diagenetic fluid circulation leading to their accumulation in the Murray formation below, which would explain the density and diversity of diagenetic features observed at that stratigraphic level and possibly affect the unique host rock composition within the Murray formation [*Morris et al.*, 2016]. This particular diagenetic setting could, in turn, be responsible for distinct redox and/or pH conditions.

The OS subset veins, encountered in the upper part of the Murray formation, are closely linked with observations on dark-toned inclusions and layers both spatially and compositionally. The presence of reduced Fe-bearing phases in association with the Ca-sulfate veins amidst an overall oxidized host rock chemistry may indicate a reduction of Fe^{3+}-rich phases in the dark-toned features upon interaction with the Ca-sulfate parent fluid. The presence of reduced Fe within veins is consistent with Mastcam images of grey-toned alteration rinds around Ca-sulfate veins within red-toned host rocks of the Murray formation near the sol 1600, which could be interpreted as an expression of reduced Fe in the host rock (e.g. Third Lake outcrop, sol 1612; Figure S3). Moreover, elevated P detection alongside reduced Fe is inconsistent with laboratory experiments that have shown that P adsorbed onto Fe-oxide readily dissolves upon reduction of Fe^{3+} to Fe^{2+} and could account for the lack of P detection in the veins. In addition, similar observations from sols 1550 and 1700 on dark-toned, erosion-resistant, sub-horizontal layers and dark-toned nodular features not directly cross-cut by light-toned veins are likely Fe^{2+}-bearing. The potential observation of Fe^{2+} phases at that location represents a lull in detections of Fe^{3+} phases in passive spectra along the traverse to Vera Rubin Ridge [*Johnson et al.*, 2017a] and hints at locally more reduced conditions during the formation of these features. Further observations from the rover *Curiosity* as it climbs Vera Rubin Ridge will help to constrain the chemistry and mineralogy of these phases. They will also help in reconstructing the diagenetic history of these sedimentary rocks and better constrain the evolution of pH and Eh conditions in the Murray formation.

3.5 Conclusion

In the lacustrine Murray formation, ChemCam has observed Fe and Mg enrichments in Ca-sulfate-bearing light-toned veins, contrasting with the consistently pure composition observed previously on similar features notably at Yellowknife Bay and Pahrump Hills [*Nachon et al.*, 2014, 2016]. These enrichments are not correlated with Si and thus likely reflect authigenic mineral phase formation, rather than a contribution from the surrounding host rock. We observed two distinct trends in the light-toned veins of the Murray formation with (1) Fe enrichments localized in the Hartmann's Valley area (HV subset) and (2) Fe+Mg enrichments in the upper part of the Murray formation near the Old Soaker outcrop, associated with dark-toned inclusions of similar composition (OS subset). These trends are associated with distinct passive reflectance spectra that suggest a Fe^{3+} phase likely accounts for the Fe detection in the light-toned veins near Naukluft Plateau, whereas a more reduced chemistry is suggested by observations near Old Soaker. These enrichments are not correlated with other major and minor elements detected by ChemCam, except for detections of elevated Al near Naukluft Plateau and P and Mn on dark-toned inclusions associated with light-toned veins near the Old Soaker outcrop.

Observations of Fe^{3+} oxide/sulfate alongside Ca-sulfate (HV subset) both before and after crossing the Naukluft Plateau, i.e., in the mudstones of the Murray formation below the unconformable contact with the eolian sandstones of the Stimson formation, suggest that oxidizing conditions prevailed there at the time of formation of the veins. These observations are also associated with a shift in the oxidation state of Fe-oxide observed in the host rock, potentially marking a redox boundary in the lake waters, groundwater, or sediments. Furthermore, the presence of Si-rich alteration halos along fractures and Al-rich erosion-resistant ridges near these Fe-rich veins also hints at more acidic fluid composition.

On the other hand, Fe+Mg enrichments in light-toned veins associated with dark-toned inclusions (OS subset) attest to a more reducing chemistry within an overall oxidizing geological context in the proximity of Vera Rubin Ridge. The presence of P and Mn in association with Fe in these dark-toned features would indicate the formation of Fe/Mn oxides in an oxidizing environment with adsorption of P on their surface and subsequent reduction during diagenesis, possibly upon interaction with the Ca-sulfate vein parent fluid.

The chemical variability observed by ChemCam in the light-toned veins encountered consistently across the ~18 km of the *Curiosity* rover traverse to date retraces changes in the pH and redox conditions at the time of formation of these features. These features thus provide valuable information on the diagenesis of the Murray formation and will likely help further studies constrain the formation mechanisms of the various diagenetic features observed at Gale Crater.



[Sol **1745**]
VERA RUBIN RIDGE HEAVILY FRACTURED OUTCROPS
NASA/JPL-Caltech/MSSS/Thomas Appéré

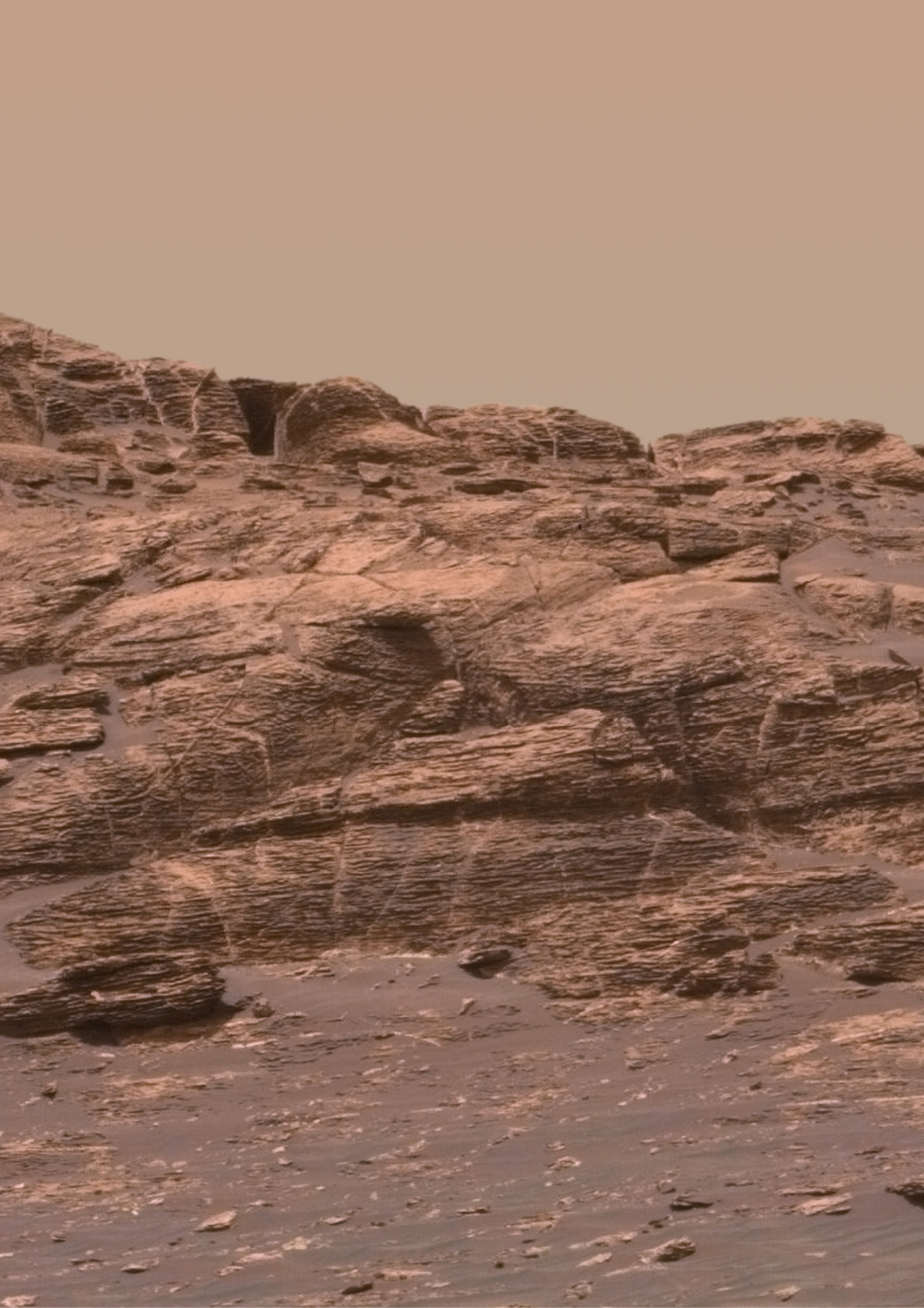

CHAPTER 4

IRON MOBILITY DURING DIAGENESIS ON VERA RUBIN RIDGE

The Vera Rubin Ridge (VRR) topographic structure was first identified from orbital observations (CTX and HiRISE images) as a high albedo and high thermal inertia prominent ridge, that stand out in erosional resistance compared to adjacent sedimentary terrains [*Anderson*, 2010]. The ridge is ~200 m wide and trends northeast-southwest over ~6.5 km. It skirts the phyllosilicates through (clay-bearing unit) and overlying sulfate deposits [*Milliken et al.*, 2010], and as such constitutes a topographic boundary between the Murray formation to the northwest and the clay-bearing unit to the southeast [*Fraeman et al.*, 2016] (Figure 4.1). At its ends, the ridge transition to an escarpment overlain by younger sedimentary strata to the southwest, and is gradually obscured by debris flows from Mount Sharp as it broadens to the northeast [*Anderson*, 2010; *Fraeman et al.*, 2013].

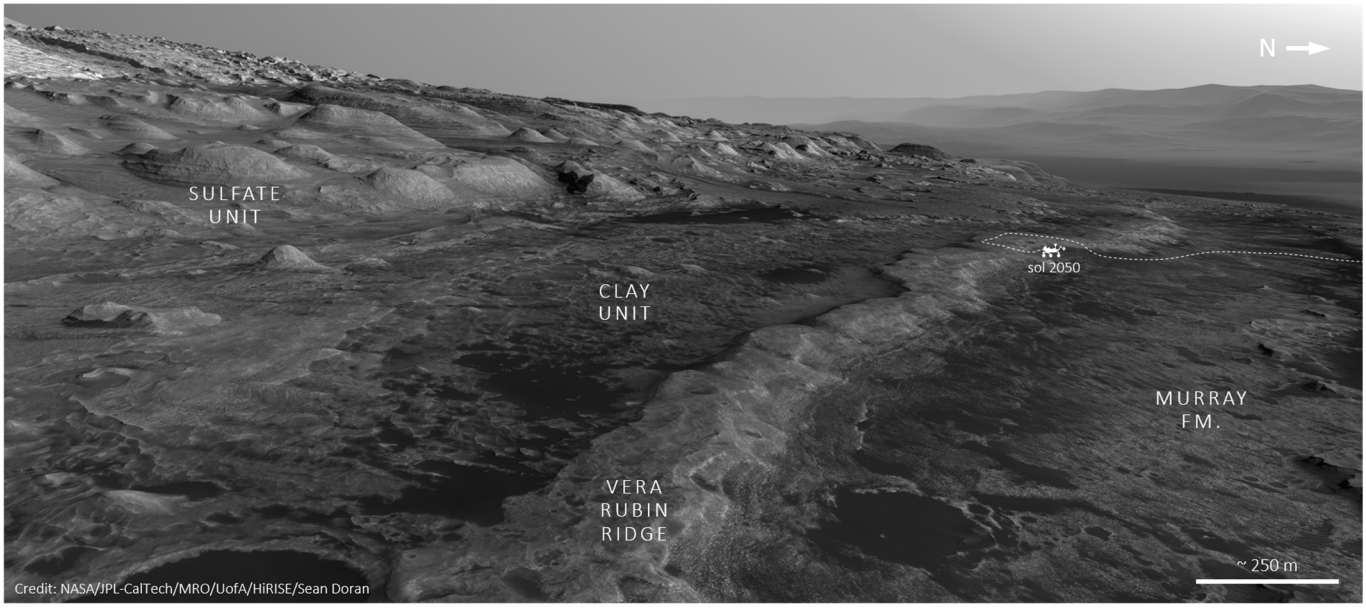

Figure 4.1: 3D representation of Vera Rubin Ridge, illustrating its geographic position relative to the Murray formation (downslope) and the clay- and sulfate-bearing units (upslope, toward Mount Sharp). The *Curiosity* rover traverse and its location on sol 2050 are represented schematically.

Orbital mineralogical studies, notably from visible and near-infrared hyperspectral observations from CRISM revealed a significant crystalline hematite signature associated with the ridge [*Milliken et al.*, 2010; *Fraeman et al.*, 2013]; which was thus initially known as the "hematite ridge". Hematite detection was inferred from the presence of ferric absorption bands near 550 and 860 nm as well as a reflectance maximum at 750 nm in CRISM spectra, consistent with laboratory data on red hematite [*Morris et al.*, 1985] (Figure 4.2). Hematite detections appear to mostly follow the southern and uppermost layers of the ridge [*Fraeman et al.*, 2013], as seen from mapping the 860 nm band depth (Figure 4.2), which is commonly used as a proxy for CRISM hematite detections. Bedding orientations measured from orbit on HiRISE images and digital elevations models within the ridge are consistent with bedding orientations in the strata above and below it, which implies that the ridge originally formed as part of the Mount Sharp sedimentary sequence [*Fraeman et al.*, 2013].

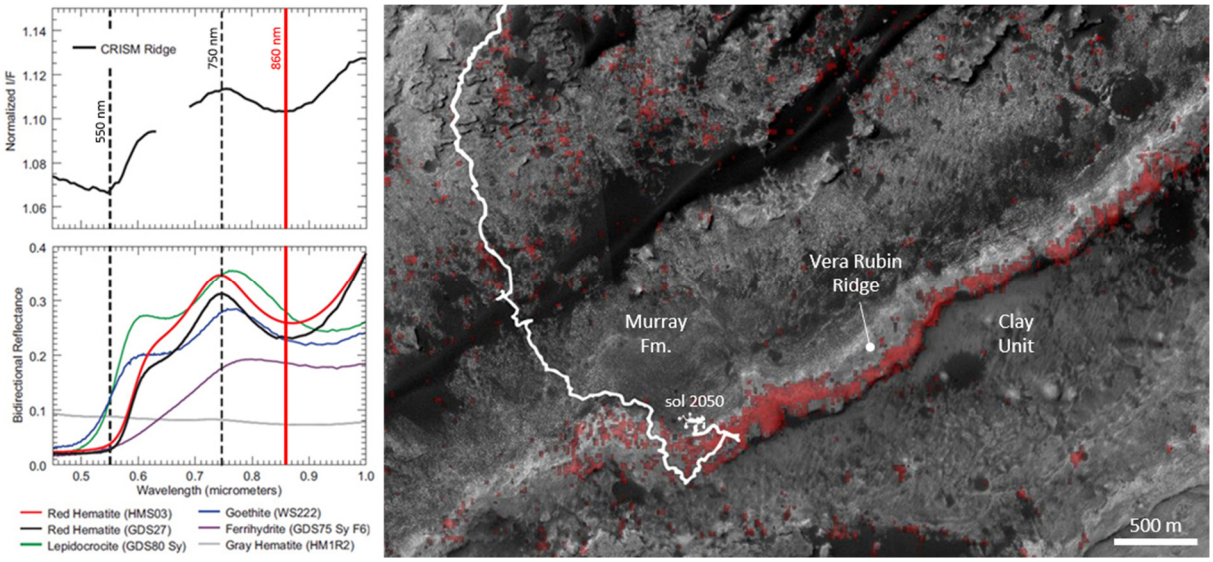

Figure 4.2: CRISM reflectance spectra observed on the ridge compared to Fe-oxide laboratory spectra (left) [modified from *Fraeman et al.*, 2013]. The 860 nm ferric absorption band is used as a proxy to map hematite detections (right; the *Curiosity* rover traverse is indicated in white), which appear to follow the southern and uppermost layer of the ridge [modified from *Fraeman et al.*, 2018].

In situ exploration of the ridge by the *Curiosity* rover confirmed the stratigraphic relationship between the Murray formation and the VRR unit, and identified two geological members associated with the lower and upper sections of the ridge [*Edgar et al.*, 2018]. The lower member, Pettegrove Point, is composed of well cemented and finely laminated mudstones, crosscut by light-toned filled-fractures (Figure 4.3), and appear to lie conformably on top of the sedimentary strata of the Murray formation. The upper member, Jura, overlies conformably Pettegrove Point and consists primarily in red blocky outcrops of displaced finely laminated mudstones (Figure 4.3). The facies and texture associated with the VRR lacustrine mudstones are consistent with deposition in a lacustrine setting [*Edgar et al.*, 2018], in continuity with the underlying lacustrine mudstones and fine-grained sandstones of the Murray formation [*Grotzinger et al.*, 2015]. In addition, the bedrock exhibits lateral color variations from red to light-toned grey (especially in the Jura member; Figure 4.3), first observed during the approach on the flanks of Vera Rubin Ridge. In the Jura member, the grey outcrops are associated with shallow topographic lows on top of the ridge (observed as bright patches on HiRISE images), probably reflecting lesser erosional resistance compared to the adjacent red blocky outcrops. These variations in bedrock color cannot be continuously tracked laterally, and do not appear to be associated with a particular stratum in the VRR stratigraphic sequence. Thus, the color patterns observed in the VRR outcrops are probably not associated with changes in the depositional lacustrine setting but instead reflect alteration during diagenesis.

Mastcam multispectral and ChemCam passive reflectance observations on brushed VRR bedrock display ferric spectral features (Figure 4.4), confirming the presence of hematite throughout the ridge lower and upper sections [*Fraeman et al.*, 2018]. Nevertheless, grey outcrops in the Jura member lack this ferric signature (Figure 4.4), and the relatively flat reflectance spectra observed on the grey outcrops suggests lower content in ferric compounds in the bedrock. However, particle size and crystallinity have a significant effect on the hematite spectral signature, with ferric diagnostic absorptions becoming less apparent or disappearing completely at large (> 5 µm) and small grain sizes (< 5-10 nm) [*Morris et al.*, 1985; *Lane et al.*, 2002; *Johnson et al.*, 2016]. As such the grey outcrops could also reflect the presence of coarse grey crystalline hematite [*Fraeman et al.*, 2018].

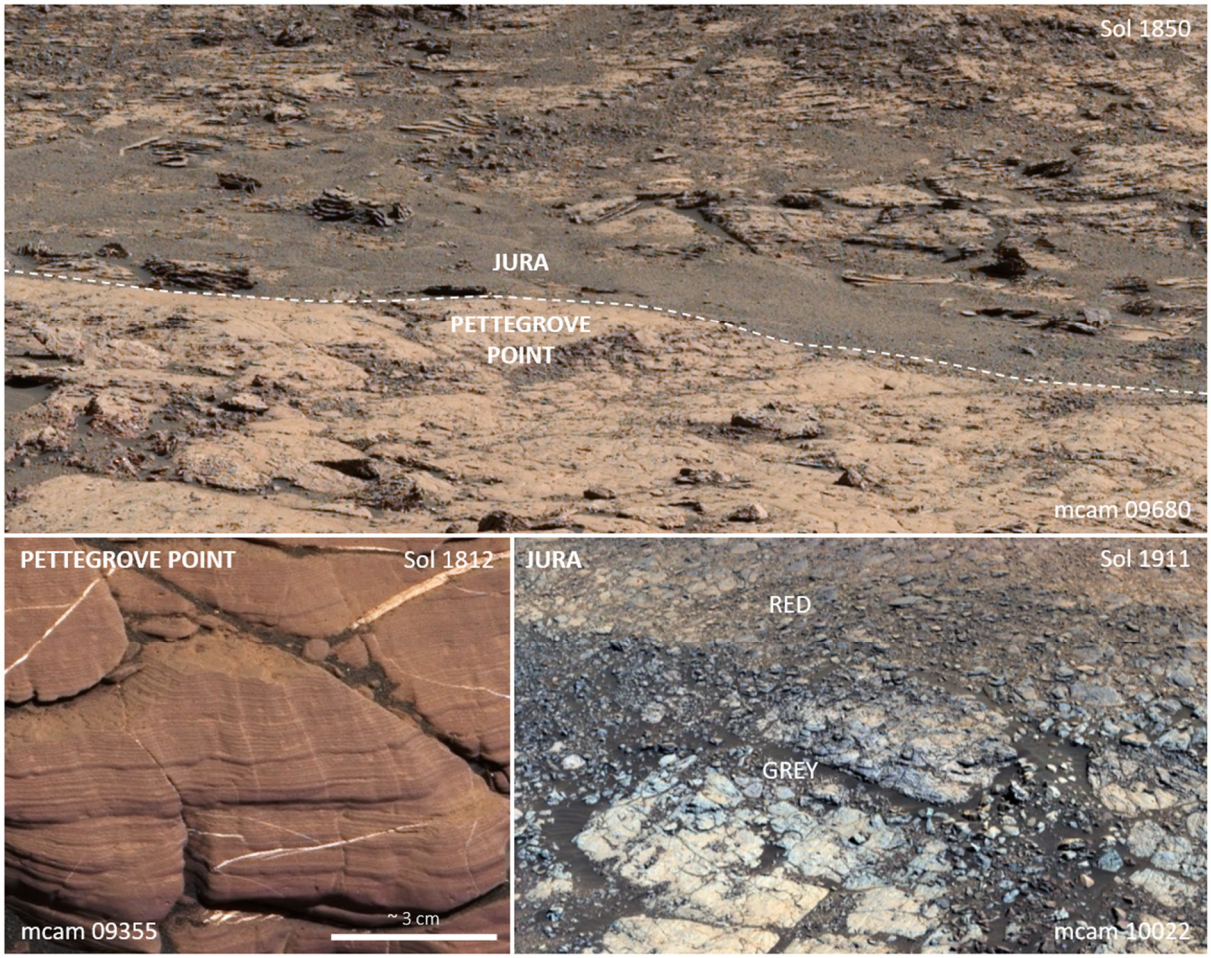

Figure 4.3: Pettegrove Point and Jura members of the VRR unit. Pettegrove Point is composed of finely laminated mudstones (lower left) while Jura consists in red blocky outcrops that transition laterally to recessive grey outcrops (lower right).

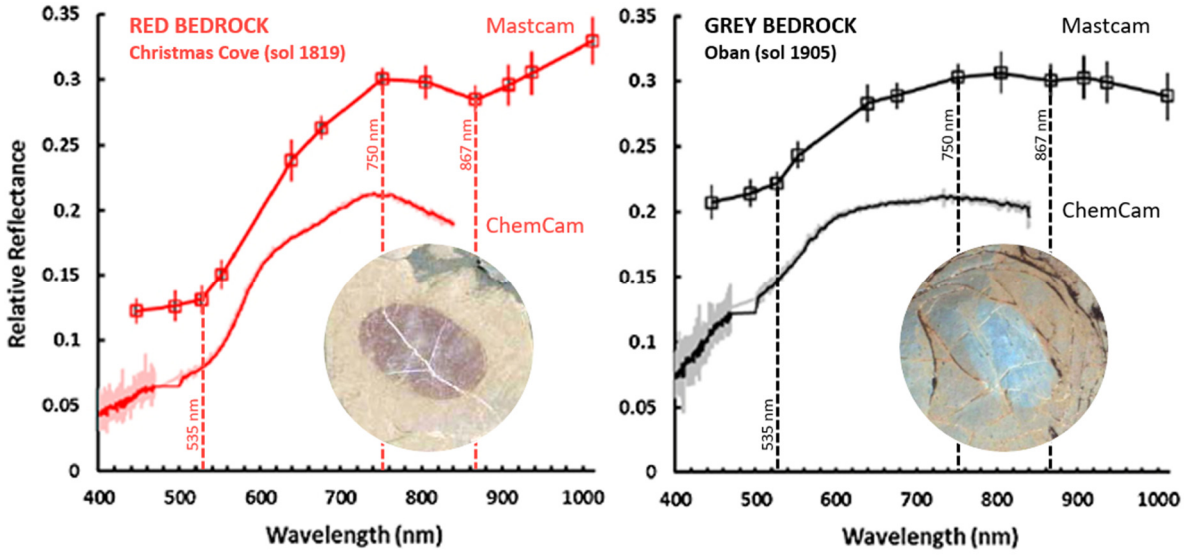

Figure 4.4: Mastcam multispectral and ChemCam passive reflectance spectra on grey and red bedrock in the Jura member. The grey bedrock (right) lack ferric absorptions features at 535 and 867 nm and peak reflectance at ~750 nm in both Mastcam and ChemCam spectra, typical of VRR red bedrock (left) and also observed in the red bedrock of the Jura member, which indicates the presence of hematite [modified from *Fraeman et al.*, 2018].

Interestingly, similar ferric absorptions were observed in the underlying Murray formation from ChemCam passive reflectance spectra, corroborated by hematite detections from the CheMin instrument (X-ray diffraction) but scarcely observed from orbit. This discrepancy between orbital and *in situ* observations is interpreted to reflect the significant contribution from dust and sand in the Murray formation, as *in situ* observations on VRR also showed that dust tends to occlude ferric absorptions in the lower VRR in CRISM spectra and Mastcam multispectral observations on un-brushed surfaces [*Fraeman et al.*, 2018].

The telltale and ubiquitous hematite signature associated with lacustrine deposits in the Murray formation and in VRR suggests that authigenic redox-driven processes were involved, notably iron oxidation where dissolve Fe^{2+} precipitates as insoluble Fe^{3+} upon encountering oxidizing conditions at a redox interface [*Fraeman et al.*, 2016]. Direct precipitation of hematite or its precursor ferric phase, from low pH fluid is not deemed likely in the Murray formation and VRR as the *Curiosity* rover did not observe evidence for other secondary phases expected to form in highly acidic environments (such as iron-bearing sulfate and sulfides) [*Fraeman et al.*, 2016], at least aside from the peculiar Pahrump Hills geological context [*Rampe et al.*, 2017]. As such, two hypotheses are proposed to account for the formation of hematite, or its precursor ferric-phase (e.g. ferrihydrite, goethite, or possibly schwertmannite) [*Hurowitz et al.*, 2010]: (1) primary deposition in an oxidizing lacustrine setting, e.g. shallower levels in a redox-stratified lake-water body subject to UV oxidation [e.g. *Hurowitz et al.*, 2017] and (2) post-depositional pervasive and relatively uniform oxidation by anoxic groundwater fluids [*Fraeman et al.*, 2016].

However, the observations of light-toned grey outcrops on the upper section of Vera Rubin Ridge, that lack ferric absorptions features in reflectance spectra, is not accounted for in either hematite formation scenarios and indicates a more complex geological history that involves changing redox and/or pH conditions. Moreover, the grey light-toned outcrops host a range of diagenetic features including nodules, fracture-fills, and crystal casts that stray from diagenetic observations in other parts of the ridge. The detailed study of the range of diagenetic items observed by the ChemCam on Vera Rubin Ridge, and notably associated with the lateral color variations observed in the Jura member, will be instrumental in understanding the post-depositional history of the VRR sedimentary rocks. In so doing, the comprehension of the diagenetic sequence of events will help provide a comprehensive geological history for the formation of Vera Rubin Ridge, which accounts for the unique topographic and mineralogical setting of the VRR sedimentary structure.

Iron mobility during diagenesis as observed by ChemCam at Gale Crater, Mars

L'Haridon J., Mangold N., Cousin A., Johnson J.R., Fraeman A.A., Rapin W., Frydenvang J., Sun V., Meslin P.-Y., David G., Gasnault O., Maurice S. and Wiens R.C. (to be submitted)
JGR: Planets, special issue on the Vera Rubin Ridge exploration campaign

HIGHLIGHTS

→ ChemCam observed diagenetic Fe-oxide features on Vera Rubin Ridge

→ Passive reflectance spectra lack ferric absorption signatures and suggest mixed-valence Fe-oxide, such as magnetite

→ Low-Fe (& Mn) bleached halos surrounding high Fe diagenetic features reveal the mobility of redox-sensitive elements during diagenesis

ABSTRACT

The *Curiosity* rover investigated a topographic structure known as Vera Rubin Ridge (VRR) that is associated with a hematite signature in orbital spectra, later confirmed *in situ* by both Mastcam multispectral and ChemCam passive spectra observations. On the ridge, *Curiosity* did not observe any significant increase in Fe abundance in the host rock from ChemCam and Alpha-Particle X-ray Spectrometer (APXS) measurements but instead discovered sporadic, dark-toned diagenetic features that display anomalously high Fe abundances commonly associated with fractures/veins also containing light-toned Ca-sulfate and with pseudomorphs after gypsum. High Fe abundances are consistent with Fe-oxide mineralogy as the enrichment in Fe is not associated with any enrichments in major (Si, Al, Ti, Mg, K, and Na) or minor (Ba, Cr, Li, Sr, Rb, and Zn) elements, nor with detections of volatiles (P, S, F and Cl). ChemCam passive reflectance spectra lack ferric absorption features (535 nm absorption band, downturn after 750 nm) which hints at relatively low Fe^{3+}-bearing mineral content such as mixed valence Fe-oxide (e.g. magnetite), or alternatively reflects the presence of coarser crystalline grey hematite. In addition, bleached halos with low-Fe content (< 10 wt.%) are observed in the host rock surrounding these features, suggesting the mobility of Fe during diagenesis. These observations are limited to specific lighter-toned grey outcrops on the upper part of the ridge that lack the telltale ferric signature of other VRR bedrock. In contrast, light-toned Ca-sulfate veins and gypsum-shaped casts are also observed on the adjacent red and ferric bedrock but do not show any association with high Fe features. Early cementation in an oxidizing environment and subsequent reducing groundwater fluid circulation could explain these lateral color variations in the bedrock, which in turn allowed for the mobility of Fe and formation of Fe-oxide in association with the late-stage diagenetic episode(s). These observations highlight the significant role played by diagenesis in the mobility and distribution of Fe (and other redox-sensitive elements) at Gale Crater and in the formation of large-scale geological structures visible from orbit.

4.1 Introduction

In 2012, the Mars Science Laboratory (MSL) *Curiosity* rover landed on the plains of a ~155 km diameter impact crater, Gale Crater, north of the 5 km high sedimentary mound (Aeolis Mound, also referred to as Mount Sharp) at its center [*Grotzinger et al.*, 2012]. After 1800 sols and ~17 km of traverse across mostly fluvio-lacustrine deposits [*Grotzinger et al.*, 2014, 2015; *Vasavada et al.*, 2014] and local remnant of draping eolian units [*Banham et al.*, 2018], the rover reached Vera Rubin Ridge (VRR), on the lower slopes of Mount Sharp (Figure 4.5). This ~6.5 km long and ~200 m wide topographic sedimentary structure trends northeast-southwest on the fringe of the phyllosilicate-bearing trough and overlying sulfate deposits [*Anderson*, 2010; *Milliken et al.*, 2010; *Fraeman et al.*, 2016]. It also displays higher thermal inertia and greater resistance to erosion compared to the adjacent terrains, from both orbital and *in situ* perspectives.

Mars Reconnaissance Orbiter (MRO) hyperspectral observations from the Compact Reconnaissance Imaging Spectrometer for Mars (CRISM) instrument revealed a significant crystalline hematite signature on the upper-most part of the ridge [*Fraeman et al.*, 2013]. The hematite-rich nature of the ridge suggests involvement of redox-driven processes (iron oxidation) in its formation [*Fraeman et al.*, 2013], either related to primary deposition at a redox interface in the lacustrine setting [e.g. *Hurowitz et al.*, 2017] or post-depositional oxidation by neutral to acidic groundwater [e.g. *Rampe et al.*, 2017]. Vera Rubin Ridge thus provides a unique opportunity to investigate redox processes on Mars, as well as a test for orbital interpretations against the ground truth, and as such constitutes a key milestone in the rover's investigation of Gale Crater's geological history and the implications for past habitability.

The VRR rocks exhibit a range of geological features that formed during diagenesis, i.e. after burial and induration of the sediments. The pervasive light-toned Ca-sulfate veins encountered in all geological units crossed by the rover traverse so far [*Nachon et al.*, 2014; *Rapin et al.*, 2016; *L'Haridon et al.*, 2018] are also abundant throughout Vera Rubin Ridge (Figure 1). Crystal molds, nodules, and concretions are also observed in close association with Ca-sulfate-filled veins. In this study, we report results from the ChemCam instrument with respect small-scale diagenetic features observed on Vera Rubin Ridge that indicates mobility of Fe during diagenesis (Figure 4.5). Furthermore, we discuss the potential implications of these findings with respect to previous observations in Gale Crater and argue for the significant role played by these diagenetic processes in the formation of Vera Rubin Ridge.

4.2 Methods

4.2.1 ChemCam instrument

ChemCam [*Maurice et al.*, 2012; *Wiens et al.*, 2012] is composed of a Laser-Induced Breakdown Spectroscopy (LIBS) system coupled with a Remote Micro-Imager (RMI; [*Le Mouélic et al.*, 2015]). The LIBS technique consists in focusing a pulsed laser on the target material (located up to 7 m from the mast of the rover), which leads to the formation of a plasma. The light emitted from the decay of its excited atoms, ions, and molecules to lower electronic states is then analyzed by three spectrometers (covering the spectral ranges of 240-342 nm, 382-469 nm, and 474-906 nm) that resolve emission peaks used for elemental analysis. ChemCam analyses consist of several closely spaced observation points, each typically composed of 30 laser shots on a given point. In this process, dust is removed from the surface of the target by the first few laser shots, thus providing the composition of the dust-free surface target material.

ChemCam provides fine-scale chemical analyses especially suited to characterizing isolated geological features such as concretions, nodules, or fracture-fills. Indeed, the ablated area covers about 300 to 600 µm in diameter, and up to a few micrometers per laser shot in depth depending on the targeted material [*Maurice et al.*, 2012], complementary to the bulk analyses of the other instruments on the rover. While ChemCam was not designed to provide information on mineralogy, mineral phases can still be inferred from ChemCam chemical compositions for geological features when their size is comparable to or larger than the laser spot size. Even at these scales, ChemCam may analyze a mixture of compositions if the LIBS point is located at the interface between distinct features. For instance, points on light-toned veins commonly show a mixing between Ca-sulfate from the veins and the surrounding host rock [*Nachon et al.*, 2014; *Rapin et al.*, 2016].

Passive reflectance spectra (without active laser use) are acquired after each ChemCam observation, recording the Martian surface radiance in the visible/near-infrared (400–840 nm) using ChemCam spectrometers. The passive reflectance data can guide interpretations on mineralogy as it provides additional information on the presence of Fe^{3+}-bearing mineral phases and crystallinity, most notably hematite [*Johnson et al.*, 2015, 2016], which is otherwise inaccessible from LIBS analyses. The angular field of view of ~0.65 mrad of the spectrometer corresponds to a 2 mm diameter area on the surface at 3 m distance from the rover (50% of ChemCam targets are within 2 to 3 m from the rover and 45% within 3-5 m [*Maurice et al.*, 2016]). It is thus wider than the LIBS ablation area.

4.2.2 Elemental composition and quantification

ChemCam is able to detect all major elements; their abundances are quantified in weight percent of oxides (SiO_2, TiO_2, Al_2O_3, FeO_T, MgO, CaO, Na_2O and K_2O) using a combination of two multivariate analytical methods – namely the "Partial Least Squares" (PLS) and "Independent Component Analysis" (ICA) methods – that result in the Multivariate Oxide Composition (MOC) dataset [*Clegg et al.*, 2017]. Expansion of the ChemCam calibration database from 66 to 408 standards and associated recalibration was completed in 2015 [*Wiens and Maurice*, 2015; *Clegg et al.*, 2017] thus refining the quantification of major elements with the ChemCam instrument. Accuracy is estimated through calculation of the root mean squared error of prediction (RMSEP) for a representative test set of standards for each major element. Since accuracy varies with elemental abundances, a sub-model approach has been developed in order to provide more accurate abundances across the distinct compositional ranges observed for each element on Mars [*Anderson et al.*, 2017; *Clegg et al.*, 2017]. The measurement precision is mainly defined by ChemCam's repeatability using point-to-point and the shot-to-shot prediction variations either on the target itself, selected homogeneous targets or the calibration targets [*Clegg et al.*, 2017, and references therein].

A number of minor and trace elements detected by ChemCam are also quantified using a univariate method, in which a single emission peak is calibrated for the abundance of that element. These include Mn [*Lanza et al.*, 2014], Sr, Li, Ba, Rb [*Payré et al.*, 2017a], Cu [*Payré et al.*, 2017b], Zn [*Lasue et al.*, 2016], B [*Gasda et al.*, 2017], and F [*Forni et al.*, 2015]. In addition, the hydration state for specific compositions can be derived from the H signal using recent calibration efforts [*Rapin et al.*, 2016]. Other volatile elements such as S, P, and Cl are so far only observed qualitatively, but are often used for chemical and mineralogical diagnostic studies [*Nachon et al.*, 2016; *Meslin et al.*, 2018], although work is currently in progress to quantify them systematically [*Meslin et al.*, 2016; *Anderson et al.*, 2017; *Clegg et al.*, 2018; *Rapin et al.*, 2018; *Thomas et al.*, 2018].

However, high-Fe compositions are still poorly represented in the current database [*Clegg et al.*, 2017], with only 2 samples showing > 40 wt.% FeO_T, leading to underestimation of FeO_T and overestimation of SiO_2 abundances in Fe-oxide dominated compositions on Mars. Recent LIBS analyses on hematite-basalt mixtures and iron meteorite samples using ChemCam EQM (Engineering Qualification Model) in simulated Martian conditions yielded improved predictions for Fe using the ICA method, especially for high-Fe compositions [*David et al.*, 2018]. Unfortunately, the incorporation of this laboratory work in the ChemCam quantification models, as well as the inclusion of relevant standards in the ChemCam calibration database, were not yet completed at the time of writing.

4.2.3 Mastcam and MAHLI cameras

The VRR outcrops were notably documented by the Mast Cameras (Mastcam) and Mars Hand Lens Imager (MAHLI). The two Mastcam cameras (34 mm and 100 mm focal lengths), located on the mast, provide contextual color images for ChemCam observations at the outcrop scale, with a 150 µm/pixel resolution at 2 m [*Malin et al.*, 2017]. MAHLI, mounted on the robotic arm of the rover, provides high-resolution (up to 14 µm/pixel at the minimum distance of 2.1 cm) color close-up images of outcrops that provide textural and structural information on fine-scale geological features, such as mineralized veins and concretions, as well as valuable mineralogical information regarding the shape, cleavage, color, fluorescence and luster of individual mineral grains [*Edgett et al.*, 2012].

4.3 Geological setting

4.3.1 Stratigraphy

The VRR structure was defined by its topographic prominence in orbital images. Following *in situ* observations, it was later divided into two members representing the lower and upper sections of the ridge [*Edgar et al.*, 2018]. The lower member, Pettegrove Point, is composed of well-cemented and finely laminated mudstones crosscut by light-toned filled-fractures. The upper member, Jura, conformably overlies Pettegrove Point and consists primarily of red blocky outcrops of displaced finely laminated mudstone. Both members also display lateral color variations in the form of grey fine-grained laminated bedrock, first noted on the flanks of Vera Rubin Ridge during the approach (Figure 4.5), and which do not appear to be stratigraphically controlled [*Edgar et al.*, 2018; *Fraeman et al.*, 2018]. The grey outcrops are more prominently observed in the Jura member, where they display less resistance to mechanical erosion compared to adjacent red blocky outcrops, forming shallow topographic depressions on top of the ridge [*Fraeman et al.*, 2018]—visible as bright patches on HiRISE orbital images—that were notably explored at the Jura and Rhynie localities (Figure 4.5).

Both member facies and texture are consistent with a deposition in a lacustrine setting [*Edgar et al.*, 2018]. The lack of clear discontinuity between VRR and the underlying fluvial and lacustrine fine-grained sandstones and mudstones of the Murray formation [*Grotzinger et al.*, 2015] suggests a continuity in the depositional environment consistent with the lack of obvious facies change. As such, VRR may be regarded as a continuation of the Murray formation, which has been observed consistently along the rover traverse since sol (Martian day) ~750 (encompassing >300 m in thickness), when *Curiosity* reached the lowest strata of Mount Sharp at Pahrump Hills [*Grotzinger et al.*, 2015; *Fedo et al.*, 2018].

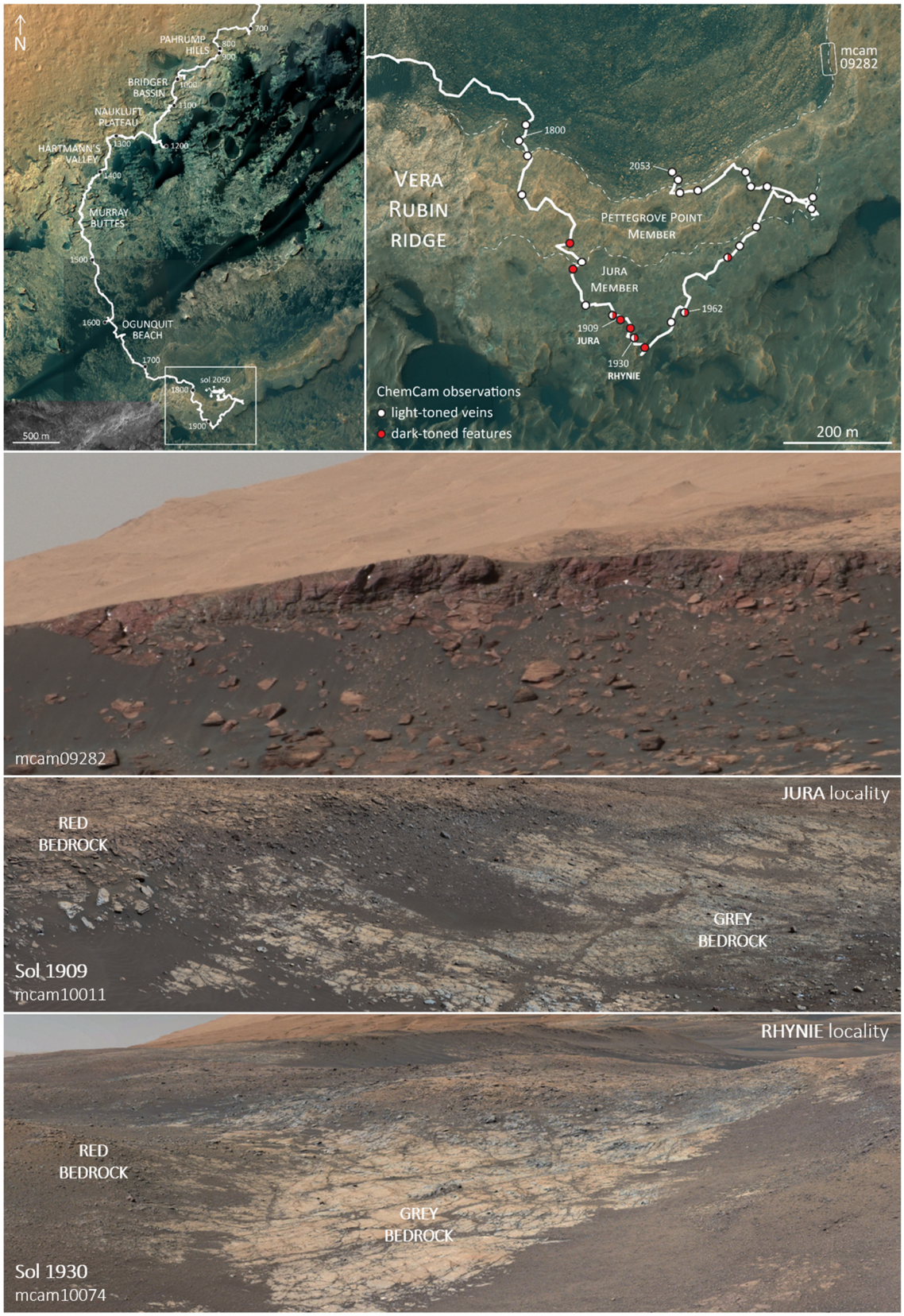

Figure 4.5: Location of Vera Rubin Ridge along the rover traverse in Gale Crater (top left), and a close-up view of the explored portion of the ridge displaying the location of ChemCam analyses of diagenetic features (top right). Mastcam mosaics illustrating the lateral red and grey color variations in the bedrock on Vera Rubin Ridge first observed during the rover approach on the north flank of the ridge (mcam09282) and later seen associated with topographic depressions, notably at the Jura (mcam10011) and Rhynie (mcam10074) localities.

4.3.2 Composition

In absence of data from the CheMin instrument due to the hardness of rocks at VRR, mineralogy is inferred only from Mastcam multispectral and ChemCam reflectance observations. *In situ* Mastcam multispectral and ChemCam passive reflectance observations on brushed VRR bedrock displayed ferric spectral features (535 nm band depth, 750 to 840 nm slope) and confirmed the presence of hematite throughout the ridge's lower and upper sections [*Fraeman et al.*, 2018], with the exception of the grey outcrops of the Jura member. Indeed, grey bedrock from the Jura member lacked such a spectral signature, which likely indicates an absence of hematite and other ferric oxides, with the possible exception of coarse grey crystalline hematite (> 5-10 µm crystals) [*Lane et al.*, 2002].

Chemical analysis from the ChemCam and Alpha-Particle X-ray Spectrometer (APXS) instruments onboard *Curiosity* report elemental bulk compositions for VRR bedrock within the compositional ranges of the Murray formation. Nevertheless, ChemCam and APXS both report chemical trends toward slightly higher Si and lower Fe and Ti in the VRR bedrock compared to the underlying Murray sedimentary rocks [*Frydenvang et al.*, 2018; *Thompson et al.*, 2018], more so in the grey outcrops of the Jura member that also show low Mn and high Fe/Mn relative to other Jura bedrock [*Thompson et al.*, 2018]. The variability in the Fe/Mn ratio, in particular, suggests the involvement of redox-driven processes and/or changes in pH in the formation of the grey outcrops of the Jura member [*Thompson et al.*, 2018]. Interestingly, these color variations appear to follow the geomorphology of VRR rather than its stratigraphy suggesting a significant diagenetic overprint on the formation of the ridge.

4.4 Results

4.4.1 Description of diagenetic features

4.4.1.1 Light-toned veins

Pervasive to all geological terrains explored so far by the *Curiosity* rover, millimeter- to centimeter scale light-toned mineralized veins are consistently observed across VRR. The Pettegrove Point member is dominated by curvi-planar light-toned veins and erosion resistant fins which transition upwards to more recessive fine veins and fracture fills in the Jura member [*Bennett et al.*, 2018]; all are clearly diagenetic as they disrupt primary sedimentary structures (i.e. sub-horizontal bedding, lamination, cross-bedding). In addition, the morphology of the fracture network exhibits no clear preference for orthogonal intersections, with light-toned fractures that often "wander" and isolate host rock fragments, which indicates that they formed via hydraulic fracturing, induced by pore-fluid pressure build-up in a compacting sedimentary basin [cf. *Caswell and Milliken*, 2017, and references therein]. The chemistry of the light-toned vein is consistent with Ca-sulfate (see section 4.4.2), in line with the previous observations on similar features along the rover traverse [*Nachon et al.*, 2014; *Rapin et al.*, 2016].

Lateral variations of vein texture and composition are observed in the Jura member. Indeed, while the thin straight fracture filling veins encountered in the red outcrops are recessive with a smooth texture and uniformly white color (Figure 4.6A), the veins encountered in the grey outcrops are more irregular, with a rugged texture and encompass dark-toned nodular inclusions that appear more resistant to the erosion compared to the adjacent host rock (Figure 4.6B, C).

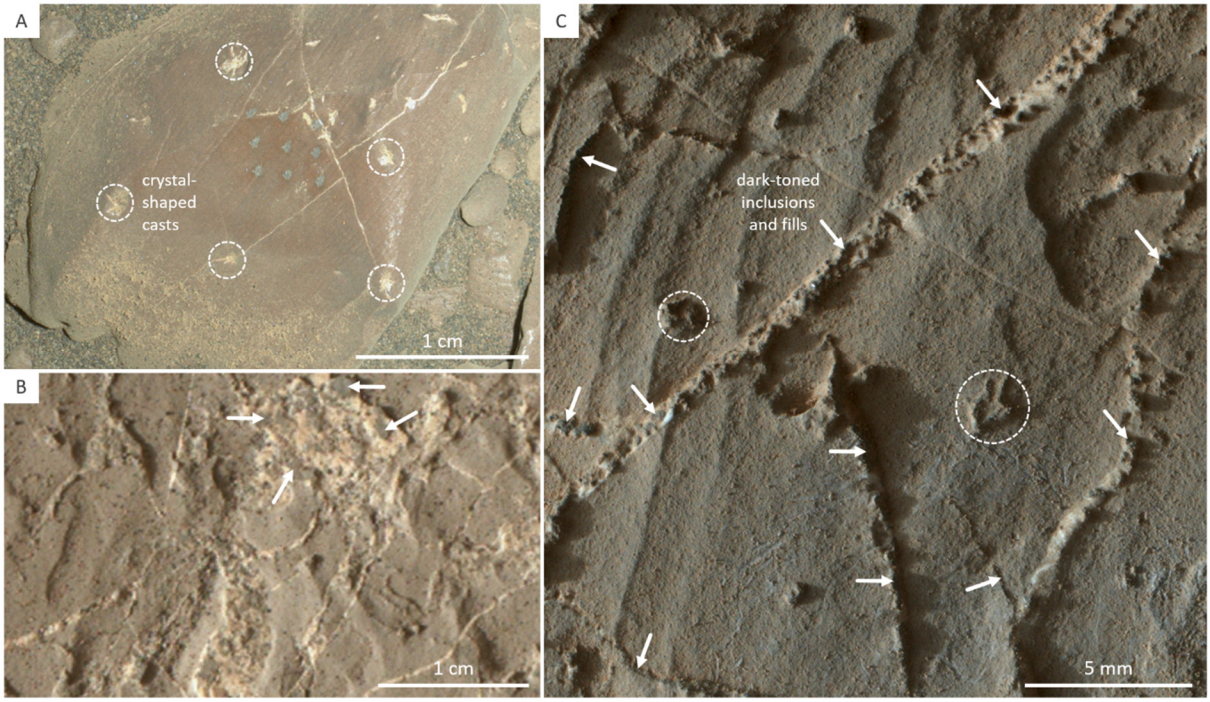

Figure 4.6: MAHLI observations on light-toned veins in the Jura member of the VRR unit. In red bedrock: (A) light-toned veins crosscutting light-toned crystals (dashed white circles) with shapes consistent with gypsum habit. In grey bedrock: (B) nodular dark-toned inclusions (white arrow) within irregular and "wandering" light-toned veins and (C) dark-toned features observed along fractures as vein fills and nodular inclusions in light-toned veins (white arrow), as well as dark-toned crystal casts. MAHLI images: 1962MH0001630000704514R00, 1982MH0001220010800006C00 and 1967MH0001630000704677R00.

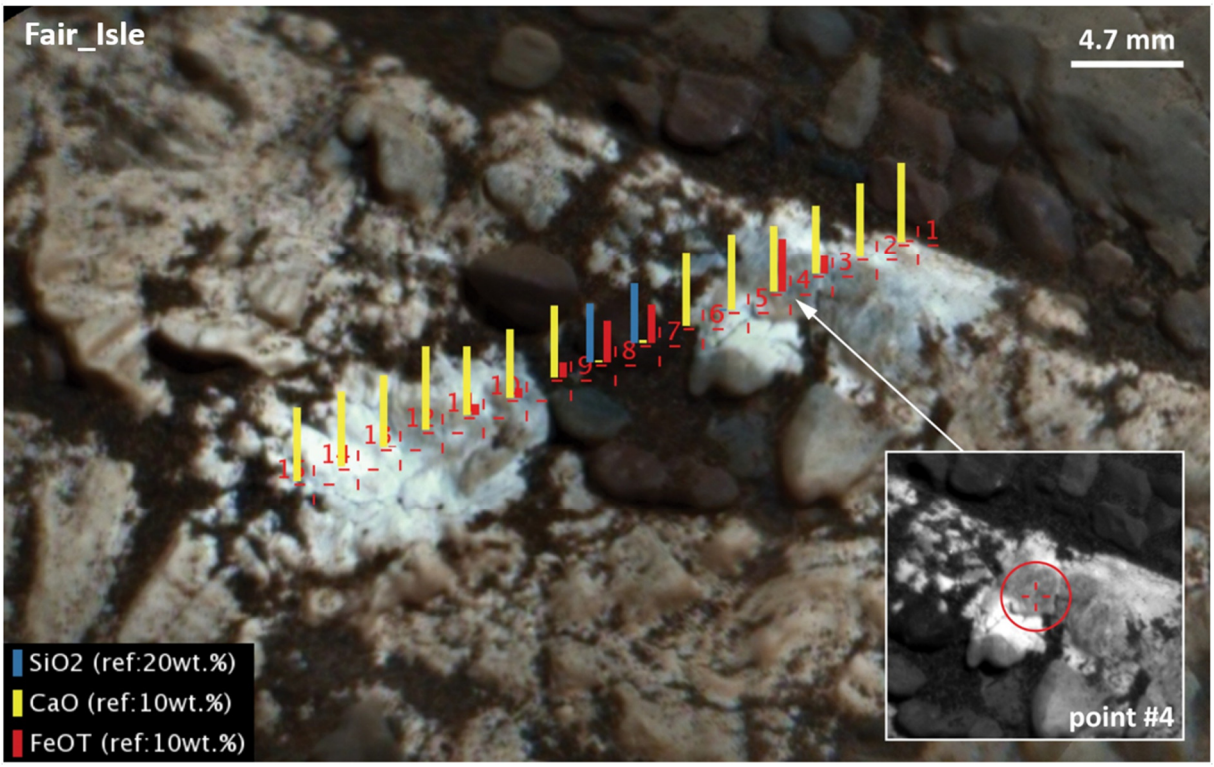

Figure 4.7: ChemCam analyses on a large light-toned Ca-sulfate vein (Fair_Isle target) show diffuse Fe-enrichment associated with a grey patch within the vein, in the grey host rocks of the Jura locality.

In addition, ChemCam observed large light-toned veins within the grey outcrops that encompass grey-toned diffuse patches with elevated Fe along with the Ca-sulfate component (Figure 4.7); reminiscent of Fe-enrichments observed within light-toned Ca-sulfate veins in the Murray formation located stratigraphically below the VRR unit [*L'Haridon et al.*, 2018].

1.1.1.1 Crystal pseudomorphs

Both red and grey Jura member outcrops host angular millimeter scale polygonal crystal-shaped casts (Figure 4.6A and Figure 4.8). While individual casts are observed and form euhedral tabular crystal shapes, they commonly coalesce into V-shaped (or "swallowtail") and star-shaped crystal aggregates (Figure 4.6A and Figure 4.8). Though crystal twinnings were not identified with absolute certainty in the VRR outcrops, the observed geometry associated with crystal casts would be consistent with the monoclinic crystal habit of gypsum [*El-Tabakh et al.*, 1997; *Paik et al.*, 2007; *Warren*, 2016].

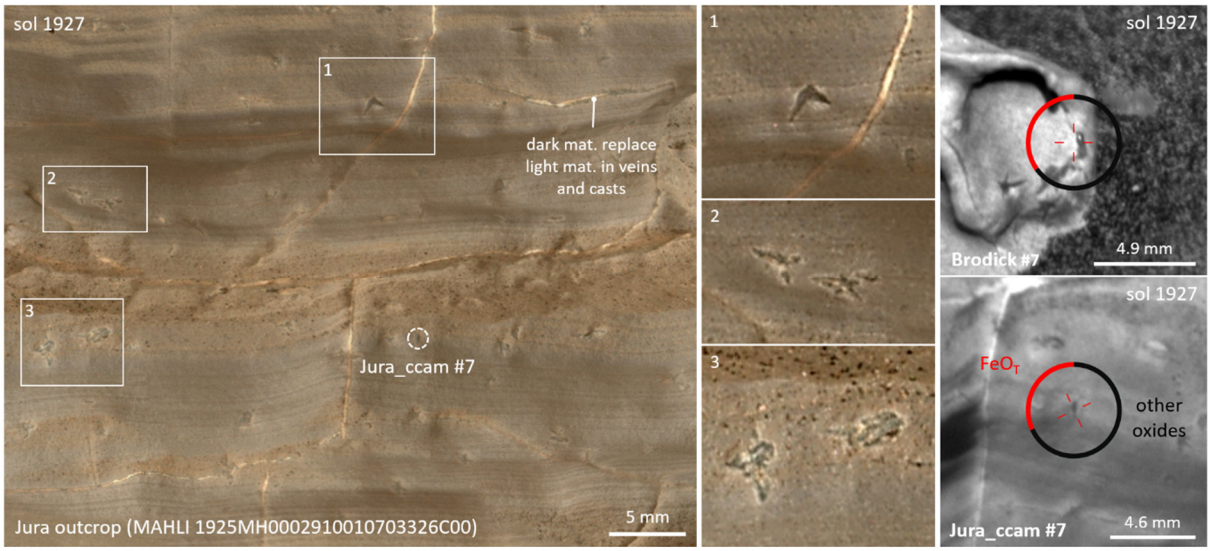

Figure 4.8: Crystal shapes and molds observed on sol 1927 ("Jura" locality, within grey outcrops) showing swallowtail-like shapes (inset "1") as well as star-shaped aggregates (insets "2" and "3") reminiscent of gypsum crystal habit. These features were sampled by ChemCam on the Brodick (point 7) and Jura_ccam (point 7) targets and show enrichment in FeO_T (31 and 29 wt.% respectively) compared to the host rock (~20 wt.%).

In the red outcrops of the Jura member, crystal casts exhibit a clear light-toned texture, strikingly similar to the adjacent light-toned veins (Figure 4.6A), suggesting a similar Ca-sulfate composition and consistent with the inferred gypsum crystal habits. Unfortunately, the light-toned crystal casts observed in the red outcrops were not sampled by the ChemCam instrument due to their tiny dimension. In contrast, the casts encountered in the grey outcrops are expressed as void spaces (crystal molds) or chiefly consist of dark-toned material with hints of residual light-toned material (Figure 4.8; residual light-toned material notably visible on inset "2"). ChemCam was more successful in targeting these features and reports an enrichment in FeO_T associated with a few observations on dark-toned crystal-shaped features (Figure 4.8). These observations suggest that dark-toned Fe-rich material substituted during diagenesis for the original light-toned mineral, inferred to be Ca-sulfate (gypsum), preserving its initial crystal shape through dissolution (formation of void crystal molds) and re-crystallization [e.g. *Lougheed*, 1983; *Paik et al.*, 2007]. Diagenetic mineral replacements (pseudomorphism) appear to be limited to the grey outcrops, as light-toned casts and aggregates in the red outcrops do not show any evidence for dissolution or mineral substitution.

The euhedral crystal casts appear to be randomly distributed in the host rocks, with no preferred orientation with respect to bedding planes (e.g. Figure 4.8). The euhedral texture suggests that crystals grew before the compaction and lithification of the sediments, as it would have then been unable to form crystal faces and would have rather filled the available porosity [*Murray*, 1964; *Bain*, 1990; *Warren*, 2016]. Additionally, at the MAHLI image resolution, the casts do not appear to disrupt primary sedimentary structures (e.g. laminations on Figure 4.6A and Figure 4.8), which would have indicated displacive mineral growth within unconsolidated sediments after burial [*Murray*, 1964; *Hardie*, 1985; *Warren*, 2016]. As such, the euhedral crystals are inferred to have formed during deposition, before the burial of the sediments. Although, the timing of formation of evaporite minerals is generally difficult to assess—even on Earth [*Hardie*, 1985]—and emplacement during diagenesis (even late) cannot be ruled from these observations alone.

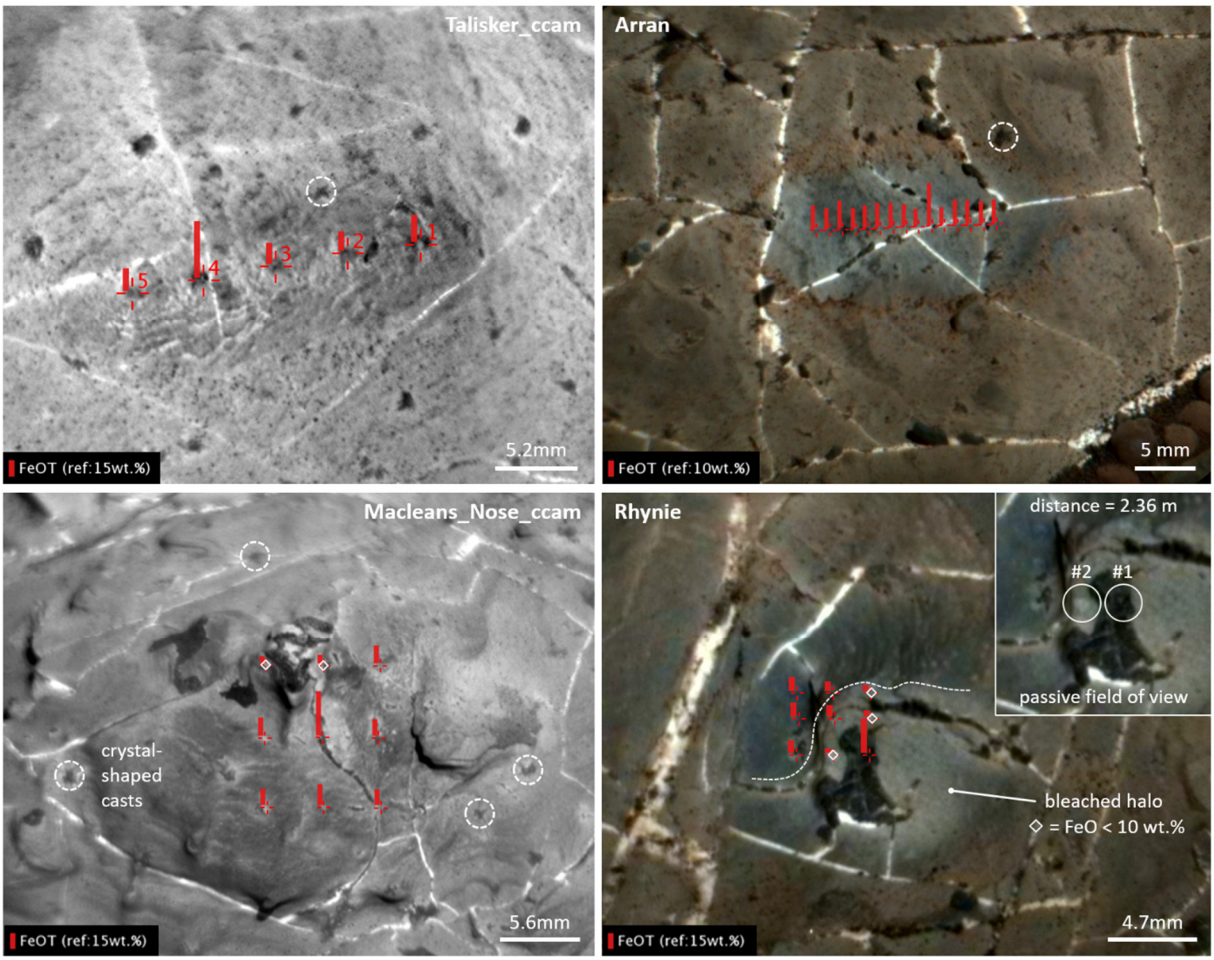

Figure 4.9: ChemCam observations of dark-toned features, encountered preferentially along light-toned Ca-sulfate veins (e.g. Arran target). Nodular dark-toned patches are also observed (e.g. Macleans_Nose_ccam & Rhynie targets), forming connected diagenetic complexes with dark-toned and light-toned veins. Dark-toned features are encountered as inclusions or partial fills in light-toned veins but are not intersected or crosscut by these veins. Dark-toned crystal-shaped casts are also observed (dashed white circles). Host rock in close proximity with the larger dark-toned features appears lighter toned (bleached halos, e.g. Rhynie target). Fe relative content for each ChemCam sample location is indicated to illustrate the association of high-Fe with dark-toned features and low-Fe with bleached light-toned halos. The field of view for passive observations is indicated on the Rhynie target, for point #1 (dark-toned Fe-rich feature) and point #2 (low-Fe bleached light-toned halo).

4.4.1.2 Dark-toned nodules and fracture fills

In addition to light-toned Ca-sulfate veins and crystal molds, the grey outcrops of the Jura member also host dark-toned nodular features (Figure 4.9) that show high Fe abundances (see section 4.4.2). These nodules are preferentially encountered along light-toned Ca-sulfate veins, as inclusions and fracture-fills (Figure 4.6 and Figure 4.9), but are also observed scattered in the adjacent host rock (e.g. Talisker_ccam target, Figure 4.9) displaying polygonal crystal shapes (see section 1.1.1.1). In addition, dark-toned fracture-fills and nodular features form interconnected complexes with light-toned Ca-sulfate veins. Indeed, fracture-fills appear to transition laterally from light-toned to dark-toned material within the same fracture (e.g. Macleans_Nose_ccam and Rhynie targets, Figure 4.9). Light-toned veins do not crosscut the dark-toned features even though both features appear to be spatially associated, which suggests that dark-toned features and light-toned veins formed simultaneously (or near so), as a late-diagenetic mineral paragenesis in the grey outcrops of the Jura member. In addition, the host rock in close proximity with some of the largest dark-toned features appears to be lighter-toned or bleached (e.g. around the nodular dark-toned patch and adjacent fracture-fills observed on the Rhynie target; Figure 4.9), suggesting chemical interactions with the host rock at the time of formation.

Lastly, *Curiosity* also observed dark-toned polygonal and elongated features that protrude from the grey outcrops in positive relief, probably along fracture planes, reflecting a higher resistance to erosion than the surrounding host rock. ChemCam probably sampled one of these erosion resistant features (Haroldswick #17; inset Figure 4.10), which also displayed elevated FeO_T, although it appeared to have been ablated during the analysis by the instrument's laser shots. Additionally, morphological similarities with neighboring dark-toned features (notably elongated and polygonal fracture-fills) and potential matches with adjacent polygonal molds observed along fractures (e.g. Islay ChemCam target, Figure 4.10), suggests a genetic link between these features.

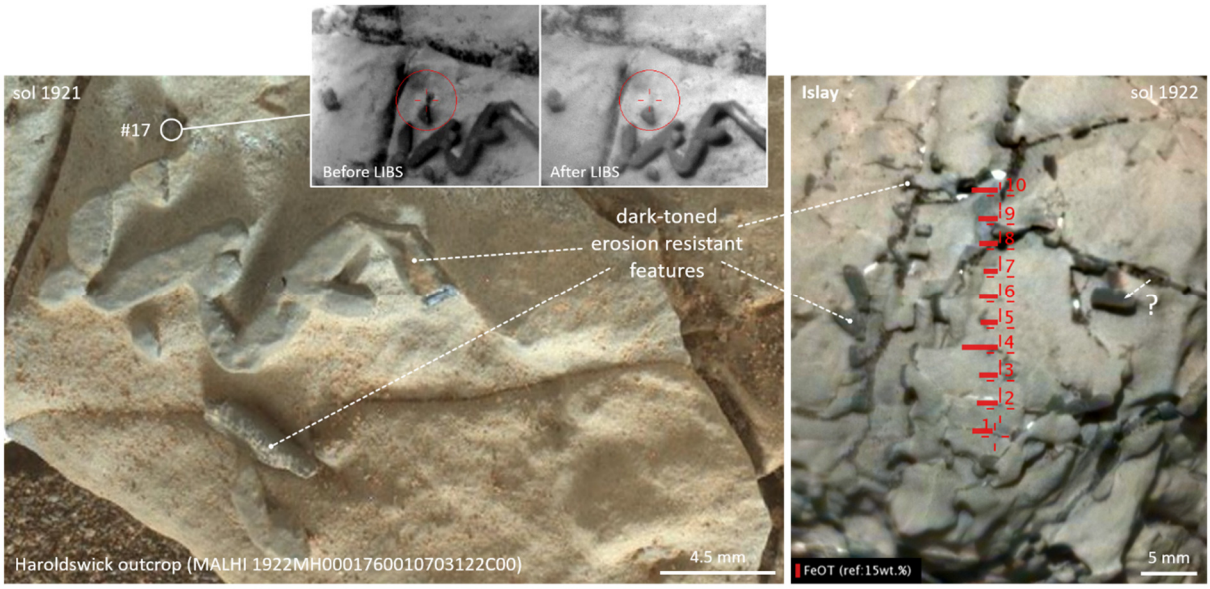

Figure 4.10: Polygonal and elongated erosion resistant dark-toned features ("stick-shaped") observed at the "Jura" locality within grey outcrops, which show morphological similarities with high-Fe dark-toned features (notably fracture-fills) and potentially associated with polygonal molds observed along fractures (e.g. Islay target). ChemCam may have sampled one dark-toned erosion resistant feature (inset; Haroldswick point #17), which showed elevated Fe abundances (~30 wt.%) but was ablated by the ChemCam laser shots.

4.4.2 ChemCam compositional observations

4.4.2.1 Chemistry (major and minor elements)

Chemical compositions of the ChemCam observations are reported in ternary diagrams in Figure 4.11 (in molar proportion, based on quantified oxide weight percent reported by ChemCam), illustrating the chemical trends between Fe and Si with respect to Al, Mg and Ca (Figure 4.11A-C) and between Fe, Si+Al and Mg+Na+K (Figure 4.11D). ChemCam data used in this study covers the sols 1809 to 2045 and includes 231 host rock targets (1903 observation points), 38 light-toned veins (92 points), 43 dark-toned features (80 points), 23 bleached host rock targets (50 points), and 5 iron-nickel meteorites (36 points) for reference in terms of high-iron abundances.

The dark-toned features, including dark-toned material within crystal-shaped features, show a composition dominated by an enrichment in Fe and corresponding decreases in other major elements (notably Si, Al, Mg, K, and Na) compared to the host rock compositions (Figure 4.9 and Figure 4.11). High-Fe observations are not associated with the detection of volatile elements (S, Cl, P, F or C), ruling out any Fe-sulfates or Fe-phosphates [c.f. *Nachon et al.*, 2016; *Meslin et al.*, 2018]. The H emission line is also low, thus pointing toward poorly hydrated Fe-oxide minerals (Figure 4.12).

Even though ChemCam quantifications are skewed for high-Fe compositions (see section 4.2.2), the highest Fe abundances reported by ChemCam on dark-toned diagenetic features fall within the range of composition of several iron-nickel meteorites sampled by ChemCam in Gale Crater [*Meslin et al.*, 2017; *Wellington et al.*, 2018]. As mentioned previously, ChemCam tends to underestimate Fe and overestimate Si abundances for high-Fe compositions, and the iron-nickel meteorite observations exhibit a similar behavior. Furthermore, ICA analyses based on laboratory spectra of hematite-basalt mixtures and terrestrial iron-nickel meteorite samples—acquired using a replica of ChemCam—reported up to ~90 wt.% equivalent FeO_T in Gale Crater meteorites and in some of the dark-toned diagenetic features (e.g. Rhynie target, point #1) [*David et al.*, 2018]. The composition of these diagenetic features thus trends toward an almost pure Fe-oxide end-member composition (Figure 4.11).

The spread observed toward elevated Ca in some of these features (Figure 4.11A) is attributed to the sampling of both dark-toned features and light-toned veins on the same ChemCam observation point, due to their close spatial association. Indeed, light-toned veins show a composition consistent with an almost pure Ca-sulfate chemistry (Figure 4.11A), with high Ca content associated with lower sum of oxides and S detection [*Nachon et al.*, 2014]; interpreted as bassanite ($CaSO_4$ x 0.5 H_2O) based on H content detected by ChemCam [*Rapin et al.*, 2016]. In addition, some large veins also display high Fe content associated with Ca-sulfate (see section 4.4.1.1 and Figure 4.7).

The lighter-toned bleached halos observed in the host rock surrounding several high-Fe dark-toned features (50 observations, e.g. Rhynie target, Figure 4.9) show depleted Fe content compared to other VRR host rock observations (commonly < 10 wt.% compared to 18-20 wt.% typical observed in the host rock, Figure 4.9 and 4.11). Interestingly, lower Fe abundances are not correlated with depletion in any other major elements, which preserve the same relative abundances (Figure 4.11B-D). As such, these observations suggest preferential leaching of Fe in these bleached halos compared to local host rock chemistry. Moreover, Fe-rich and low-Fe observations in dark-toned features and bleached halos neatly plot along a mixing-line between Fe-oxide and "Fe-free" host rock compositions, suggesting that Fe was mobilized from the host rock to form the Fe-oxide dark-toned features during diagenesis.

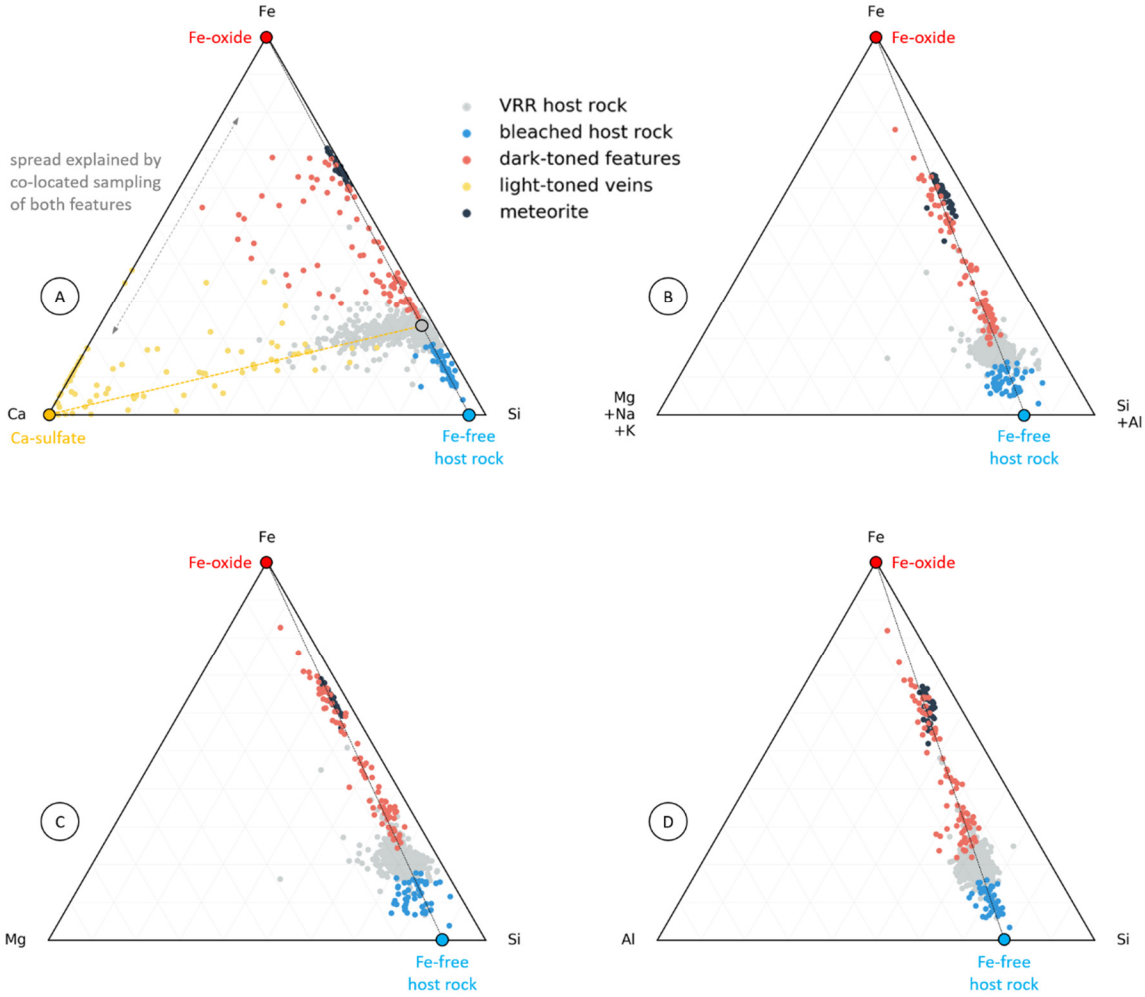

Figure 4.11: Ternary diagrams showing ChemCam quantified abundances (molar percentages) for major elements: dark-toned features (in red) are associated with very high Fe content, trending toward a pure Fe composition (in line with ChemCam observations of iron-nickel meteorites on Mars), coupled with low-Fe observations on bleached light-toned halos. Diagram (A) shows a spread toward Ca for dark-toned features due to the contribution of Ca-sulfate from adjacent light-toned veins, and sampling at the interface between both features. Diagrams (B), (C) and (D) show that the low-Fe content in bleached host rock targets is not associated with a loss in any other major elements and as such show mobilization of Fe from the host rock.

Minor element abundances reported by ChemCam show mostly depleted contents in dark-toned Fe-rich features for Ba, Rb, Sr and Li compared to host rock values (from the grey outcrops of the Jura member) whereas low-Fe bleached halo abundances for the same elements are within range of host rock values, except for a slight enrichment in Ba and Sr (Figure 4.12). In contrast, the MnO abundance appears to be elevated in dark-toned features compared to host rock values, but appear depleted in low-Fe bleached halos (Figure 4.12). In essence, Fe and Mn appear to exhibit similar behavior during diagenesis, which hints at the involvement of redox-driven chemical processes in the formation of these features. Alternatively, pH variations could also produce similar trends in both Fe and Mn, but would also affect elements that are not as redox-sensitive (e.g. [*Rampe et al.*, 2017; *Yen et al.*, 2017]), which is not observed here. In addition, the lack of discrepancies in abundance for highly soluble Li in bleached halos compared to the adjacent host rock suggests limited water-rock interactions and dissolution in the formation of the bleached zones.

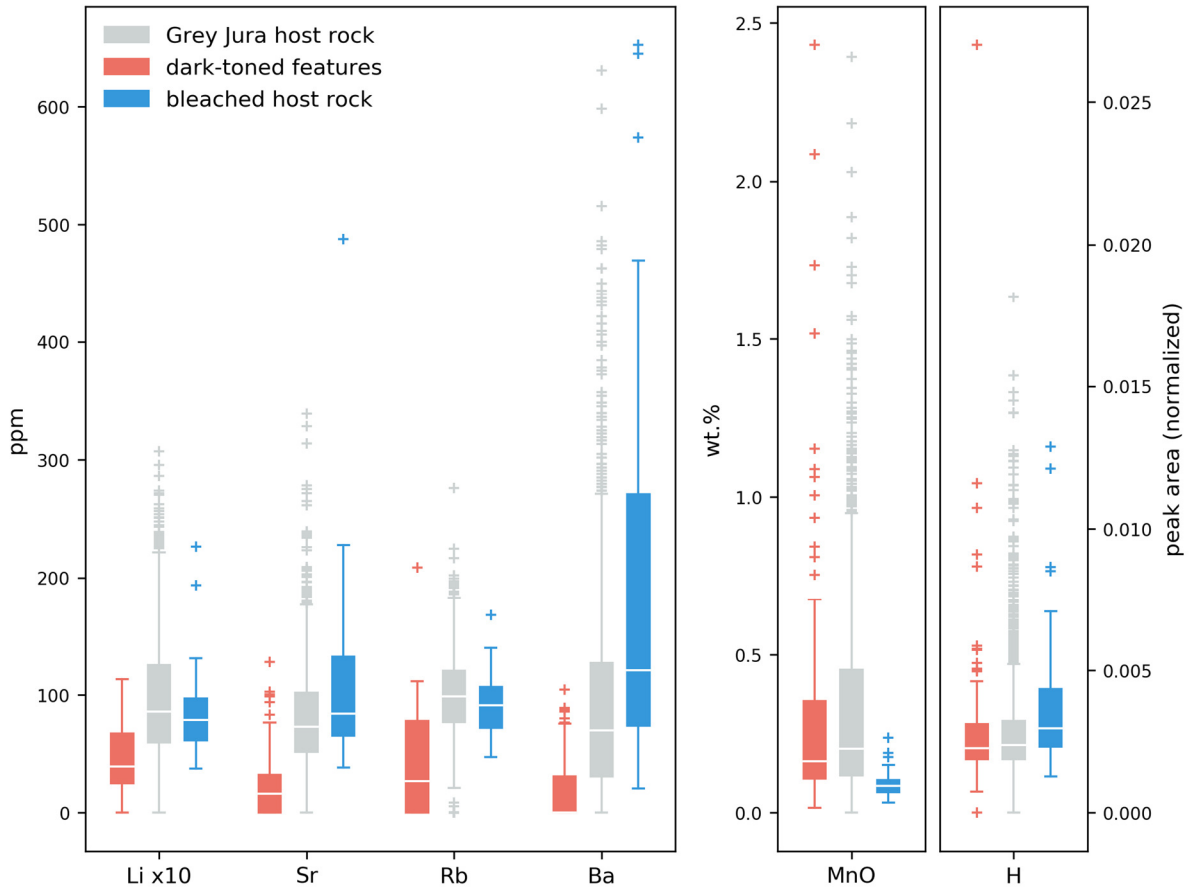

Figure 4.12: Box plots representing quantified abundances for Li, Rb, Sr, Ba, and MnO, as well as H normalized peak area [c.f. *Rapin et al.*, 2017], in dark-toned Fe-rich features (red), grey host rock of the Jura member (grey), and low-Fe bleached host (blue). Abundances in Ba, Rb, Sr, and Li for bleached low-Fe targets are in range with typical host rock values (although somewhat enriched in Ba and Sr) but are depleted in dark-toned Fe-rich features. However, MnO content in dark-toned Fe-rich features is in line with host rock values and appears depleted in low-Fe bleached targets. H appears to be in line with the low host rock values in dark-toned Fe-rich features but slightly enriched in low-Fe bleached targets.

4.4.2.2 Passive spectra observations

ChemCam passive spectral analyses on the distinct rocks of the ridge reveal variability in the strength of the spectral features diagnostic of ferric iron (i.e. absorptions near 535 and 670 nm and a downturn after ~750 nm). Most of the VRR host rocks show a ferric signature in passive reflectance spectra, including the red outcrops of the Jura member (e.g. Holyrood target, Figure 4.13), consistent with the presence of hematite [*Fraeman et al.*, 2013; *Johnson et al.*, 2017]. In contrast, the passive spectra observed in the grey outcrops are much flatter in the 600-800 nm spectral region, which is attributed to a relative lack of Fe^{3+} bearing minerals (e.g. Oban and Ben Loyal targets, Figure 4.13) [*Fraeman et al.*, 2018]. These observations indicate that the lateral color variations observed in the Jura member are associated with a mineral change in the Fe-oxide component of these rocks; hematite ($Fe^{3+}_2O_3$) in the red outcrops is giving way to less spectrally ferric mineral phases in the grey patches. Low-Fe bleached halos do not show any spectral evidence for the presence of ferric iron, in line with the observations on the adjacent grey host rocks (e.g. Rhynie target, point 2; Figure 4.13).

Similarly, the relatively flat passive reflectance spectra (i.e. lacking ferric absorption features) associated with dark-toned Fe-oxide features (e.g. Laphroaig and Rhynie, point 1, targets, Figure 4.13) suggests the presence of mixed-valence Fe-oxide (magnetite) instead of hematite or other hydrated ferric oxides. Nevertheless, the presence of magnetite is expected to decrease the albedo in these features, which is not observed (Figure 4.13) even for relatively large dark-toned concretions (e.g. Rhynie, point 1). In some cases, the larger field of view of the passive spectra (e.g. Figure 4.9; inset) may overlap lighter-toned material as well. However, this should not affect the outcome, as the lighter-toned host rock material is not expected to contribute significantly to the passive reflectance spectra. Alternatively, coarse-grained grey (crystalline) hematite could be consistent with these passive spectral observations (c.f. USGS reference spectra, Figure 4.13) as grain size, contaminants and crystallinity can also impact these spectral ferric features [*Morris et al.*, 1985; *Lane et al.*, 2002; *Johnson et al.*, 2015].

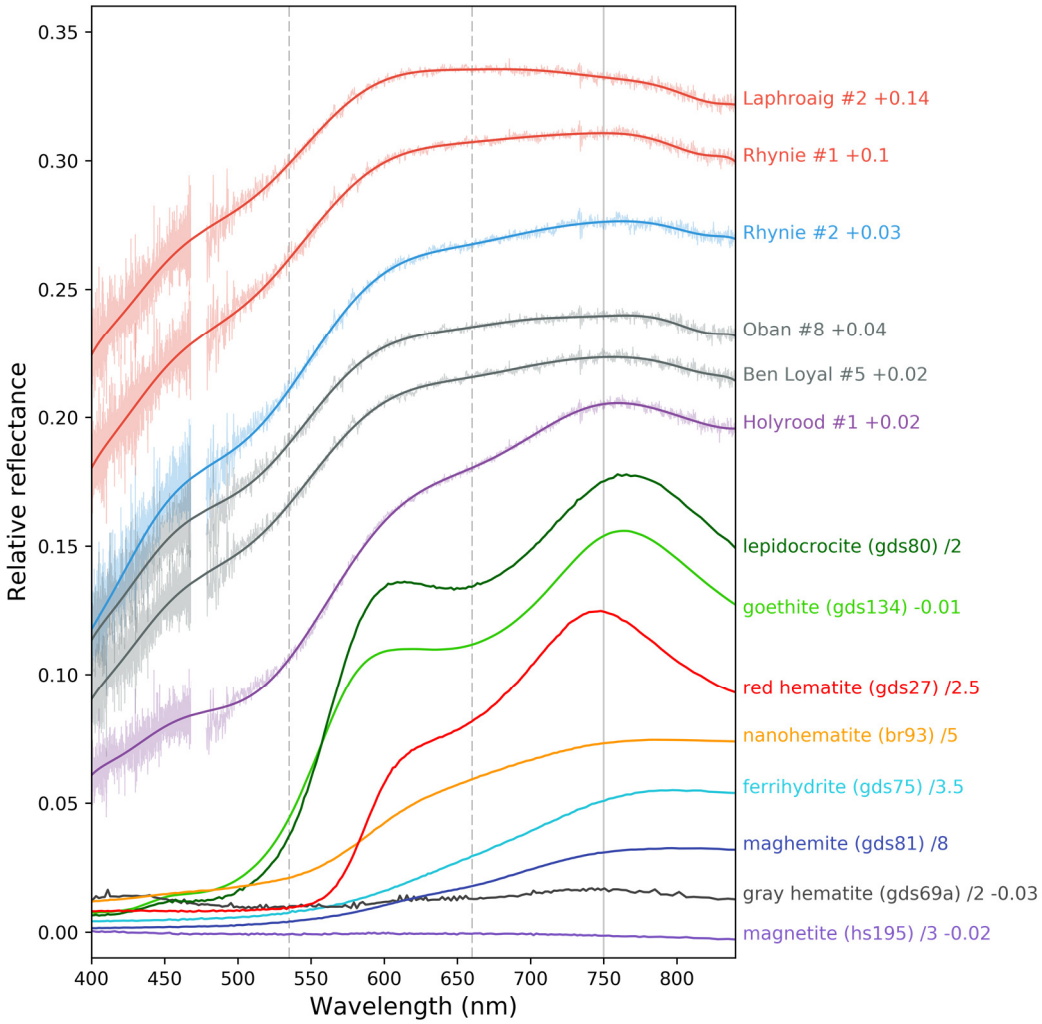

Figure 4.13: Passive reflectance spectra for high-Fe dark-toned features (in red), low-Fe bleaching halo (in blue), as well as grey (in grey) and red (in purple) host rock targets. The solid line overprinted on spectral data corresponds to a 15th order polynomial fit, shown here for clarity. High-Fe dark-toned features, low-Fe bleached halos, and grey host rocks lack adsorption bands near 535 nm and 670 nm (dashed grey lines) and a downturn after 750 nm (solid grey line) consistent with Fe^{3+} phases observed on red host rocks. Library spectra from the USGS database for hematite [α-Fe_2O_3] (red, grey and nanophase), maghemite [γ-Fe_2O_3], magnetite [$Fe^{2+}Fe^{3+}{}_2O_4$], ferrihydrite [$Fe^{3+}{}_2O_3 \times 0.5H_2O$], goethite [$\alpha$-FeO(OH)] and lepidocrocite [γ-FeO(OH)] are provided for comparison. Scaling and offsets are indicated for each spectrum.

	Feature	Description (section 4.4.1)	Chemistry (section 4.4.2.1)
RED OUTCROPS	Light-toned veins	– straight and thin morphology – smooth texture, uniform white color – crosscut primary sedimentary structures and crystal-shaped casts	high Ca and S, variable Sr H consistent with bassanite
	Crystal-shaped casts	– euhedral and tabular crystal shapes – form V-shaped and star-shaped aggregates – uniform white color (similar to light-toned veins) – do not deform primary sedimentary structures	(no data, inferred to be similar to light-toned veins)
GREY OUCROPS	Light-toned veins	– irregular morphology – rugged texture and encompass dark-toned inclusions and diffuse grey patches – partially replacement of light-toned material by dark-toned material within fractures – crosscut primary structures, but not dark-toned features or dark-toned pseudomorphs	high Ca and S, variable Sr H consistent with bassanite high Fe for dark-toned inclusions, partial fills and grey patches
	Crystal-shaped casts	– euhedral and tabular crystal shapes, commonly – form V-shaped and star-shaped aggregates – occasionally observed as crystal molds – substitution of precursor light-toned material by dark-toned material through dissolution recrystallization (pseudomorphism) – do not deform primary sedimentary structures	elevated Fe compared to host rock, associated with dark-toned material
	Dark-toned features, fracture-fills, and erosion-resistant casts	– nodular features observed in association with light-toned veins (inclusions and fracture-fills) – polygonal and elongated casts resistant to mechanical erosion, similar to dark-toned fracture-fills and possibly match adjacent polygonal molds along fractures	very high Fe, low H slightly elevated Mn depleted in other elements lack ferric absorption bands
	Bleached halos	– lighter-toned halos in the host rock – observed around the larger dark-toned nodular features and facture-fills	low Fe and low Mn other elements in line w/ host rock lack ferric absorption bands

Table 4.1: Summary of diagenetic observations in the Jura member of Vera Rubin Ridge

4.5 Discussion

4.5.1 Diagenetic history of Vera Rubin Ridge

The VRR sedimentary rocks, deposited in a lacustrine environment, record a complex post-depositional geological history, as evidenced in part by the variety of small-scale diagenetic features observed on the ridge (Table 4.1). Crosscutting relationships between the observed diagenetic features, and how they affect the primary sedimentary structures, provide insights into the relative timings of formation (Figure 4.14).

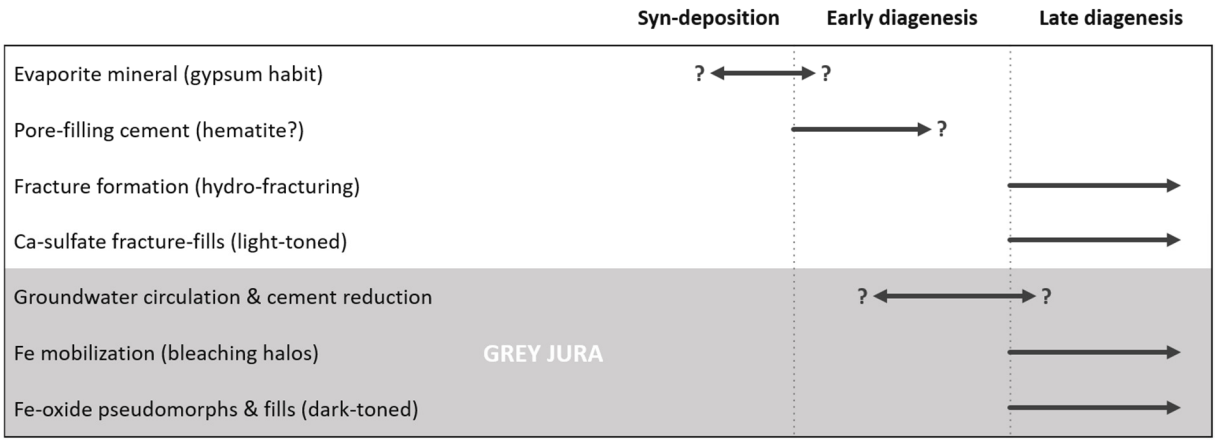

Figure 4.14: Paragenetic sequence of the events that occurred during the diagenesis of Vera Rubin Ridge.

Euhedral crystal-shaped casts, interpreted as gypsum based on the observed crystal habits and textural similarities with adjacent Ca-sulfate light-toned veins, are probably syn-depositional. Although, the timing of their formation remains ambiguous, and it could potentially have occurred during the early stages of diagenesis. In essence, the crystals formed before significant burial, cementation and lithification of the sediments occurred, which would have precluded the growth of euhedral crystal shapes [*Warren*, 2016].

Most of the VRR rocks show a significant resistance to erosion, as well as rock hardness, and are associated with a consistent ferric signature in Mastcam multi-spectral analyses and ChemCam passive reflectance spectra [*Fraeman et al.*, 2018]. These observations suggest cementation of the sediments in oxidizing conditions, with the formation of hematite as fined-grained pore-filling cement that resulted in the lithification and hardening of the sedimentary rocks. The preservation of the gypsum crystals in the red outcrops of the Jura member indicates that cementation probably occurred in interstitial pore-water early in the diagenesis, and as such reflects near-surface oxidizing conditions, and did not involve groundwater fluid circulation which would have likely resulted in the dissolution of the evaporite minerals [*Murray*, 1964; *Warren*, 2016].

Lateral variations in outcrop color observed on the Jura member (Figure 4.5), from red to grey, are attributed to a change in the ferric component of these rocks. Indeed, the grey rocks encountered in shallow depressions on top of the ridge are associated with a relative lack of hematite (or Fe^{3+} bearing minerals), based on ChemCam passive reflectance and Mastcam multispectral observations. The lateral color variations in outcrops do not appear to be consistent with variations in the depositional lacustrine environment [e.g. redox stratification, *Hurowitz et al.*, 2017] and are thus inferred to be diagenetic in origin. In addition, the observation of crystal molds and mineral substitution in the grey outcrops by Fe-oxides indicates (c.f. section 1.1.1.1, Figure 4.8) dissolution of the early evaporite minerals and formation of Fe-oxide pseudomorphs. These observations are consistent with mobilization and chemical reduction of ferric phases (likely present as cement in the surrounding rocks) by reducing or anoxic groundwater flow(s) (see section 4.5.2). Furthermore, the groundwaters ability to propagate through the sediments (or sedimentary rocks) depends on its permeability, so it probably occurred before the compaction and lithification of the sediment reduce drastically its connected porosity (i.e. before late diagenesis). Besides, reducing or anoxic groundwater circulation could also be concomitant with hematite cementation in the VRR, altering the oxidizing pore-fluid chemistry to form more reduced Fe-bearing phases as cement instead.

Light-toned Ca-sulfate veins are also observed in the VRR outcrops and are interpreted as late-diagenetic products that formed through hydraulic-fracturing (see section 4.4.1.1), in line with previous observations along the rover traverse. However, the diversity of textures and morphologies observed in these features [*Bennett et al.*, 2018] could indicate multiple successive episodes of fracturing and mineralization [*Caswell and Milliken*, 2017], or distinct interactions with the enclosing host rocks.

Lastly, dark-toned Fe-rich features are encountered within the grey outcrops. These features are often associated with light-toned Ca-sulfate veins, as either nodular inclusions or vein-fills, and appear to be contemporary with the formation of fractures and Ca-sulfate mineralization. Low-Fe bleached halos are also observed in association with the larger Fe-rich nodules in the surrounding host rock, which suggests mobilization of Fe at the time of formation of these features. In addition, Fe-rich diagenetic observations that do not appear to be directly associated with light-toned Ca-sulfate veins are—for the most part—associated with gypsum crystal shapes and interpreted as substitution pseudomorphs. The dark-toned pseudomorphs are not crosscut by light-toned veins either (e.g. Figure 4.8), which indicates that pseudomorphism likely occurred during, or after, emplacement of light-toned veins. Since the dissolution of such crystal-shaped casts appears to be related to the formation of grey outcrops, the relative timing between fracture formation and the reduction of the rocks in the grey outcrops by groundwater flows is ambiguous.

4.5.2 Potential chemical processes involved during diagenesis

The diagenetic color variations associated with varying redox conditions, evaporite crystal molds and Fe-oxide nodular features observed on Vera Rubin Ridge bear similarities with outcrops of the Burns sedimentary formation, explored by the *Opportunity* rover at Meridiani Planum, on Mars. While it consists of evaporitic sandstones formed in transient eolian and shallow water conditions [*Squyres*, 2004; *Grotzinger et al.*, 2005], the Burns formation outcrops appear to have experienced an extended history of diagenetic alteration consistent with burial and periodic groundwater interaction(s) [*McLennan et al.*, 2005]. There, syn-depositional and early-diagenetic intrasedimentary evaporite crystal molds are observed, followed by at least two distinct episodes of cementation associated with interstitial pore-water and groundwater recharge(s) as well as the formation of hematite “blueberry” concretions [*McLennan et al.*, 2005; *Squyres and Knoll*, 2005].

Earth analog studies have been conducted in order to provide insights into the diagenetic processes that occurred at Meridiani Planum, especially regarding the formation of hematite concretions. Among them, the extensive study of the Jurassic Navajo Sandstones [*Chan et al.*, 2000, 2004, 2005, 2007; *Ormö et al.*, 2004; *Beitler et al.*, 2005; *Parry et al.*, 2009] is particularly relevant to Vera Rubin Ridge. Indeed, outcrops there exhibit dramatic lateral color variations associated with syn-sedimentary to early-diagenetic red hematite formation in oxidizing conditions and subsequent diagenetic alteration by reducing fluid, bleaching the outcrops white-grey at millimeter to regional scales [*Chan et al.*, 2004, 2005; *Parry et al.*, 2009]. Fe is either leached at that stage, incorporated into diagenetic fluids as Fe^{2+} and later forming hematite concretions upon encountering oxidizing groundwater [*Chan et al.*, 2005], or immediately fixed in ferroan dolomite, pyrite and large crystallites of grey hematite [*Parry et al.*, 2009]. Similar processes would also be consistent with lateral color variations observed on top of Vera Rubin Ridge, with early-cementation of hematite (early-diagenesis) in oxidizing conditions and subsequent bleaching by reducing fluids leading to the formation of probably less ferric Fe-oxide.

However, the diagenetic Fe-oxide nodules observed at Vera Rubin Ridge display very distinct morphologies compared to the well-rounded cemented "blueberry" concretions observed at Meridiani, and as such likely originated from different diagenetic processes. In addition, the sedimentary rocks of the Burns formation at Meridiani Planum incorporate a significant sulfate component (up to 40 wt.%), including Fe-sulfates such as Jarosite and Melanterite [*Squyres*, 2004; *Grotzinger et al.*, 2005], which favor mobility of Fe during diagenesis through dissolution of precursor Fe-sulfate minerals [*McLennan et al.*, 2005; *Tosca and McLennan*, 2006]. At VRR, Fe-oxide diagenetic features appear to be systematically associated with Ca-sulfate, either as nodular inclusions, diffuse patches, and partial fills in Ca-sulfate-filled fractures or as mineral replacements in gypsum-shaped crystal casts. Thus, the formation of the diagenetic Fe-oxide features likely results from chemical interactions and dissolution/recrystallization processes at the interface between Ca-sulfate features and the adjacent reduced grey outcrops minerals, while concretions at Meridiani Planum were pervasive through the whole rock.

The mobility of Fe in grey outcrops, as dissolved Fe^{2+} species, are probably linked with the reduction of ferric mineral phases by groundwater fluids. Indeed, Fe would have been either directly mobilized during groundwater flows or later by the hydro-fracturing fluids that emplaced Ca-sulfate veins, destabilizing the Fe-bearing phases (possibly reduced) in the grey outcrops but not the less soluble ferric phases (likely hematite) in the red outcrops. In both case, mobilized Fe would have then precipitated at the interface with light-toned Ca-sulfate veins and crystal-shaped casts as grey crystalline hematite or magnetite (see section 4.4). As such, Fe-oxides gradually replace Ca-sulfates by dissolution/recrystallization and form nodular inclusions and fills in veins, as well as pseudomorphs in gypsum-shaped crystal casts [e.g. *Lougheed*, 1983; *Warren*, 2016].

Formation of low-Fe halos in the adjacent host rock would thus represent the mobility of Fe from the host rock toward the interface with Ca-sulfate, following chemical potential gradients [e.g. similar to water/sediment interface, *Santschi et al.*, 1990]. Formation of Fe-oxide could indicate a shift to higher pH and/or more oxidizing conditions upon interaction with Ca-sulfate. Moreover, Ca and S species were probably leached in solution as no enrichments in Ca or S are observed in the adjacent host rock (c.f. section 4.4.2.1). In the absence of interface with Ca-sulfate to drive such chemical processes, Fe likely recrystallized *in situ*, in the form of Fe-bearing phases lacking ferric spectral features [*Fraeman et al.*, 2018]. Similar processes could also explain the behavior of Mn during diagenesis, which is also sensitive to redox-driven reactions [*Santschi et al.*, 1990], as it appears to be slightly enriched in Fe-oxide diagenetic features and depleted in low-Fe bleached halos compared to grey host rocks (c.f. section 4.4.2.1).

In summary, the formation of the Vera Rubin Ridge sedimentary deposits involved: (1) sedimentation in a lacustrine setting; (2a) emplacement of gypsum euhedral crystals, inferred to have occurred during deposition and (2b) cementation in oxidizing conditions during early-diagenesis, probably resulting in the formation of an hematitic pore-filling cement throughout the structure; (3a) formation of the red/grey color patterns within the outcrops of the ridge, potentially by reducing and/or anoxic groundwater flows before lithification of the sediments (and loss of permeability) and (3b) substitution pseudomorphism of gypsum crystals by Fe-oxide in the grey outcrops; (4a) late-diagenesis hydro-fracturing and formation of Ca-sulfate veins, associated in the grey outcrops with the mobilization of Fe from the adjacent host rock to form of Fe-oxide as nodular inclusions and vein-fills (Figure 4.15).

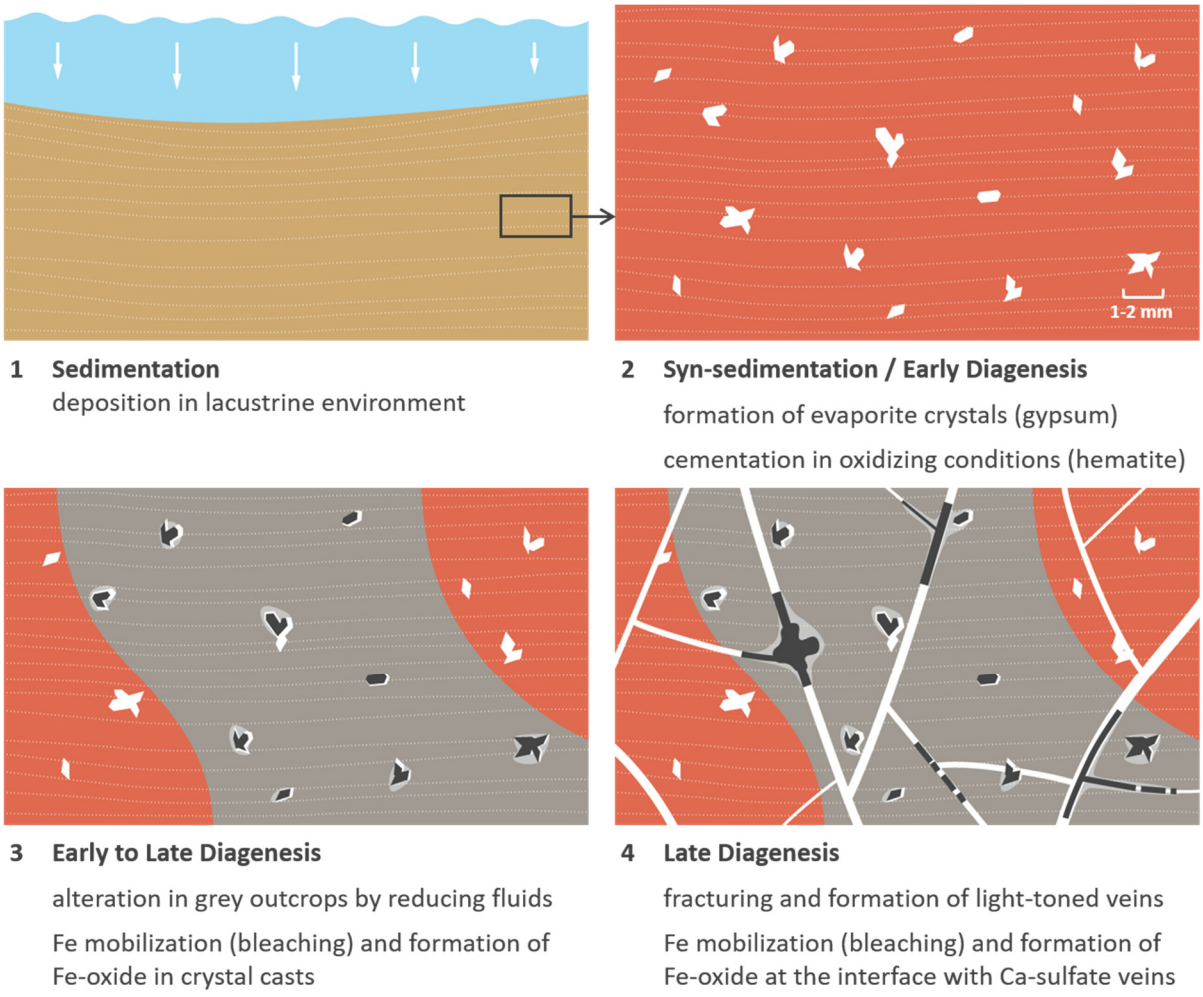

Figure 4.15: Schematic sequence of events involved in the formation of Vera Rubin Ridge.

4.6 Conclusion

The *in situ* exploration of Vera Rubin Ridge by the rover *Curiosity* revealed a complex post-depositional geological history, notably in the lacustrine mudstones of the Jura member that constitutes the upper part of this sedimentary structure. There, the lateral color patterns observed notably in the Jura outcrops are attributed to syn-depositional or early diagenesis cementation of ferric hematite (red color), and subsequent alteration by reducing and/or anoxic groundwater fluids (grey color). Within the grey outcrops, ChemCam highlighted that Fe was mobilized from the host rock—by either groundwater flows or later hydro-fracturing fluids—to form Fe-oxide at the interface with euhedral syn-depositional gypsum crystals (as pseudomorphs) and with late-diagenetic Ca-sulfate fracture-fills (as nodular inclusions and vein-fills). As a result, Fe is effectively leached from the adjacent host rock along chemical potential gradients, forming low-Fe bleached halos. The formation of these diagenetic Fe-oxide minerals, interpreted as magnetite or grey coarse-grained crystalline hematite, highlight the complex redox-driven processes that occurred during diagenesis and the induced mobility of redox-sensitive elements (mainly Fe, but also Mn to a lesser extent) occurring after deposition and sedimentation. Thus, millimeter-scale observations from ChemCam show that diagenetic processes likely played a predominant role in the formation of a regional structure visible from orbit.



[Sol **930**]
DIAGENETIC VEIN COMPLEX AT GARDEN CITY
NASA/JPL-Caltech/MSSS/Thomas Appéré



CHAPTER 5

DIAGENESIS AND REDOX PROCESSES AT GALE CRATER: IMPLICATIONS

The *Curiosity* exploration of Gale Crater sedimentary deposits, notably the fluvio-lacustrine rocks of the Murray formation and Vera Rubin Ridge, has revealed that redox-driven processes were intrinsically involved in their formation, expressed as local mineralogical and chemical trends in the host rock, but also as fine-scale geological items associated with diagenesis. In this chapter, we first synthesize in section 5.1 several studies made with Curiosity data, which have analyzed and interpreted the chemical and mineralogical characteristics of Gale Crater. We especially focus on the comparison between bulk host rock and diagenetic features, as well as the distinct hypotheses proposed in order to account for the rover's observations that we have made in this thesis (section 5.2). In section 5.3, we use basic geochemical modeling to provide some insights into the fluid conditions and the potentials redox and/or pH driven chemical reactions involved in the diagenetic history of Gale sedimentary rocks. Finally, we discuss the broader implications of *Curiosity*'s discoveries in the context of the planet, and the clues it may provide in understanding geological processes observed elsewhere on Mars.

5.1 Redox and pH conditions inferred from *Curiosity*'s observations

The chemical and mineralogical observations of sedimentary rocks in Gale Crater, from the different instruments on board the rover *Curiosity*, allow for the reconstitution of their geological history including sediment provenance, depositional environment, burial, and lithification. Variability in provenance was notably observed in the Kimberley area, where the fine-grained sandstones and conglomerates are likely derived from a more evolved (felsic) primary material compared to the other geological units [*Lasue et al.*, 2016; *Le Deit et al.*, 2016; *Mangold et al.*, 2016; *Treiman et al.*, 2016]. Variability in depositional environment was also observed across the rover traverse, with the recognition of fluvio-lacustrine settings in the Yellowknife Bay [*Grotzinger et al.*, 2014] and the Murray formation [*Grotzinger et al.*, 2015] but also erosional remnants of eolian deposits associated with the Stimson formation, which formed much later in the history [*Banham et al.*, 2018]. Nevertheless, fluvio-lacustrine deposits, which compose the vast majority of observations in Gale Crater, also exhibit chemical and mineralogical variability attributed to changing depositional and/or diagenetic environments, which relates to specific redox and/or pH conditions prevailing at the time of mineral formation.

The CheMin, APXS and ChemCam instruments identified distinct mineralogical facies within lacustrine deposits at Gale Crater. While the Yellowknife Bay rocks are characterized by magnetite-phyllosilicate (MP) mineral assemblage [*Vaniman et al.*, 2014], the Murray formation displays mineralogical variations along the stratigraphy, with transitions from hematite-phyllosilicate facies (HP) to magnetite-silica facies (MS) [*Hurowitz et al.*, 2017]. Figure 5.1 summarizes the mineralogical variability observed in fluvio-lacustrine deposits of the Bradbury and Mount Sharp groups. CheMin observations notably highlight varying hematite / magnetite ratio in the rocks [*Vaniman et al.*, 2014; *Rampe et al.*, 2017; *Bristow et al.*, 2018], which can also be tracked with ferric spectral parameters (e.g. 535 nm band depth) in ChemCam passive reflectance observations [*Johnson et al.*, 2016; *Fraeman et al.*, 2018].

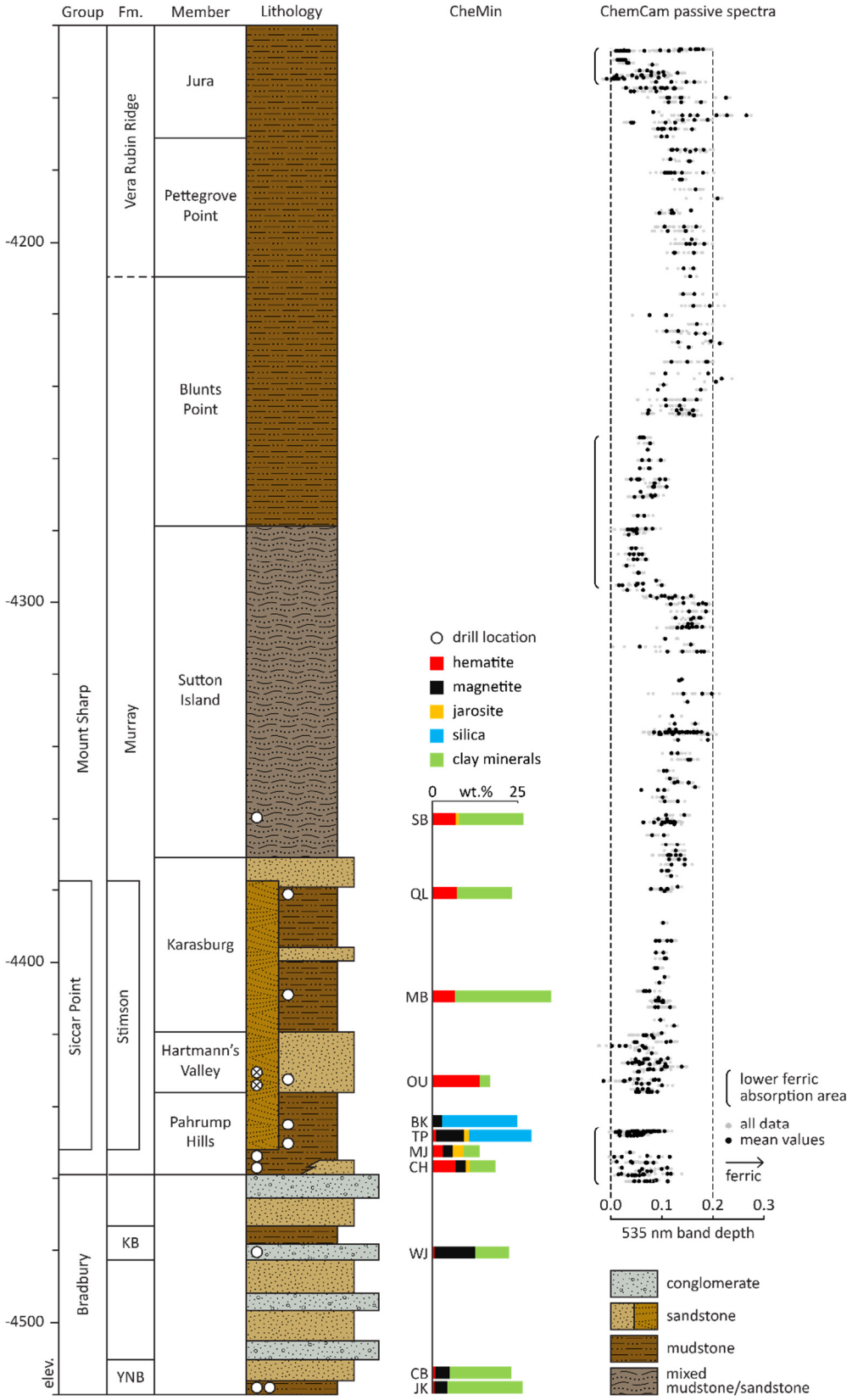

Figure 5.1: Mineralogical observations in lacustrine deposits with respect to stratigraphy for the terrains explored by the *Curiosity* rover in Gale Crater [stratigraphy from *Fedo et al.*, 2018]. CheMin mineral abundances [*Vaniman et al.*, 2014; *Rampe et al.*, 2017; *Bristow et al.*, 2018] and ChemCam passive reflectance data [*Fraeman et al.*, 2018] show variability in ferric components in the lacustrine deposits, suggesting changing redox conditions. Observations in the eolian deposits of the Stimson formation are excluded (crossed drill locations).

5.1.1 Varying redox conditions

In the Murray formation, hematite appears to be associated with phyllosilicates while magnetite is observed in strata in association with high-silica phases (opal-CT, cristobalite, tridymite). This transition from abundant Fe^{3+} oxides (hematite) to mixed valence Fe-oxides (magnetite) suggests varying redox conditions at the time of mineral formation [*Hurowitz et al.*, 2017].

The observed variations with stratigraphy in redox-sensitive mineral assemblages in the Murray formation have been interpreted by [*Hurowitz et al.*, 2017] to reflect redox stratification in the lacustrine setting, resulting from differences in the mass balance of atmospheric oxidants with respect to oxidizable cations (Figure 5.2). In this model, groundwater fluids provide dissolved cations (Fe^{2+} and Mn^{2+}), which interacts in the shallow portions of the lake with diffused atmospheric oxidants (photochemically generated O_2 and UV-light) to produce oxidized minerals, such as hematite and Mn-oxide. In contrast, the water in the deeper portions of the lake remains largely anoxic and favors the formation of authigenic magnetite over more oxidized iron minerals. Low FeO/MnO ratios reported by APXS in the HP facies compared to MS facies suggest that Mn-oxide formation only occurred in oxidizing shallow waters, and was inhibited in the deeper anoxic conditions.

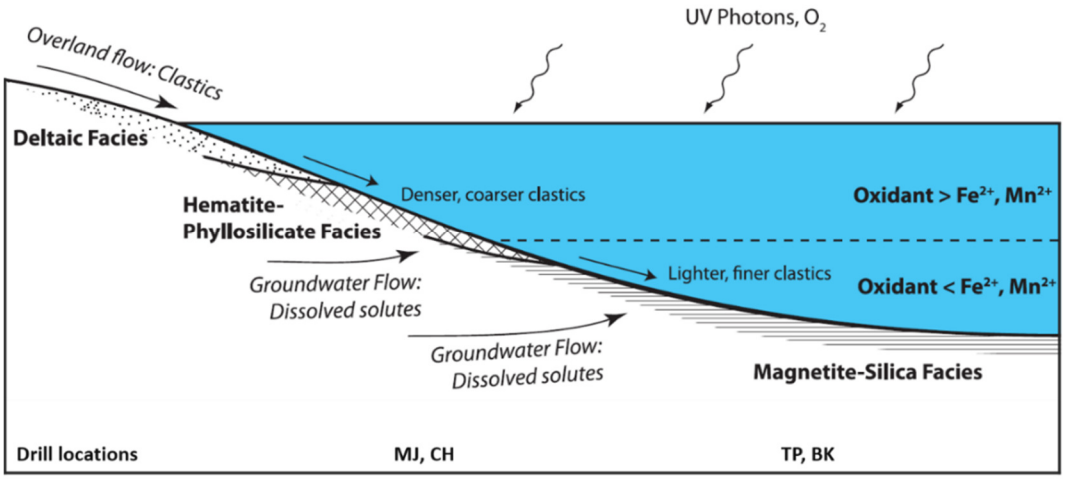

Figure 5.2: Redox stratified lake model, proposed to account for the observed hematite-phyllosilicate to magnetite-silica facies change observed in the Murray mudstones [modified from *Hurowitz et al.*, 2017].

In the Yellowknife Bay mudstones, however, no variability in redox conditions was observed, and anoxic conditions likely prevailed during deposition and throughout diagenesis as evidenced by the preservation of detrital sulfide minerals and formation of authigenic magnetite [*Grotzinger et al.*, 2014]. Textural (massive bedding) and mineralogical observations associated with the Yellowknife Bay mudstones indicate that deposition occurred rapidly in near-shore environments, with limited interactions with atmospheric oxidants [*McLennan et al.*, 2014; *Hurowitz et al.*, 2017]. Moreover, the Chemical Index of Alteration (CIA) values derived from ChemCam (Figure 5.3) and APXS chemical analysis suggest that the Yellowknife Bay mudstones deposited in arid, and possibly cold climatic conditions [*McLennan et al.*, 2014], whereas higher CIA values consistent with open-system weathering (leaching of cations under high water-rock ratios) are observed in the Murray mudstones and indicate more temperate paleo-climates [*Hurowitz et al.*, 2017; *Mangold et al.*, 2018a]. Colder climate conditions implied by low-CIA values in Yellowknife Bay could also have contributed to the preservation and precipitation of reduced iron- and sulfur-bearing mineral phases with lower redox kinetics [*Hurowitz et al.*, 2017].

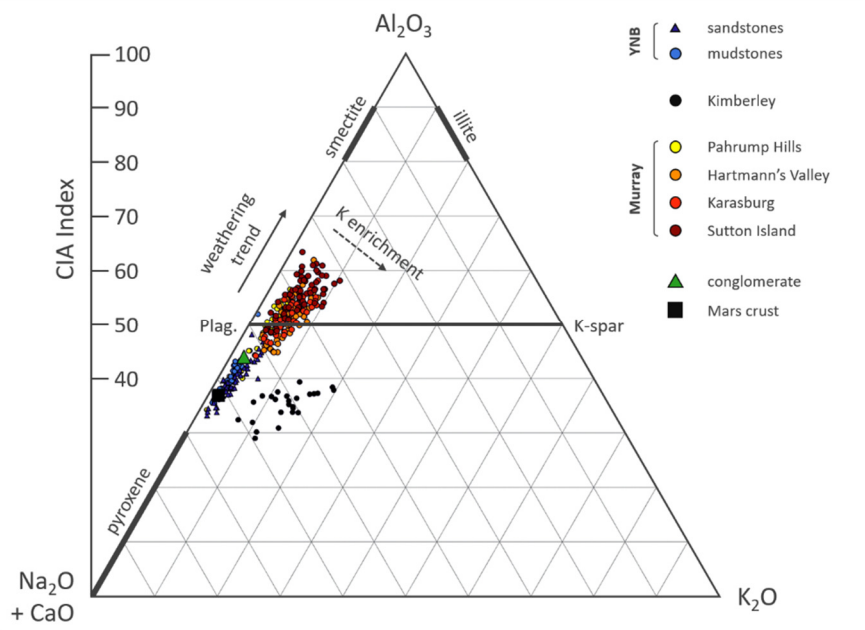

Figure 5.3: A-CN-K ternary diagram of ChemCam observations (molar values). The Chemical Index of Alteration (CIA) values are also reported on the vertical axis and highlight chemical weathering trends in the Murray formation, where targets above the 50-50 feldspar join suggest a limited contribution from primary minerals [modified from *Mangold et al.*, 2018a].

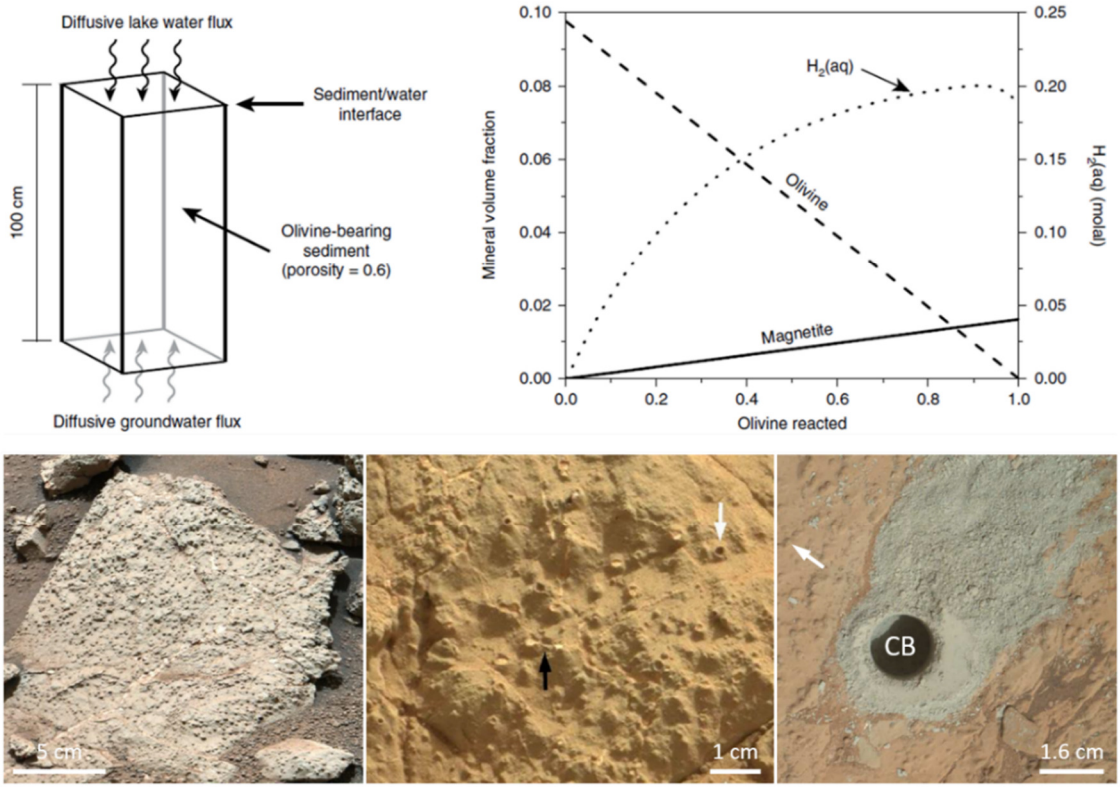

Figure 5.4: Geochemical modeling (top panel) illustrating the formation of magnetite during diagenesis from the dissolution of primary olivine by alkaline groundwater infiltration fluids, associated with the production of H_2 [*Tosca et al.*, 2018]. Abundant hollow mm-scale nodules (white arrow), partially filled during late-diagenesis by Ca-sulfate (black arrow), are observed in the Yellowknife Bay formation (bottom panel) and interpreted as voids formed by gas bubbles in the sediment, which is consistent with the production of H_2 gas associated with magnetite authigenesis [*Grotzinger et al.*, 2014; *Stack et al.*, 2014]. Indeed, magnetite is notably identified in the Cumberland (CB) drill hole, located on an outcrop featuring abundant diagenetic nodules [*Vaniman et al.*, 2014].

Alternatively, magnetite authigenesis may have occurred during diagenesis without requirements of changing near-surface redox conditions. Indeed, the formation of authigenic magnetite and smectite in Yellowknife Bay is attributed to nearly isochemical alteration of olivine during early diagenesis [*McLennan et al.*, 2014]. Laboratory experiments and geochemical modeling suggest that magnetite authigenesis readily occur following alkaline groundwater infiltration (at pH ~8-9), through the dissolution of detrital olivine and formation of Fe-hydroxide and green-rust intermediary phases under anoxic conditions (Figure 5.4) [*Tosca et al.*, 2018]. In addition, the alteration of primary olivine to form magnetite and smectite produce H_2 gas as byproduct [*Dehouck et al.*, 2014; *Vaniman et al.*, 2014; *Tosca et al.*, 2018], consistent with the formation of abundant diagenetic hollow nodules observed in the Yellowknife Bay formation, interpreted as voids formed by gas bubbles in the sediments (Figure 5.4), and would also explain their association with Fe-bearing cement (i.e. magnetite and/or Fe-saponite) [*Grotzinger et al.*, 2014; *McLennan et al.*, 2014; *Stack et al.*, 2014].

5.1.2 Varying pH conditions

Neutral to alkaline pH conditions are generally surmised for aqueous environments (including lake-waters) at Gale Crater, in order to account for the preservation and/or precipitation of phyllosilicates [*Grotzinger et al.*, 2014]. Alkaline groundwater fluids could also potentially solubilize detrital silica minerals in order to account for the magnetite-silica mineral assemblage observed in the Murray mudstones at Pahrump Hills [e.g. *Tosca et al.*, 2018].

At that location, however, CheMin also identified jarosite (Figure 5.1), a Fe-sulfate typically encountered in acidic and oxidizing environments (pH < 2); though it is unclear whether jarosite is coeval with the other minerals observed there. While redox stratification could accommodate locally more acidic conditions with near-shore oxidation of detrital sulfides minerals and subsequent formation of jarosite [*Hurowitz et al.*, 2017], it does not account for the chemical trends observed in the outcrops. Indeed, APXS reports increasing Fe, Mg, Mn, Zn and Ni abundances down section, anti-correlated with Si and Ti, consistent with top-down leaching by acidic fluids (Figure 5.5) [*Rampe et al.*, 2017].

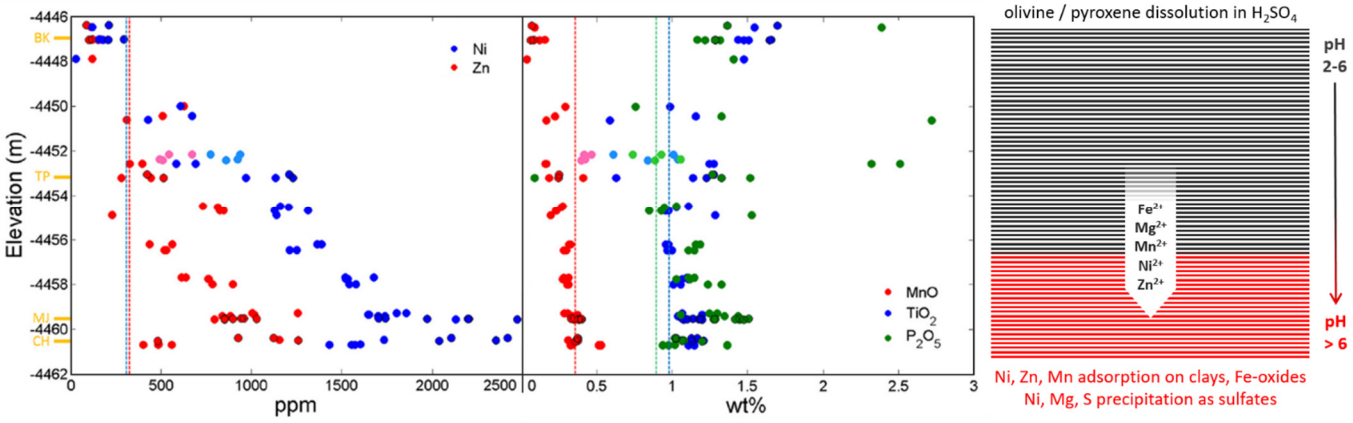

Figure 5.5: Chemical observations from the APXS instrument suggests that top-down acid leaching occurred during diagenesis, mobilizing Fe, Mg, Ni, Zn and Mn (but not Si, Al or Ti) in the strata of the Pahrump Hills mudstones [modified from *Rampe et al.*, 2017].

In addition, in the lower parts of Pahrump Hills, ChemCam and APXS observed Ni-rich Mg-sulfate and Fe-sulfate associated with diagenetic features [*Nachon et al.*, 2016; *VanBommel et al.*, 2016] as well as dark-toned fracture-fills enriched in F (as fluorite) and Ge within the diagenetic veins cluster at Garden City [*Nachon et al.*, 2016; *Berger et al.*, 2017], suggesting that acidic conditions prevailed during diagenesis. As such, acidic diagenetic fluids are inferred to have leached cations mobile at low-pH (e.g. Fe, Mg, Mn, Zn, and Ni), which would have then adsorbed onto mineral surfaces upon interaction with hematite and phyllosilicates in the lower parts of Pahrump Hills (Mn, Zn and Ni) [*Rampe et al.*, 2017], and precipitated as discrete mineral phases (e.g. Mg- and Fe-sulfates) to form the distinct diagenetic features observed [*Nachon et al.*, 2016; *Berger et al.*, 2017].

This acidic leaching process would also have resulted in passive enrichments in immobile cations (i.e. Ti and Si) up-section, though it cannot entirely account for the high-Si abundances observed at Marias Pass (upper-part of the Pahrump Hills) [*Frydenvang et al.*, 2017; *Hurowitz et al.*, 2017; *Yen et al.*, 2017]. Indeed, the identification of tridymite (in the Buckskin drill-hole), a high-temperature silica polymorph associated with silicic volcanism [*Morris et al.*, 2016], suggests that high-Si observations also partially reflect the addition of Si via an influx of detrital silicic primary minerals. Additionally, light-toned halos with similar Si-rich composition are observed along fractures in Stimson eolian sandstones, crossing into the underlying the Murray lacustrine mudstones at Marias Pass and Hartmann's Valley, interpreted to reflect diagenetic acidic fluid alteration also in relation with the remobilization of silica from Si-rich layers [*Frydenvang et al.*, 2017; *Yen et al.*, 2017].

Nevertheless, the two scenarios proposed to account for Pahrump Hills chemical and mineralogical variations (i.e. anoxic and acidic conditions) are not mutually exclusives as in both cases magnetite is proposed to have formed at the time of deposition in neutral to alkaline lake waters [*Hurowitz et al.*, 2017; *Rampe et al.*, 2017]. In addition, subsequent acidic groundwater influxes are interpreted to have been relatively short-lived and not extremely acidic (pH > 2) in order to account for the persistence of magnetite and fluorapatite minerals during diagenesis [*Rampe et al.*, 2017].

5.1.3 Increasing variability in the upper Murray formation

Further up section, the lower ferric absorption observed in ChemCam passive reflectance spectra near the transition between the Sutton Island and Blunts Point members and the spectral variability associated with the Jura member of Vera Rubin Ridge (Figure 5.1) remain largely unaccounted for by such redox and/or pH models [*Hurowitz et al.*, 2017; *Rampe et al.*, 2017]. The stratigraphic transition between the Sutton Island and Blunts Point members in the Murray formation is marked by abundant detections of Fe- and Mn-oxides [*Gasda et al.*, 2018; *Meslin et al.*, 2018] associated with high-P detection (possibly adsorbed onto oxides) and potential near-surface evaporitic cementation inferred from Ca-sulfate and Mg-sulfate detections in the host rock [*Newsom et al.*, 2017; *Rapin et al.*, 2018]. Such observations, in association with desiccation cracks observed in the vicinity [*Stein et al.*, 2018], are diagnostic of shallower lake levels and subaerial exposures. While low-standing lake environment would account for the formation of Fe- and Mn-oxide as well as evaporites [*Hurowitz et al.*, 2017], the absence of ferric signature in the ChemCam passive reflectance data is enigmatic and could indicate subsequent reduction during diagenesis. Similarly, lateral variations in ferric components observed in the Jura member of Vera Rubin Ridge do not appear to be related to stratigraphic changes and evolving depositional conditions and are attributed to groundwater alteration. As such, the mineralogical and chemical trends observed in the Murray formation do not appear to reflect solely changes in depositional environments and involve water-rock interactions during diagenesis.

The main observations from the *Curiosity* rover in the lacustrine deposits of Gale crater (Yellowknife Bay and Murray formation) are summarized in Table 5.1, as well as interpretations on the redox and pH conditions that likely prevailed at the time of deposition and later involved in the diagenesis of the sediments. In the Murray formation, however, the varying redox and/or pH conditions associated with the formation of fine-scale distinct diagenetic features are more subtle, not necessarily picked-up in the bulk host rock analyses (APXS, CheMin), and were thus investigated by ChemCam.

stratigraphy		mineralogy	chemistry	notable diagenetic features	deposition	diagenesis
Murray fm.	beyond PH	hematite +/- smectite	high CIA (weathering)	Localized Fe-oxide formation in association with Ca-sulfate light-toned veins	oxidizing conditions	mobilization of Fe by acidic and/or reducing fluids
	upper PH	magnetite silica	high Si, Al, Ti other elements depleted	Si-rich halo along fractures	anoxic conditions?	acidic alteration (leaching)
	lower PH	hematite smectite jarosite	high Fe, Mg, Mn, Ni, and Zn	Ni-rich Mg-sulfate and Fe-sulfate Ge-rich fluorite dark-toned fracture-fills	oxidizing conditions	precipitation in acidic conditions
Yellowknife Bay fm.		magnetite smectite	low CIA	void nodules (from H_2 gas)	anoxic conditions	alkaline
		CheMin	*APXS/ChemCam*	*observations*		*interpretations*

Table 5.1: Summary of *Curiosity* observations related to redox and/or pH processes in sedimentary deposits (PH = Pahrump Hills)

5.2 Variability associated with the Ca-sulfate light-toned veins

Ca-sulfate light-toned veins are observed consistently across all geological terrains observed so far by the rover, emplaced during the later-stages of diagenesis by hydrofracturing. As such, the systemic geochemical analyses by ChemCam trace variability in composition in these features, which can then be used as a proxy to highlight changes in fluid conditions during the diagenesis of the fluvio-lacustrine sediments. The studies described in this manuscript identified three specific locations along the rover traverse where the formation of Ca-sulfate light-toned veins is associated with variability in Fe-bearing components, and as such suggests post-depositional mobility of Fe from redox- and/or pH-driven water-rock interactions (Figure 5.6).

In the Hartmann's Valley (c.f. Chapter 3), anastomosing light-toned veins are associated with Fe^{3+} enrichments suggestive of oxidizing fluid conditions at the time of formation (e.g. Grillental target, Figure 5.6). These observations occur stratigraphically near the unconformable contact between Murray mudstones and Stimson eolian sandstones where acidic conditions are inferred to have mobilized cations, including Fe^{2+}, which would have precipitated as Fe^{3+} mineral phases (likely Fe-oxides) upon interacting with SO_4^{2-} bearing fluids in fractures. In addition, this stratigraphic contact forms a physical boundary in the sedimentary rocks along which diagenetic fluids would tend to propagate, and would account for the high density of light-toned Ca-sulfate diagenetic features observed at these locations [*Nachon et al.*, 2017].

In the Sutton Island member (c.f. Chapter 3), light-toned veins show complex interactions with Fe- and Mn-oxides, onto which P readily adsorbed. Fe-oxides and Mn-oxides are interpreted to have formed during early diagenesis in oxidizing conditions [*Gasda et al.*, 2018; *Meslin et al.*, 2018], and were subsequently incorporated within light-toned veins as dark-toned inclusions during late-diagenesis (e.g. Blue_Hill target, Figure 5.6). The lack ferric absorptions in passive reflectance spectra in such features were interpreted to reflect the reduction Fe^{3+}-bearing mineral compounds in the process. Additionally, bleached alteration rinds observed around Ca-sulfate veins in the vicinity are interpreted to reflect either more acidic or reducing fluid conditions associated with the emplacement of veins (e.g. Third Lake target, Figure 5.6).

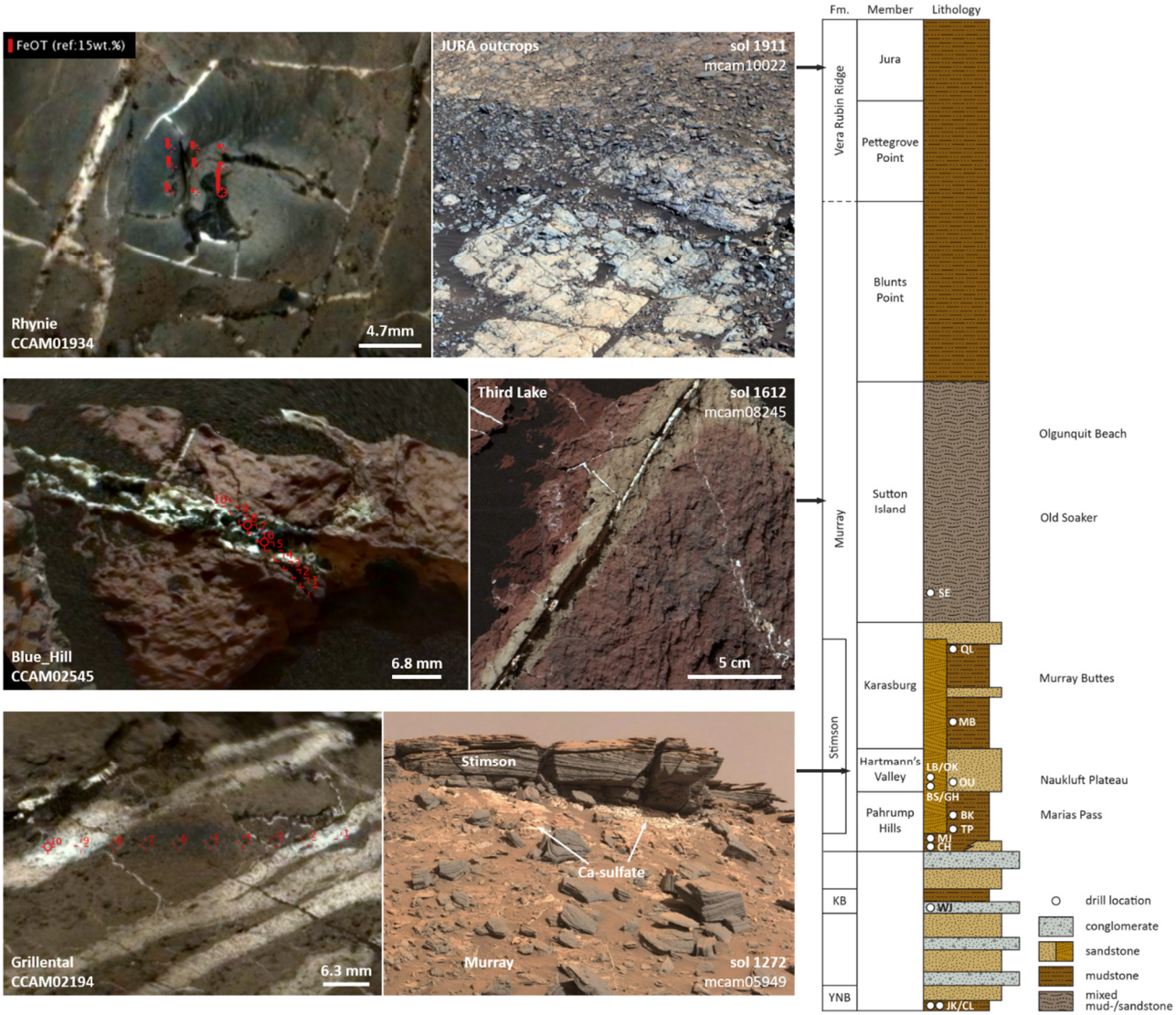

Figure 5.6: Locations along the stratigraphy where ChemCam observed variability in Fe-bearing components in association with Ca-sulfate light-toned veins (high-Fe points indicated by red circles), i.e. in the Hartmann's Valley, Sutton Island, and Jura members.

Lastly, Curiosity observed lateral color patterns in the outcrops of Vera Rubin Ridge, related to variations in ferric components (e.g. Jura outcrops, Figure 5.6), probably formed after the circulation of reducing groundwaters after deposition and cementation in oxidizing conditions (i.e. isochemical reduction of ferric components; Chapter 4). In the grey outcrops that lack ferric spectral signatures, ChemCam also observed Fe-oxide diagenetic features as nodular inclusions and fracture-fills within

Ca-sulfate light-toned veins (e.g. Rhynie target, Figure 5.6) as well as substitution pseudomorphs in gypsum-shaped crystalline casts (c.f. Chapter 4). As such, Fe-oxide formation involved mobilizing Fe from the host rock during diagenesis and subsequent precipitation upon interaction with Ca-sulfate in both syn-depositional crystals and late-diagenetic fractures.

In summary, ChemCam observed precipitation of Fe-oxide in association with the formation of Ca-sulfate fracture-fills during diagenesis, but only at specific locations along the rover traverse. There, Fe was mobilized by distinct fluid event(s) and precipitated upon interaction with Ca-sulfate, or its parent S-rich diagenetic fluid(s). In order to provide constraints on the diagenetic fluid(s) chemistry and potential reaction pathways, we use geochemical modeling tools to explore the pH and redox conditions associated with the formation of the observed mineral assemblage.

5.3 Implications for fluid conditions

The redox and pH conditions associated with the formation of Fe-oxide during diagenesis can be explored with Pourbaix diagrams which maps the thermodynamical equilibrium of aqueous and mineral phases for a given chemical element as a function of Eh (redox potential, in volts) and pH [*Latimer*, 1952; *Pourbaix*, 1966]. Pourbaix diagrams shown in this section were generated with the Geochemist's Workbench (GWB) geochemical modeling software [*Bethke et al.*, 2018]. Thermodynamic data for equilibrium reaction involving mineral, gases, and aqueous complexes are extracted from the expanded and revised LLNL database [*Delany and Lundeen*, 1990]. Since we model diagenetic fluid conditions, thermodynamical equilibrium stability fields for aqueous and mineral phases are displayed within liquid water (H_2O) boundaries. In addition, the generated diagrams only describe aqueous and mineral phases in thermodynamic equilibrium for simplified fluid conditions and do not account for meta-stable phases that may form in natural environments outside of equilibrium, nor reaction kinetics.

The temperature and pore-pressure ranges associated with the diagenesis of Gale Crater sediments are poorly constrained, but upper limits can be inferred from mineralogical and textural observations associated with late-diagenetic features (i.e. bassanite light-toned veins formed by hydro-fracturing, and desiccation of precursor gypsum mineral phase) which indicates temperatures below 50-60°C and realistic pore-pressure estimates of 10 MPa for the inferred 3 km maximum burial depth [*Borlina et al.*, 2015; *Rapin et al.*, 2016; *Caswell and Milliken*, 2017]. In order to account for both early and late-diagenesis conditions, Pourbaix diagrams are generated at 5°C and 1 MPa (near-surface sediments), as well as 50°C and 10 MPa (lithified and compacted sedimentary rocks).

Diagenetic fluid compositions modeled for Yellowknife Bay provide reasonable constraints for the activity of species considered in the construction of Pourbaix diagrams [*Bridges et al.*, 2015; *Schwenzer et al.*, 2016], and show that fluids were likely anoxic and CO_2 poor. As such, only Fe, S, and Mn are considered in solution, with respective activities of 10^{-4} (Fe^{2+}), 10^{-3} (SO_4^{2-}) and 10^{-6} (Mn^{2+}). SO_4^{2-} activity is inferred from geochemical modeling of diagenetic fluid compositions at Yellowknife Bay [*Schwenzer et al.*, 2016], which constitutes a lower-end estimate. Indeed, Ca-sulfate formation during late-diagenesis is interpreted to involve the dissolution of precursor sulfate deposits, leading to enrichment in S in fluids [*Schwenzer et al.*, 2016]. Fe^{2+} and Mn^{2+} activities are set higher compared to the low activities reported in modeled fluid compositions in order to reflect the observed mobility of Fe and Mn in fluids during diagenesis. Lower activities in Fe^{2+} and Mn^{2+} would increase the thermodynamical stability of aqueous species (to higher pH).

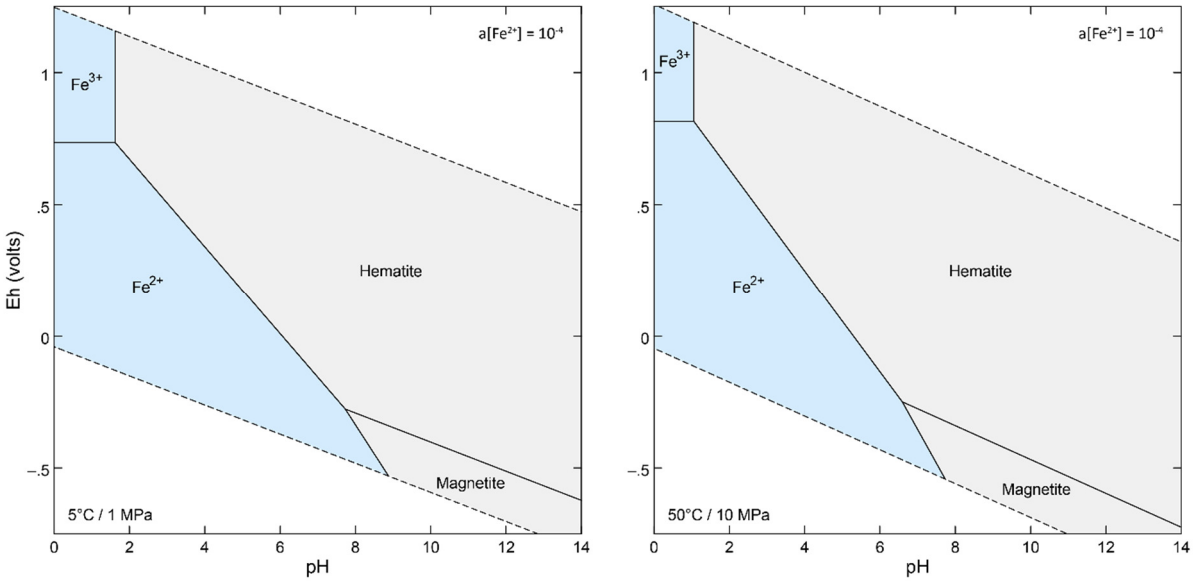

Figure 5.7: Pourbaix diagram of Fe species for early (left) and (right) late-diagenetic conditions.

The formation of Fe-oxide mineral phases is especially subject to pH and Eh variations, as shown in Figure 5.7 where we only consider Fe in solution. Iron is mobile in fluids as Fe^{2+} in acidic to neutral pH and moderate redox conditions while aqueous Fe^{3+} is only encountered in fluids under extremely acidic (pH < 2) and oxidizing conditions. As for mineral formation, hematite is produced in a wide range of pH and Eh conditions while magnetite formation only occurs under reducing and alkaline conditions (Eh < -0.2V and pH > 8). Variations in fluid temperature and pore-pressure associated with early and late diagenesis do not seem to affect significantly the thermodynamical stability of Fe aqueous and mineral phases, aside from constraining the presence of Fe^{3+} in solution to even more acidic conditions (pH < 1) and slightly increasing the range of pH under which magnetite may form (pH > 7).

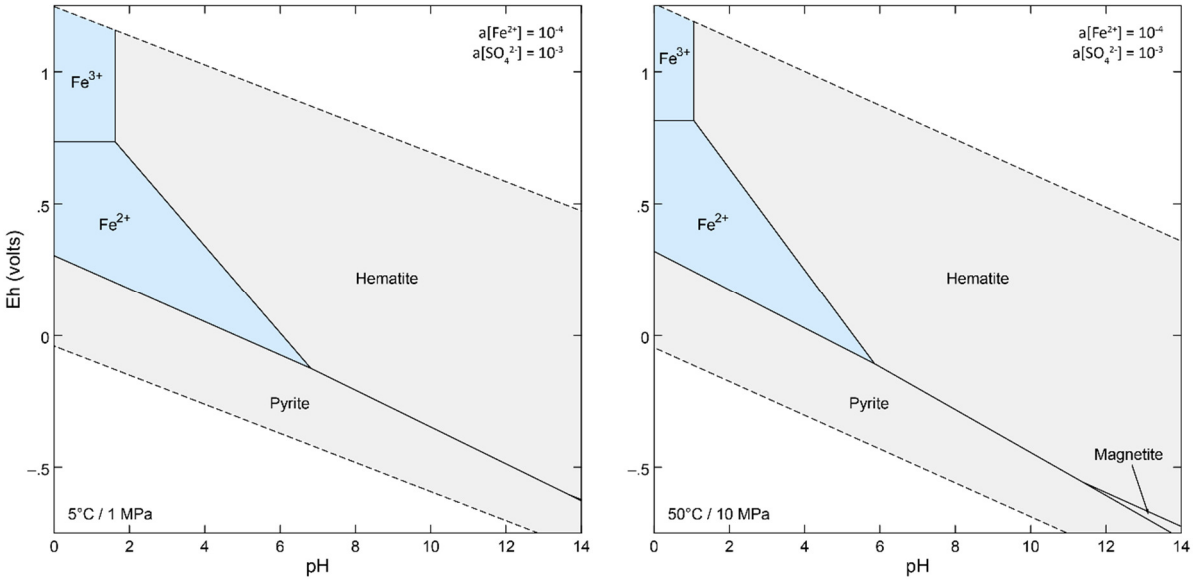

Figure 5.8: Pourbaix diagram of Fe species for early (left) and late (right) diagenetic conditions, in presence of SO_4^{2-} in solution resulting from the interaction with $CaSO_4$ mineral phases.

ChemCam observations indicate that formation of Fe-oxides during diagenesis in Gale Crater appears to be associated with the emplacement of Ca-sulfate, interpreted to reflect interaction with sulfate ions (c.f. Chapter 3 and 4). In presence of SO_4^{2-} (Figure 5.8), aqueous Fe is only observed in solution for pH < 6 and moderate (as Fe^{2+}) to oxidizing (as Fe^{3+}) redox conditions but readily form pyrite (FeS_2) under more reducing conditions. Hematite formation occurs in similar pH and Eh ranges than before (i.e. without S in the system) but magnetite appears to be thermodynamically unstable in the presence of SO_4^{2-}, only produced in extremely reducing and alkaline (pH > 12) conditions during late diagenesis (i.e. 50 °C and 10 MPa).

Additionally, the dissolution of Ca-sulfate by diagenetic fluid(s) could produce distinct sulfur complexing species in solution depending on pH and Eh conditions, aside from SO_4^{2-}. Figure 5.9 (mosaic diagram; combining the Pourbaix diagrams for both Fe and S) describes the stability of Fe aqueous and mineral phases in the Fe – S system with respect to pH and Eh. In this context, magnetite may form under extremely reducing (Eh < −0.5V) and alkaline conditions (pH > 11 − 13 depending on temperature and pore-pressure), as well as pyrrhotite (FeS) in slightly less alkaline conditions. Increase in SO_4^{2-} activity would expand the stability field of pyrite at the expense of magnetite (and pyrrhotite), and lead Fe^{3+} to complex in solution forming $FeSO_4^+$ ions. An associated increase in Fe^{2+} activity would also trigger the formation of melanterite (Fe^{2+} sulfate), but it is not observed in Gale Crater.

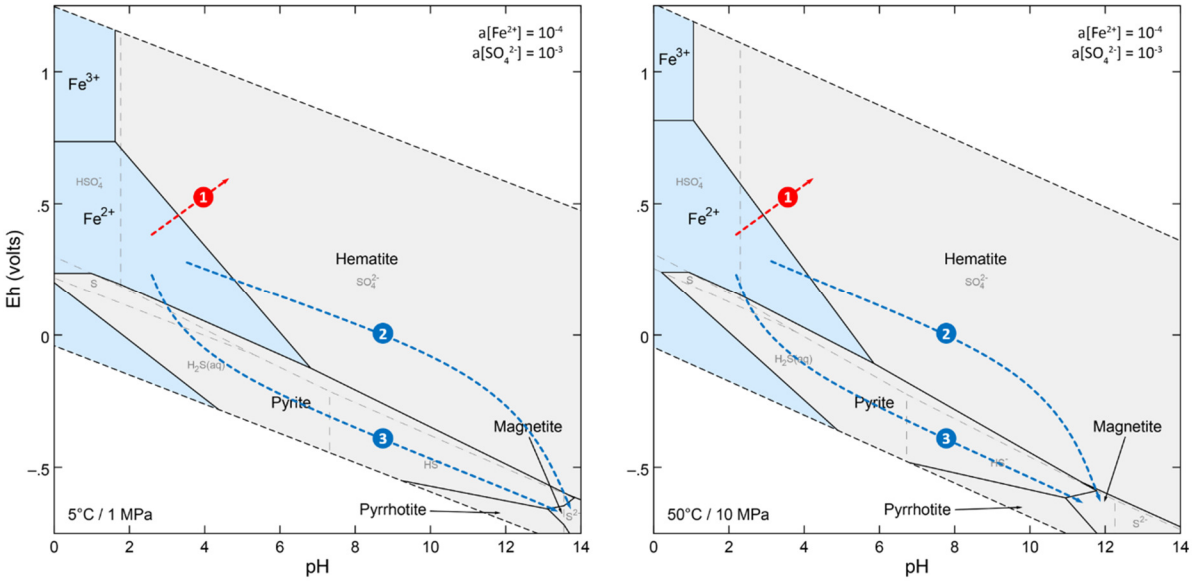

Figure 5.9: Mosaic diagram of Fe species for early (left) and late (right) diagenetic conditions, in presence of complexing S species (light grey) resulting from the interaction with $CaSO_4$ mineral phases. Potential reaction paths for the formation of hematite (red) and magnetite (blue) are indicated.

ChemCam observations on diagenetic features do not provide strong constraints on the Fe-oxide mineralogy. Indeed, the passive reflectance spectra that lack ferric absorption features could either reflect the contribution from mixed valence Fe-oxide (e.g. magnetite) or the influence of grain-size and crystallinity (e.g. grey crystalline hematite). The formation of hematite would be more straightforward, only requiring a slight increase in pH and/or Eh (path 1; Figure 5.9) to precipitate from the Fe^{2+} mobilized in solution by acidic (e.g. Hartmann's Valley) and/or reducing fluids (e.g. VRR). If magnetite was observed, it would involve extremely alkaline and reducing fluid conditions and the formation of hematite or pyrite precursors (path 2 and 3; Figure 5.9).

Nevertheless, if the formation of hematite and goethite were precluded because of low reaction kinetics [e.g. *Elwood Madden et al.*, 2004], magnetite would become the metastable Fe-oxide over most of the pH and Eh range of hematite, and would thus form instead (path 1; Figure 5.10).

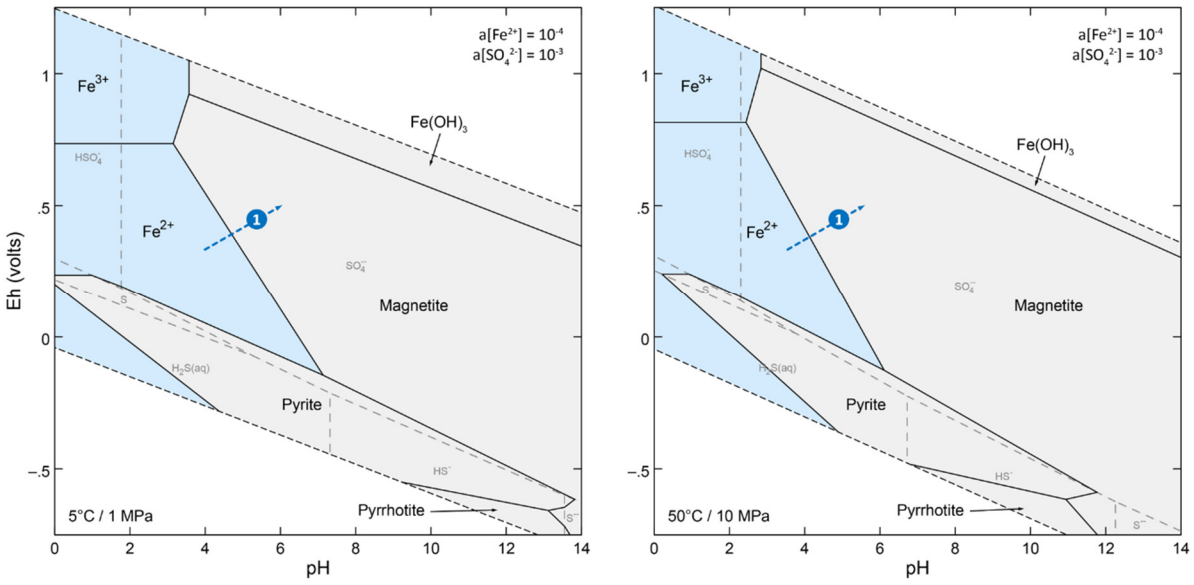

Figure 5.10: Mosaic diagram of Fe species for early (left) and late (right) diagenetic conditions, in presence of complexing S species (light grey) resulting from the interaction with $CaSO_4$ mineral phases. Hematite and goethite mineral phases are suppressed. As a result, magnetite becomes metastable over a wider range of pH and Eh, and the potential reaction path for its formation (blue) becomes more straightforward.

In the end, the lack of rationale to preclude the formation of goethite or hematite in the Murray formation (as hematite was detected throughout the unit by CheMin) would support the formation of hematite rather than magnetite during diagenesis, in association with Ca-sulfate light-toned veins. The lack of ferric signature in the passive spectra would then be due to crystallinity and/or grain size effects (i.e. grey crystalline and/or coarser grained hematite rather than red hematite).

The formation of hematite involves the oxidation of Fe^{2+}, following a slight increase in pH or Eh. In anoxic conditions, Fe^{2+} oxidation usually occurs from interaction with dissolve H^+:

(1) $$2Fe^{2+}_{(aq)} + 2H^{+}_{(aq)} \rightarrow 2Fe^{3+}_{(aq)} + H_{2\,(g)}$$

In this scenario, however, Fe^{2+} oxidation could also occur upon interaction with SO_4^{2-} ions (2) upon interaction with Ca-sulfate, which subsequently lead to the formation of hematite (Fe_2O_3), either directly or via formation of Fe-hydroxide precursors such as goethite (3) or ferrihydrite (4).

(2) $$2Fe^{2+}_{(aq)} + SO^{2-}_{4\,(aq)} + 2H^{+}_{(aq)} \rightarrow 2Fe^{3+}_{(aq)} + SO^{2-}_{3\,(aq)} + H_2O_{\,(aq)}$$

(3)
$$Fe^{3+}_{(aq)} + 3OH^{-}_{(aq)} \rightarrow FeOOH_{\,(s)} + H_2O_{\,(aq)}$$
$$2FeOOH_{\,(s)} \rightarrow Fe_2O_{3\,(s)} + H_2O_{\,(aq)}$$

(4)
$$Fe^{3+}_{(aq)} + 3OH^{-}_{(aq)} \rightarrow Fe(OH)_{3\,(s)}$$
$$2Fe(OH)_{3\,(s)} \rightarrow Fe_2O_{3\,(s)} + 3H_2O_{\,(aq)}$$

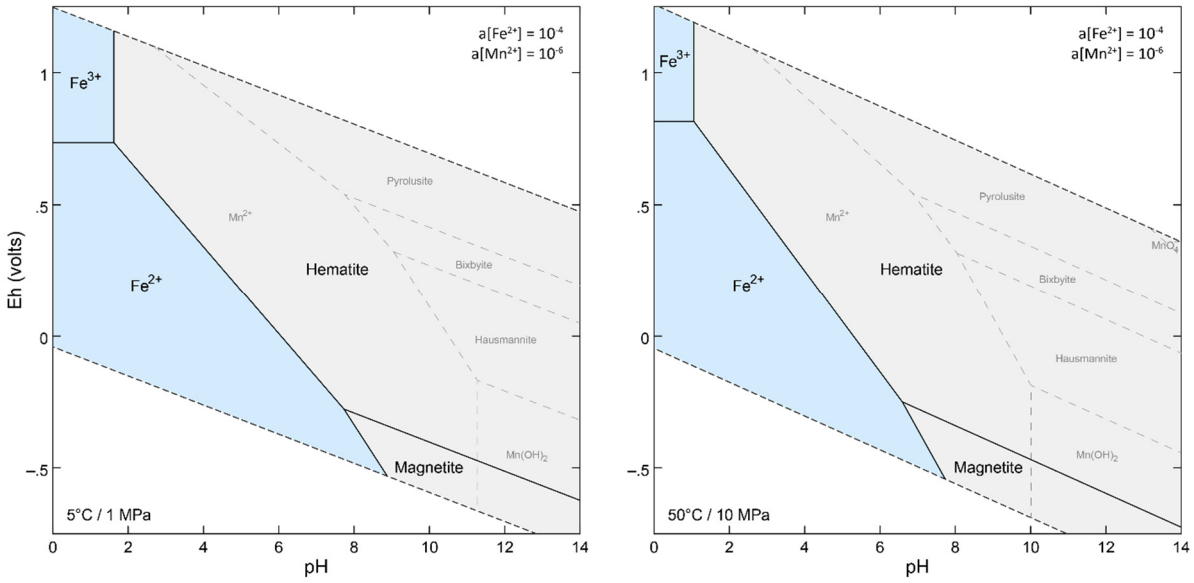

Figure 5.11: Mosaic diagram of Fe and Mn species for early (left) and late (right) diagenetic conditions.

Additionally, Mn-oxide detections in association with Fe-oxide in the Sutton Island and Blunts Point members in early diagenetic features [*Gasda et al.*, 2018; *Meslin et al.*, 2018] provides further constraints on pH and redox conditions (Figure 5.11). Indeed, since Mn^{2+} is soluble under a wider range of pH and Eh compared to Fe, the formation of Fe-oxide + Mn-oxide mineral assemblages indicate more alkaline and/or oxidizing fluid conditions compared to the formation of Fe-oxide alone. As a result, observations in the Sutton Island and Blunts Point member trace strongly oxidizing and/or alkaline fluid conditions during early diagenesis. Similarly, the possible correlation between Mn and Fe in diagenetic features on the grey outcrops of the Jura member could also hint at higher oxidation and/or alkaline conditions at the time of formation. In contrast, the absence of Mn-oxide detection in the Hartmann's Valley likely indicates either less oxidizing and/or more acidic conditions in fluids.

The formation of bleached alteration rinds associated with fracturing and emplacement of Ca-sulfate remain unaccounted for in Sutton Island (Figure 5.6), based on ChemCam observations, but the color patterns from red to grey around the veins may suggest the reduction of ferric compounds.

5.4 Evolving redox and pH conditions at Gale Crater and broader implications

Fe-oxides compounds observed in the host rock across the *Curiosity* traverse show variability attributed to varying pH and/or redox conditions at the time of formation. In the Yellowknife Bay outcrops, near the landing area, magnetite (and smectite) likely result from the isochemical alteration of detrital olivine during early diagenesis in neutral pH and anoxic conditions and are associated with arid and cold paleo-climates. In contrast, the formation of hematite (and locally Mn-oxides) in the Murray lacustrine deposits reflect interactions with diffused atmospheric oxidants in shallow lake waters (and possibly near-surface pore-waters in the unconsolidated sediments) and are associated with more temperate paleo-climates. The sedimentary rocks observed at Gale Crater thus appear to record a change in surface conditions from arid, cold and anoxic conditions at the time of deposition of the Yellowknife Bay deposits to more temperate and oxidizing environments during the sedimentation of the Murray mudstones. With respect to the planet's climatic evolution, these

observations indicate that the Yellowknife Bay sedimentary rocks formed later in its history, which is consistent with orbital observations at Gale Crater [*Le Deit et al.*, 2013].

The Murray formation also records the evolution of the sediments during diagenesis associated with more reducing and/or acidic fluid conditions. Indeed, while the magnetite + silica mineral assemblage observed at Pahrump Hills could reflect sedimentation in deeper and anoxic lake waters, it is also associated with detections of jarosite as well as the mobility in some metals (including Al and Fe) during diagenesis, arguing for post-depositional acidic fluid conditions. Additionally, ChemCam observed Fe-oxide diagenetic features associated with late-diagenesis Ca-sulfate fracture-fills. Fe-oxide formation probably involved the mobilization of Fe from the host rock by groundwater fluids, either through the isochemical reduction of ferric components (i.e. in the grey patches of Vera Rubin Ridge) or acid leaching (e.g. Hartmann's Valley). Incidentally, the origin of acidic conditions during diagenesis may result from the oxidation of Fe-oxide phases [*Hurowitz et al.*, 2010].

As such, Gale Crater records evolving near-surface conditions, between the Yellowknife Bay and Murray lacustrine deposits, but also varying water-rock interactions during diagenesis with evidence for acidic and/or reducing groundwater events that significantly altered the chemistry and mineralogy of the sedimentary rocks after deposition. Diagenetic processes were also observed at Meridiani Planum by the *Opportunity* rover, where evaporitic sandstones were heavily reworked during diagenesis, upon interaction with a rising groundwater table [*McLennan et al.*, 2005]. On the other hand, the *Spirit* rover did not observe extensive diagenesis but instead highlighted alteration by hydrothermal fluids [*Squyres et al.*, 2008; *Yen et al.*, 2008; *Ruff et al.*, 2011]. At Gale Crater, however, hydrothermal alteration was inferred in the source region of the Kimberley sedimentary rocks from detrital Cu, Zn and Ge enrichments [*Berger et al.*, 2017; *Payré et al.*, 2017b], but so far not conclusively observed *in situ*.

In summary, the recent *in situ* exploration missions on Mars have revealed that significant aqueous interactions occurred after deposition in sedimentary deposits, and quite extensively at Gale Crater. In addition, groundwater alteration often appears to involve the mobilization of Fe and was notably observed in locations first recognized as hematite deposits from orbit, by CRISM at Gale Crater [i.e. Vera Rubin Ridge, *Fraeman et al.*, 2013] and by TES at Meridiani Planum [*Christensen et al.*, 2001]. As such, other sites on Mars where orbital instruments have recognized Fe-oxide (notably hematite) in sedimentary deposits would provide strong candidate landing sites to investigate groundwater interactions. In particular, the OMEGA instrument on-board Mars Express identified Fe-oxide associated with layered sulfate deposits in localized regions of Valles Marineris, Terra Meridiani, and Margaritifer Terra [*Bibring et al.*, 2006], suggestive of groundwater interactions.

Lastly, the study of groundwater systems on Mars is instrumental in deciphering the aqueous history of its sedimentary rocks and allow for a better understanding of past climatic conditions by constraining the textural, chemical and mineralogical evolution of the sediments after burial. Moreover, sub-surface fluids provide extended periods of liquid water interactions which could have persisted throughout the Amazonian [*Malin and Edgett*, 2000], compared to surface processes which have gradually recessed on Mars since the early Hesperian (after ~3.5 Ga). Such environments would also constitute favorable conditions for the preservation of organics and potentially habitable conditions for living organisms.

In the end, these diagenetic environments would represent key candidates for future sample return missions, such as the future NASA rover mission *Mars2020*, but also for the investigation of water and geochemical environments as a function of depth in the shallow sub-surface by the future ESA rover mission, *ExoMars*.

CONCLUSION

The *in situ* exploration by the *Curiosity* rover of the layered sedimentary deposits of the Mt. Sharp, at Gale Crater, has shown that liquid water once flowed on Mars. Moreover, the presence of perennial fluvio-lacustrine systems, possibly spanning hundred thousands of years, provides evidence for potentially habitable environments in the past. The outcrops, however, are also packed with small-scale features (nodules, concretions, and fracture-fills) that formed after the burial of the sediments, highlighting the significant imprint diagenetic processes had on their formation. Notably, the widespread occurrences of Ca-sulfate light-toned veins, formed by hydrofracturing, indicate that regional late-diagenesis S-rich groundwater fluid(s) have interacted with all sedimentary deposits. In addition, acid leaching processes associated with groundwater interactions have been inferred locally, altering the chemistry and mineralogy of lacustrine sediments during diagenesis.

Over the first 1700 sols (Martian days) of the mission, we have investigated the chemical variability associated with light-toned veins. The formation of Ca-sulfate fracture-fills is associated with authigenic Fe-bearing components at specific locations along the rover traverse, hinting at the post-depositional mobility of Fe from redox- and/or pH-driven water-rock interactions. Anastomosing light-toned veins associated with Fe^{3+} enrichments occur stratigraphically bellow an unconformable contact between the lacustrine mudstones and overlying eolian sandstones, suggesting oxidizing fluid conditions at the time of formation. There, acidic conditions are inferred to have mobilized cations, including Fe^{2+}, which would have later precipitated as Fe^{3+}-oxides upon interaction with S-bearing fluids in fractures. Up-section, where *Curiosity* observed evidence for shallower lake-levels (e.g. desiccation cracks), light-toned veins show complex interactions with Fe- and Mn-oxides, onto which P readily adsorbed. Fe-oxides and Mn-oxides are interpreted to have formed during early diagenesis in oxidizing conditions and subsequently incorporated within light-toned veins during late-diagenesis. Reducing (or acidic) fluid conditions could account for the lack of ferric signature in these features and would be consistent with the observation of bleached rinds around Ca-sulfate veins in the vicinity.

Afterward, the *Curiosity* rover reached a prominent topographic structure known as Vera Rubin Ridge (VRR) characterized by a hematite signature from orbit and later confirmed *in situ*. During its investigation, however, the rover did not observe any significant increase in Fe abundance in the sedimentary rocks. Instead, the outcrops exhibit lateral color patterns that relate to variations in the ferric components in the host rock. In the lighter-toned outcrops that lack ferric spectral signatures, Fe-oxide diagenetic features are again associated with Ca-sulfate light-toned veins, emplaced during late-diagenesis, but also observed as substitution pseudomorphs in Ca-sulfate (gypsum) crystals that originally formed during or shortly after deposition. Authigenic Fe-oxide formation is interpreted to result from (1) mobilization of Fe^{2+} in the surrounding host rock by reducing or anoxic groundwaters, which also produced alteration patterns in the outcrops (i.e. isochemical reduction of ferric components), and (2) formation of Fe-oxide upon interaction with Ca-sulfate bearing diagenetic features during the later stages of diagenesis. These observations highlight the significant role played by diagenesis in the mobility and distribution of Fe (and other redox-sensitive elements) at Gale Crater and in the formation of large-scale geological structures visible from orbit.

These diagenetic observations also relate to variability in mineralogy and chemistry observed in the fluvio-lacustrine host rocks, in particular with respect to the Fe-oxide component. In the Gale Crater floor deposits, the fluvio-lacustrine sedimentary rocks—deposited rapidly in a cold and/or arid

paleoclimate—comprises magnetite and smectite that likely formed from the isochemical alteration of detrital olivine in the early stages of diagenesis. In these rocks, our studies did not reveal any clear evidence for subsequent alteration associated with the emplacement of Ca-sulfate veins. In contrast, the widespread detection of hematite in the lacustrine mudstones of the Murray formation likely reflects deposition in oxidizing near-surface conditions and a more temperate paleoclimate, while local mineralogical facies variation would be attributed to a later diagenetic imprint. Indeed, these variations are associated with geochemical variability in Ca-sulfate light-toned veins that indicates the involvement of reducing and/or acidic groundwaters during diagenesis, which altered the chemistry and mineralogy of the rock and formed the various diagenetic features observed.

In summary, the results presented in this manuscript indicate that groundwater alteration often appears to involve the mobilization of Fe, notably at locations first recognized as Fe-oxide-rich deposits from orbit. In-line with the likely diagenetic origin of the Meridiani Planum hematite orbital detections inferred by *Opportunity*, our studies suggest that other sites on Mars where orbital instruments have recognized Fe-oxide (notably hematite) in sedimentary deposits may constitute worthy candidate landing sites to investigate groundwater interactions.

Furthermore, groundwater systems may still be active nowadays, and thus provide an extended period of liquid water interactions compared to surface processes, which have gradually recessed on Mars since the Hesperian. Such active sub-surface environments would constitute favorable conditions for the preservation of organics as well as potentially habitable conditions for living organisms, and thus be of particular interest for future sample return and life-detection missions.

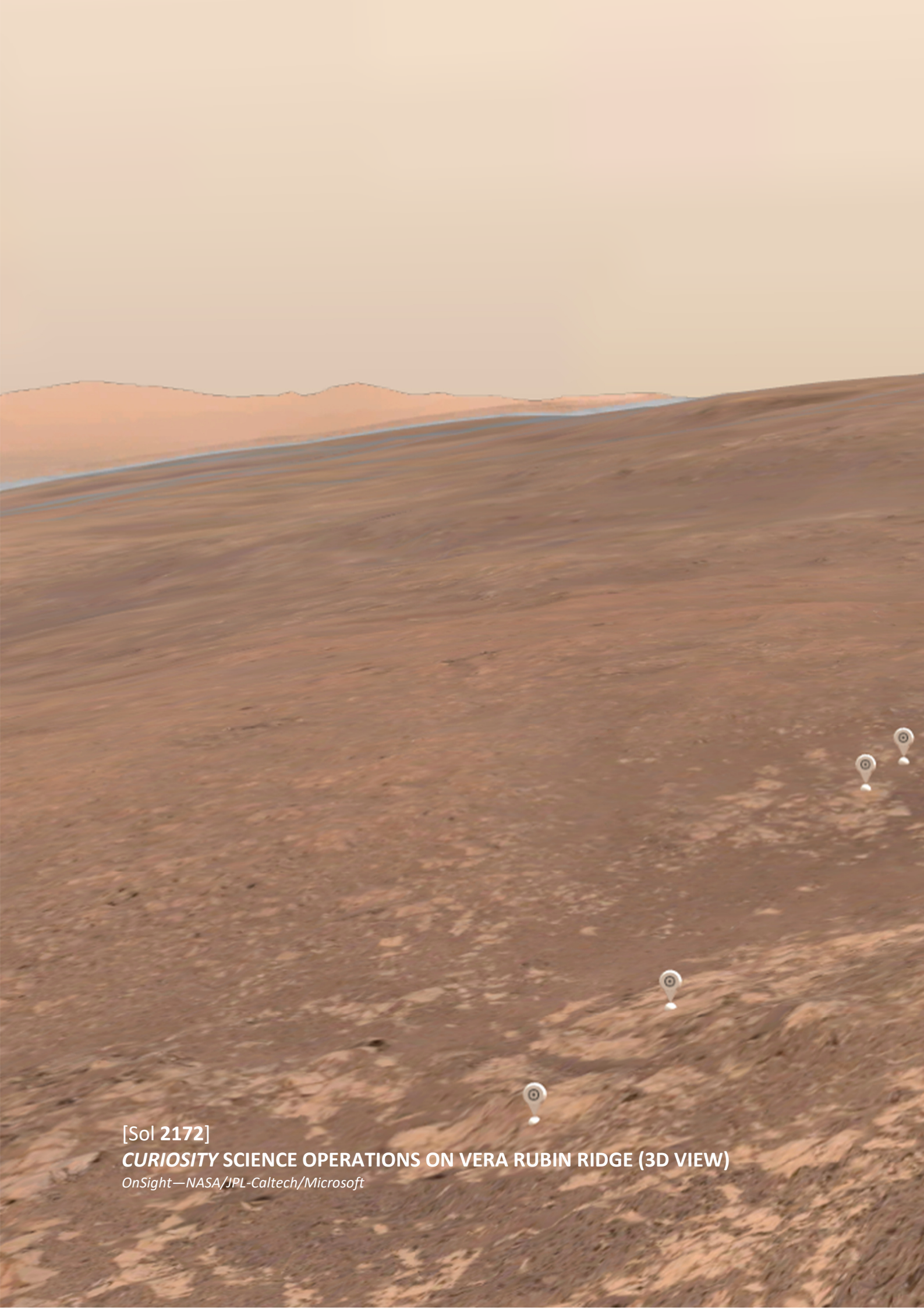

[Sol **2172**]

CURIOSITY **SCIENCE OPERATIONS ON VERA RUBIN RIDGE (3D VIEW)**

OnSight—NASA/JPL-Caltech/Microsoft



ANNEX A

CONTRIBUTION TO CHEMCAM OPERATIONS

In contrast with orbital missions for which observations can be planned a long time in advance, the *in situ* missions are discovery-driven, requiring constant attention to assess each new locations on the ground. As such, a large team of scientists and engineers convene on a daily basis to operate the *Curiosity* rover and to produce scientific analyses and observations on the Martian surface. ChemCam, in particular, provides chemical analyses remotely and at a low energy cost for the rover. It is thus routinely used to estimate the scientific value of outcrops surrounding the rover, before involving more time- and energy-consuming analyses. This annex describes the day-to-day rover operations, as well as the distinct roles on the ChemCam team. Lastly, I will also discuss my personal contribution to ChemCam operations, including the development of tools to assist in this on-going effort.

CURIOSITY **SURFACE OPERATIONS**

The *in situ* exploration of Mars constitutes a peculiar research environment for geologists used to roam the site of their study on Earth, at it is located at ~200 million kilometers from the Earth. In order to close the distance, virtually, a number of tools have been perfected over the last missions on the surface of Mars to facilitate its investigation. Researcher and engineer gather each day (sol n on Mars) from various parts of the world to define the rover's plan of activity for the next day (sol n+1 on Mars). If the day-to-day rover operations reflect short-term decisions and require flexibility to account for unexpected observations on the ground, the rover's investigations are articulated along longer-term exploration campaigns, revolving around the mission's objectives and often guided by orbital observations.

This two-level approach is also reflected in the organization of the operation teams, which are composed of "tactical" roles focusing on the day-to-day rover operations and the analysis of the acquired scientific data, and "strategic" roles to ensure that the rover activities are in line with the identified long-term science objectives and strategic goals. The tactical roles are divided into two groups, tasked with the analysis of the images and data received from the rover during the day (downlink) for one and planning of the activities of the following day (uplink) for the other.

Downlink depends on orbiter telecom pass over the rover position in order to transmit data to the Deep Space Network back on Earth. Such passes occur in average four times a day, but with limited data volume transmitted as information on telemetry, rover health, and images are given priority over the transmission of the instruments' scientific data. The scientific data is rapidly reviewed upon reception to provide a tactical feedback to the operation team on the same day, followed by more in-depth analyses that will be reported on to the science team over the week.

For each instrument, the tactical roles provide information on its technical and scientific capabilities in the design of science activities by the scientific groups. Rover activities are created in the "Mars Science Laboratory Interface" (MSLICE), used by all MSL team members to share key information in real-time on the proposed science targets as well as the details of the proposed science activities to be carried out on Mars.

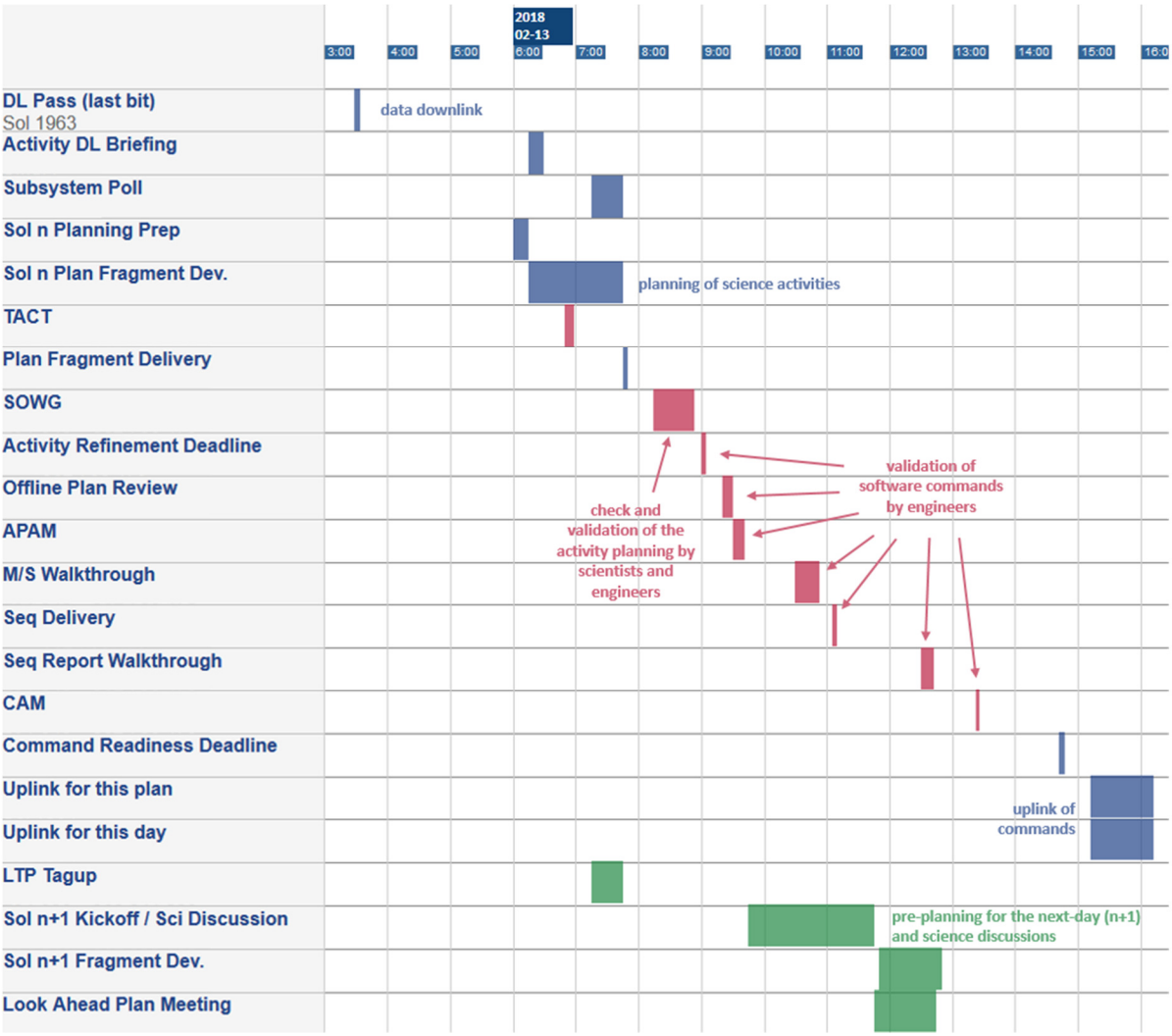

Figure A.1: Daily planning of teleconferences followed by the scientists and engineers on shift during the MSL operations to plan the rover activities for the following day, discuss previous observations and uplink commands to the rover on Mars.

Therefore, each day, scientists and engineers "on shift" propose and discuss the activities for the next day on Mars, based on the data received during the day (images and instrumental analysis), in order to come up with instrument sequences and commands to be uplinked to the rover (Figure A.1).

CHEMCAM OPERATIONS

Due to its low energy consumption and its capability to retrieve rapidly both images and compositional information on targets around the rover, ChemCam is extensively used for operations to help with tactical and strategic decisions (~300 spectra acquired per day) [*Maurice et al.*, 2016]. Upon reaching a new location, ChemCam also has the capability to probe autonomously the composition of the bedrock, without requiring inputs from Earth [AEGIS; *Francis et al.*, 2017] (Figure A.2). As such, ChemCam can provide a preliminary analysis of a new study area on the day the rover reached it, allowing the team to make an informed decision on whether to deploy the rover arm and involve "contact-science" activities (MAHLI and APXS) over the next day, which are more costly in time and energy.

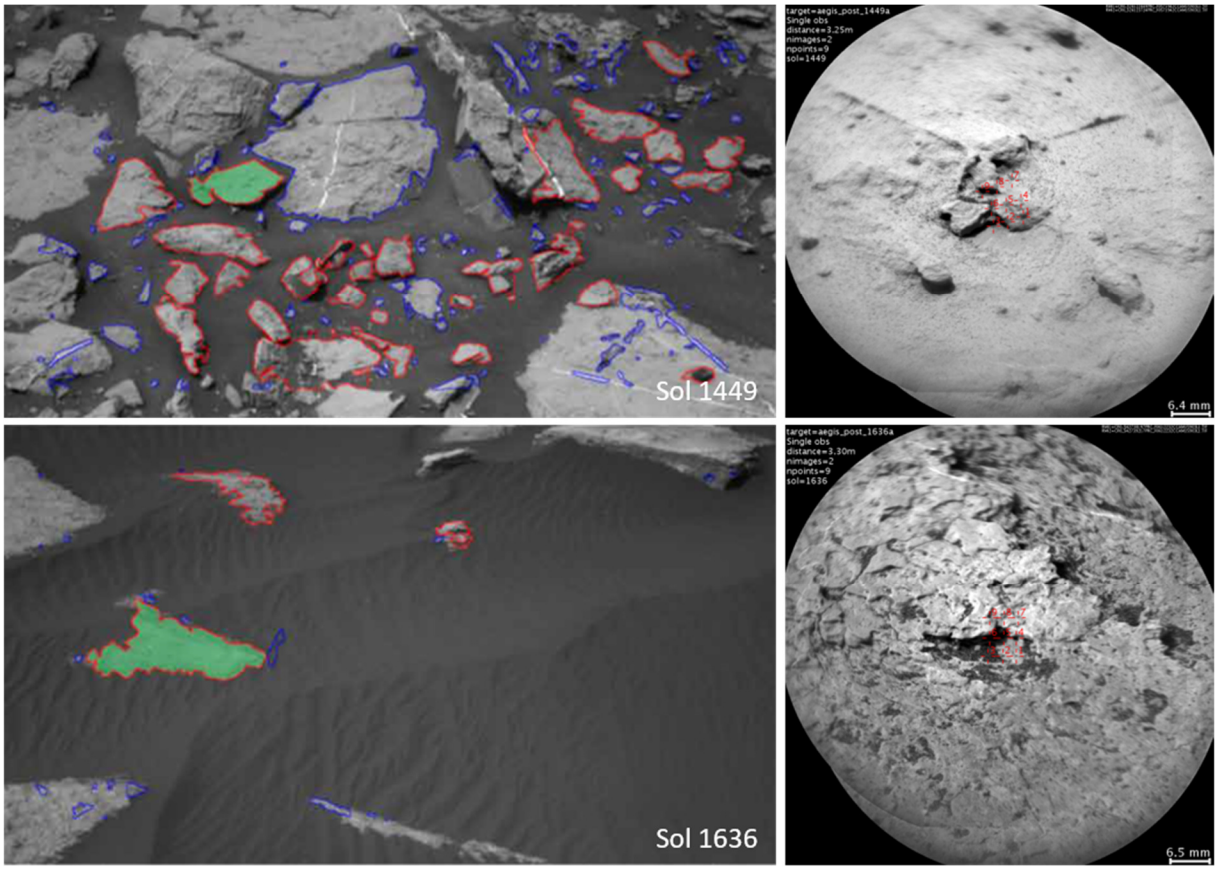

Figure A.2: Example of AEGIS autonomous post-drive target selection (left) [from *Francis et al.*, 2017] and associated ChemCam target (right). Target selection is based on analysis of Navcam images (the selected target is in green; red outlines correspond to other potential targets and blue outlines to rejected targets).

Since the objectives of the MSL mission are located outside of the landing ellipse, mobility is often favored in order to make progress towards the area of interest identified from orbit. Indeed, even after six years on the Martian surface, the rover Curiosity has not yet reached the clay and sulfate units that constitute the main objectives of the mission. As such, when priority is given to mobility over the detailed analysis of outcrops, ChemCam is still able to provide opportunistic measurements between two drives. ChemCam thus records continuously the composition of rocks along the rover traverse, whereas APXS and CheMin are only deployed more discretely. For example, ChemCam sampled igneous float rocks scattered in the sedimentary rocks that portray a more evolved composition than previously envisioned [*Sautter et al.*, 2015], and identified iron-nickel meteorites for the first time on another planet [*Wellington et al.*, 2018]. In some cases, these opportunistic analyses have led to unexpected discoveries, such as the high-Si halos along fractures in the Stimson formation (e.g. Figure A.3), which incited the rover to turn back in order to study such features in more details, and in that case, even conduct a drilling campaign.

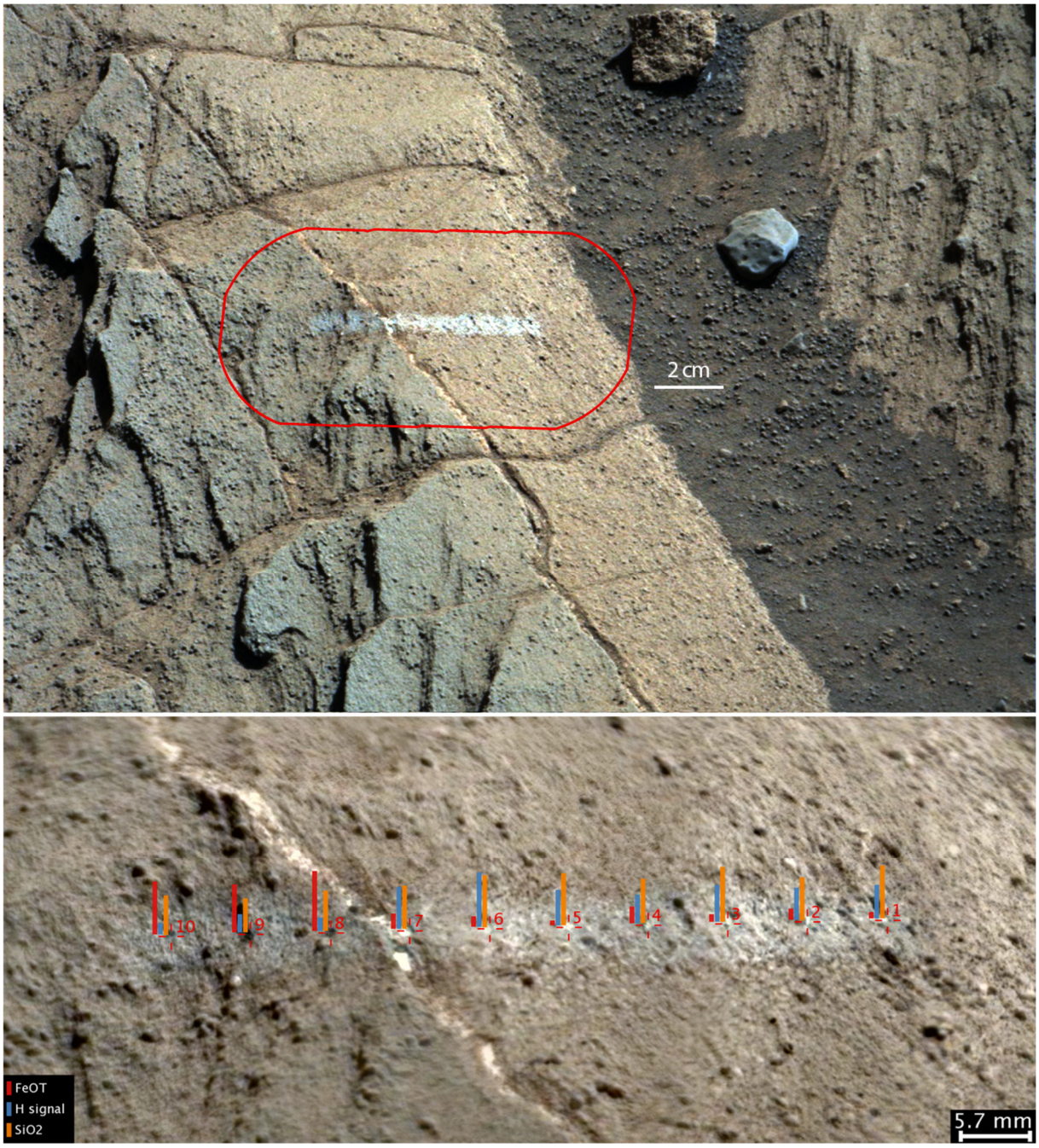

Figure A.3: ChemCam observation on the Iona target in the Stimson formation, displaying high-Si (and H) compositions on the right of the light-toned vein and typical host rock composition on the left side of the vein (higher FeOT but lower Si and H contents) [*Rapin*, 2016].

For in-depth investigations at specific locations, such as drill sites, ChemCam is able to cover a large array of targets to characterize the geochemical variability in outcrops at the sub-millimeter scale. It thus complements the bulk analyses of the APXS and CheMin instruments and provides comparative analyses in the nearby outcrops up to 5-6 meters from the rover (e.g. Figure A.4).

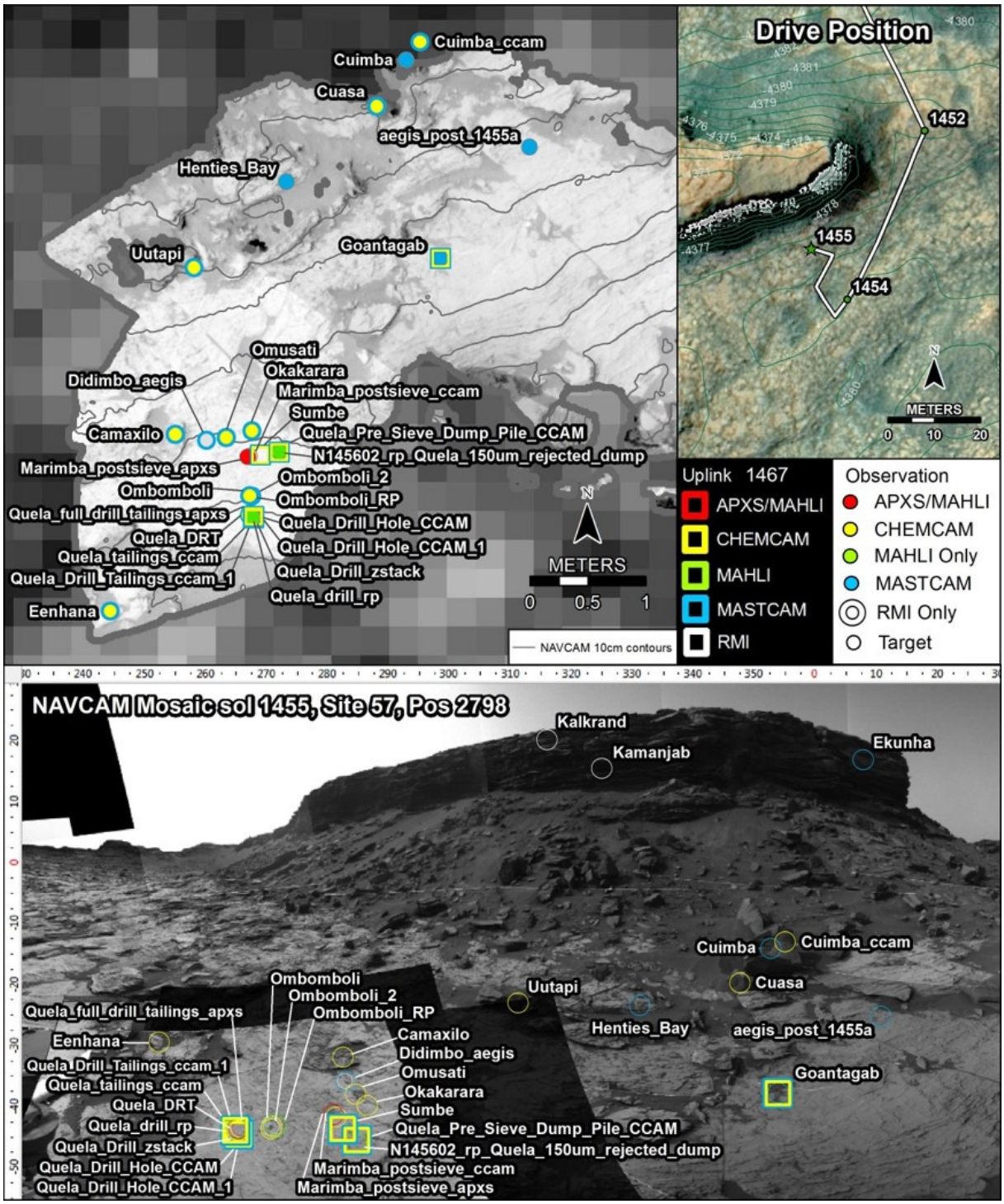

Figure A.4: Example of a drill site (Quela) investigation involving all instruments onboard the *Curiosity* rover. In particular, the ChemCam instrument was extensively used at this location: RMI images on the escarpment in the background, compositional analysis on fallen rock blocks at 3-4 meters from the rover and characterization of the geochemical variability of the mudstones near the rover, in close proximity to the drill-hole.

Lastly, ChemCam is also used to survey terrains at long-distance, with an increased resolution compared to the other cameras on the rover, as well as orbital images. Such long-distance images reveal fine-scale textural and structural details in outcrops (Figure A.5) and help plan future rover activities and exploration campaigns.

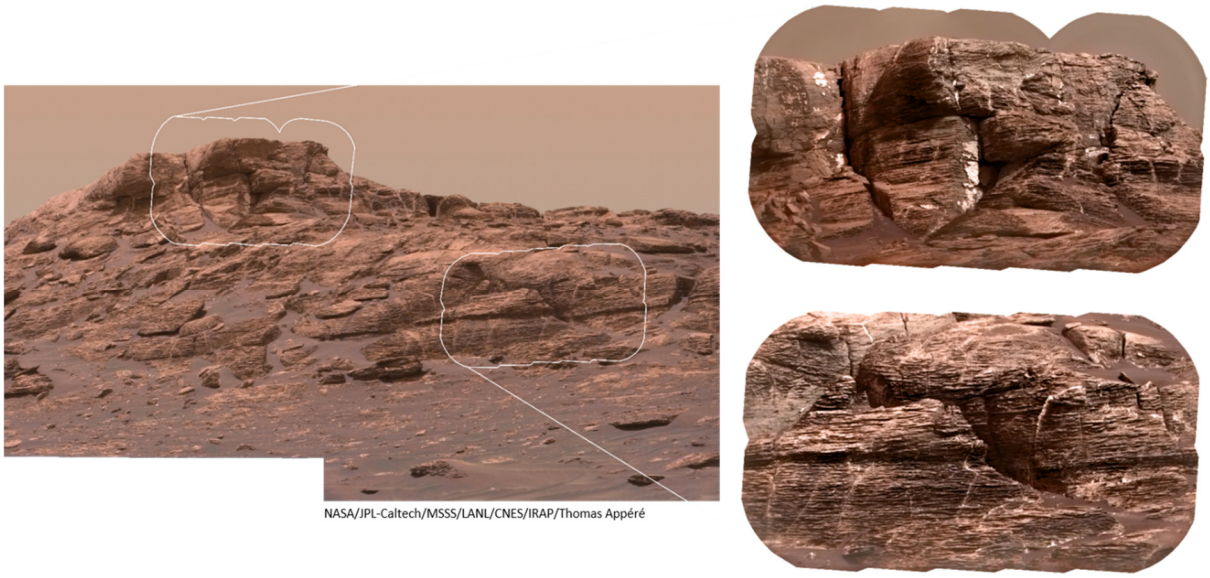

Figure A.5: Long-distance RMI images (right) of Vera Rubin Ridge, observed during the rover approach, that reveal finer details compared to Mastcam images (left) and highlight sub-vertical light-toned fracture fills cutting through the outcrops.

THE CHEMCAM TEAM

ChemCam operations are shared between the French and American teams, switching every week. On each shift, the PEL (Payload Element Lead) supervises operations for the instrument, assisted by the SPUL (Science Payload Uplink Lead) responsible for the design of activities for uplink and the STG (Science Theme Group member) to assess the scientific value of such activities. The SPDL (Science Payload Downlink Lead) is tasked with the analysis of the data downlinked and reporting. Lastly, the engineer's counterparts of the scientific roles (EPUL and EPDL) ensure that scientific activities comply with the engineering requirements. For my part, I have participated in the ChemCam operations as both STG and SPDL.

The STG work hand-in-hand with the SPUL and ensure the link between the SPDL and the LTP (Long Term Planner), who outlines the rover science activities for the near future. While the SPUL work on the details of the science activities, such as distance to the target, pointing refinements and generation of footprints, the STG assess the relevance of such activities to the science objectives and incorporate feedbacks from the SPDL on targets previously analyzed in the area (for the sol n plan and sol n+1 pre-plan; Figure A.1). I belonged to the "Geology" Science Theme Group, one of the four MSL theme groups.

Upon reception of the instrument data back on Earth, the SPDL provide a preliminary analysis of the information downlinked and assess its integrity. The analysis of the data needs to be done quickly in order to pass on any relevant information to the PEL and STG before the "Scientific Operation Working Group" (SOWG) teleconference, ~3 hours after the start of operations (Figure A.1). The SPDL scientific analysis of each ChemCam target is then compiled into a PDF report and shared with the MSL team (Figure A.6). These preliminary reports will later facilitate the more in-depth studies on the area of interests along the rover traverse.

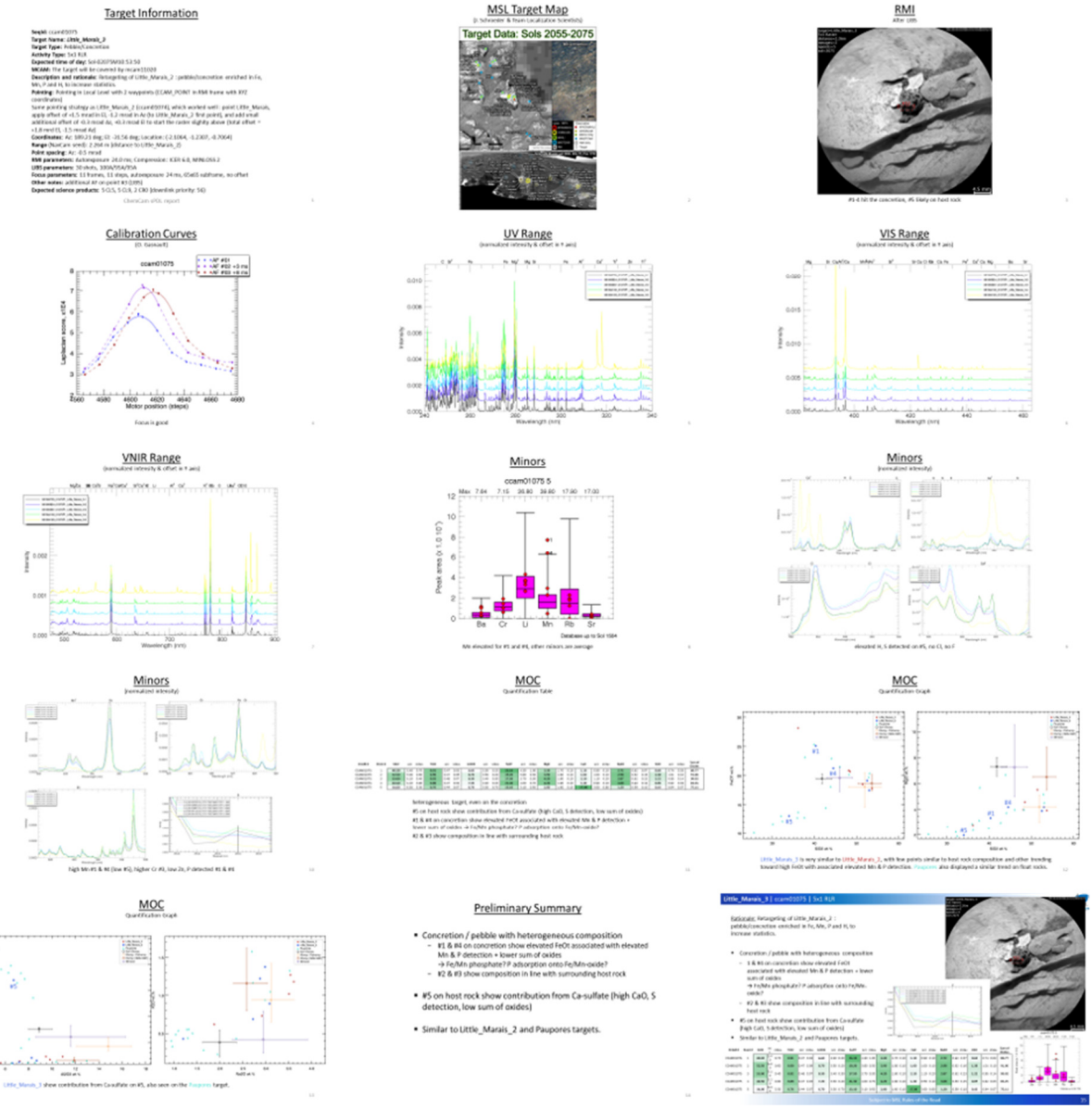

Figure A.6: Overview of one ChemCam SPDL report shared with the MSL team. The report feature information on the target localization, the RMI mosaic image, normalized spectra for each spectrometers and for some minor elements of interest (e.g. H, P, Cl and F), concentrations in major (table) and minor (boxplot) elements, graphs comparing the target composition with averages for geologic units along the traverse as well as recent ChemCam observations and lastly, a summary of the preliminary results from the target.

Lastly, each Wednesday, one of ChemCam scientists (usually an SPDL) provides a summary of the instrument observations over the past week during a specific Science Discussion teleconference (Figure A.1), known as the “Instruments Happy Hour”.

AUTOMATED REPORTING TOOL

The workload of an SPDL varies drastically depending on the amount of ChemCam data received since the last SPDL shift and how extensively the instrument was used over the same period. For example, Monday’s SPDL will need to analyze the data collected over the weekend (three days’ worth of data). Additionally, the amount of data generated by ChemCam has increased significantly over the course of the mission, notably after the introduction of the autonomous target selection and data acquisition routine (AEGIS) but also in order to cope with the lack of drill capability over the last year. As a result,

the SPDLs may be faced with up to 10-15 targets to process in a day, which involves time-consuming activities such as data retrieval and preparation of the target reports, on top of the critical scientific analysis of the data.

As such, in order to alleviate the workload of the SPDLs during “downlink rush”, I have developed a small software to automate the retrieval of relevant data from the MSL servers and the creation of a partially filled-in target report (Figure A.7). The SPDL input the sequence ID of one or several targets and the software will download the related products available on the MSL servers and create the skeleton of the report(s) partially filled in with the downloaded products.

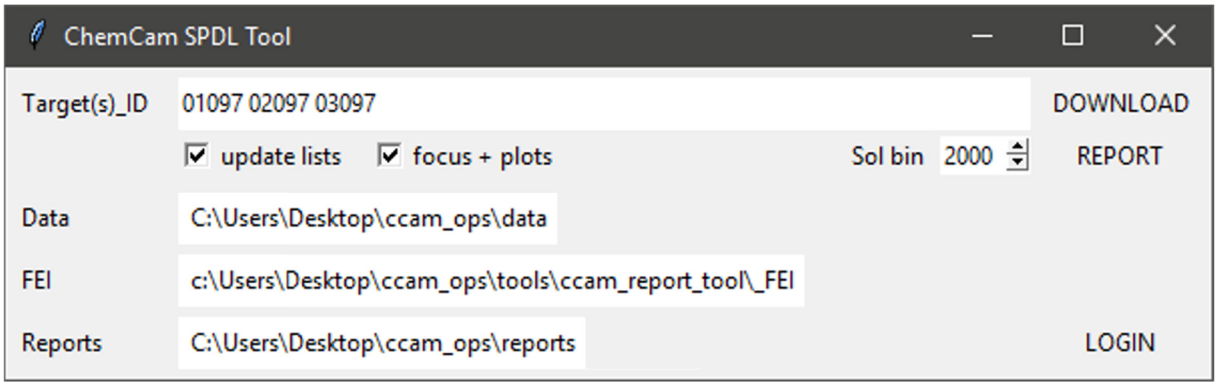

Figure A.7: ChemCam SPDL Tool interface, where the user can input the ID of the ChemCam target(s) considered, and if some additional products need to be downloaded as well.

The automation of these tasks allows the SPDLs to focus on the scientific analysis of the data, such as the detailed review of spectra to spot detections in minor elements not routinely quantified (e.g. Cl, P, F or Ni), shot-to-shot analyses to identify chemical trends with depth or comparison with recent data (ChemCam and/or APXS) to highlight variations in composition. As a result, the SPDL will be able to provide the MSL science operation teams with in-depth preliminary results on the data on a shorter notice. Indeed, if the SPDL spend ~15 min (probably more) per target to retrieve the relevant data and draft the report before proceeding to its scientific analysis, it would mean at least two and half hours devoted to the task for a 10-targets shift. Instead, the tool automates the process and frees as much time to work on the science behind the data. In the future, the ChemCam team intends to automate the generation of additional data products such as RMI image mosaics and various graphs used by SPDLs. The ability to either generate such products directly in the software, or retrieve them from MSL servers, would further increase its efficiency.

Furthermore, the future NASA rover (*Mars2020*) carries onboard the SuperCam instrument, an enhanced version of ChemCam that provides Raman and Infrared spectrometry on top of the LIBS. As a result, operations are expected to be significantly more complex compared to ChemCam, with an increased amount of data to be assessed each day. Additionally, in order to avoid “restricted sols” (i.e. when downlink is not received before the science planning), the mission aims to complete the operations within 5 hours (down from 8 to 10 hours for *Curiosity*; Figure A.1). As such, it appears that automation of part of the operations, notably for downlink activities, will doubtless prove more crucial to SuperCam than it is to ChemCam. Lastly, *Curiosity* may still be active by the time the *Mars2020* rover land on the surface of Mars, which would imply that SuperCam and ChemCam might operate simultaneously.

IMPLICATIONS ON THE WORK CONDUCTED OVER THE PH.D.

The ability to take part in ChemCam operations was invaluable in order to understand how the *Curiosity* rover and the ChemCam instrument operate, and to appreciate the collaborative nature of the work involved behind the acquisition of data. It also allowed me to propose additional observations to be carried out on Mars, either in the form of feedback from previous observations as SPDL or more directly as STG when discussing the scientific rationale for prospective ChemCam targets. As a result, the studies presented in this manuscript are built on preliminary observations made during the ChemCam SPDL shifts, weeks after weeks, and fleshed by additional observations requested by the ChemCam SPUL and/or STG.

For example, the chemical variability in Ca-sulfate veins was noted sporadically along the rover traverse, and logged in the SPDL reports, until chemical trends emerged from the ChemCam dataset. Upon further investigation, we managed to reconnect *a posteriori* the scattered observations together.

Similarly, the thorough analysis of the ChemCam spectra by SPDLs allowed for the identification of P enrichments on dark-toned inclusions and sub-horizontal layers in the Sutton Island member of the Murray formation. Without such detailed tactical analyses of the data, the presence of P in the spectra might have been noticed much later, after the rover moved on. It would thus have prevented ChemCam from performing additional analysis on similar features.

Lastly, the ChemCam SPDLs and SPULs rapidly identified Fe-rich dark-toned mineral phases on Vera Rubin Ridge. The preliminary reports drafted by the ChemCam SPDLs incited the team to perform additional analyses on similar geological features in the vicinity, which then enabled the observation of low-Fe bleached halos around the Fe-rich features indicating that the iron was mobilized from the adjacent host rock during diagenesis.

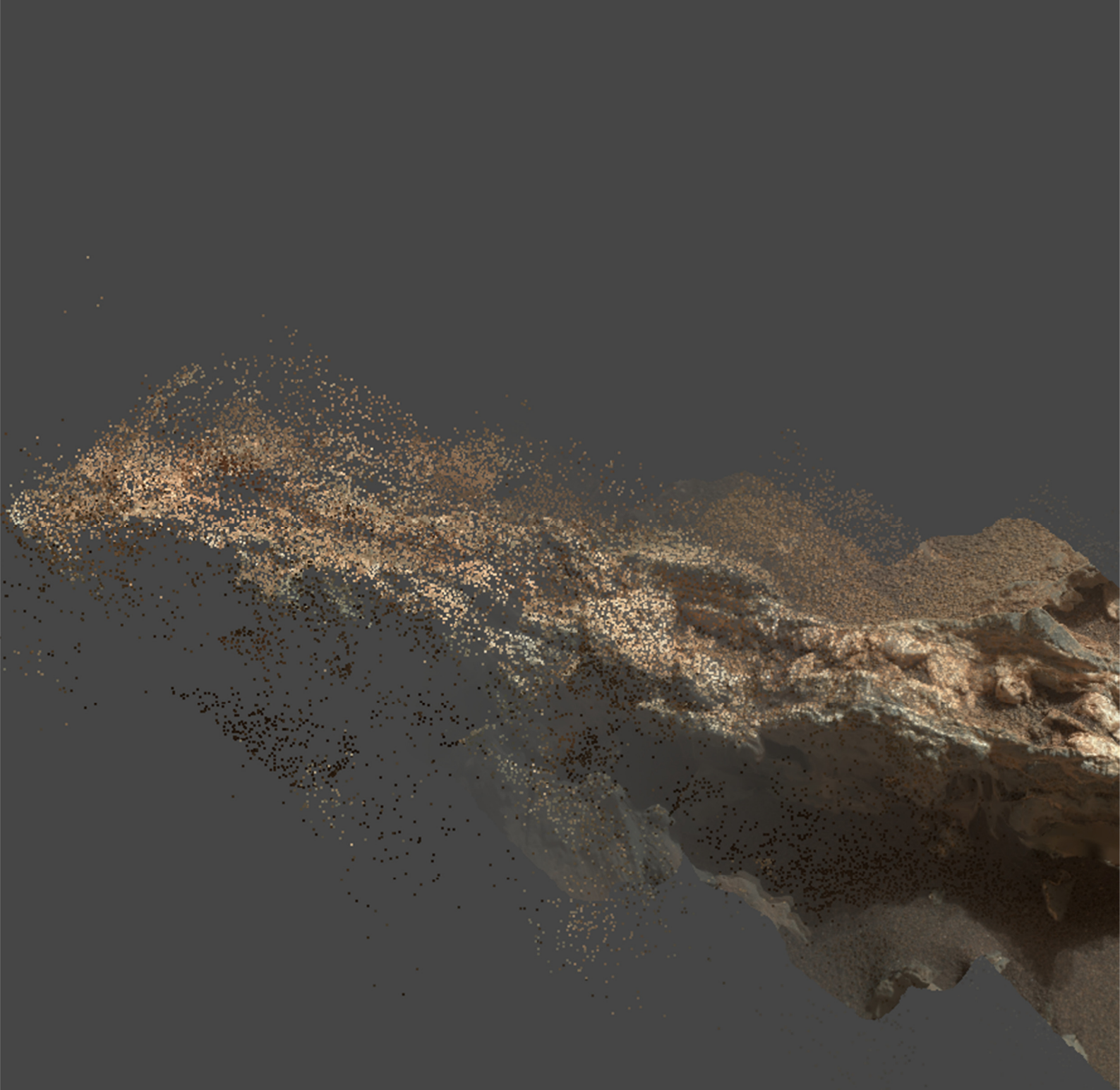

PHOTOGRAMMETRIC RECONSTITUTION OF GARDEN CITY VEINS

Agisoft PhotoScan [credit: Gwénaël Caravaca]

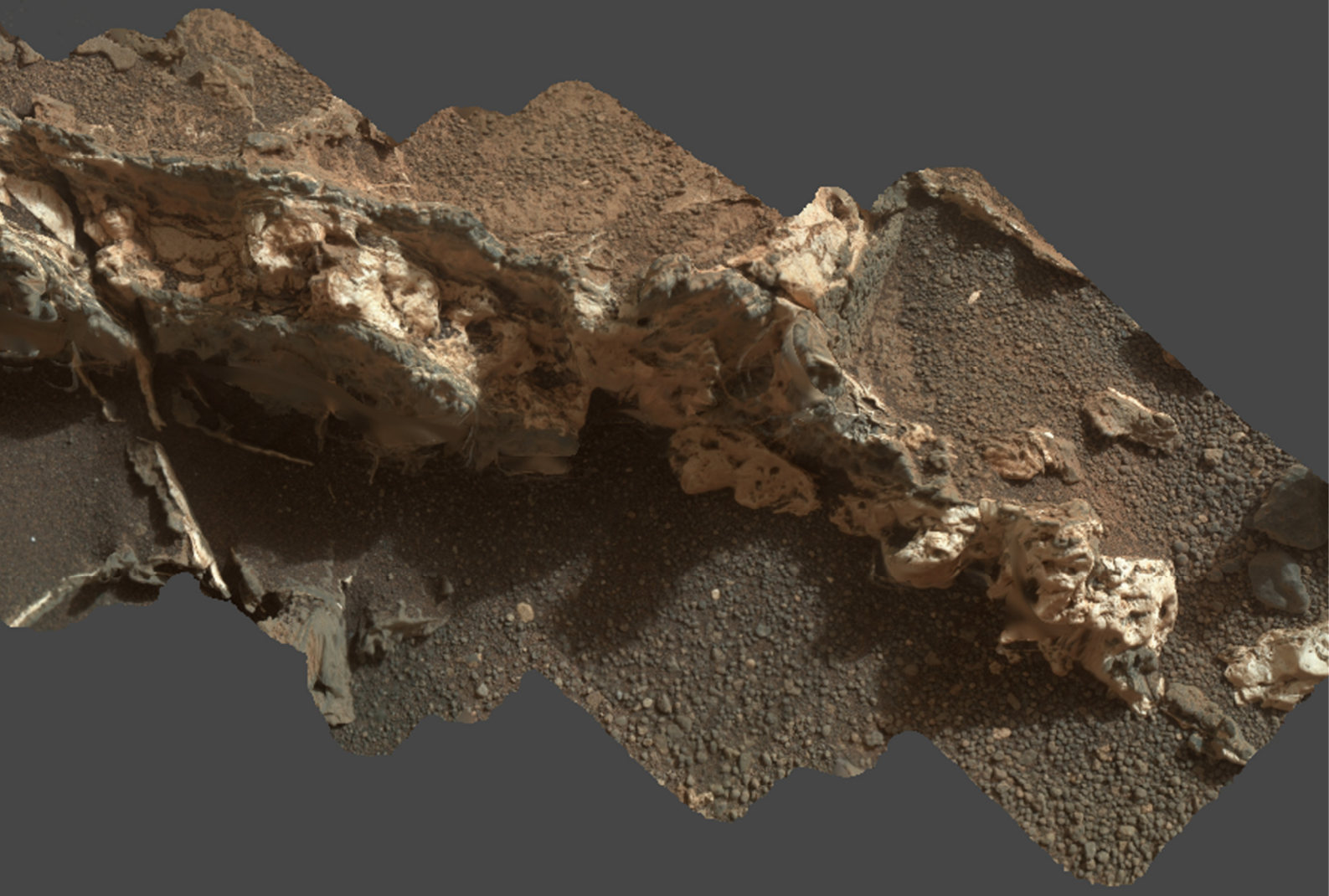

ANNEX B

RECONSTRUCTION OF DIGITAL OUTCROP MODELS FROM THE *CURIOSITY* ROVER IMAGES

While the *Curiosity* rover brings on the Martian surface an impressive suite of instruments to characterize the texture, chemistry, and mineralogy of the rocks, it cannot truly substitute to the work accomplished by geologists on the field. Indeed, even though the rover carries 17 cameras onboard, the produced images (both color and greyscales) cannot capture the depth of the outcrops, making it hard for planetary geologists to conceptualize the geometry of the geological textures and structures observed in three dimensions (3-D). In addition, to get a broader view of the outcrops, geologists often stitch together several images to form mosaics (distinct point of views) and panoramas (same point of view), but this process also introduces distortions in the individual images.

In order to perceive depth to some degree on Mars, the navigation cameras (Navcam) and the hazard avoidance cameras (Hazcam) located on the MER rovers (*Opportunity* and *Spirit*) and on the MSL rover (*Curiosity*) acquire stereo images ("left" and "right" paired cameras) with sufficient overlap to produce stereo view "anaglyph" of the outcrops (Figure B.1). The 3-D position of each pixel can then be calculated by stereo triangulation to produce terrain maps (3-D model) and range maps (distance contour lines). These products are used by engineers to examine the topography of the terrains ahead on the rover path, but also by the rover itself during the drive to autonomously navigate the path of least resistance [*Maki et al.*, 2003, 2012]. The terrain models are also used to provide the MSL team with a virtual environment to contextualize the observations of the rover in their 3-D setting[2].

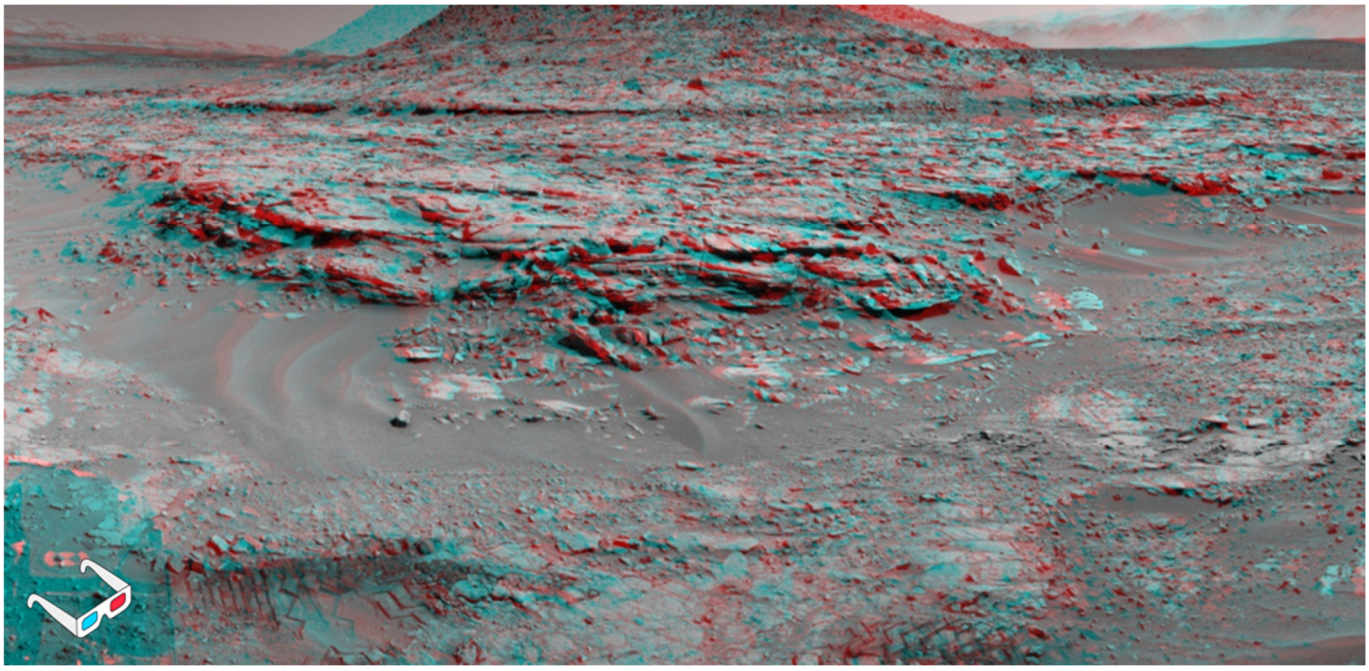

Figure B.1: Navcam anaglyph of Mt. Remarkable, at the Kimberley waypoint along the Curiosity rover traverse. The scene appears in 3-D when viewed through red-blue glasses (red lens on the left) [credit: NASA/JPL-Caltech]

[2] OnSight tool, more information at https://www.jpl.nasa.gov/news/news.php?feature=4451

The resolution of these navigation 3-D products, however, is often insufficient to retrieve valuable information that can be used by planetary geologists to study in details the geometry and morphology of outcrops. On Earth, field geologists are starting to use high resolution 3-D models of outcrops, also known as Digital Outcrop Models (DOM), to characterize inaccessible geological structures and provide inputs for quantitative structural modelling [*Bistacchi et al.*, 2015; e.g. *Smith et al.*, 2016; *Corradetti et al.*, 2018]. These studies rely on the "Structure from Motion" (SfM) photogrammetric method to reconstruct high fidelity 3-D models from overlapping images taken from distinct locations and orientations [e.g. *Westoby et al.*, 2012].

Over the course of my Ph.D., I had the chance to interact with scientists and engineers that used such image photogrammetry techniques to produce detailed 3-D virtual environments of the planetary landscapes, from orbital and *in situ* images, notably for public outreach and educational purposes[3]. With their help, we have started to produce high-resolution Digital Outcrop Models (DOMs) from the images acquired by *Curiosity* at Gale Crater in order to quantitatively assess the geometry of Martian outcrops.

IMAGE DATASETS AND PROCESSING

First and foremost, I have developed a small program to automatically retrieve the relevant image datasets from the NASA Planetary Data System (PDS[4]). In order to have both extensive coverage and high-resolution images of the outcrops, we considered the image datasets from 5 distinct cameras: the two Navcam, the two Mastcam and MAHLI.

The two Navcam stereo cameras (left and right; 14.67nm focal length) provide greyscales images (2.5 mm/pixel at 3 m from the rover) with significant overlap and extensive spatial coverage of the surface, in the form of 360° panorama at each rover locations and target images of interest (NCAM) as well as low-resolution degraded images acquired automatically during the drives (TRAV). Additionally, rover mask files (MXY) are also available on the PDS to mask parts of the rover visible in the Navcam images. The spatial coverage of the Navcam is required to generate a low-quality model and locate the higher resolution images.

The two Mastcam cameras (34 mm and 100 mm focal lengths) provide true color images at the outcrop scales, with increased resolution (up to 150 µm/pixel at 2 m from the rover) compared to the Navcam images but significantly lower spatial coverage and image overlap. Mastcam images can also include parts of the rover, which need to be manually masked as the associated mask files do not exist on the PDS to do so automatically. The resolution of the Mastcam images allows to retrieve valuable information on the texture and structure of the outcrops.

Finally, the MAHLI camera (18.3 mm focal length), mounted on the robotic arm of the rover, produces high-resolution close-up true color images (up to 14 µm/pixel at the minimum distance of 2.1 cm) but with a narrow field of view. MALHI is also able to acquire a series of images focused at different distances (z-stack) that provide additional information on depth. The camera reveals fine-scale details on outcrops, enabling the reconstitution of highly detailed 3-D models (e.g. Figure B.2) where it was used extensively to characterize fine-scale geological features such as fracture-fills.

[3] VR2Planets, more information at https://vr2planets.com
[4] PDS Imaging Node for the MSL mission: https://pds-imaging.jpl.nasa.gov/

Each image file (.IMG) is associated with a label file (.LBL) that includes information on the rover position (including the relative positions of the mast and the arm) and camera metrics. The images are processed and converted to the TIFF image format using a software[5] provided by the PDS, and then cropped to remove JPEG artifacts and black pixels on the edge of the images. For Navcam images, the mask files are incorporated into the alpha channel (transparency). Lastly, the rover planetocentric coordinates for each image are extracted from the corresponding label files and incorporated into the image along with the camera specifications (focal length and pixel size) as EXIF metadata, using a dedicated software[6].

RECONSTRUCTION OF 3-D MODEL USING SFM PHOTOGRAMMETRY

Agisoft Photoscan Pro was used to model the outcrops observed by *Curiosity* on Mars. The software relies on the digital photogrammetry approach, which is based on the apparent displacement of the position of a feature with respect to a reference point (i.e. parallax), caused by a shift in the point of view (location of the cameras). Photoscan then uses the Structure-from-Motion (SfM) algorithm to compute the geometry of an object to model using the parallax [*Micheletti et al.*, 2015; *Carrivick et al.*, 2016].

The georeferenced rover images are imported into Photoscan, which automatically recognize the metadata of each image including camera specifications (focal length and pixel size), used to calibrate the parameters of each camera, as well as the image coordinates that will pre-locate the camera. As we are located on another planet, we also need to change the coordinate system to Mars. I have therefore implemented the Mars2000 projection parameters.

The software will first align the cameras, refining their positions (notably their orientations) and calibration parameters by finding common points in overlapping images to match. As a result, the software produces a sparse point cloud of 3-D tie points (Figure B.2.1) as well as a set of camera positions. At this stage, the sparse cloud may include some outliers which can be realigned or deleted and subsequently ignored if no improvement is observed. For relatively confined outcrops with significant image coverage and overlap, this step may be relatively straightforward (e.g. Figure B.2). However, for larger scenes involving multiple rover locations, trying to "blindly" align all rover cameras at the same time may not work. In order to successfully compute the sparse point cloud, we will first need to align the low-resolution grayscales Navcam only, and then, align the higher resolution Mastcam and MAHLI cameras based on the Navcam cameras position. If the automatic alignment fails, additional tie points can be manually implemented to help to process the unaligned images. Based on the sparse point cloud and camera positions, Photoscan will look for additional matching points in the aligned camera images to compute a high-resolution point cloud, or dense point cloud (Figure B.2.2). From there, Photoscan will generate the surface mesh linking the tie points together (Figure B.2.3), and which can then be textured using the input images (Figure B.2.4).

As a result, Photoscan thus produces a 3-D reconstitution of the outcrops imaged by the *Curiosity*, georeferenced and textured, which can then be exported to extract lithological and structural information using additional 3-D visualization and processing software such as Cloud Compare.

[5] IMG2PNG software, http://bjj.mmedia.is/utils/img2png/
[6] ExifTool software, https://www.sno.phy.queensu.ca/~phil/exiftool/

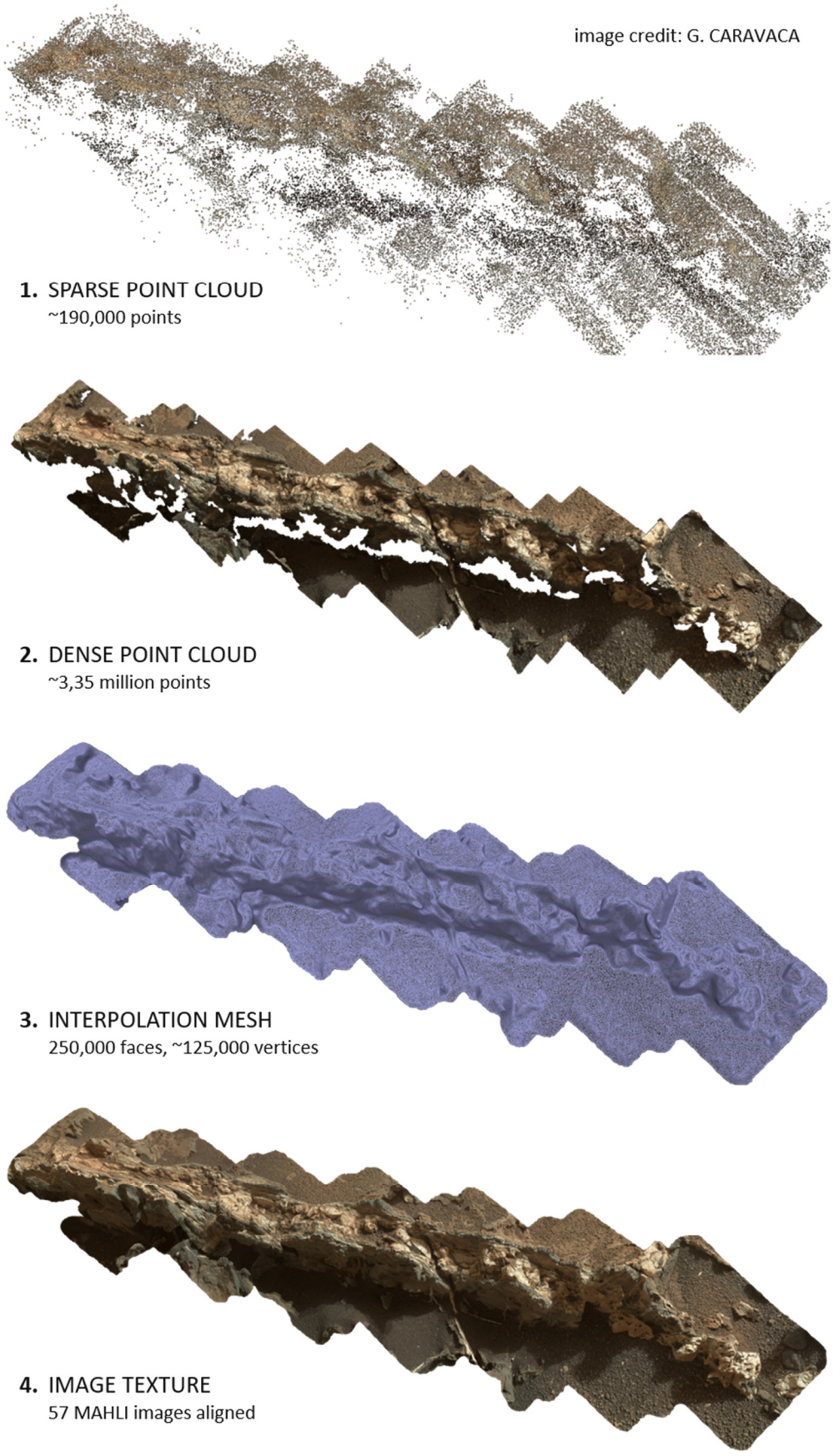

Figure B.2: Photogrammetry processing steps to produce the DOM of a vein at Garden City (MAHLI images)

STRUCTURAL ANALYSIS OF VEIN NETWORKS ON MARS USING DIGITAL OUTCROP MODELS

In order to assess the mechanisms behind the formation of the widespread Ca-sulfate vein networks at Gale Crater, we have produced DOM of the outcrops of the Sutton Island member of the Murray formation (between the sols 1536 and 1545), where well exposed crack system display multiple orientations (Figure B.3A) [*De Toffoli et al.*, n.d.]. Indeed, at that location, sub-horizontal Ca-sulfate veins could be potentially interpreted as primary evaporite layers or early diagenesis cementation [*Newsom et al.*, 2017; *Nellessen et al.*, 2018], while sub-vertical and oblique veins indicate later diagenetic fluid circulations [*Nachon et al.*, 2014; *L'Haridon et al.*, 2018].

The DOMs were processed using the Cloud Compare software, to extract measurements on the orientation of fractures (marked by polylines and plane fit; Figure B.3A). The outcrops feature neatly identifiable sets of fractures with specific orientations: the sub-horizontal fractures, and two oblique sets (Figure B.3B).

- Sub-horizontal veins do not show significant thickness variations and present undulate, slightly wandering trend recognizable in the measurements by ~15° variation range in dipping angles and a large variability in dip directions (Figure B.3C). The veins appear to follow the rock's layer boundaries but also crosscut the layers on occasions.
- The oblique veins are rarer and display significant variations in thickness due to clear en-echelon structures, indicating an extensional regime (i.e. the vertical stress exceeds the horizontal ones). Two sets of oblique fractures were identified based on dip/dip-direction trends: N290 with 67° dip, and N155 with 53° dip (Figure B.3B, C), thus intersecting at a 60° dip angle.

In addition, mutual cross-cuttings between the two sets of veins suggests a syn-genetic formation and no evidence for displacement or recurrent truncation one set on the other was observed to determine the relative sequence of events.

The observed vein textures and orientation trends in Gale outcrops bear similarities with networks of intersecting sulfate veins in the Watchet Bay and Bletterbach terrestrial analog sites, formed by hydrofracturing within mudstones levels. At Gale, the fracture formation is attributed to two different contributions: (i) oblique fractures produced by an extensional regime with principal stress on the vertical axis and wandering horizontal minimum stresses, and (ii) sub-horizontal fractures formed by hydrofracturing, synchronous with the extensional deformation, where fluid overpressure exploited pre-existing weakness planes in the form of mudstone layering. The extensional regime is consistent with the Gale geological context, with progressive sediment overload, while hydrofracturing can occur either during compaction or exhumation to destabilize pore-fluid pressure and initiate buoyancy.

Thus, the study of fracture orientations from digital outcrop models on Mars shows that light-toned Ca-sulfate vein, including sub-horizontal layers, formed contemporarily during the diagenesis of the sediments [*De Toffoli et al.*, n.d.]. As such, these observations invalidate the hypothesis for primary or early diagenesis formation of sub-horizontal Ca-sulfate cement attributed to evaporitic surface or near-surface conditions.

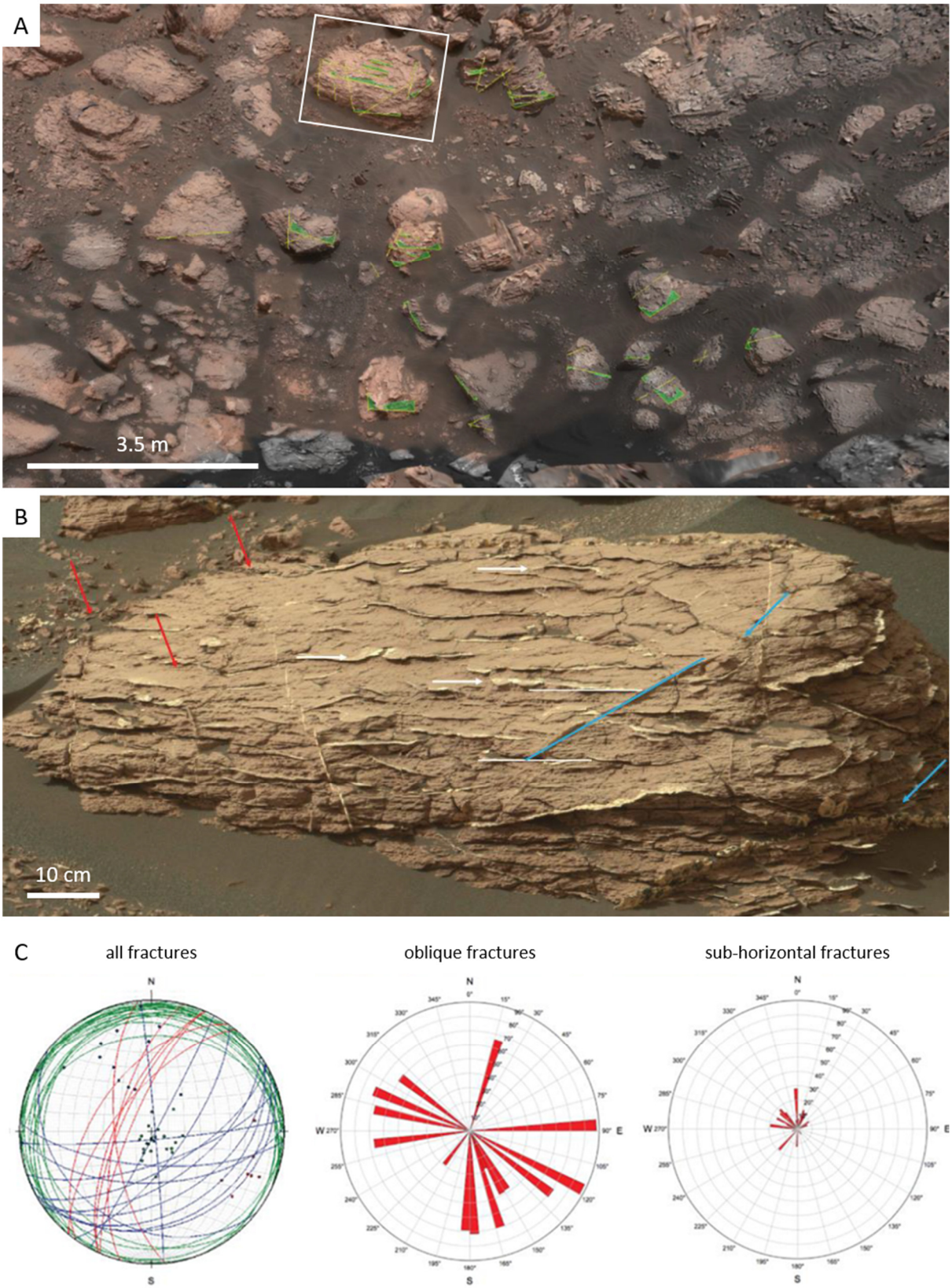

Figure B.3: (A) 3-D reconstruction of the outcrops explored by the *Curiosity* rover between the sols 1536 and 1545 (Sutton Island member of the Murray formation), with some interpreted fracture planes highlighted in green. (B) Mastcam image of one outcrop illustrating the three distinct vein sets observed: the two oblique sets (red and blue) and the sub-horizontal veins (white). (C) Dip direction and dip angle measurements on the fractures observed in this study area [modified from *De Toffoli et al.*, n.d., in prep].

PERSPECTIVES

The digital modeling of outcrops becomes an increasingly attractive tool for Earth geologist to investigate inaccessible geological structure (e.g. confined cave systems or high hanging cliffs), it reflects more a convenience than an absolute necessity. On Mars, however, until geologists are able to roam the planet to fully appreciate first-hand the outcrops geometry–which is not likely to happen before at least 2030—they will always need to rely on proxies to do so. Augmented Reality (AR) and/or Virtual Reality (VR) tools can therefore prove to be extremely valuable in this case.

As briefly shown here, using digital photogrammetry to reconstitute outcrops in three-dimension appears to be a promising method to retrieve meaningful and quantitative structural data on Mars. In addition, *in situ* exploration of Mars does not seem to have any other reliable way to provide such measurements, and the study of structural processes on its surface will likely rely on the development of similar tools in the future. This development will need to be twofold: upstream, with the acquisition of images tailored for that use (high overlap and observation of the object under different angles, which will be implemented natively with *Mars2020* Navcam and Mastcam-Z instruments), and downstream with the development of software (and AR/VR hardware) to produce and process DOM from Mars, but also from other bodies explored in space.

ANNEX C

OTHER RESOURCES

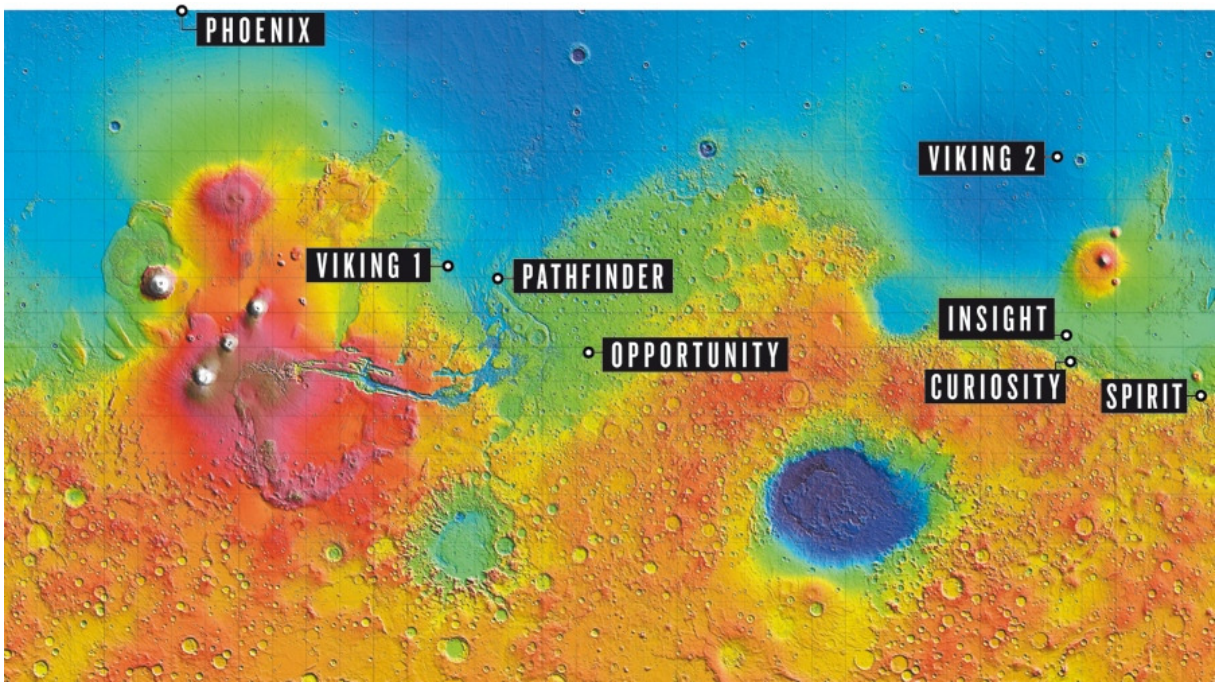

Figure C.1: Locations of the landing sites for *in-situ* missions on Mars [credit: JPL-Caltech/NASA/Nature]

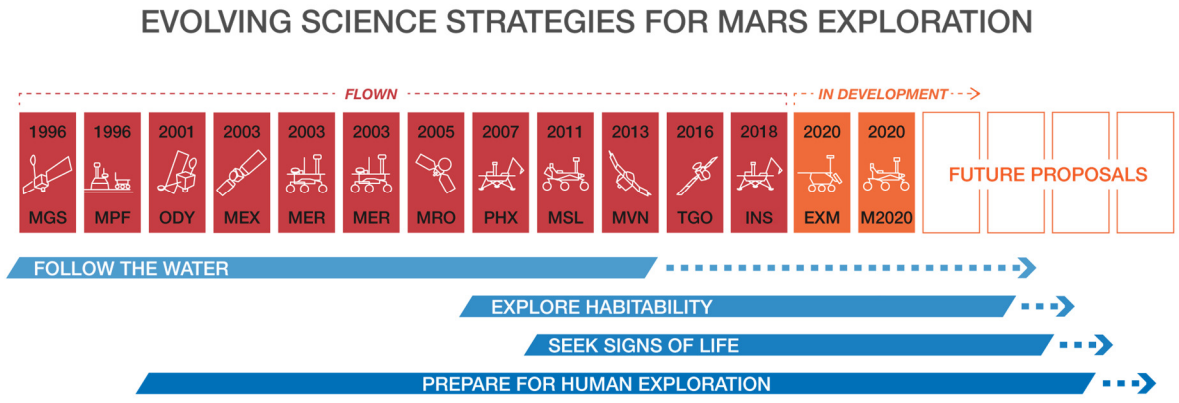

Figure C.2: Timeline of the recent Mars exploration missions and science objectives [credit: NASA/JPL-Caltech]

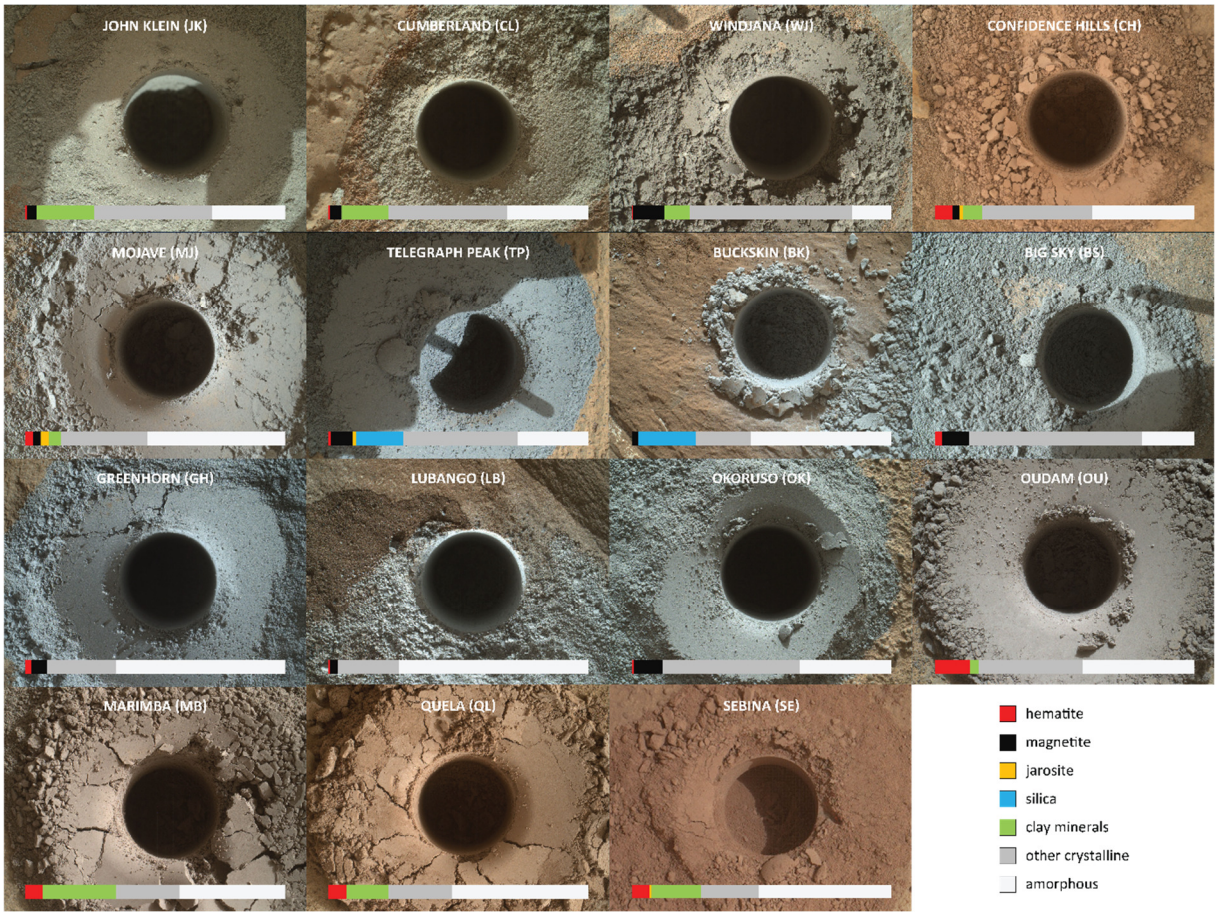

Figure C.3: *Curiosity* drill-holes (MAHLI images) and mineral abundances from CheMin [image credit: N*ASA / JPL / MSSS / Emily Lakdawalla*]

REFERENCES

Anderson, R. (2010), Geologic mapping and characterization of Gale Crater and implications for its potential as a Mars Science Laboratory landing site, *Mars J.*, *5*, 76–128, doi:10.1555/mars.2010.0004.

Anderson, R. B., S. M. Clegg, J. Frydenvang, R. C. Wiens, S. McLennan, R. V. Morris, B. Ehlmann, and M. D. Dyar (2017), Improved accuracy in quantitative laser-induced breakdown spectroscopy using sub-models, *Spectrochim. Acta Part B At. Spectrosc.*, *129*, 49–57, doi:10.1016/j.sab.2016.12.002.

Antelo, J., M. Avena, S. Fiol, R. López, and F. Arce (2005), Effects of pH and ionic strength on the adsorption of phosphate and arsenate at the goethite–water interface, *J. Colloid Interface Sci.*, *285*(2), 476–486, doi:10.1016/j.jcis.2004.12.032.

Arvidson, R. E. et al. (2006), Overview of the Spirit Mars Exploration Rover Mission to Gusev Crater: Landing site to Backstay Rock in the Columbia Hills, *J. Geophys. Res. E Planets*, doi:10.1029/2005JE002499.

Arvidson, R. E. et al. (2010), Spirit Mars Rover Mission: Overview and selected results from the northern Home Plate Winter Haven to the side of Scamander crater, *J. Geophys. Res.*, *115*(E7), E00F03, doi:10.1029/2010JE003633.

Arvidson, R. E. et al. (2014), Ancient Aqueous Environments at Endeavour Crater, Mars, *Science (80-.).*, *343*(6169), 1248097–1248097, doi:10.1126/science.1248097.

Arvidson, R. E. et al. (2016), High concentrations of manganese and sulfur in deposits on Murray Ridge, Endeavour Crater, Mars, *Am. Mineral.*, *101*(6), 1389–1405, doi:10.2138/am-2016-5599.

Bain, R. J. (1990), Diagenetic, nonevaporative origin for gypsum, *Geology*, *18*(5), 447, doi:10.1130/0091-7613(1990)018<0447:DNOFG>2.3.CO;2.

Banham, S. G., S. Gupta, D. M. Rubin, J. A. Watkins, D. Y. Sumner, J. P. Grotzinger, K. W. Lewis, K. S. Edgett, L. A. Edgar, and K. M. Stack (2016), Reconstruction of an Ancient Eolian Dune Field at Gale Crater, Mars: Sedimentary Analysis of the Stimson Formation, *47th Lunar Planet. Sci. Conf.*, Abstract #2346.

Banham, S. G. et al. (2018), Ancient Martian aeolian processes and palaeomorphology reconstructed from the Stimson formation on the lower slope of Aeolis Mons, Gale crater, Mars, *Sedimentology*, *65*(4), 993–1042, doi:10.1111/sed.12469.

Beck, P. et al. (2017), Searching for Carbon on Mars with MSL/ChemCam, *48th Lunar Planet. Sci. Conf.*, Abstract #1216.

Beitler, B., W. T. Parry, and M. A. Chan (2005), Fingerprints of Fluid Flow: Chemical Diagenetic History of the Jurassic Navajo Sandstone, Southern Utah, U.S.A., *J. Sediment. Res.*, *75*(4), 547–561, doi:10.2110/jsr.2005.045.

Bell, J. F. et al. (2003), Mars Exploration Rover Athena Panoramic Camera (Pancam) investigation, *J. Geophys. Res. Planets*, *108*(E12), doi:10.1029/2003JE002070.

Bennett, K. A., K. Edgett, D. Fey, L. A. Edgar, A. Fraeman, M. McBride, and C. Edwards (2018), Fine-Scale Textural Observations at Vera Rubin Ridge, Gale Crater, from the Mars Hand Lens Imager (MAHLI), *49th Lunar Planet. Sci. Conf.*, Abstract #1769.

Berger, J. A. et al. (2017), Zinc and germanium in the sedimentary rocks of Gale Crater on Mars indicate hydrothermal enrichment followed by diagenetic fractionation, *J. Geophys. Res. Planets*, *122*(8), 1747–1772, doi:10.1002/2017JE005290.

Berner, R. A. (1973), Phosphate removal from sea water by adsorption on volcanogenic ferric oxides, *Earth Planet. Sci. Lett.*, *18*(1), 77–86, doi:10.1016/0012-821X(73)90037-X.

Berner, R. A. (1984), Sedimentary pyrite formation: An update, *Geochim. Cosmochim. Acta*, *48*(4), 605–615, doi:10.1016/0016-7037(84)90089-9.

Bethke, C. M., B. Farrell, and S. Yeakel (2018), GWB- Essentials Guide, *Geochemist's Work. Release 12*, 186.

Beverskog, B., and I. Puigdomenech (1996), Revised pourbaix diagrams for iron at 25–300 °C, *Corros. Sci.*, *38*(12), 2121–2135, doi:10.1016/S0010-938X(96)00067-4.

Bibring, J.-P. (2005), Mars Surface Diversity as Revealed by the OMEGA/Mars Express Observations, *Science (80-.).*, *307*(5715), 1576–1581, doi:10.1126/science.1108806.

Bibring, J.-P. et al. (2006), Global Mineralogical and Aqueous Mars History Derived from OMEGA/Mars Express Data, *Science (80-.).*, *312*(5772), 400–404, doi:10.1126/science.1122659.

Bibring, J.-P. et al. (2007), Coupled Ferric Oxides and Sulfates on the Martian Surface, *Science (80-.).*, *317*(5842), 1206–1210, doi:10.1126/science.1144174.

Biemann, K. et al. (1977), The search for organic substances and inorganic volatile compounds in the surface of Mars, *J. Geophys. Res.*, *82*(28), 4641–4658, doi:10.1029/JS082i028p04641.

Bistacchi, A., F. Balsamo, F. Storti, M. Mozafari, R. Swennen, J. Solum, C. Tueckmantel, and C. Taberner (2015), Photogrammetric digital outcrop reconstruction, visualization with textured surfaces, and three-dimensional structural analysis and modeling: Innovative methodologies applied to fault-related dolomitization (Vajont Limestone, Southern Alps, Italy), *Geosphere*, *11*(6), 2031–2048, doi:10.1130/GES01005.1.

Blake, D. et al. (2012), Characterization and Calibration of the CheMin Mineralogical Instrument on Mars Science Laboratory, *Space Sci. Rev.*, *170*(1–4), 341–399, doi:10.1007/s11214-012-9905-1.

Blaney, D. L. et al. (2015), Chemo-stratigraphy at the Pahrump outcrop and Garden City Vein Complex in Gale Crater using ChemCam., , Abstract 391B.

Booth, M. C., and H. H. Kieffer (1978), Carbonate formation in Marslike environments, *J. Geophys. Res. Solid Earth*, *83*(B4), 1809–1815, doi:10.1029/JB083iB04p01809.

Borlina, C. S., B. L. Ehlmann, and E. S. Kite (2015), Modeling the thermal and physical evolution of Mount Sharp's sedimentary rocks, Gale Crater, Mars: Implications for diagenesis on the MSL Curiosity rover traverse, *J. Geophys. Res. Planets*, *120*(8), 1396–1414, doi:10.1002/2015JE004799.

Bouley, S., and R. A. Craddock (2014), Age dates of valley network drainage basins and subbasins within Sabae and Arabia Terrae, Mars, *J. Geophys. Res. Planets*, *119*(6), 1302–1310, doi:10.1002/2013JE004571.

Bouley, S., D. Baratoux, I. Matsuyama, F. Forget, A. Séjourné, M. Turbet, and F. Costard (2016), Late Tharsis formation and implications for early Mars, *Nature*, *531*(7594), 344–347, doi:10.1038/nature17171.

Boynton, W. V. et al. (2002), Distribution of hydrogen in the near surface of Mars: Evidence for subsurface ice deposits, *Science (80-.).*, doi:10.1126/science.1073722.

Brennetot, R., J. L. Lacour, E. Vors, A. Rivoallan, D. Vailhen, and S. Maurice (2003), Mars Analysis by Laser-Induced Breakdown Spectroscopy (MALIS): Influence of Mars Atmosphere on Plasma Emission and Study of Factors Influencing Plasma Emission with the Use of Doehlert Designs,

Appl. Spectrosc., *57*(7), 744–752, doi:10.1366/000370203322102816.

Bridges, J. C., S. P. Schwenzer, R. Leveille, F. Westall, R. C. Wiens, N. Mangold, T. Bristow, P. Edwards, and G. Berger (2015), Diagenesis and clay mineral formation at Gale Crater, Mars, *J. Geophys. Res. Planets*, *120*(1), 1–19, doi:10.1002/2014JE004757.

Bristow, T. F. et al. (2015), The origin and implications of clay minerals from Yellowknife Bay, Gale crater, Mars, *Am. Mineral.*, *100*(4), 824–836, doi:10.2138/am-2015-5077CCBYNCND.

Bristow, T. F. T. F. et al. (2018), Clay mineral diversity and abundance in sedimentary rocks of Gale crater, Mars, *Sci. Adv.*, *4*(6), 1–9, doi:10.1126/sciadv.aar3330.

Burns, R. G. (1993), *Mineralogical applications of crystal field theory*, Cambridge University Press.

Burr, D. M., A. S. McEwen, and S. E. H. Sakimoto (2002), Recent aqueous floods from the Cerberus Fossae, Mars, *Geophys. Res. Lett.*, *29*(1), 1013, doi:10.1029/2001GL013345.

Cabrol, N., and E. Grin (2001), The Evolution of Lacustrine Environments on Mars: Is Mars Only Hydrologically Dormant?, *Icarus*, *149*(2), 291–328, doi:10.1006/icar.2000.6530.

Campbell, J. L., G. M. Perrett, R. Gellert, S. M. Andrushenko, N. I. Boyd, J. A. Maxwell, P. L. King, and C. D. M. Schofield (2012), Calibration of the Mars Science Laboratory Alpha Particle X-ray Spectrometer, *Space Sci. Rev.*, *170*(1–4), 319–340, doi:10.1007/s11214-012-9873-5.

Carr, M. H. (1979), Formation of Martian flood features by release of water from confined aquifers, *J. Geophys. Res.*, *84*(B6), 2995, doi:10.1029/JB084iB06p02995.

Carr, M. H. (1995), The Martian drainage system and the origin of valley networks and fretted channels, *J. Geophys. Res.*, *100*(E4), 7479, doi:10.1029/95JE00260.

Carrivick, J., M. Smith, and D. Quincey (2016), *Structure from motion in the geosciences*, John Wiley & Sons.

Carter, J., F. Poulet, J.-P. Bibring, N. Mangold, and S. Murchie (2013), Hydrous minerals on Mars as seen by the CRISM and OMEGA imaging spectrometers: Updated global view, *J. Geophys. Res. Planets*, *118*(4), 831–858, doi:10.1029/2012JE004145.

Carter, J., D. Loizeau, N. Mangold, F. Poulet, and J.-P. Bibring (2015), Widespread surface weathering on early Mars: A case for a warmer and wetter climate, *Icarus*, *248*, 373–382, doi:10.1016/j.icarus.2014.11.011.

Caswell, T. E., and R. E. Milliken (2017), Evidence for hydraulic fracturing at Gale crater, Mars: Implications for burial depth of the Yellowknife Bay formation, *Earth Planet. Sci. Lett.*, *468*, 72–84, doi:10.1016/j.epsl.2017.03.033.

Chaïrat, C., J. Schott, E. H. Oelkers, J.-E. Lartigue, and N. Harouiya (2007), Kinetics and mechanism of natural fluorapatite dissolution at 25°C and pH from 3 to 12, *Geochim. Cosmochim. Acta*, *71*(24), 5901–5912, doi:10.1016/j.gca.2007.08.031.

Chan, M. A., W. T. Parry, and J. R. Bownman (2000), Diagenetic Hematite and Manganese Oxides and Fault-Related Fluid Flow in Jurassic Sandstones, Southeastern Utah, *Am. Assoc. Pet. Geol. Bull.*, *84*(9), 1281–1310, doi:10.1306/A9673E82-1738-11D7-8645000102C1865D.

Chan, M. A., B. Beitler, W. T. Parry, J. Ormö, and G. Komatsu (2004), A possible terrestrial analogue for haematite concretions on Mars, *Nature*, *429*(6993), 731–734, doi:10.1038/nature02600.

Chan, M. A., B. B. Bowen, W. T. Parry, J. Ormö, and G. Komatsu (2005), Red rock and red planet diagenesis: Comparisons of Earth and Mars concretions, *GSA Today*, *15*(8), 4–10, doi:10.1130/1052-5173(2005)15<4:TEOTDI>2.0.CO;2.

Chan, M. A., J. Ormö, A. J. Park, M. Stich, V. Souza-Egipsy, and G. Komatsu (2007), Models of iron oxide concretion formation: field, numerical, and laboratory comparisons, *Geofluids*, *7*(3), 356–368, doi:10.1111/j.1468-8123.2007.00187.x.

Chan, W. T., and R. E. Russo (1991), Study of laser-material interactions using inductively coupled plasma-atomic emission spectrometry, *Spectrochim. Acta Part B At. Spectrosc.*, *46*(11), 1471–1486, doi:10.1016/0584-8547(91)80199-D.

Chassefière, E., F. Leblanc, and B. Langlais (2007), The combined effects of escape and magnetic field histories at Mars, *Planet. Space Sci.*, *55*(3), 343–357, doi:10.1016/J.PSS.2006.02.003.

Chojnacki, M., and B. M. Hynek (2008), Geological context of water-altered minerals in Valles Marineris, Mars, *J. Geophys. Res.*, *113*(E12), E12005, doi:10.1029/2007JE003070.

Christensen, P. R. et al. (2000), Detection of crystalline hematite mineralization on Mars by the Thermal Emission Spectrometer: Evidence for near-surface water, *J. Geophys. Res. Planets*, *105*(E4), 9623–9642, doi:10.1029/1999JE001093.

Christensen, P. R., R. V. Morris, M. D. Lane, J. L. Bandfield, and M. C. Malin (2001), Global mapping of Martian hematite mineral deposits: Remnants of water-driven processes on early Mars, *J. Geophys. Res. Planets*, *106*(E10), 23873–23885, doi:10.1029/2000JE001415.

Clark, B. C., A. K. Baird, R. J. Weldon, D. M. Tsusaki, L. Schnabel, and M. P. Candelaria (1982), Chemical composition of Martian fines, *J. Geophys. Res.*, *87*(B12), 10059, doi:10.1029/JB087iB12p10059.

Clegg, S. M., E. Sklute, M. D. Dyar, J. E. Barefield, and R. C. Wiens (2009), Multivariate analysis of remote laser-induced breakdown spectroscopy spectra using partial least squares, principal component analysis, and related techniques, *Spectrochim. Acta Part B At. Spectrosc.*, *64*(1), 79–88, doi:10.1016/j.sab.2008.10.045.

Clegg, S. M. et al. (2017), Recalibration of the Mars Science Laboratory ChemCam instrument with an expanded geochemical database, *Spectrochim. Acta Part B At. Spectrosc.*, *129*, 64–85, doi:10.1016/j.sab.2016.12.003.

Clegg, S. M. et al. (2018), ChemCam Sulfur Quantitative Analysis and Interpretation, *49th Lunar Planet. Sci. Conf.*, Abstract #2576.

Cloutis, E., M. Craig, L. Kaletzke, K. McCormack, and L. Stewart (2006), HOSERLab: A new planetary spectrophotometer facility, *37th Lunar Planet. Sci. Conf.*, Abstract 2121.

Connerney, J. E. (1999), Magnetic Lineations in the Ancient Crust of Mars, *Science (80-.).*, *284*(5415), 794–798, doi:10.1126/science.284.5415.794.

Corradetti, A., S. Tavani, M. Parente, A. Iannace, F. Vinci, C. Pirmez, S. Torrieri, M. Giorgioni, A. Pignalosa, and S. Mazzoli (2018), Distribution and arrest of vertical through-going joints in a seismic-scale carbonate platform exposure (Sorrento peninsula, Italy): insights from integrating field survey and digital outcrop model, *J. Struct. Geol.*, *108*, 121–136, doi:10.1016/J.JSG.2017.09.009.

Costard, F., F. Forget, N. Mangold, and J. P. Peulvast (2002), Formation of recent martian debris flows by melting of near-surface ground ice at high obliquity, *Science (80-.).*, doi:10.1126/science.1066698.

Cousin, A. et al. (2017), Classification of igneous rocks analyzed by ChemCam at Gale crater, Mars, *Icarus*, *288*, 265–283, doi:10.1016/j.icarus.2017.01.014.

Cremers, D. A., and L. J. Radziemski (2013), *Quantitative LIBS analysis*, John Wiley & Sons Ltd.

Cristoforetti, G., A. De Giacomo, M. Dell'Aglio, S. Legnaioli, E. Tognoni, V. Palleschi, and N. Omenetto (2010), Local Thermodynamic Equilibrium in Laser-Induced Breakdown Spectroscopy: Beyond the McWhirter criterion, *Spectrochim. Acta Part B At. Spectrosc.*, *65*(1), 86–95, doi:10.1016/j.sab.2009.11.005.

Cutts, J. A., and R. S. U. Smith (1973), Eolian deposits and dunes on Mars, *J. Geophys. Res.*, *78*(20), 4139–4154, doi:10.1029/JB078i020p04139.

David, G. et al. (2018), Laboratory Analyses of Hematite-Rich Martian Analogues: Implications for ChemCam Data at Vera Rubin Ridge, *49th Lunar Planet. Sci. Conf.*, Abstract #2079.

Dehouck, E., V. Chevrier, A. Gaudin, N. Mangold, P.-E. Mathé, and P. Rochette (2012), Evaluating the role of sulfide-weathering in the formation of sulfates or carbonates on Mars, *Geochim. Cosmochim. Acta*, *90*, 47–63, doi:10.1016/j.gca.2012.04.057.

Dehouck, E., A. Gaudin, N. Mangold, L. Lajaunie, A. Dauzères, O. Grauby, and E. Le Menn (2014), Weathering of olivine under CO2 atmosphere: A martian perspective, *Geochim. Cosmochim. Acta*, *135*, 170–189, doi:10.1016/j.gca.2014.03.032.

Le Deit, L., E. Hauber, F. Fueten, M. Pondrelli, A. P. Rossi, and R. Jaumann (2013), Sequence of infilling events in Gale Crater, Mars: Results from morphology, stratigraphy, and mineralogy, *J. Geophys. Res. Planets*, *118*(12), 2439–2473, doi:10.1002/2012JE004322.

Le Deit, L. et al. (2016), The potassic sedimentary rocks in Gale Crater, Mars, as seen by ChemCam on board Curiosity, *J. Geophys. Res. Planets*, *121*(5), 784–804, doi:10.1002/2015JE004987.

Delany, J. M., and S. R. Lundeen (1990), The LLNL thermodynamic database, *Lawrence Livermore Natl. Lab. Rep. UCRL-21658. Lawrence Livermore Natl. Lab. Livermore, California, USA*.

Dodd, M. S., D. Papineau, T. Grenne, J. F. Slack, M. Rittner, F. Pirajno, J. O'Neil, and C. T. S. Little (2017), Evidence for early life in Earth's oldest hydrothermal vent precipitates, *Nature*, *543*(7643), 60–64, doi:10.1038/nature21377.

Dundas, C. (2016), Mars on dry ice, *Nat. Geosci.*, *9*(1), 10–11, doi:10.1038/ngeo2625.

Dundas, C. M., S. Diniega, and A. S. McEwen (2015), Long-term monitoring of martian gully formation and evolution with MRO/HiRISE, *Icarus*, doi:10.1016/j.icarus.2014.05.013.

Dundas, C. M., A. S. McEwen, M. Chojnacki, M. P. Milazzo, S. Byrne, J. N. McElwaine, and A. Urso (2017), Granular flows at recurring slope lineae on Mars indicate a limited role for liquid water, *Nat. Geosci.*, *10*(12), 903–907, doi:10.1038/s41561-017-0012-5.

Edgar, L. A. et al. (2018), Sedimentology and Stratigraphy Observed at Vera Rubin Ridge by the Mars Science Laboratory Curiosity Rover, *49th Lunar Planet. Sci. Conf.*, Abstract #1704.

Edgett, K. S. et al. (2012), Curiosity's Mars Hand Lens Imager (MAHLI) Investigation, *Space Sci. Rev.*, *170*(1–4), 259–317, doi:10.1007/s11214-012-9910-4.

Effenberger, A., and J. Scott (2010), Effect of Atmospheric Conditions on LIBS Spectra, *Sensors*, *10*(5), 4907–4925, doi:10.3390/s100504907.

Egger, M., T. Jilbert, T. Behrends, C. Rivard, and C. P. Slomp (2015), Vivianite is a major sink for phosphorus in methanogenic coastal surface sediments, *Geochim. Cosmochim. Acta*, *169*, 217–235, doi:10.1016/j.gca.2015.09.012.

Ehlmann, B. L. et al. (2008), Orbital Identification of Carbonate-Bearing Rocks on Mars, *Science (80-.).*, *322*(5909), 1828–1832, doi:10.1126/science.1164759.

Ehlmann, B. L. et al. (2009), Identification of hydrated silicate minerals on Mars using MRO-CRISM:

Geologic context near Nili Fossae and implications for aqueous alteration, *J. Geophys. Res.*, *114*(E2), E00D08, doi:10.1029/2009JE003339.

Ehlmann, B. L., J. F. Mustard, S. L. Murchie, J.-P. Bibring, A. Meunier, A. a. Fraeman, and Y. Langevin (2011), Subsurface water and clay mineral formation during the early history of Mars, *Nature*, *479*(7371), 53–60, doi:10.1038/nature10582.

Ehlmann, B. L., G. Berger, N. Mangold, J. R. Michalski, D. C. Catling, S. W. Ruff, E. Chassefière, P. B. Niles, V. Chevrier, and F. Poulet (2013), Geochemical Consequences of Widespread Clay Mineral Formation in Mars' Ancient Crust, *Space Sci. Rev.*, *174*(1–4), 329–364, doi:10.1007/s11214-012-9930-0.

El-Tabakh, M., R. Riccioni, and B. Schreiber (1997), Evolution of late Triassic rift basin evaporites (Passaic Formation): Newark Basin, Eastern North America, *Sedimentology*, *44*(4), 767–790, doi:10.1046/j.1365-3091.1997.d01-47.x.

Elwood Madden, M. E., R. J. Bodnar, and J. D. Rimstidt (2004), Jarosite as an indicator of water-limited chemical weathering on Mars, *Nature*, *431*(7010), 821–823, doi:10.1038/nature02971.

Fabre, C., S. Maurice, A. Cousin, R. C. Wiens, O. Forni, V. Sautter, and D. Guillaume (2011), Onboard calibration igneous targets for the Mars Science Laboratory Curiosity rover and the Chemistry Camera laser induced breakdown spectroscopy instrument, *Spectrochim. Acta Part B At. Spectrosc.*, *66*(3–4), 280–289, doi:10.1016/J.SAB.2011.03.012.

Fabre, C. et al. (2014), In situ calibration using univariate analyses based on the onboard ChemCam targets: first prediction of Martian rock and soil compositions, *Spectrochim. Acta Part B At. Spectrosc.*, *99*, 34–51, doi:10.1016/j.sab.2014.03.014.

Farrand, W. H., T. D. Glotch, J. W. Rice, J. A. Hurowitz, and G. A. Swayze (2009), Discovery of jarosite within the Mawrth Vallis region of Mars: Implications for the geologic history of the region, *Icarus*, doi:10.1016/j.icarus.2009.07.014.

Fassett, C. I., and J. W. Head (2008), The timing of martian valley network activity: Constraints from buffered crater counting, *Icarus*, *195*(1), 61–89, doi:10.1016/j.icarus.2007.12.009.

Fedo, C. M. et al. (2018), Sedimentology and Stratigraphy of the Murray Formation, Gale Crater, Mars, *49th Lunar Planet. Sci. Conf.*, Abstract #2078.

Fernández-Remolar, D. C., R. V. Morris, J. E. Gruener, R. Amils, and A. H. Knoll (2005), The Río Tinto Basin, Spain: Mineralogy, sedimentary geobiology, and implications for interpretation of outcrop rocks at Meridiani Planum, Mars, *Earth Planet. Sci. Lett.*, *240*(1), 149–167, doi:10.1016/j.epsl.2005.09.043.

Flahaut, J., C. Quantin, P. Allemand, P. Thomas, and L. Le Deit (2010), Identification, distribution and possible origins of sulfates in Capri Chasma (Mars), inferred from CRISM data, *J. Geophys. Res.*, *115*(E11), E11007, doi:10.1029/2009JE003566.

Forni, O., S. Maurice, O. Gasnault, R. C. Wiens, A. Cousin, S. M. Clegg, J.-B. Sirven, and J. Lasue (2013), Independent component analysis classification of laser induced breakdown spectroscopy spectra, *Spectrochim. Acta Part B At. Spectrosc.*, *86*, 31–41, doi:10.1016/j.sab.2013.05.003.

Forni, O. et al. (2015), First detection of fluorine on Mars: Implications for Gale Crater's geochemistry, *Geophys. Res. Lett.*, *42*(4), 1020–1028, doi:10.1002/2014GL062742.

Forni, O. et al. (2017), Detection of Fluorine-Rich Phases, Phosphates, and Halite in the Stimson-Murray Units, Gale Crater, Mars, *48th Lunar Planet. Sci. Conf.*, Abstract #1838.

Fraeman, A. A. et al. (2013), A hematite-bearing layer in Gale Crater, Mars: Mapping and implications

for past aqueous conditions, *Geology*, *41*(10), 1103–1106, doi:10.1130/G34613.1.

Fraeman, A. A., B. L. Ehlmann, R. E. Arvidson, C. S. Edwards, J. P. Grotzinger, R. E. Milliken, D. P. Quinn, and M. S. Rice (2016), The stratigraphy and evolution of lower Mount Sharp from spectral, morphological, and thermophysical orbital data sets, *J. Geophys. Res. Planets*, *121*(9), 1713–1736, doi:10.1002/2016JE005095.

Fraeman, A. A. et al. (2018), Curiosity's Investigation at Vera Rubin Ridge, *49th Lunar Planet. Sci. Conf.*, Abstract #1557.

Francis, R. et al. (2017), AEGIS autonomous targeting for ChemCam on Mars Science Laboratory: Deployment and results of initial science team use, *Sci. Robot.*, *2*(7), eaan4582, doi:10.1126/scirobotics.aan4582.

Frydenvang, J. et al. (2017), Diagenetic silica enrichment and late-stage groundwater activity in Gale crater, Mars, *Geophys. Res. Lett.*, *44*(10), 4716–4724, doi:10.1002/2017GL073323.

Frydenvang, J. et al. (2018), Geochemical Variations Observed with the ChemCam Instrument on Vera Rubin Ridge in Gale Crater, Mars, *49th Lunar Planet. Sci. Conf.*, Abstract #2310.

Gasda, P. J. et al. (2017), In situ detection of boron by ChemCam on Mars, *Geophys. Res. Lett.*, *44*(17), 8739–8748, doi:10.1002/2017GL074480.

Gasda, P. J. et al. (2018), Evidence of Redox Sensitive Elements Associated with Possible Shoreline Deposits in Gale Crater, *49th Lunar Planet. Sci. Conf.*, Abstract #2483.

Gellert, R., and B. C. Clark (2015), In Situ Compositional Measurements of Rocks and Soils with the Alpha Particle X-ray Spectrometer on NASA's Mars Rovers, *Elements*, *11*(1), 39–44, doi:10.2113/gselements.11.1.39.

Gendrin, A. (2005), Sulfates in Martian Layered Terrains: The OMEGA/Mars Express View, *Science (80-.).*, *307*(5715), 1587–1591, doi:10.1126/science.1109087.

Geoffrey Wheat, C., R. A. Feely, and M. J. Mottl (1996), Phosphate removal by oceanic hydrothermal processes: An update of the phosphorus budget in the oceans, *Geochim. Cosmochim. Acta*, *60*(19), 3593–3608, doi:10.1016/0016-7037(96)00189-5.

Gomez, E., C. Durillon, G. Rofes, and B. Picot (1999), Phosphate adsorption and release from sediments of brackish lagoons: pH, O2 and loading influence, *Water Res.*, *33*(10), 2437–2447, doi:10.1016/S0043-1354(98)00468-0.

Greeley, R., and J. Guest (1987), Geologic map of the eastern equatorial region of Mars, *Scale 115,000,000, U.S. Geol. Surv. Map I-1802-B*.

Grotzinger, J. P. et al. (2005), Stratigraphy and sedimentology of a dry to wet eolian depositional system, Burns formation, Meridiani Planum, Mars, *Earth Planet. Sci. Lett.*, *240*(1), 11–72, doi:10.1016/j.epsl.2005.09.039.

Grotzinger, J. P. et al. (2012), Mars Science Laboratory mission and science investigation, *Space Sci. Rev.*, doi:10.1007/s11214-012-9892-2.

Grotzinger, J. P. et al. (2014), A Habitable Fluvio-Lacustrine Environment at Yellowknife Bay, Gale Crater, Mars, *Science (80-.).*, *343*(6169), 1242777–1242777, doi:10.1126/science.1242777.

Grotzinger, J. P. et al. (2015), Deposition, exhumation, and paleoclimate of an ancient lake deposit, Gale crater, Mars, *Science (80-.).*, *350*(6257), aac7575-aac7575, doi:10.1126/science.aac7575.

de Haas, T., E. Hauber, S. J. Conway, H. van Steijn, A. Johnsson, and M. G. Kleinhans (2015), Earth-like aqueous debris-flow activity on Mars at high orbital obliquity in the last million years, *Nat.*

Commun., *6*(1), 7543, doi:10.1038/ncomms8543.

Hahn, D. W., and N. Omenetto (2010), Laser-Induced Breakdown Spectroscopy (LIBS), Part I: Review of Basic Diagnostics and Plasma—Particle Interactions: Still-Challenging Issues within the Analytical Plasma Community, *Appl. Spectrosc.*, *64*(12), 335A–336A, doi:10.1366/000370210793561691.

Hardie, L. (1985), The problem of distinguishing between primary and secondary features in evaporites, *Sixth Int. Symp. salt*, *1*, 173–195.

Haskin, L. A. et al. (2005), Water alteration of rocks and soils on Mars at the Spirit rover site in Gusev crater, *Nature*, doi:10.1038/nature03640.

De Hon, R. A. (1992), Martian lake basins and lacustrine plains, *Earth. Moon. Planets*, *56*(2), 95–122, doi:10.1007/BF00056352.

Hunt, G. R. (1977), Spectral signatures of particulate minerals in the visible and near infrared, *GEOPHYSICS*, *42*(3), 501–513, doi:10.1190/1.1440721.

Hunt, G. R., and J. Salisbury (1970), *Visible and near-infrared spectra of minerals and rocks: I silicate minerals*.

Hurowitz, J. A., W. W. Fischer, N. J. Tosca, and R. E. Milliken (2010), Origin of acidic surface waters and the evolution of atmospheric chemistry on early Mars, *Nat. Geosci.*, *3*(5), 323–326, doi:10.1038/ngeo831.

Hurowitz, J. A. et al. (2017), Redox stratification of an ancient lake in Gale crater, Mars, *Science (80-.).*, *356*(6341), eaah6849, doi:10.1126/science.aah6849.

Hynek, B. M., M. Beach, and M. R. T. Hoke (2010), Updated global map of Martian valley networks and implications for climate and hydrologic processes, *J. Geophys. Res.*, *115*(E9), E09008, doi:10.1029/2009JE003548.

Hyvarinen, A. (2001), Blind source separation by nonstationarity of variance: a cumulant-based approach, *IEEE Trans. Neural Networks*, *12*(6), 1471–1474, doi:10.1109/72.963782.

Iida, Y. (1990), Effects of atmosphere on laser vaporization and excitation processes of solid samples, *Spectrochim. Acta Part B At. Spectrosc.*, *45*(12), 1353–1367, doi:10.1016/0584-8547(90)80188-O.

Irwin, R. P., A. D. Howard, R. A. Craddock, and J. M. Moore (2005), An intense terminal epoch of widespread fluvial activity on early Mars: 2. Increased runoff and paleolake development, *J. Geophys. Res.*, *110*(E12), E12S15, doi:10.1029/2005JE002460.

Izawa, M. R. M., N. R. Banerjee, G. R. Osinski, R. L. Flemming, J. Parnell, and C. S. Cockell (2011), Weathering of Post-Impact Hydrothermal Deposits from the Haughton Impact Structure: Implications for Microbial Colonization and Biosignature Preservation, *Astrobiology*, *11*(6), 537–550, doi:10.1089/ast.2011.0612.

Johnson, J. R. et al. (2015), ChemCam passive reflectance spectroscopy of surface materials at the Curiosity landing site, Mars, *Icarus*, *249*, 74–92, doi:10.1016/j.icarus.2014.02.028.

Johnson, J. R. et al. (2016), Constraints on iron sulfate and iron oxide mineralogy from ChemCam visible/near-infrared reflectance spectroscopy of Mt. Sharp basal units, Gale Crater, Mars, *Am. Mineral.*, *101*(7), 1501–1514, doi:10.2138/am-2016-5553.

Johnson, J. R., E. A. Cloutis, A. A. Fraeman, R. C. Wiens, and S. Maurice (2017a), Ferric oxide variability in the Murray formation from ChemCam passive reflectance, , Abstract #12-1.

Johnson, J. R. et al. (2017b), Visible/near-infrared spectral diversity from in situ observations of the Bagnold Dune Field sands in Gale Crater, Mars, *J. Geophys. Res. Planets*,

doi:10.1002/2016JE005187.

King, P. L., and S. M. McLennan (2010), Sulfur on Mars, *Elements*, *6*(2), 107–112, doi:10.2113/gselements.6.2.107.

Klein, H. P. (1978), The Viking biological experiments on Mars, *Icarus*, *34*(3), 666–674, doi:10.1016/0019-1035(78)90053-2.

Knight, A. K., N. L. Scherbarth, D. A. Cremers, and M. J. Ferris (2000), Characterization of Laser-Induced Breakdown Spectroscopy (LIBS) for Application to Space Exploration, *Appl. Spectrosc.*, *54*(3), 331–340, doi:10.1366/0003702001949591.

Kronyak, R. E., L. C. Kah, M. Nachon, N. Mangold, R. C. Weins, R. Williams, J. Schieber, and J. Grotzinger (2015), Distribution of Mineralized Veins from Yellowknife Bay to Mount Sharp, Gale Crater, Mars: Insight from Textural and Compositional Variation, *46th Lunar Planet. Sci. Conf.*, Abstract #1903.

L'Haridon, J., N. Mangold, W. Rapin, A. Cousin, J. Johnson, P.-Y. Meslin, A. Fraeman, O. Gasnault, S. Maurice, and R. Wiens (2018a), Chemical diversity of diagenetic features analyzed by ChemCam at Gale crater, Mars, *EGU Conf.*, Abstract #6077.

L'Haridon, J. et al. (2018b), Chemical variability in mineralized veins observed by ChemCam on the lower slopes of Mount Sharp in Gale crater, Mars, *Icarus*, *311*, 69–86, doi:10.1016/j.icarus.2018.01.028.

L'Haridon, J., N. Mangold, W. Rapin, A. Cousin, J. R. Johnson, A. A. Fraeman, P.-Y. Meslin, O. Gasnault, S. Maurice, and R. Wiens (2018c), Diagenetic Iron Enrichments Observed by ChemCam on Vera Rubin Ridge, Gale Crater, Mars, *49th Lunar Planet. Sci. Conf.*, Abstract #1333.

Lammer, H. et al. (2013), Outgassing History and Escape of the Martian Atmosphere and Water Inventory, *Space Sci. Rev.*, *174*(1–4), 113–154, doi:10.1007/s11214-012-9943-8.

Lane, M. D., R. V. Morris, S. A. Mertzman, and P. R. Christensen (2002), Evidence for platy hematite grains in Sinus Meridiani, Mars, *J. Geophys. Res. Planets*, *107*(E12), 9-1-9–15, doi:10.1029/2001JE001832.

Langevin, Y., F. Poulet, J.-P. Bibring, and B. Gondet (2005), Sulfates in the north polar region of Mars detected by OMEGA/Mars Express., *Science*, *307*(5715), 1584–6, doi:10.1126/science.1109091.

Lanza, N. L. et al. (2014), High manganese concentrations in rocks at Gale crater, Mars, *Geophys. Res. Lett.*, *41*(16), 5755–5763, doi:10.1002/2014GL060329.

Lasue, J., R. C. Wiens, S. M. Clegg, D. T. Vaniman, K. H. Joy, S. Humphries, A. Mezzacappa, N. Melikechi, R. E. McInroy, and S. Bender (2012), Remote laser-induced breakdown spectroscopy (LIBS) for lunar exploration, *J. Geophys. Res. Planets*, *117*(E1), doi:10.1029/2011JE003898.

Lasue, J. et al. (2014), ChemCam Analysis of Martian Fine Dust, *45th Lunar Planet. Sci. Conf.*, Abstract #1224.

Lasue, J. et al. (2016), Observation of > 5 wt % zinc at the Kimberley outcrop, Gale crater, Mars, *J. Geophys. Res. Planets*, *121*(3), 338–352, doi:10.1002/2015JE004946.

Latimer, W. M. (1952), *Oxidation potentials*, LWW.

Lee, Y.-I., K. Song, H.-K. Cha, J.-M. Lee, M.-C. Park, G.-H. Lee, and J. Sneddon (1997), Influence of Atmosphere and Irradiation Wavelength on Copper Plasma Emission Induced by Excimer and Q-Switched Nd:YAG Laser Ablation, *Appl. Spectrosc.*, *51*(7), 959–964, doi:10.1366/0003702971941610.

Leighton, R. B., B. C. Murray, R. P. Sharp, J. D. Allen, and R. K. Sloan (1965), Mariner IV Photography of Mars: Initial Results, *Science (80-.).*, *149*(3684), 627–630, doi:10.1126/science.149.3684.627.

Léveillé, R. J. et al. (2014), Chemistry of fracture-filling raised ridges in Yellowknife Bay, Gale Crater: Window into past aqueous activity and habitability on Mars, *J. Geophys. Res. Planets*, *119*(11), 2398–2415, doi:10.1002/2014JE004620.

Lillis, R. J., J. Dufek, J. E. Bleacher, and M. Manga (2009), Demagnetization of crust by magmatic intrusion near the Arsia Mons volcano: Magnetic and thermal implications for the development of the Tharsis province, Mars, *J. Volcanol. Geotherm. Res.*, *185*(1–2), 123–138, doi:10.1016/j.jvolgeores.2008.12.007.

Lougheed, M. S. (1983), Origin of Precambrian iron-formations in the Lake Superior region, *Geol. Soc. Am. Bull.*, *94*(3), 325, doi:10.1130/0016-7606(1983)94<325:OOPIIT>2.0.CO;2.

Lucchitta, B. K., N. K. Isbell, and A. Howington-Kraus (1994), Topography of Valles Marineris: Implications for erosional and structural history, *J. Geophys. Res.*, *99*(E2), 3783, doi:10.1029/93JE03095.

Maki, J., D. Thiessen, A. Pourangi, P. Kobzeff, T. Litwin, L. Scherr, S. Elliott, A. Dingizian, and M. Maimone (2012), The Mars Science Laboratory engineering cameras, *Space Sci. Rev.*, *170*(1–4), 77–93, doi:10.1007/s11214-012-9882-4.

Maki, J. N. et al. (2003), Mars Exploration Rover Engineering Cameras, *J. Geophys. Res. Planets*, *108*(E12), doi:10.1029/2003JE002077.

Malin, M. C. (1998), High resolution images of Mars; new perspectives and mysteries, in *Geological Society of America, 1998 annual meeting.*

Malin, M. C., and K. S. Edgett (2000), Evidence for recent groundwater seepage and surface runoff on Mars., *Science*, *288*(5475), 2330–5, doi:10.1126/science.288.5475.2330.

Malin, M. C., K. S. Edgett, L. V. Posiolova, S. M. McColley, and E. Z. N. Dobrea (2006), Present-day impact cratering rate and contemporary gully activity on Mars., *Science*, *314*(5805), 1573–7, doi:10.1126/science.1135156.

Malin, M. C. et al. (2017), The Mars Science Laboratory (MSL) Mast cameras and Descent imager: Investigation and instrument descriptions, *Earth Sp. Sci.*, *4*(8), 506–539, doi:10.1002/2016EA000252.

Manga, M. (2004), Martian floods at Cerberus Fossae can be produced by groundwater discharge, *Geophys. Res. Lett.*, *31*(2), doi:10.1029/2003GL018958.

Mangold, N. (2003), Debris flows over sand dunes on Mars: Evidence for liquid water, *J. Geophys. Res.*, *108*(E4), 5027, doi:10.1029/2002JE001958.

Mangold, N., C. Quantin, V. Ansan, C. Delacourt, and P. Allemand (2004), Evidence for Precipitation on Mars from Dendritic Valleys in the Valles Marineris Area, *Science (80-.).*, *305*(5680), 78–81, doi:10.1126/science.1097549.

Mangold, N., A. Gendrin, B. Gondet, S. LeMouelic, C. Quantin, V. Ansan, J.-P. Bibring, Y. Langevin, P. Masson, and G. Neukum (2008), Spectral and geological study of the sulfate-rich region of West Candor Chasma, Mars, *Icarus*, *194*(2), 519–543, doi:10.1016/J.ICARUS.2007.10.021.

Mangold, N., J. Carter, F. Poulet, E. Dehouck, V. Ansan, and D. Loizeau (2012), Late Hesperian aqueous alteration at Majuro crater, Mars, *Planet. Space Sci.*, *72*(1), 18–30, doi:10.1016/j.pss.2012.03.014.

Mangold, N. et al. (2016), Composition of conglomerates analyzed by the Curiosity rover: Implications

for Gale Crater crust and sediment sources, *J. Geophys. Res. Planets*, *121*(3), 353–387, doi:10.1002/2015JE004977.

Mangold, N. et al. (2018a), Chemical alteration of fine-grained sedimentary rocks at Gale crater, *Icarus (accepted)*.

Mangold, N. et al. (2018b), Overview of the composition of the Gale Crater lacustrine sediments from Chemcam onboard Curiosity, *EGU Conf.*, Abstract #6031.

Massé, M., S. Le Mouélic, O. Bourgeois, J.-P. Combe, L. Le Deit, C. Sotin, J.-P. Bibring, B. Gondet, and Y. Langevin (2008), Mineralogical composition, structure, morphology, and geological history of Aram Chaos crater fill on Mars derived from OMEGA Mars Express data, *J. Geophys. Res.*, *113*(E12), E12006, doi:10.1029/2008JE003131.

Massé, M., O. Bourgeois, S. Le Mouélic, C. Verpoorter, L. Le Deit, and J. P. Bibring (2010), Martian polar and circum-polar sulfate-bearing deposits: Sublimation tills derived from the North Polar Cap, *Icarus*, *209*(2), 434–451, doi:10.1016/J.ICARUS.2010.04.017.

Masursky, H. (1973), An overview of geological results from Mariner 9, *J. Geophys. Res.*, *78*(20), 4009–4030, doi:10.1029/JB078i020p04009.

Maurice, S. et al. (2012), The ChemCam Instrument Suite on the Mars Science Laboratory (MSL) Rover: Science Objectives and Mast Unit Description, *Space Sci. Rev.*, *170*(1–4), 95–166, doi:10.1007/s11214-012-9912-2.

Maurice, S. et al. (2016), ChemCam activities and discoveries during the nominal mission of the Mars Science Laboratory in Gale crater, Mars, *J. Anal. At. Spectrom.*, *31*(4), 863–889, doi:10.1039/C5JA00417A.

McEwen, A. S. et al. (2007), A Closer Look at Water-Related Geologic Activity on Mars, *Science (80-.).*, *317*(5845), 1706–1709, doi:10.1126/science.1143987.

McEwen, A. S., L. Ojha, C. M. Dundas, S. S. Mattson, S. Byrne, J. J. Wray, S. C. Cull, S. L. Murchie, N. Thomas, and V. C. Gulick (2011), Seasonal Flows on Warm Martian Slopes, *Science (80-.).*, *333*(6043), 740–743, doi:10.1126/science.1204816.

McLennan, S. M. et al. (2005), Provenance and diagenesis of the evaporite-bearing Burns formation, Meridiani Planum, Mars, *Earth Planet. Sci. Lett.*, *240*(1), 95–121, doi:10.1016/j.epsl.2005.09.041.

McLennan, S. M. et al. (2014), Elemental Geochemistry of Sedimentary Rocks at Yellowknife Bay, Gale Crater, Mars, *Science (80-.).*, *343*(6169), 1244734–1244734, doi:10.1126/science.1244734.

Meslin, P.-Y. et al. (2016), Calibration of the Fluorine, Chlorine, and Hydrogen Content of Apatites with the ChemCam LIBS Instrument, *47th Lunar Planet. Sci. Conf.*, Abstract #1703.

Meslin, P.-Y. et al. (2017), Egg Rock Encounter: Analysis of an Iron-Nickel Meteorite Found in Gale Crater by Curiosity, *48th Lunar Planet. Sci. Conf.*, Abstract #2258.

Meslin, P.-Y. et al. (2018), Detection of Hydrous Manganese and Iron Oxides with Variable Phosphorus and Magnesium Contents in the Lacustrine Sediments of the Murray Formation, Gale, Mars, *49th Lunar Planet. Sci. Conf.*, Abstract #1447.

Michalski, J. R., and P. B. Niles (2010), Deep crustal carbonate rocks exposed by meteor impact on Mars, *Nat. Geosci.*, doi:10.1038/ngeo971.

Micheletti, N., J. H. Chandler, and S. N. Lane (2015), Structure from motion (SFM) photogrammetry, in *Geomorphological Techniques (Online Edition)*, p. Chap. 2, Sec. 2.2., British Society for Geomorphology.

Milbury, C., G. Schubert, C. A. Raymond, S. E. Smrekar, and B. Langlais (2012), The history of Mars' dynamo as revealed by modeling magnetic anomalies near Tyrrhenus Mons and Syrtis Major, *J. Geophys. Res. Planets*, *117*(E10), 4–11, doi:10.1029/2012JE004099.

Milliken, R. E. et al. (2008), Opaline silica in young deposits on Mars, *Geology*, doi:10.1130/G24967A.1.

Milliken, R. E., J. P. Grotzinger, and B. J. Thomson (2010), Paleoclimate of Mars as captured by the stratigraphic record in Gale Crater, *Geophys. Res. Lett.*, *37*(4), 1238670–1238670, doi:10.1029/2009GL041870.

Milton, D. J. (1973), Water and processes of degradation in the Martian landscape, *J. Geophys. Res.*, *78*(20), 4037–4047, doi:10.1029/JB078i020p04037.

Miziolek, A. W., V. Palleschi, and I. Schechter (2006), *Laser induced breakdown spectroscopy*, Cambridge university press.

Mojzsis, S. J., G. Arrhenius, K. D. McKeegan, T. M. Harrison, A. P. Nutman, and C. R. L. Friend (1996), Evidence for life on Earth before 3,800 million years ago, *Nature*, *384*(6604), 55–59, doi:10.1038/384055a0.

Morris, R. V., H. V. Lauer, C. A. Lawson, E. K. Gibson, G. A. Nace, and C. Stewart (1985), Spectral and other physicochemical properties of submicron powders of hematite (α-Fe 2 O 3), maghemite (γ-Fe 2 O 3), magnetite (Fe 3 O 4), goethite (α-FeOOH), and lepidocrocite (γ-FeOOH), *J. Geophys. Res.*, *90*(B4), 3126, doi:10.1029/JB090iB04p03126.

Morris, R. V. et al. (2006a), Mössbauer mineralogy of rock, soil, and dust at Gusev crater, Mars: Spirit's journey through weakly altered olivine basalt on the plains and pervasively altered basalt in the Columbia Hills, *J. Geophys. Res. Planets*, *111*(E2), n/a-n/a, doi:10.1029/2005JE002584.

Morris, R. V. et al. (2006b), Mössbauer mineralogy of rock, soil, and dust at Meridiani Planum, Mars: Opportunity's journey across sulfate-rich outcrop, basaltic sand and dust, and hematite lag deposits, *J. Geophys. Res. Planets*, *111*(E12), n/a-n/a, doi:10.1029/2006JE002791.

Morris, R. V. et al. (2010), Identification of carbonate-rich outcrops on Mars by the spirit rover, *Science (80-.).*, doi:10.1126/science.1189667.

Morris, R. V. et al. (2016), Silicic volcanism on Mars evidenced by tridymite in high-SiO2 sedimentary rock at Gale crater, *Proc. Natl. Acad. Sci.*, 201607098, doi:10.1073/pnas.1607098113.

Morse, J. W., and G. M. Marion (1999), The role of carbonates in the evolution of early Martian oceans, *Am. J. Sci.*, doi:10.2475/ajs.299.7-9.738.

Le Mouélic, S. et al. (2015), The ChemCam Remote Micro-Imager at Gale crater: Review of the first year of operations on Mars, *Icarus*, *249*, 93–107, doi:10.1016/j.icarus.2014.05.030.

van der Mullen, J. A. M. (1989), On the atomic state distribution function in inductively coupled plasmas—I. Thermodynamic equilibrium considered on the elementary level, *Spectrochim. Acta Part B At. Spectrosc.*, *44*(11), 1067–1080, doi:10.1016/0584-8547(89)80107-7.

Murray, R. C. (1964), Origin and Diagenesis of Gypsum and Anhydrite, *SEPM J. Sediment. Res.*, *Vol. 34*(3), 512–523, doi:10.1306/74D710D2-2B21-11D7-8648000102C1865D.

Mustard, J. F. et al. (2008), Hydrated silicate minerals on Mars observed by the Mars Reconnaissance Orbiter CRISM instrument, *Nature*, doi:10.1038/nature07097.

Nachon, M. et al. (2014), Calcium sulfate veins characterized by ChemCam/Curiosity at Gale crater, Mars, *J. Geophys. Res. Planets*, *119*(9), 1991–2016, doi:10.1002/2013JE004588.

Nachon, M. et al. (2016), Chemistry of diagenetic features analyzed by ChemCam at Pahrump Hills,

Gale crater, Mars, *Icarus*, *0*, 1–16, doi:10.1016/j.icarus.2016.08.026.

Nachon, M. et al. (2017), Stratigraphic distribution of veins in the Murray and Stimson formations, Gale crater, Mars: Implications for ancient groundwater circulation, *AGU Fall Meet.*, Abstract #P24B-03.

Nedell, S. S., S. W. Squyres, and D. W. Andersen (1987), Origin and evolution of the layered deposits in the Valles Marineris, Mars, *Icarus*, *70*(3), 409–441, doi:10.1016/0019-1035(87)90086-8.

Nellessen, M. A. et al. (2018), Distribution and Analysis of Calcium Sulfate-Cemented Sandstones Along the MSL Traverse, Gale Crater, Mars, *49th Lunar Planet. Sci. Conf.*, Abstract #2858.

Newsom, H. E. et al. (2017), Increasing Occurrence of Sandstone Cemented with Calcium Sulfate on Mount Sharp, Gale Crater, Mars, *48th Lunar Planet. Sci. Conf.*, Abstract #2495.

Oelkers, E. H., J. Schott, and J.-L. Devidal (1994), The effect of aluminum, pH, and chemical affinity on the rates of aluminosilicate dissolution reactions, *Geochim. Cosmochim. Acta*, *58*(9), 2011–2024, doi:10.1016/0016-7037(94)90281-X.

Ojha, L., M. B. Wilhelm, S. L. Murchie, A. S. McEwen, J. J. Wray, J. Hanley, M. Massé, and M. Chojnacki (2015), Spectral evidence for hydrated salts in recurring slope lineae on Mars, *Nat. Geosci.*, *8*(11), 829–832, doi:10.1038/ngeo2546.

Ollila, A. M., J. G. Blank, R. C. Wiens, J. Lasue, H. E. Newsom, S. M. Clegg, A. Cousin, and S. Maurice (2011), Preliminary Results on the Capabilities of the ChemCam Laser-Induced Breakdown Spectroscopy (LIBS) Instrument to Detect Carbon on Mars, *42nd Lunar Planet. Sci. Conf.*, Abstract #2395.

Ormö, J., G. Komatsu, M. A. Chan, B. Beitler, and W. T. Parry (2004), Geological features indicative of processes related to the hematite formation in Meridiani Planum and Aram Chaos, Mars: a comparison with diagenetic hematite deposits in southern Utah, USA, *Icarus*, *171*(2), 295–316, doi:10.1016/j.icarus.2004.06.001.

Paik, I. S., M. Huh, Y. H. So, J. E. Lee, and H. J. Kim (2007), Traces of evaporites in Upper Cretaceous lacustrine deposits of Korea: Origin and paleoenvironmental implications, *J. Asian Earth Sci.*, *30*(1), 93–107, doi:10.1016/j.jseaes.2006.07.013.

Parry, W. T., M. A. Chan, and B. P. Nash (2009), Diagenetic characteristics of the Jurassic Navajo Sandstone in the Covenant oil field, central Utah thrust belt, *Am. Assoc. Pet. Geol. Bull.*, *93*(8), 1039–1061, doi:10.1306/04270908170.

Patrick, W. H., and R. A. Khalid (1974), Phosphate Release and Sorption by Soils and Sediments: Effect of Aerobic and Anaerobic Conditions, *Science (80-.).*, *186*(4158), 53–55, doi:10.1126/science.186.4158.53.

Payré, V. et al. (2017a), Alkali trace elements in Gale crater, Mars, with ChemCam: Calibration update and geological implications, *J. Geophys. Res. Planets*, *119*(6), 1276–1301, doi:10.1002/2016JE005201.

Payré, V. et al. (2017b), Copper Enrichments at Kimberley, Gale Crater, Mars, *48th Lunar Planet. Sci. Conf.*, Abstract #2097.

Pilorget, C., and F. Forget (2016), Formation of gullies on Mars by debris flows triggered by CO2 sublimation, *Nat. Geosci.*, *9*(1), 65–69, doi:10.1038/ngeo2619.

Pourbaix, M. (1966), Atlas of Electrochemical Equilibria in Aqueous Solutions, *Pergamon Press*.

Rampe, E. B. et al. (2017), Mineralogy of an ancient lacustrine mudstone succession from the Murray

formation, Gale crater, Mars, *Earth Planet. Sci. Lett.*, *471*, 172–185, doi:10.1016/j.epsl.2017.04.021.

Rapin, W. (2016), Hydratation de la surface de Mars à partir des données du rover Curiosity, Université de Toulouse.

Rapin, W. et al. (2016), Hydration state of calcium sulfates in Gale crater, Mars: Identification of bassanite veins, *Earth Planet. Sci. Lett.*, *452*, 197–205, doi:10.1016/j.epsl.2016.07.045.

Rapin, W. et al. (2017), Quantification of water content by laser induced breakdown spectroscopy on Mars, *Spectrochim. Acta Part B At. Spectrosc.*, *130*, 82–100, doi:10.1016/j.sab.2017.02.007.

Rapin, W. et al. (2018), Briny Waters Evidenced by Magnesium Sulfate Rich Layers Discovered In Situ at Gale Crater, *49th Lunar Planet. Sci. Conf.*, Abstract #2936.

Robertson, K., and D. Bish (2013), Constraints on the distribution of CaSO4·nH2O phases on Mars and implications for their contribution to the hydrological cycle, *Icarus*, doi:10.1016/j.icarus.2012.10.028.

Ruff, S. W. et al. (2011), Characteristics, distribution, origin, and significance of opaline silica observed by the Spirit rover in Gusev crater, Mars, *J. Geophys. Res.*, *116*(E7), E00F23, doi:10.1029/2010JE003767.

Sallé, B., D. A. Cremers, S. Maurice, and R. C. Wiens (2005), Laser-induced breakdown spectroscopy for space exploration applications: Influence of the ambient pressure on the calibration curves prepared from soil and clay samples, *Spectrochim. Acta Part B At. Spectrosc.*, *60*(4), 479–490, doi:10.1016/J.SAB.2005.02.009.

Santschi, P., P. Höhener, G. Benoit, and M. Buchholtz-ten Brink (1990), Chemical processes at the sediment-water interface, *Mar. Chem.*, *30*, 269–315, doi:10.1016/0304-4203(90)90076-O.

Sautter, V. et al. (2014), Igneous mineralogy at Bradbury Rise: The first ChemCam campaign at Gale crater, *J. Geophys. Res. Planets*, *119*(1), 30–46, doi:10.1002/2013JE004472.

Sautter, V. et al. (2015), In situ evidence for continental crust on early Mars, *Nat. Geosci.*, *8*(8), 605–609, doi:10.1038/ngeo2474.

Sautter, V. et al. (2016), Magmatic complexity on early Mars as seen through a combination of orbital, in-situ and meteorite data, *Lithos*, *254–255*, 36–52, doi:10.1016/j.lithos.2016.02.023.

Schmidt, F., F. Andrieu, F. Costard, M. Kocifaj, and A. G. Meresescu (2017), Formation of recurring slope lineae on Mars by rarefied gas-triggered granular flows, *Nat. Geosci.*, *10*(4), 270–273, doi:10.1038/ngeo2917.

Schmidt, M. E. et al. (2014), Geochemical diversity in first rocks examined by the Curiosity Rover in Gale Crater: Evidence for and significance of an alkali and volatile-rich igneous source, *J. Geophys. Res. Planets*, *119*(1), 64–81, doi:10.1002/2013JE004481.

Schwenzer, S. P. et al. (2012), Gale Crater: Formation and post-impact hydrous environments, *Planet. Space Sci.*, *70*(1), 84–95, doi:10.1016/j.pss.2012.05.014.

Schwenzer, S. P. et al. (2016), Fluids during diagenesis and sulfate vein formation in sediments at Gale crater, Mars, *Meteorit. Planet. Sci.*, *28*, doi:10.1111/maps.12668.

Scott, D. H., K. L. Tanaka, and P. Geology (1986), *Geologic map of the western equatorial region of Mars, Scale 1:15,000,000,* .

Sefton-Nash, E., D. C. Catling, S. E. Wood, P. M. Grindrod, and N. A. Teanby (2012), Topographic, spectral and thermal inertia analysis of interior layered deposits in Iani Chaos, Mars, *Icarus*,

221(1), 20–42, doi:10.1016/J.ICARUS.2012.06.036.

Sharp, R. P. (1973), Mars: Troughed terrain, *J. Geophys. Res.*, *78*(20), 4063–4072, doi:10.1029/JB078i020p04063.

Siebach, K. L., J. P. Grotzinger, L. C. Kah, K. M. Stack, M. Malin, R. Léveillé, and D. Y. Sumner (2014), Subaqueous shrinkage cracks in the Sheepbed mudstone: Implications for early fluid diagenesis, Gale crater, Mars, *J. Geophys. Res. Planets*, *119*(7), 1597–1613, doi:10.1002/2014JE004623.

Sirven, J.-B., B. Sallé, P. Mauchien, J.-L. Lacour, S. Maurice, and G. Manhès (2007), Feasibility study of rock identification at the surface of Mars by remote laser-induced breakdown spectroscopy and three chemometric methods, *J. Anal. At. Spectrom.*, *22*(12), 1471, doi:10.1039/b704868h.

Smith, M. W., J. L. Carrivick, and D. J. Quincey (2016), Structure from motion photogrammetry in physical geography, *Prog. Phys. Geogr.*, *40*(2), 247–275, doi:10.1177/0309133315615805.

Smith, P. H. et al. (2009), H2O at the Phoenix landing site., *Science*, doi:10.1126/science.1172339.

Squyres, S. W. (2004), In Situ Evidence for an Ancient Aqueous Environment at Meridiani Planum, Mars, *Science (80-.).*, *306*(5702), 1709–1714, doi:10.1126/science.1104559.

Squyres, S. W., and A. H. Knoll (2005), Sedimentary rocks at Meridiani Planum: Origin, diagenesis, and implications for life on Mars, *Earth Planet. Sci. Lett.*, doi:10.1016/j.epsl.2005.09.038.

Squyres, S. W. et al. (2004), The Spirit Rover's Athena science investigation at Gusev crater, Mars, *Science (80-.).*, doi:10.1126/science.3050794.

Squyres, S. W. et al. (2008), Detection of Silica-Rich Deposits on Mars, *Science (80-.).*, *320*(5879), 1063–1067, doi:10.1126/science.1155429.

Squyres, S. W. et al. (2012), Ancient Impact and Aqueous Processes at Endeavour Crater, Mars, *Science (80-.).*, *336*(6081), 570–576, doi:10.1126/science.1220476.

Stack, K. M., and J. P. Grotzinger (2015), Constraining the Relative Timing and Duration of an Ancient Fluvio-Lacustrine System in Gale Crater Using MSL Curiosity Rover Observations, *46th Lunar Planet. Sci. Conf.*, Abstract #2012.

Stack, K. M. et al. (2014), Diagenetic origin of nodules in the Sheepbed member, Yellowknife Bay formation, Gale crater, Mars, *J. Geophys. Res. Planets*, *119*(7), 1637–1664, doi:10.1002/2014JE004617.

Stein, N. et al. (2018), Desiccation cracks provide evidence of lake drying on Mars, Sutton Island member, Murray formation, Gale Crater, *Geology*, *46*(6), 515–518, doi:10.1130/G40005.1.

Stillman, D. E., T. I. Michaels, and R. E. Grimm (2017), Characteristics of the numerous and widespread recurring slope lineae (RSL) in Valles Marineris, Mars, *Icarus*, *285*, 195–210, doi:10.1016/j.icarus.2016.10.025.

Tanaka, K. L. (1986), The stratigraphy of Mars, *J. Geophys. Res.*, *91*(B13), E139, doi:10.1029/JB091iB13p0E139.

Tanaka, K. L., and D. H. Scott (1987), Geologic map of the polar regions of Mars, *IMAP*.

Tanaka, K. L., S. J. Robbins, C. M. Fortezzo, J. A. Skinner, and T. M. Hare (2014), The digital global geologic map of Mars: Chronostratigraphic ages, topographic and crater morphologic characteristics, and updated resurfacing history, *Planet. Space Sci.*, *95*, 11–24, doi:10.1016/J.PSS.2013.03.006.

Thomas, N. H., B. L. Ehlmann, D. E. Anderson, W. Rapin, S. Schröder, O. Forni, S. M. Clegg, R. C. Wiens,

O. Gasnault, and S. Maurice (2017), ChemCam Survey of Volatile Elements in the Murray Formation, Gale Crater, Mars, *48th Lunar Planet. Sci. Conf.*, Abstract #2756.

Thomas, N. H. et al. (2018), MSL ChemCam Observations of Chloride Salts in Gale Crater, Mars, *49th Lunar Planet. Sci. Conf.*, Abstract #2876.

Thompson, L. M., A. A. Fraeman, J. A. Berger, N. I. Boyd, E. Desouza, R. Gellert, C. O'Connell-Cooper, J. G. Spray, and A. S. Yen (2018), APXS Determined Chemistry of the Vera Rubin (Hematite) Ridge, Gale Crater, Mars: Implications for Hematite Signature Origin, *49th Lunar Planet. Sci. Conf.*, Abstract #2826.

Thomson, B. J., N. T. Bridges, R. Milliken, A. Baldridge, S. J. Hook, J. K. Crowley, G. M. Marion, C. R. de Souza Filho, A. J. Brown, and C. M. Weitz (2011), Constraints on the origin and evolution of the layered mound in Gale Crater, Mars using Mars Reconnaissance Orbiter data, *Icarus*, *214*(2), 413–432, doi:10.1016/j.icarus.2011.05.002.

De Toffoli, B., N. Mangold, M. Massironi, R. Pozzobon, J. L'Haridon, and G. Cremonese (n.d.), Comparative planetary structural asset analysis: insights on Martian sulfate vein networks and at Bletterbach, north-eastern Italy, *(in prep)*.

Tognoni, E., V. Palleschi, M. Corsi, and G. Cristoforetti (2002), Quantitative micro-analysis by laser-induced breakdown spectroscopy: a review of the experimental approaches, *Spectrochim. Acta Part B At. Spectrosc.*, *57*(7), 1115–1130, doi:10.1016/S0584-8547(02)00053-8.

Tosca, N. J., and S. M. McLennan (2006), Chemical divides and evaporite assemblages on Mars, *Earth Planet. Sci. Lett.*, *241*(1–2), 21–31, doi:10.1016/j.epsl.2005.10.021.

Tosca, N. J., S. M. McLennan, B. C. Clark, J. P. Grotzinger, J. A. Hurowitz, A. H. Knoll, C. Schröder, and S. W. Squyres (2005), Geochemical modeling of evaporation processes on Mars: Insight from the sedimentary record at Meridiani Planum, *Earth Planet. Sci. Lett.*, *240*(1), 122–148, doi:10.1016/j.epsl.2005.09.042.

Tosca, N. J., I. A. M. Ahmed, B. M. Tutolo, A. Ashpitel, and J. A. Hurowitz (2018), Magnetite authigenesis and the warming of early Mars, *Nat. Geosci.*, doi:10.1038/s41561-018-0203-8.

Treiman, A. H. et al. (2016), Mineralogy, provenance, and diagenesis of a potassic basaltic sandstone on Mars: CheMin X-ray diffraction of the Windjana sample (Kimberley area, Gale Crater), *J. Geophys. Res. Planets*, *121*(1), 75–106, doi:10.1002/2015JE004932.

Valente, T. M., and C. Leal Gomes (2009), Occurrence, properties and pollution potential of environmental minerals in acid mine drainage, *Sci. Total Environ.*, *407*(3), 1135–1152, doi:10.1016/j.scitotenv.2008.09.050.

VanBommel, S. J., R. Gellert, J. A. Berger, J. L. Campbell, L. M. Thompson, K. S. Edgett, M. J. McBride, M. E. Minitti, I. Pradler, and N. I. Boyd (2016), Deconvolution of distinct lithology chemistry through oversampling with the Mars Science Laboratory Alpha Particle X-Ray Spectrometer, *X-Ray Spectrom.*, *45*(3), 155–161, doi:10.1002/xrs.2681.

Vaniman, D., M. D. Dyar, R. Wiens, A. Ollila, N. Lanza, J. Lasue, J. M. Rhodes, S. Clegg, and H. Newsom (2012), Ceramic ChemCam Calibration Targets on Mars Science Laboratory, *Space Sci. Rev.*, *170*(1–4), 229–255, doi:10.1007/s11214-012-9886-0.

Vaniman, D. T. et al. (2014), Mineralogy of a mudstone at Yellowknife Bay, Gale crater, Mars., *Science*, *343*(6169), 1243480, doi:10.1126/science.1243480.

Vaniman, D. T. et al. (2017), Calcium Sulfates at Gale Crater and Limitations on Gypsum Stability, *48th Lunar Planet. Sci. Conf.*, Abstract #1661.

Vasavada, A. R. et al. (2014), Overview of the Mars Science Laboratory mission: Bradbury Landing to Yellowknife Bay and beyond, *J. Geophys. Res. E Planets*, *119*(6), 1134–1161, doi:10.1002/2014JE004622.

Wang, A. et al. (2006), Evidence of phyllosilicates in Wooly Patch, an altered rock encountered at West Spur, Columbia Hills, by the Spirit rover in Gusev crater, Mars, *J. Geophys. Res. E Planets*, doi:10.1029/2005JE002516.

Ward, A. W. (1979), Yardangs on Mars: Evidence of recent wind erosion, *J. Geophys. Res.*, *84*(B14), 8147, doi:10.1029/JB084iB14p08147.

Warren, J. K. (2016), *Evaporites*, Springer International Publishing, Cham.

Watkins, J. A., J. Grotzinger, N. Stein, S. G. Banham, S. Gupta, D. Rubin, K. M. Stack, and K. S. Edgett (2016), Paleotopography of Erosional Unconformity, Base of Stimson Formation, Gale Crater, Mars, *47th Lunar Planet. Sci. Conf.*, Abstract #2939.

Wellington, D. F., J. F. Bell, J. R. Johnson, K. M. Kinch, M. S. Rice, A. Godber, B. L. Ehlmann, A. A. Fraeman, and C. Hardgrove (2017), Visible to near-infrared MSL/Mastcam multispectral imaging: Initial results from select high-interest science targets within Gale Crater, Mars, *Am. Mineral.*, *102*(6), 1202–1217, doi:10.2138/am-2017-5760CCBY.

Wellington, D. F., J. R. Johnson, P.-Y. Meslin, and J. F. I. I. I. Bell (2018), Iron Meteorite Candidates Within Gale Crater, Mars, from MSL/Mastcam Multispectral Observations, *49th Lunar Planet. Sci. Conf.*, Abstract #1832.

Westoby, M. J., J. Brasington, N. F. Glasser, M. J. Hambrey, and J. M. Reynolds (2012), 'Structure-from-Motion' photogrammetry: A low-cost, effective tool for geoscience applications, *Geomorphology*, *179*, 300–314, doi:10.1016/J.GEOMORPH.2012.08.021.

Wiens, R. C., and S. Maurice (2015), ChemCam: Chemostratigraphy by the First Mars Microprobe, *Elements*, *11*(1), 33–38, doi:10.2113/gselements.11.1.33.

Wiens, R. C. et al. (2012), The ChemCam Instrument Suite on the Mars Science Laboratory (MSL) Rover: Body Unit and Combined System Tests, *Space Sci. Rev.*, *170*(1–4), 167–227, doi:10.1007/s11214-012-9902-4.

Wiens, R. C. et al. (2013), Pre-flight calibration and initial data processing for the ChemCam laser-induced breakdown spectroscopy instrument on the Mars Science Laboratory rover, *Spectrochim. Acta Part B At. Spectrosc.*, *82*, 1–27, doi:10.1016/j.sab.2013.02.003.

Williams, R. M. E., and M. C. Malin (2004), Evidence for late stage fluvial activity in Kasei Valles, Mars, *J. Geophys. Res.*, *109*(E6), E06001, doi:10.1029/2003JE002178.

Williams, R. M. E. et al. (2013), Martian Fluvial Conglomerates at Gale Crater, *Science (80-.).*, *340*(6136), 1068–1072, doi:10.1126/science.1237317.

Williams, S. H., and J. R. Zimbelman (1994), "White Rock": An eroded Martian lacustrine deposit(?), *Geology*, *22*(2), 107, doi:10.1130/0091-7613(1994)022<0107:WRAEML>2.3.CO;2.

Wordsworth, R. D., L. Kerber, R. T. Pierrehumbert, F. Forget, and J. W. Head (2015), Comparison of "warm and wet" and "cold and icy" scenarios for early Mars in a 3-D climate model, *J. Geophys. Res. Planets*, *120*(6), 1201–1219, doi:10.1002/2015JE004787.

Wray, J. J., S. L. Murchie, S. W. Squyres, F. P. Seelos, and L. L. Tornabene (2009), Diverse aqueous environments on ancient Mars revealed in the southern highlands, *Geology*, *37*(11), 1043–1046, doi:10.1130/G30331A.1.

Yen, A. S. et al. (2008), Hydrothermal processes at Gusev Crater: An evaluation of Paso Robles class soils, *J. Geophys. Res.*, *113*(E6), E06S10, doi:10.1029/2007JE002978.

Yen, A. S. et al. (2017), Multiple stages of aqueous alteration along fractures in mudstone and sandstone strata in Gale Crater, Mars, *Earth Planet. Sci. Lett.*, *1*, 1–13, doi:10.1016/j.epsl.2017.04.033.

Zhou, A., H. Tang, and D. Wang (2005), Phosphorus adsorption on natural sediments: Modeling and effects of pH and sediment composition, *Water Res.*, *39*(7), 1245–1254, doi:10.1016/j.watres.2005.01.026.

UNIVERSITE ECOLOGIE BRETAGNE GEOSCIENCES LOIRE AGRONOMIE ALIMENTATION

UNIVERSITÉ DE NANTES

Titre Processus diagénétiques sur Mars : analyse par l'instrument ChemCam à bord du rover Curiosity

Mots clés Mars, cratère Gale, exploration *in situ*, LIBS, géochimie, diagénèse

Résumé L'exploration de la surface de Mars par le rover *Curiosity*, au niveau du cratère Gale, a permis de révéler la présence de conditions habitables par le passé, à travers l'observation de dépôts sédimentaires fluvio-lacustres attestant d'une activité hydrologique prolongée. Ces roches portent également les stigmates de l'évolution complexe des sédiments lors de la diagénèse, sous forme de veines, nodules et concrétions s'étant formés par la circulation de fluides en sub-surface.

À bord du rover, la spectroscopie de plasma induit par laser (LIBS) de l'instrument ChemCam permet une mesure chimique à petite échelle, particulièrement adaptée à l'analyse de tels éléments géologiques. Cette étude démontre que les veines de Ca-sulfate, observées dans toutes les unités géologiques traversées par le rover, présentent des enrichissements ponctuels en Fe témoignant de conditions de formation oxydantes lors de la diagénèse tardive. Par ailleurs, l'une des structures sédimentaires du cratère est caractérisée par des signatures spectrales d'hématite depuis l'orbite, suggérant que sa formation est en partie liée à des processus d'oxydo-réduction, pendant et/ou après le dépôt des sédiments. À cet endroit, ChemCam a mis en évidence la mobilité du Fe lors de la diagénèse, ainsi que la formation d'oxyde de Fe en association avec les veines de Ca-sulfate.

Pour conclure, ces travaux montrent l'importance des interactions fluides-roches, comme les réactions d'oxydo-réduction, lors de l'enfouissement des sédiments martiens, processus devant être pris en compte pour éviter des erreurs d'interprétation sur l'environnement de dépôt et l'intérêt exo-biologique des sédiments étudiés.

Title Diagenetic processes on Mars: analysis by the ChemCam instrument on the Curiosity rover

Keywords Mars, Gale crater, *in situ* exploration, LIBS, geochemistry, diagenesis

Abstract The exploration of the Martian surface by the rover *Curiosity*, at Gale crater, has unveiled past habitable conditions on the planet with evidences for sustained period of surface aqueous activity recorded in fluvio-lacustrine sedimentary deposits. In addition, the rocks also bear traces of the complex post-depositional evolution of the sediments during diagenesis, in the form of small-scale fracture-fills, nodules, and concretions that formed by sub-surface fluid circulations.

On board, the rover, the Laser-Induced Breakdown Spectroscopy (LIBS) performed by the ChemCam instrument provide remote fine-scale chemical measurements, especially suited to the analysis of such geological items. This study demonstrates that the Ca-sulfate-bearing veins, observed across all geological terrains, show enrichments in Fe at specific locations along the rover traverse, tracing localized oxidizing conditions at the time of their formation in the later stages of diagenesis. Additionally, a key sedimentary structure in Gale crater is characterized by hematite spectral signatures from orbit, suggesting the involvement of redox-driven processes in its formation, either related to primary deposition or post-depositional conditions. There, *in situ* ChemCam observations highlight the mobility of Fe during diagenesis and the authigenic formation of Fe-oxide in association with Ca-sulfate bearing features.

As such, this work attests of significant fluid interactions, and notably redox-driven chemical reactions, affecting the Martian sediments after their deposition and burial, which need to be taken into account in order to avoid any misinterpretations on the environment of deposition and its habitability.